INFORMATION TO USERS

This manuscript has been reproduced from the microfilm master. UMI films the text directly from the original or copy submitted. Thus, some thesis and dissertation copies are in typewriter face, while others may be from any type of computer printer.

The quality of this reproduction is dependent upon the quality of the copy submitted. Broken or indistinct print, colored or poor quality illustrations and photographs, print bleedthrough, substandard margins, and improper alignment can adversely affect reproduction.

In the unlikely event that the author did not send UMI a complete manuscript and there are missing pages, these will be noted. Also, if unauthorized copyright material had to be removed, a note will indicate the deletion.

Oversize materials (e.g., maps, drawings, charts) are reproduced by sectioning the original, beginning at the upper left-hand corner and continuing from left to right in equal sections with small overlaps. Each original is also photographed in one exposure and is included in reduced form at the back of the book.

Photographs included in the original manuscript have been reproduced xerographically in this copy. Higher quality 6" x 9" black and white photographic prints are available for any photographs or illustrations appearing in this copy for an additional charge. Contact UMI directly to order.

U·M·I

University Microfilms International
A Bell & Howell Information Company
300 North Zeeb Road, Ann Arbor, MI 48106-1346 USA
313/761-4700 800/521-0600

Order Number 9408466

Advanced techniques for measuring primary mirrors for astronomical telescopes

Burge, James Howard, Ph.D.

The University of Arizona, 1993

Copyright ©1993 by Burge, James Howard. All rights reserved.

U·M·I
300 N. Zeeb Rd.
Ann Arbor, MI 48106

ADVANCED TECHNIQUES FOR MEASURING PRIMARY MIRRORS FOR ASTRONOMICAL TELESCOPES

by

James Howard Burge

Copyright © James H. Burge 1993

A Dissertation Submitted to the Faculty of the

COMMITTEE ON OPTICAL SCIENCES (GRADUATE)

In Partial Fulfillment of the Requirements
For the Degree of

DOCTOR OF PHILOSOPHY

In the Graduate College

THE UNIVERSITY OF ARIZONA

1 9 9 3

THE UNIVERSITY OF ARIZONA
GRADUATE COLLEGE

As members of the Final Examination Committee, we certify that we have read the dissertation prepared by JAMES HOWARD BURGE

entitled Advanced Techniques for Measuring Primary Mirrors for Astronomical Telescopes

and recommend that it be accepted as fulfilling the dissertation requirement for the Degree of PhD

Roger Angel	Roger Angel	7/23/93 Date
Hubert Martin III	Hubert Martin III	7/23/93 Date
Roland Shack	Roland Shack	7/23/93 Date
John Greivenkamp	J E Greivenkamp	7/23/93 Date
		Date

Final approval and acceptance of this dissertation is contingent upon the candidate's submission of the final copy of the dissertation to the Graduate College.

I hereby certify that I have read this dissertation prepared under my direction and recommend that it be accepted as fulfilling the dissertation requirement.

Roger Angel Roger Angel 7/23/93
Dissertation Director Date

STATEMENT BY AUTHOR

This dissertation has been submitted in partial fulfillment of requirements for an advanced degree at The University of Arizona and is deposited in the University Library to be made available to borrowers under rules of the Library.

Brief quotations from this dissertation are allowable without special permission, provided that accurate acknowledgment of source is made. Requests for permission for extended quotation from or reproduction of this manuscript in whole or in part may be granted by the copyright holder.

SIGNED: 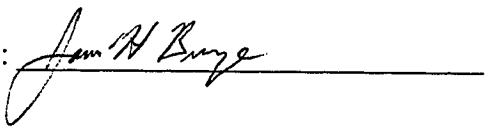

ACKNOWLEDGMENTS

This research would not have been possible without the strong support from Steward Observatory and the National Science Foundation. My research was aimed at supporting the fabrication of primary mirrors for Steward Observatory telescope projects. Steward Observatory, in turn, supported my research and my professional growth. This work was largely funded by the National Science Foundation under Cooperative agreement AST 8911701.

This work has benefited from discussions with so many individuals that I could not possibly acknowledge each person. In addition, much of the hardware described in this dissertation was fabricated at Steward Observatory by a talented and enthusiastic team of scientists, opticians, engineers, and technicians. The success of primary mirror polishing and testing at the Steward Observatory Mirror Lab is a direct result of this group effort under the leadership of Dr. Buddy Martin. I am grateful for the opportunity to contribute to such a successful team.

I thank the many people who reviewed this manuscript in its various stages and suggested numerous improvements. I especially thank my committee -- Drs. Angel, Greivenkamp, Martin, and Shack -- for putting in the long hours to carefully review this large amount of information.

Most importantly, I thank my wife, Laura, and children, Charlie and Max for their understanding and support. Much of this manuscript was written using time that rightfully belonged to them.

TABLE OF CONTENTS

page

LIST OF FIGURES 10

LIST OF TABLES 16

ABSTRACT 18

INTRODUCTION 20

CHAPTER 1
OPTICAL MEASUREMENT OF PRIMARY MIRRORS:
AN INTRODUCTION AND HISTORICAL BACKGROUND 24

1.1. INTRODUCTION 24

1.2. REFLECTIVE TELESCOPES: PAST, PRESENT, AND FUTURE 25

1.3. SHAPE OF THE PRIMARY MIRROR 31

1.4. SPHERICAL ABERRATION 32

1.5. PRIMARY MIRROR FABRICATION 36

1.6. CENTER OF CURVATURE TESTING FOR PRIMARY MIRRORS 38

1.7. ALTERNATIVES TO CENTER OF CURVATURE TESTS 42

1.8. SPECIFICATION OF THE OPTICAL FIGURE 44

1.9. ADVANCED OPTICAL TESTING OF PRIMARY MIRRORS 51

TABLE OF CONTENTS -- *continued*

page

SECTION I CLASSICAL SLOPE TESTS 54

CHAPTER 2
THE WIRE TEST 55

2.1. INTRODUCTION 55

2.2. DESCRIPTION OF TEST 56

2.3. DATA REDUCTION 59

2.4. ANALYSIS OF SYSTEMATIC ERROR FROM BEAMSPLITTER 62

2.5. RESULTS FROM TESTING A 3.5-m *f*/1.75 PRIMARY MIRROR 66

2.6. INTERFEROMETRIC MEASUREMENT OF LONGITUDINAL SPHERICAL ABERRATION 71

2.7. CONCLUSION 75

CHAPTER 3
THE SCANNING PENTAPRISM TEST 76

3.1. INTRODUCTION 76

3.2. TEST DESCRIPTION 77

3.3. ALIGNMENT SENSITIVITY 79

3.4. TEST OF A 1.8-m *f*/1 PRIMARY MIRROR 87

3.5. IMPROVEMENT BY SCANNING FULL DIAMETER 99

3.6. CONCLUSION 103

TABLE OF CONTENTS -- *continued*

page

SECTION II INTERFEROMETRY WITH NULL CORRECTORS 104

CHAPTER 4
INTERFEROMETRIC MEASUREMENT OF PRIMARY MIRRORS
WITH NULL CORRECTORS 105

4.1. INTRODUCTION 105

4.2. DESCRIPTION OF NULL TEST 108

4.3. TYPES OF NULL CORRECTORS 109

4.4. INTERNAL ALIGNMENT OF THE NULL LENS 114

4.5. IMAGING DISTORTION 116

4.6. DIFFRACTION EFFECTS IN OPTICAL TESTING 121

4.7. GHOST REFLECTIONS AND SPURIOUS FRINGES 123

4.8. IMAGING OPTICS 126

4.9. ENVIRONMENTAL EFFECTS 126

4.10. SUBTRACTION OF LOW ORDER AZIMUTHAL ERRORS 130

4.11. INTERFEROMETRIC EVALUATION TECHNIQUES 132

4.12. IMPLEMENTATION OF NULL TEST 134

4.13. CONCLUSION 135

CHAPTER 5
OPTICAL DESIGN OF NULL CORRECTORS
FOR HIGHLY ASPHERIC PRIMARY MIRRORS 136

5.1. INTRODUCTION 136

5.2. SYSTEM DESIGN STRATEGY FOR NULL CORRECTORS 137

5.3. COMPUTER-ASSISTED OPTICAL DESIGN OF NULL
CORRECTORS 142

TABLE OF CONTENTS -- *continued*

page

5.4. TOLERANCE ANALYSIS OF NULL CORRECTORS 146

5.5. REFRACTIVE NULL CORRECTOR FOR 6.5-m *f*/1.25 PRIMARY MIRRORS 158

5.6. INFRARED NULL CORRECTORS USING ASPHERIC SURFACES 163

5.7. REFLECTIVE NULL CORRECTOR FOR 8.4-m *f*/1.14 PRIMARY MIRRORS 167

5.8. CONCLUSION 172

SECTION III HOLOGRAPHIC TEST OF NULL CORRECTORS 174

CHAPTER 6
HOLOGRAPHIC MEASUREMENT OF NULL CORRECTORS: THEORY AND DESIGN 175

6.1. INTRODUCTION 175

6.2. DESCRIPTION OF HOLOGRAPHIC NULL LENS TEST 177

6.3. OPTICAL TESTING WITH COMPUTER-GENERATED HOLOGRAMS 179

6.4. DESIGN AND FABRICATION OF CGH FOR NULL LENS TEST 186

6.5. OPTIMIZATION OF DIFFRACTION EFFECTS 196

6.6. ERROR ANALYSIS 1: ERRORS FROM FABRICATION OF CGH 204

6.7. ERROR ANALYSIS 2: ERRORS IN USE OF CGH 211

6.8. ERROR ANALYSIS 3: ERRORS IN DATA REDUCTION 217

6.9. CONCLUSION 218

TABLE OF CONTENTS -- *continued*

page

CHAPTER 7
HOLOGRAPHIC MEASUREMENT OF NULL CORRECTORS: MEASUREMENT RESULTS AND ANALYSIS 219

7.1. INTRODUCTION 219

7.2. CGH NULL LENS TESTS FOR TWO 3.5-m *f*/1.75 PRIMARY MIRRORS 221

7.3. MEASUREMENT OF NULL LENS WITH A KNOWN ERROR 235

7.4. VERIFICATION WITH A CGH REPRESENTING A SPHERICAL MIRROR 236

7.5. HOLOGRAM ERRORS FOR A NULL LENS TEST FOR A 3.5-m *f*/1.5 PRIMARY MIRROR 241

7.6. FUTURE RESEARCH FOR HOLOGRAPHIC TESTING OF NULL CORRECTORS 244

7.7. CONCLUSION 248

CONCLUSION 250

APPENDIX A PRIMARY MIRRORS FOR ASTRONOMICAL TELESCOPES 252

APPENDIX B NULL CORRECTOR TOLERANCES FOR THE WIYN 3.5-m *f*/1.75 PRIMARY MIRROR 255

APPENDIX C VISIBLE NULL CORRECTOR FOR A 6.5-m *f*/1.25 PRIMARY MIRROR: OPTICAL PRESCRIPTION AND TOLERANCE ANALYSIS 258

APPENDIX D INFRARED NULL CORRECTORS USING ASPHERIC SURFACES: OPTICAL PRESCRIPTION AND TOLERANCE ANALYSIS 261

APPENDIX E GREGORIAN NULL CORRECTORS: OPTICAL PRESCRIPTION AND TOLERANCE ANALYSIS 264

REFERENCES 276

LIST OF FIGURES

page

Figure 1.1. Schematic drawing of a typical optical telescope....26

Figure 1.2. Primary mirror diameter vs. year. 30

Figure 1.3. Relationship between wave aberration and transverse ray aberration....34

Figure 1.4. Graphical representations of spherical aberration through focus. 35

Figure 1.5. Foucault knife-edge test of a concave mirror. 39

Figure 1.6. Autocollimation test of a paraboloidal mirror....43

Figure 1.7. Structure function plots. 49

Figure 1.8. Historical increase in peak-to-valley asphericity of primary mirrors. 52

Figure 2.1. Diagram of wire test for 3 zones....57

Figure 2.2. Layout of the wire test as implemented for the testing of a 3.5-m *f*/1.75 primary....58

Figure 2.3. Layout of imaging geometry for the pins. 62

Figure 2.4. Spot diagram showing how a point on a pin will be asymmetrically blurred. 63

Figure 2.5. Variation in image shift of the outer pin with pupil diameter. 64

Figure 2.6. Variation of induced error in conic constant with pupil diameter. 65

Figure 2.7. Plot of the axial wire position showing the fit of the raw data for the radius measurement of the 3.5-m primary mirror....67

Figure 2.8. Residual surface slope errors from wire test of 3.5-m mirror....68

LIST OF FIGURES -- *continued*

page

Figure 2.9. Surface profile of 3.5-m mirror computed by integration of slope data.....69

Figure 2.10. Inferred error in apparent pin position based on the measured data and assuming +0.15% image shift.....70

Figure 2.11. Computer generated interferogram showing the normal zone aligned to reference marks.....72

Figure 2.12. Axial center of curvature position for infrared "wire test" of the WIYN primary mirror during asphérization.....73

Figure 2.13. Surface profile from IR wire test of the WIYN primary mirror during asphérization.....74

Figure 3.1. Schematic layout of the scanning pentaprism test.....78

Figure 3.2. Errors in the scanning beam.....82

Figure 3.3. Errors in the camera position.....82

Figure 3.4. Misalignment of the collimator, pentaprism, and scanning beam.....83

Figure 3.5. Angular errors in rail used to test the 1.8-m primary mirror.....90

Figure 3.6. Computer generated interferogram showing the measured figure of the 1.8-m *f*/1 primary mirror.....95

Figure 3.7. Sagittal spot motion for a single scan of the 1.8-m primary mirror.....96

Figure 3.8. Tangential spot motion for a single scan of the 1.8-m primary mirror.....96

Figure 3.9. Variation in conic constant fit with the radial extent of the data used for the fit.....97

Figure 3.10. Average radial sagittal ray deviation.....98

Figure 3.11. Average radial surface height.....99

Figure 3.12. Cubic spot motion with no balancing, balanced across a full diameter, and balanced only across a radius.....101

LIST OF FIGURES -- *continued*

page

Figure 3.13. Simulation of a radial scan of the 1.8-m primary mirror. 102

Figure 3.14. Simulation of a diametrical scan of the 1.8-m primary mirror. 103

Figure 4.1. Schematic drawing of null test. 105

Figure 4.2. Types of refractive null correctors used for the testing of large primary mirrors. 111

Figure 4.3. Shack cube interferometer. 113

Figure 4.4. Optomechanical layout of an integral null lens. 115

Figure 4.5. Fit of mapping function to measured positions of fiducial marks for the SOR primary. 120

Figure 4.6. Effect of diffraction from the edge of an optic. 122

Figure 4.7. Ghost fringe visibility as a function of surface reflectivity. 124

Figure 4.8. Isolated test tower at Steward Observatory Mirror Lab. 128

Figure 4.9. Sensitivity of Parks' algorithm for separating azimuthal test optic errors from those in the mirror. 131

Figure 5.1. Offner-type refractive null corrector. 138

Figure 5.2. Interferograms showing alignment errors of pure tilt, focus, and coma. 152

Figure 5.3. Optical layout of the visible null lens for 6.5-m $f/1.25$ primary mirrors with Shack cube interferometer and distortion-correcting relay. 159

Figure 5.4. Residual wavefront errors for visible refractive null lens for testing the 6.5-m $f/1.25$ primary mirror. 160

Figure 5.5. Mapping error for the null lens for testing the 6.5-m $f/1.25$ primary mirror. 161

Figure 5.6. Structure function from the error analysis of the visible null corrector for the 6.5-m $f/1.25$ primary. 162

LIST OF FIGURES -- *continued*

page

Figure 5.7. A compact infrared null corrector for the testing of a 6.5-m $f/1.25$ paraboloidal primary mirror. 165

Figure 5.8. Infrared null corrector for the testing of a 6.5-m $f/1.25$ paraboloidal primary mirror. 166

Figure 5.9. Optical layout of null lens for the LBT 8.4-meter $f/1.14$ primary mirrors. 168

Figure 5.10. Residual wavefront errors for visible reflective null lens for testing the 8.4-m $f/1.14$ primary mirrors. 169

Figure 5.11. Structure function from the error analysis of the visible null corrector for the LBT 8.4-m $f/1.14$ primaries. 170

Figure 6.1. Layout of CGH test of null lens. 178

Figure 6.2. Cross-section of a transmissive diffraction ruling. 181

Figure 6.3. Modified Twyman-Green interferometer for testing an aspheric mirror with a CGH. 182

Figure 6.4. Geometry for defining a CGH such that it returns the same wavefront as a perfect primary mirror. 187

Figure 6.5. Wavefront phase function required of a paraxial-focus CGH to test a null corrector for a 3.5-m $f/1.75$ primary mirror. 190

Figure 6.6. Center-to-center groove spacing for a paraxial-focus CGH used in third order to test a null corrector for a 3.5-m $f/1.75$ primary mirror. 191

Figure 6.7. CGH mapping function showing the relationship between mirror position and position on hologram. 192

Figure 6.8. Complex amplitude of light modulated by diffraction grating. 197

Figure 6.9. Variation in diffraction efficiency as a function of duty cycle D for a binary phase reflective CGH with an aluminum coating and quarter wave etch depth. 200

LIST OF FIGURES -- *continued*

page

Figure 6.10. Variation in diffraction efficiency as a function of etch depth for a binary phase reflective CGH with an aluminum coating and 50% duty cycle.....201

Figure 6.11. Rejection of stray diffraction orders.....202

Figure 6.12. Dependence of diffracted phase variation on etch depth and duty cycle variations for a pure phase grating centered around the design values of D=0.5 and 0.25λ etch depth.....210

Figure 7.1. Interferogram of computer-generated hologram through the ARC null lens.....224

Figure 7.2. Contour map of a single CGH measurement showing high-frequency hologram errors. 225

Figure 7.3. Contour map showing measured null lens error of 7.6 nm rms for ARC primary mirror as represented by a 36-term Zernike polynomial fit. 230

Figure 7.4. Contour map showing measured null lens error of 5.1 nm rms for WIYN primary mirror. 232

Figure 7.5. Comparison showing the excellent agreement between the predicted and actual measured effect of intentionally inducing a 90 μm spacing change in the ARC null lens. 236

Figure 7.6. Fizeau test of CGH as both convex and concave spheres. 238

Figure 7.7. Interferogram from mis-printed CGH of a spherical reflector. 239

Figure 7.8. Contour map of the errors in the hologram for testing a null lens for a 3.5-m *f*/1.5 primary mirror.....242

Figure 7.9. Interferograms showing the measurements of the second and third holograms with the null corrector for a 3.5-m *f*/1.5 primary mirror. 243

Figure B.1. Contributions of each error in the WIYN null lens to the system uncertainty in rms wavefront 257

LIST OF FIGURES -- *continued*

page

Figure B.2. Contributions of each error in the WIYN null lens to the system uncertainty in conic constant 257

Figure C.1. Layout of the visible null corrector for the 6.5-m *f*/1.25 primary mirrors. 258

Figure D.1. Layout with prescription of an interesting infrared null corrector for a 6.5-m *f*/1.25 primary mirror. 262

Figure D.2. Layout with prescription of the infrared null corrector that will be used for testing the 6.5-m *f*/1.25 primary mirrors 262

Figure E.1. Layout with prescription of the Gregorian null corrector for infrared testing of the MMT and Magellan 6.5-m *f*/1.25 primary mirrors. 266

Figure E.2. Layout with prescription of the Gregorian null corrector for visible testing of the MMT and Magellan 6.5-m *f*/1.25 primary mirrors. 268

Figure E.3. Layout with prescription of the infrared Gregorian null test for the LBT primary mirrors. 270

Figure E.4. Layout with prescription of the visible Gregorian null test for the LBT primary mirrors. 272

LIST OF TABLES

page

Table 1.1. Spherical aberration measured in existing telescopes 51

Table 2.1. Results from wire test on ARC 3.5-m $f/1.75$ primary 66

Table 3.1. Alignment degrees of freedom for scanning pentaprism test 81

Table 4.1. Null correctors analyzed for primary mirrors at Steward Observatory 107

Table 5.1. Adjustable parameters and sources of error associated with a single lens 140

Table 5.2. Contribution to rms wavefront from surface figures and index inhomogeneity 148

Table 5.3. Surface structure function for polished spherical surfaces. 156

Table 5.4. Null tests using the LBT Gregorian null corrector. 171

Table 6.1. Approximations to relevant functions for error analysis. 194

Table 6.2. Diffraction efficiency for reflection CGH with Al coating, $\lambda/4$ grooves, and 50% duty cycle. 199

Table 7.1. Summary of null lens measurements for 3.5-m $f/1.75$ primary mirrors. 222

Table 7.2. Corrections for CGH measurement of ARC null lens. 229

Table 7.3. Corrections for CGH measurement of WIYN null lens. 231

Table 7.4. Error budget for CGH null lens measurements for WIYN and ARC tests. 234

Table 7.5. Error budget for CGH null lens measurements for a 6.5-m $f/1.25$ primary mirror 247

LIST OF TABLES -- *continued*

page

Table A.1. Primary mirrors for astronomical telescopes. 252

Table B.1. Table of tolerances and error budget for null corrector for WIYN 3.5-m *f*/1.75 primary....255

Table C.1. Table of tolerances showing the structure function for the null corrector. 259

Table C.2. Table of tolerances showing the dependence of the rms wavefront and conic constant on the fabrication tolerances. 260

Table D.1. Table of tolerances for the MMT IR null corrector. 263

Table E.1. Tolerances for the infrared Gregorian null test of the 6.5-m *f*/1.25 primary mirrors.. 266

Table E.2. Tolerances for the visible Gregorian null test of the MMT and Magellan primary mirrors.. 268

Table E.3. Tolerances for the infrared Gregorian null test of the LBT primary mirror.. 270

Table E.4. Tolerances for the visible Gregorian null test of the LBT primary mirror... 272

Table E.5. LBT Gregorian null test -- tolerance table showing structure functions.... 274

ABSTRACT

The optical measurement of primary mirrors for astronomical telescopes has become increasingly challenging for two reasons. The mirrors, in addition to being larger, are faster and more aspheric in order to shorten the length of the telescope, and the required accuracy of the optical surfaces is more stringent. This dissertation presents improved methods for measuring these mirrors in the laboratory to the required accuracy.

The wire test and the scanning pentaprism test, which measure surface slope errors, were designed and run under computer control. The wire test was used to measure the conic constant of a 3.5-m $f/1.75$ primary mirror to an accuracy of ± 0.003 and the scanning pentaprism test measured the conic constant of a 1.8-m $f/1$ primary to ± 0.003. Improvements in these tests were identified that could increase the accuracy significantly.

Interferometric optical testing with null correctors is widely used for measuring aspheric surfaces to high accuracy. A system-level analysis of the null test is given. The test is optimized for wavefront accuracy, imaging distortion, and measurement noise from ghost reflections and diffraction. The optical design and analysis of null correctors, including designs for testing 6.5-m $f/1.25$ and 8.4-m $f/1.14$ primary mirrors are given. Several new null corrector designs and a method for performing tolerance analysis using structure functions are given.

An error in the null corrector, if not detected, would cause the primary mirror to be polished to the wrong shape. (The primary mirrors for the Hubble Space Telescope and the European New Technology Telescope were misshapen because of faulty null correctors.) A new test of null correctors is presented that uses a computer-generated

hologram (CGH) to synthesize a perfect primary mirror. When the CGH is measured through the null corrector, it appears as a perfect primary mirror. Apparent surface errors in this measurement can be attributed to errors in the null corrector. A complete error analysis of this test is given. This method has been proven on null correctors for 3.5-m primary mirrors, where it measured errors as small as 5.1 nm rms and confirmed the conic constants to ±0.000078.

INTRODUCTION

Reflecting telescopes have been used for over 300 years, since Sir Isaac Newton. Early in this century mirrors were established as superior to lenses for the largest telescopes. The size of the reflectors increased irregularly through the century, from the 60-inch and 100-inch mirrors on Mt. Wilson -- planned by Hale and polished and measured by Ritchey in the 1900's and 1910's -- to the 200-inch mirror on Mt. Palomar finished in the 1940's, and finally to a number of 6.5- to 10-m mirrors currently being fabricated for new generation of telescopes. These new mirrors are more steeply curved than previous primaries, so they have a larger departure from spherical. Measuring small figure errors in the presence of this large asphericity has required the development of new testing methods.

Not only size and difficulty but also quality has increased as astronomers have located observing sites that deliver sharper images and have designed telescopes and domes that cause less local image degradation. The current generation of giant mirrors have figure specifications more stringent than the previous generation of smaller mirrors.

The historical improvement in the quality of optical telescopes has required the development of more accurate testing methods because the ability to accurately fabricate large mirrors depends strongly on the ability to measure their shapes. The work described in this dissertation was motivated by the desire to make the world's most difficult primary mirrors to exceptional quality.

The optical measurement of primary mirrors for the next generation optical telescopes presents a serious challenge. These giant mirrors are more steeply curved than those of existing telescopes so they can collect much more light without requiring a much larger dome. These steeper curves make these mirrors an order of magnitude more difficult to test than previous mirrors. Not only are the mirrors more difficult to test, but the specifications have become tighter. The telescopes are expected to provide images with quarter arc second FWHM, matching the atmospheric blurring in the best conditions. To achieve this, errors due to the optical testing of the primary mirror are expected to degrade the image by less than 0.04 arc seconds.

The primary mirrors must be polished to about 20 nm rms to meet the stringent telescope requirements. To put this into perspective, if a finished eight-meter mirror were scaled up 125,000 times to the size of the Gulf of Mexico, the average bump would be only a tenth of an inch high.

The measurement of these mirrors is made difficult by the large departure from a spherical shape that the mirrors must have. This departure, as much as 1.4 mm peak-to-valley for the LBT 8.4-m $f/1.14$ primary mirrors, must be compensated in the optical test to an accuracy of about 100 parts-per-million. The testing can be done geometrically with a scanning test or interferometrically with the use of a null corrector. In either case, the large aspheric compensation by the optical measurement is extremely sensitive to errors in the test design and implementation.

The metrology (defined as the science of measurement) that is developed in this dissertation is limited to laboratory measurements. No attempt has been made to cover new research for measuring the mirror figure in the telescope using real or artificial star light. Also, the scope of this dissertation is limited to metrology for optical (including

infrared) telescopes. Radio telescopes and x-ray telescopes have completely different requirements and challenges that are not addressed in this work.

This dissertation is divided into a background chapter and three sections that cover different types of tests. Section I, which includes Chapters 2 and 3, describes two classical slope tests that were performed and analyzed at Steward Observatory. Section II includes Chapters 4 and 5 which describe design and analysis for interferometric tests using null correctors. Section III contains Chapters 6 and 7 which present analysis and results from a holographic optical test of null correctors.

Chapter 1 gives a review of optical testing for primary mirrors. It also gives the background and history of modern testing techniques and establishes some concepts and notation that are used in the rest of the dissertation. In this chapter, the shape of the mirror and the form of its aspheric departure are defined and explained. A review of fabrication and testing methods for primary mirrors is given. Optical specifications using structure functions are reviewed.

The simplest tests use reflected light to measure the slope of an optical surface. Chapter 2 gives a description of the wire test, which is a scanning measurement of the spherical aberration. This test was implemented to measure a 3.5-m $f/1.75$ primary mirror. An interesting application of this test using an infrared interferometer is explained. Chapter 3 describes the scanning pentaprism test, which is a highly accurate method of measuring spherical aberration in a primary mirror. This test was implemented on a 1.8-m $f/1.0$ primary mirror. These slope tests were not sufficiently accurate to meet the stringent telescope specifications.

Surface errors in primary mirrors are measured directly using interferometers with null correctors, which compensate for the aspheric departure of the surface. Chapter 4 gives a description of the null test and a review of null correctors. Important aspects that

should be considered in the design and fabrication of the systems to perform the null test are given. Chapter 5 outlines the procedure for designing and analyzing null correctors. Several examples of null correctors that were designed for the next generation telescope mirrors are given.

Null correctors that compensate for large amounts of asphericity are extremely sensitive to manufacturing errors. Since the primary mirrors are shaped according to the optical test, it is essential that an accurate certification of the test is made. The recent flaws in the Hubble Space Telescope and the New Technology Telescope were due to errors in the null correctors that were not detected until the telescopes were operational.

A new method for testing null correctors using computer-generated holograms (CGH) is presented in Chapter 6. The method is introduced and a review of optical testing with CGH is given. Descriptions of the hologram design and fabrication process are given, and a thorough error analysis is also presented in this chapter. Chapter 7 gives data to support the accuracy of the CGH null lens test. Three null correctors were tested and one system was deliberately misaligned and remeasured to show the ability of the test to quantify null lens errors. The best results were obtained for the null corrector for the WIYN 3.5-m $f/1.75$ primary mirror where the CGH measured null corrector errors of only 5.1 nm rms. Some future work on CGH null lens testing is outlined to solve some problems in the fabrication of the holograms.

CHAPTER 1

OPTICAL MEASUREMENT OF PRIMARY MIRRORS: AN INTRODUCTION AND HISTORICAL BACKGROUND

1.1. INTRODUCTION

Primary mirrors for reflective telescopes have progressed for over 300 years with fairly steady improvement in size and quality. Optical measurement techniques for these mirrors have evolved from purely qualitative tests of relatively benign surface shapes to highly accurate measurements of steeply curved aspheric surfaces. Requirements for a new generation of large optical telescopes, that are planned to be operational by the end of this decade, have pushed optical testing technology to new limits. The testing of these new mirrors is an order of magnitude more difficult than for any existing telescope, and the required accuracy is considerably tighter. Before discussing the detailed techniques developed for testing these mirrors in Chapters 2-7, some background is useful. This chapter reviews the development of optical telescopes, primary mirrors, and optical testing to show the motivation for new testing methods. This chapter also presents a historical perspective to the problems, and the establishes terminology used to explain the solutions.

1.2. REFLECTIVE TELESCOPES: PAST, PRESENT, AND FUTURE

Telescopes are used to gather information about distant objects and events by collecting light coming from them. The ability to study faint objects in the sky (these are always the most interesting) is limited by the amount of light collected. Since larger telescopes collect more light, astronomers are always eager to build new telescopes as large as the current technology will allow. Between 1970 and 1990, eleven new telescopes with primary mirrors three to six meters in diameter were built. In the next decade, eleven new telescopes with apertures 6.5 to 10 meters are planned to be constructed (Bahcall 1991). These new telescopes will enable astronomers to see deeper into space with unprecedented clarity.

The new telescopes are designed not only to collect more light, but also to give sharper images. Optical ground-based telescopes operate over a spectral range from ultraviolet to far infrared (about 0.3 to 30 μm wavelength). The performance at wavelengths below 5 μm is limited by distortion from the atmosphere and by the quality of the optics. The image quality for this short wavelength light will be improved by making better mirrors and using adaptive optics to compensate for the atmospheric distortion. For light above 10-μm wavelength, telescopes are limited by diffraction, so better resolution is obtained by using larger mirrors.

In addition to the development of larger primary mirrors, telescopes have progressed toward the use of shorter focal ratios. There is significant motivation for using a "fast" primary mirror (one with a small focal ratio or f-number -- defined as the focal length divided by the diameter). Telescopes with fast primary mirrors are short and compact. As such, they require a smaller building, they are less susceptible to wind, and they have less structure that can interact with the air to distort images. The fact that faster primaries require tighter alignment tolerances is compensated by the increased

stiffness of the shorter telescope (Meinel 1960; 1969). Most existing primary mirrors were made with long focal ratios of $f/2.2$ and above because of the difficulty in polishing and testing faster mirrors. However, recent advances in polishing technology have demonstrated the ability to polish surfaces as fast as $f/1$ (Martin, Anderson, *et al.* 1992).

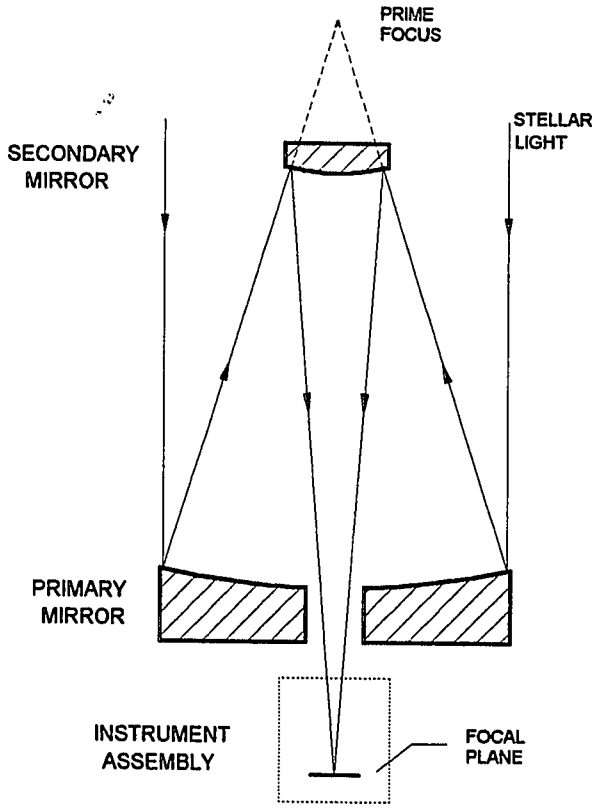

Figure 1.1. Schematic drawing of a typical optical telescope.

Large optical telescopes typically consist of a primary mirror, a secondary mirror, and an instrument package (see Fig. 1.1). The primary mirror reflects the light from a distant source, forming an image at the prime focus of the mirror. The size of the primary mirror determines the amount of light collected. The light is reflected from the secondary mirror to go through a hole in the primary and form a real image at the desired

position. An instrument makes a measurement of the image and outputs data to the astronomer. The instrument may be a complex optical system containing mirrors, lenses, diffraction gratings and solid-state electronic detectors or it may be simply an eyepiece and an eye. Telescopes usually have a fixed primary mirror, several interchangeable secondary mirrors, and many instruments. New instruments are constantly implemented in telescopes to utilize advances in technology and to meet the changing needs of astronomers. However, the mirrors and the telescope structure are used for generations.

Due to its size and required precision, the primary mirror is the most expensive and difficult component in the telescope. Advances in telescopes have closely followed technological improvements in the fabrication and measurement of primary mirrors. The first primary mirrors, such as those made by Newton and Herschel, were made of solid disks of metal, highly polished to give a good reflection. These early metal mirrors were limited by the mechanical instability of the metal, its extreme sensitivity to temperature changes, and its tendency to quickly tarnish. Foucault (1859) developed the technique of making the mirrors out of glass and applying a thin layer of reflective silver. Glass is an ideal material for mirrors due to its mechanical and chemical stability, and its ability to be smoothly polished. Nearly all modern telescopes use glass primary mirrors coated with reflective aluminum.

Improvements in glass technology have resulted in mirrors that are less susceptible to deformations caused by temperature changes. The first large telescopes used primary mirrors made of soda-lime glass, having a relatively large coefficient of thermal expansion, α, of about 10 ppm per °C. The next generation primary mirrors were made with low expansion glass commonly used for ovenware. The 200-inch primary for the Palomar telescope (King 1955), cast in 1934, is made of Pyrex (α = 2.8 ppm/°C). Fused silica (α = 0.5 ppm/°C) was used in the 1960's and 1970's for several large telescopes in-

cluding the Mayall 4-m on Kitt Peak. Several of today's 4-m-class telescopes use primary mirrors made of glass or glass-ceramic with effectively *zero* expansion such as Corning ULE™ or Schott Zerodur™.

Even for a mirror that does not suffer shape changes due to thermal effects, a temperature difference between the mirror and the ambient air will cause "mirror seeing", which degrades the image quality. When the mirror is not at thermal equilibrium with the air around it, convective air currents are formed that distort the star light, resulting in blurred images (Woolf 1982; Barr *et al.* 1988; Racine *et al.* 1991). The solution to this problem is to control the temperature of the mirror.

For large mirrors, the support of the primary mirror is critical to maintaining its shape. In the telescope, the primary mirror is acted upon by substantial forces from the wind and gravity, but the shape of the mirror is required to be constant to millionths of an inch. Until the 1980's most large primary mirrors were made of thick, solid glass disks that are stiff enough to maintain their shape resting on a simple support. It is not practical to scale these designs up for the new large telescopes due to the prohibitive weight, associated deflection, and poor thermal properties.

Most modern telescopes use lighter, more flexible primary mirrors that rely on active supports to adjust the shape of the mirror during use of the telescope. The active support can correct the deflection of the mirror as the telescope points from zenith to horizon. The ability to correct low-frequency figure errors also eases the manufacturing and support tolerances (Wilson, Franza, and Noethe 1987). The European New Technology Telescope (NTT) used its active support to correct three microns of spherical aberration that was induced by an error in the optical test (Wilson, Franza, Noethe, and Andreoni 1991).

There are three new technologies currently being pursued for primary mirrors of large telescopes. The Keck Telescope in Hawaii (Nelson and Mast 1992) uses a mosaic of 1.8-m hexagonal Zerodur™ mirrors that are precisely controlled to work as a single 10-meter primary. This method reduces the mass of the primary mirror, but it requires a complex servo-controlled alignment system that works to optical tolerances. Another technique for making 8-m primary mirrors uses thin, solid zero-expansion glass mirrors with an active support (Müller and Höness 1988; Van Dyke 1988). The weight reduction in these meniscus mirrors is accompanied by a lack of stiffness that requires a complex support system to maintain the shape of the mirror. Although these mirrors are thinner than conventional mirrors, they are still about 20 cm thick and will not readily come to thermal equilibrium with the nighttime air. Zero-expansion 8-m meniscus mirrors are planned to be used in three new telescope projects: the European Very Large Telescope or VLT (Beckers and Tarenghi 1992), the U.S.-led Gemini Project (Osmer 1992), and the Japanese Suburu Telescope (Kodaira 1992). A third method of making 8-m mirrors, pursued by the University of Arizona, uses a light-weighted blank of low-expansion borosilicate glass similar to Pyrex (Angel 1988). This glass does not have zero expansion, but it is readily cast into complex shapes. The mirrors are cast in a rotating oven to create a thin curved face-sheet (to become the optical surface) and a flat back-sheet (to provide attachment points for the support) held together by a honeycomb pattern of ribs. These mirrors are stiff and quickly come to thermal equilibrium with the air. However, they require a thermal control system to avoid surface distortions caused by temperature variations. These mirrors will be used in the Large Binocular Telescope or LBT (Strittmatter 1990), the Multiple Mirror Telescope conversion or MMT (Chaffee, Blanco, *et al.* 1990) and the Magellan Telescope (Dressler 1990).

This next generation of optical telescopes follows the historical trend of increasing aperture diameter as shown in Fig. 1.2. Noted on the plot are the metal mirrors of Newton, Herschel, and Rosse, the 100-inch Hooker Telescope on Mt. Wilson, the 200-inch Hale Telescope on Palomar Mountain, and the 10-m (394-inch) mosaic-primary Keck Telescope on Mauna Kea. Note the steady trend (on the logarithmic scale) towards increasing diameter.

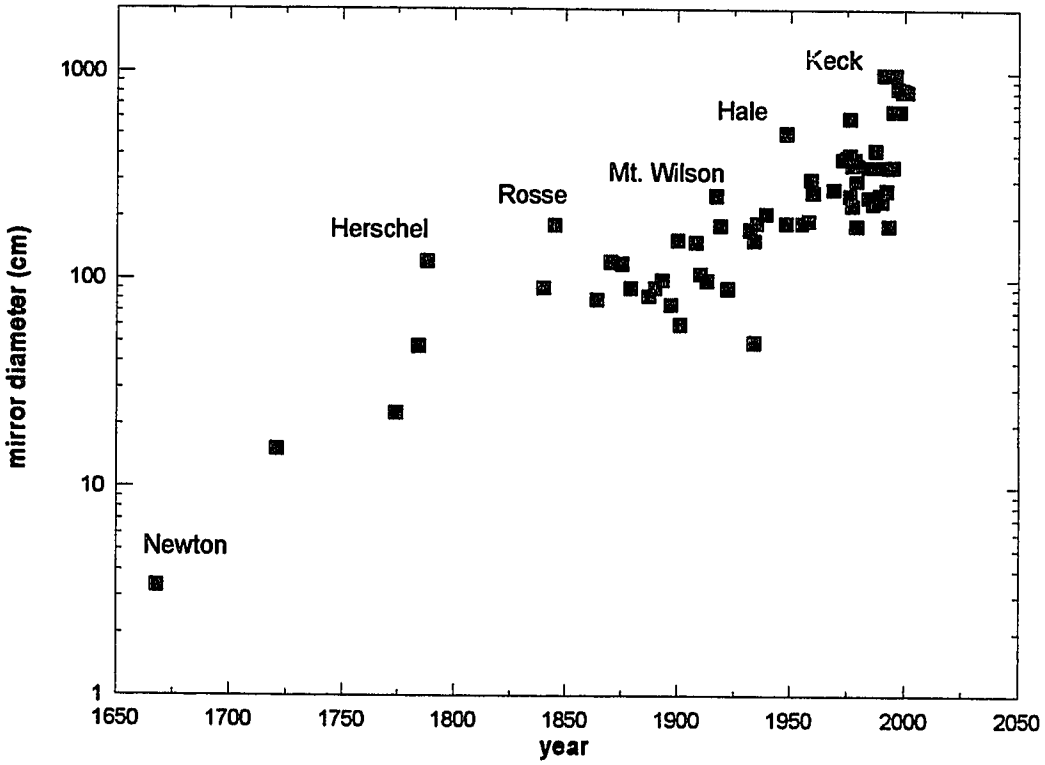

Figure 1.2. Primary mirror diameter vs. year. See Appendix A for tabulation.

1.3. SHAPE OF THE PRIMARY MIRROR

Primary mirrors for large telescopes typically have shapes described as conic sections of revolution. These surfaces are rotationally symmetric about the z-axis, and are described by

$$z(r) = \frac{r^2}{R + \sqrt{R^2 - (K+1)r^2}} \tag{1.1}$$

where $z(r)$ = surface height

r = radial position ($r^2 = x^2 + y^2$)

R = radius of curvature

K = conic constant ($K = -e^2$ where e is eccentricity).

The types of conic surfaces, determined by the conic constant, are as follows:

$K < -1$	hyperboloid
$K = -1$	paraboloid
$-1 < K < 0$	prolate ellipsoid (rotated about its major axis)
$K = 0$	sphere
$K > 0$	oblate ellipsoid (rotated about its minor axis).

Paraboloidal mirrors image light from a distant star to a perfect point. For this reason, most telescope primary mirrors are near-paraboloidal with K varying only several percent from -1.

A wavefront matching the shape of this surface may be approximated as a sphere of radius R perturbed by spherical aberration of the form

$$S(r) = \frac{Kr^4}{8R^3} + \frac{1 \cdot 3\left[(K+1)^2 - 1\right]r^6}{2^3 3! R^5} + \frac{1 \cdot 3 \cdot 5\left[(K+1)^3 - 1\right]r^8}{2^4 4! R^7} + \ldots \tag{1.2}$$

The mirror shape is fully defined by the two parameters R and K that are chosen in the telescope design. An error in R shifts the focal position, but an error in K causes spherical aberration that degrades the telescope performance. The acceptable tolerances for R and K flow down from the full telescope error budget and must be met during fabrication and testing of the primary. Typically, R must be held to ±0.1% and K to ±0.05%. In addition, the deviation of the surface from an ideal conic of revolution should be less than about 0.02 μm rms (a typical hair is about 100 μm in diameter).

1.4. SPHERICAL ABERRATION

Nearly all of the spherical aberration in Eq. (1.2) is-low order or Seidel spherical aberration of the form

$$S(\rho) = W_{040}\rho^4 \tag{1.3}$$

Using notation from Shack (1988), the value of the Seidel coefficient W_{040} is

$$W_{040} = \frac{KD}{1024 f_n^3} \tag{1.4}$$

where D = mirror diameter

f_n = primary f-number = $\frac{R}{2D}$

ρ = normalized radial position = $\frac{2r}{D}$

($\rho = 0$ at the center and 1 at the edge of the mirror).

The spherical aberration of the reflected light may equivalently be described as wavefront aberration or transverse ray aberration. Since the rays point in the direction of propagation, which is locally perpendicular to the wavefront, the ray aberrations are easily computed from the wavefront.

Both the wave aberration and transverse ray aberration are computed relative to an arbitrary reference sphere. The choice of the reference sphere is usually made to minimize the rms wavefront aberration. Fig. 1.3 shows the geometry of the in-plane component of the aberration.

The transverse ray aberrations ε_x and ε_y give the x and y ray intercepts with a plane at the center of curvature of the reference sphere. The ray aberrations, in air, are given to an excellent approximation by Rayces (1964) to be

$$\varepsilon_x = -R\frac{\partial W}{\partial x}, \quad \varepsilon_y = -R\frac{\partial W}{\partial y}. \tag{1.5}$$

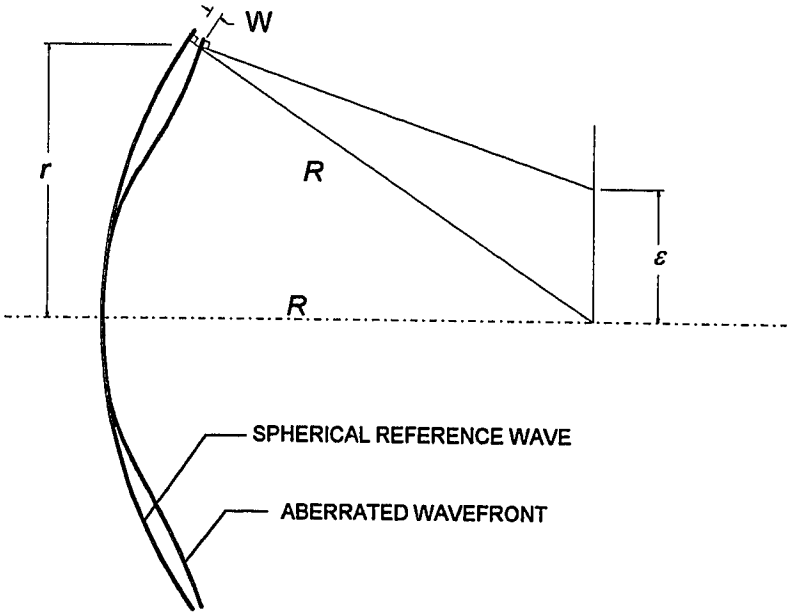

Figure 1.3. Relationship between wave aberration and transverse ray aberration. The aberration is grossly exaggerated for clarity, but typically, R is thousands of times larger than W.

Since a wavefront with spherical aberration is rotationally symmetric, all of the light from a particular radial zone will come to focus at the same point. The axial variation of this zonal focus is called the longitudinal spherical aberration. The rays from the outer zone converge upon the marginal focus, and the innermost rays converge upon the paraxial focus. The wavefront aberrations are computed at any focal position relative to a reference sphere centered on that location. Fig. 1.4 shows the form of spherical aberration through focus. The outer envelope, where the rays are crossing their neighbors, is the caustic.

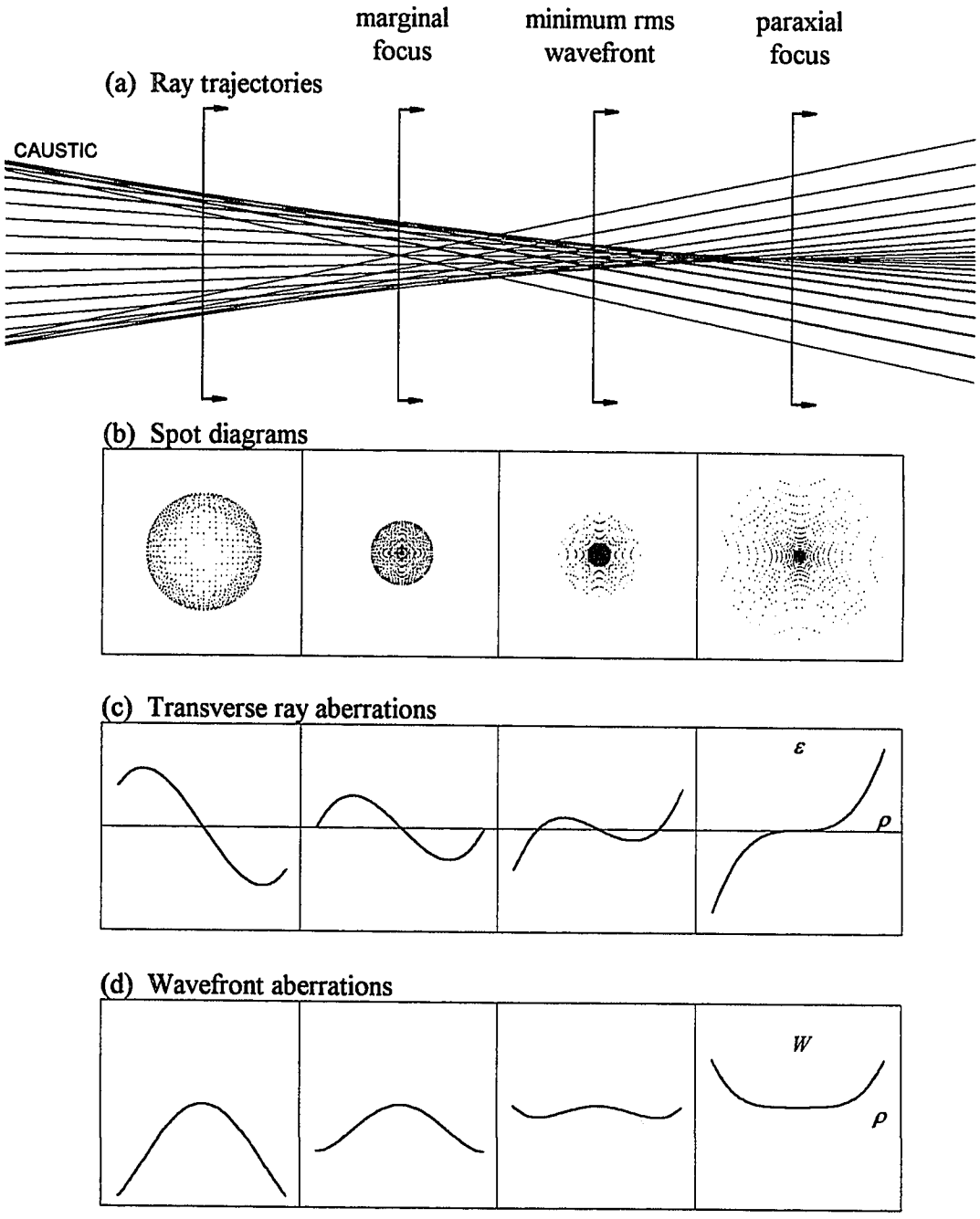

Figure 1.4. Graphical representations of spherical aberration through focus. (a) aberrated rays coming to focus; (b) spot diagrams through focus showing what an image of a point would look like; (c) transverse ray aberrations showing ray intercept as a function of pupil position; (d) wavefront aberrations focus showing the effect of change in reference sphere.

The amount of spherical aberration is often described in terms of peak-to-valley (P-V) or root mean square (rms) wavefront variation. These refer to the wavefront relative to the optimal reference sphere that gives both minimum rms and P-V wavefront error. This occurs for the reference sphere centered halfway between marginal and paraxial focus (see Fig. 1.4). The relationships are shown as

$$W_{\text{P-V}} = \frac{W_{040}}{4} = \frac{KD}{4096 f_n^{\,3}}$$
$$W_{\text{rms}} = \frac{W_{040}}{\sqrt{180}} = \frac{KD}{6144\sqrt{5} f_n^{\,3}} \qquad (1.6)$$

A mirror with a small error in the conic constant ΔK will have spherical aberration W_{040} in its shape according to

$$W_{040} = \frac{D}{1024 f_n^3} \Delta K. \qquad (1.7)$$

A small amount of spherical aberration can be fully corrected in the telescope by moving both the secondary mirror and the focal plane with respect to the primary mirror. The allowable range of motion and image degradation across the field from higher-order aberrations set the tolerances on the conic constants for both mirrors.

1.5. PRIMARY MIRROR FABRICATION

The fabrication of a primary mirror involves several steps: machining, grinding, and polishing. The specific process by which large mirrors are fabricated at the University of Arizona is described below, but similar methods are employed thoughout the optics industry. The glass blank is first cast to roughly the correct dimensions. The

blank is then generated or machined using rotating diamond-impregnated tools under computer control. The edges and back surface are generated to the final dimensions, and the optical surface is generated to an accuracy of about 5 μm rms. After generating, the surface is ground by lapping with loose-abrasives. The traditional practice for fabricating aspheres was to generate to a spherical surface and to lap in the asphere. The shape of the ground surface is measured using interferometry with infrared laser light. Grinding proceeds until the surface takes the correct shape to within about 500 nm rms. The final figuring is performed by polishing with a pitch-faced lap and metallic oxide polishing compound (similar to rouge). The polished surface is measured interferometrically using visible-wavelength laser light. The polishing continues until the surface meets its final specification.

The strategy for figuring the surface by grinding and polishing is to measure the surface and rub on it to wear down the high spots. The efficiency of the process depends both on the ability of the optician to control the glass removal and on the ability to make rapid, accurate measurements of the surface. The optician must use a conservative approach to avoid removing too much glass, creating a depression. If a low zone is created, it must be corrected by bringing the entire surface down to that level. Many polish/test cycles may be required for the completion of a single large mirror.

Historically, primary mirrors were made with large focal ratios, departing only slightly from spherical, because spherical surfaces are readily polished and tested. The polishing process tends to wear both the tool and the mirror to produce matching spherical surfaces. Since a sphere has constant curvature everywhere on its surface, the matching polishing tool will tend to maintain intimate contact with the surface. A highly aspheric surface, such as a fast paraboloidal mirror, has curvature varying strongly with position and direction. For a large tool to fit this surface either the tool must be

compliant to conform to the shape of the mirror, or it must be actively driven to take the correct shape.

The optician bases the polishing entirely on the results from the optical test. An error in the optical test will result in the mirror being polished to the wrong shape. If no other test is performed, a flaw in the mirror due to the testing error will not be discovered until the mirror is in the operational telescope.

1.6. CENTER OF CURVATURE TESTING FOR PRIMARY MIRRORS

A concave spherical mirror is easily tested from its center of curvature, but this test is complicated by the asphericity of a paraboloid. The testing of a sphere takes advantage of the fact that any ray going through the center of curvature intersects the surface at normal incidence. Thus, light from a point source at the center of curvature of a spherical mirror will reflect exactly back to the center. If the spherical surface has small errors in it, the reflected light will not converge to a point and the deviations may be used to measure the surface errors. Testing a paraboloid is not as easy.

Light reflected from a point source at the center of curvature of a paraboloid will have spherical aberration equal to twice the surface asphericity given in Eq. (1.4). Only very slow or small paraboloidal mirrors, with P-V asphericity less than a few wavelengths of visible light (0.4 to 0.7 μm wavelength), are close enough to spherical to be tested directly from the center of curvature. Light reflected from the center of curvature of an 8.4-m $f/1.14$ primary for the LBT would have over 2.8 mm or about 4500 waves P-V asphericity coming to focus with a minimum spot diameter of 101 mm!

The knife-edge test, developed by Foucault (1859), is a common technique for testing spheres and small paraboloids. This test, described in detail by Ojeda-Castañeda

(1992), uses a sharp edge such as a razor blade to block some of the converging rays (see Fig. 1.5). A point source is placed near the center of curvature of the mirror and the knife is moved laterally and axially near the focus. Rays that are blocked by the knife are observed as a shadow, giving a qualitative measure of the transverse ray aberrations, or the slope errors on the surface. This test does not work well for fast paraboloids because of the large amount of spherical aberration.

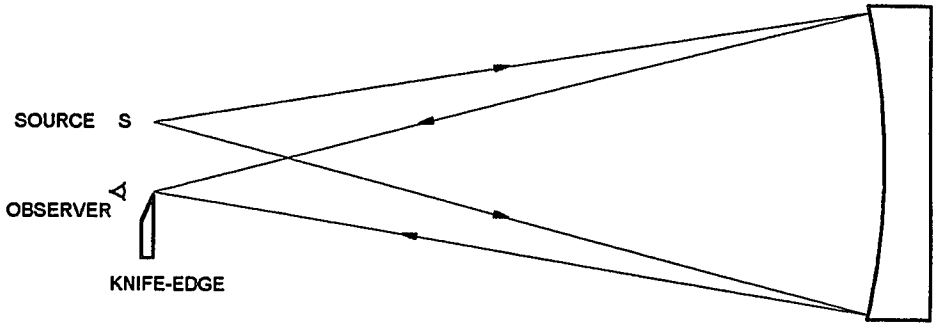

Figure 1.5. Foucault knife-edge test of a concave mirror.

The knife-edge test measures the slope errors on a converging wavefront. For a perfect spherical mirror, the light will converge to a sharp point. As the knife edge moves through that point, it will either block all of the rays or none of them. If the mirror has slope errors, the light will not converge to a point so the knife edge will block rays with slope errors. It takes a trained optician to convert this qualitative slope information into real surface shape to guide the polishing. The polishing of the McDonald Observatory 2.08-m primary was held back months due to an incorrect interpretation of a knife-edge test (Evans and Mulholland 1986). Techniques for interpreting the knife-edge test are given by Gaviola (1936) and Linfoot (1948).

There are several other optical tests that measure slope deviations from a spherical wave. The Zernike or phase contrast test, reviewed by Ojeda-Castañeda (1992) is a variation of the knife-edge test that modulates the phase of the light rather than blocking it. The Ronchi test (Ronchi 1923, 1964; Anderson and Porter 1929; Cornejo-Rodriguez 1992) uses a grating located in the converging light. A moiré pattern is set up that displays contours of the wavefront slope. This test may be used for mild aspheres with the use of a special ruling (Malacara and Cornejo 1974).

A center of curvature test devised by Hartmann (1908) has been used to test primary mirrors. This test uses a point source near the center of curvature and a screen with holes in it near the mirror. The narrow beams of light defined by the holes can be used to quantitatively determine the slope of the mirror. The positions of these light beams show up on a detector or film as bright spots. The size and separation of the holes can be optimized for measurement accuracy (Morales and Malacara 1983). A common implementation of this test (Ghozeil 1992) records the spots in photographic film and measures the positions of the spots. A comparison between the expected and measured spot positions gives the slope errors of the mirror. The slope errors are integrated to get the surface shape. The accuracy of the Hartmann test is limited by the size of the spots on the film and by the mechanical tolerances in the system. Since this test only samples the mirror at discrete locations, it cannot measure high frequency errors. It has been used successfully in combination with other tests (Bowen 1950; Ghozeil and Simmons 1974) for the testing of telescope primary mirrors. Korhonen (1984) has developed a more sensitive version of this test that uses interference between the different pencil beams.

The accuracy of the above tests is high for a spherical mirror, but is not adequate to test a fast paraboloid. Since these tests measure shape departures from spherical, they

would require unreasonable dynamic range to measure λ/20 surface errors in the presence of hundreds of waves of spherical aberration. To test a fast paraboloid accurately using these tests, a null corrector must be used to cancel the spherical aberration.

The most accurate method for testing optical surfaces is interferometry (Michelson 1918), which compares a wavefront reflected from a test mirror to one reflected from a reference mirror. Test accuracy of hundredths of a wave can be achieved. Interferometry determines wavefront phase variations that correspond to surface errors on the mirror. Interferometers generally measure wavefront deviations from spherical since the accurate reference surfaces are spherical. When testing a highly aspheric mirror, a null corrector (Chaps. 4 and 5) must be used to correct the spherical aberration. For mild aspheres, two-wavelength holography (Wyant 1971), two-wavelength interferometry (Cheng and Wyant 1984; Creath and Wyant 1986), or sub-Nyquist interferometry (Greivenkamp 1987) may be used.

For highly aspheric mirrors, a null corrector is required for accurate interferometric testing. A properly designed and fabricated null corrector will eliminate all of the spherical aberration to allow a null test of the mirror. However, null correctors are sensitive to alignment errors so they must be verified with some other test.

For verifying for null correctors, tests that directly measure the spherical aberration from the center of curvature are useful. The wire test (Platzeck and Gaviola 1939; Saunders 1954; Ojeda-Castañeda 1992) described in detail in Ch. 2 measures the spherical aberration of the mirror by measuring the axial variation of zonal center of curvature. It measures the slope and is only sensitive to axisymmetric errors. The caustic test (Platzeck and Gaviola 1939; Cornejo and Malacara 1978) measures curvature deviations by finding the local sagittal center of curvature for different regions of the mirror. Since

both of these tests measure deviations from spherical, they become less accurate for fast, highly aspheric primary mirrors.

1.7. ALTERNATIVES TO CENTER OF CURVATURE TESTS

Primary mirrors may be optically measured using methods other than center of curvature testing. The natural conjugate to test a paraboloidal mirror is with a source at infinity, which reflects to form a perfect image at the focal point, halfway between the mirror and its center of curvature. A primary mirror may be tested by using a bright star with the knife-edge test, Ronchi test, Zernike phase contrast test, Hartmann test, or shearing interferometry. These types of tests can be performed quite accurately in the correct conditions (Welford 1960; Saunders and Bruening 1968). Unfortunately the required conditions are in the telescope, on top of a mountain, in the middle of a clear night. Historically, the final figuring of primary mirrors was based on such testing (Bowen 1950; Texereau 1964). The expense and difficulty of polishing a large mirror at the telescope site preclude this option for modern telescopes.

It is possible to test a paraboloid by using a source at a position more accessible than infinity, but still several focal lengths away. This reduces the spherical aberration to a level small enough that other errors may be seen. The Lower test (Rank *et al.* 1949; Yoder 1959) uses this principle to test small paraboloids as fast as $f/1.5$. It is not practical to perform this test on a large mirror due to the large distances required.

A common method for testing small paraboloids is autocollimating with a flat mirror (Ritchey 1904). This method (see Fig. 1.6) uses a point source at the focus of the primary to create collimated light on reflection. A flat mirror reflects this light directly back to the mirror where it reflects to form a point image. This test can be carried out

with a knife-edge or similar method or it can be performed interferometrically. This test is impractical for large mirrors because it requires a high-quality flat mirror as large as the primary.

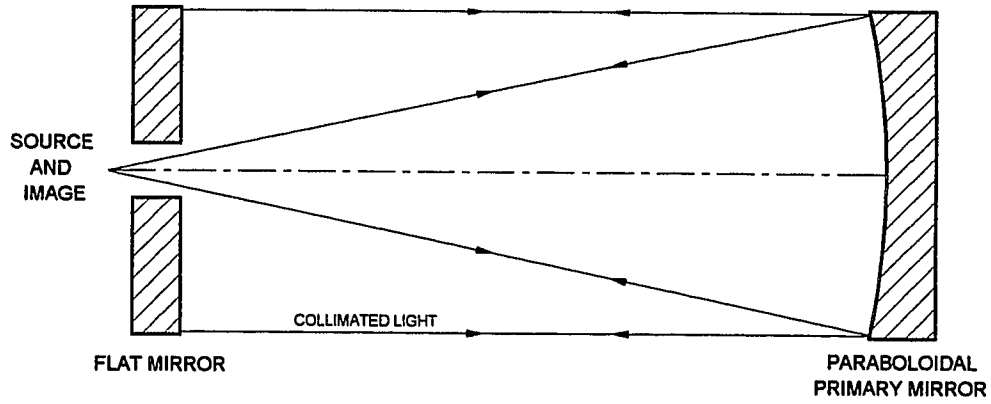

Figure 1.6. Autocollimation test of a paraboloidal mirror.

The scanning pentaprism test is useful for measuring axisymmetric errors in a paraboloid. This test, described in Ch. 3, uses a pentaprism to scan a laser beam across the diameter of the mirror (see Fig. 3.1). The use of a pentaprism assures that the laser beam always points in the same direction as it is scanned across the mirror. This scanning beam is identical to illuminating the mirror with light from a distant source, one small area at a time. A perfect paraboloid will reflect this collimated light to the focal point of the mirror. Slope deviations in the surface cause the reflected spot to depart from the focal point. This spot motion is easily recorded with a CCD video camera and processed in real time with a computer. Since this test measures surface slope deviation *from a paraboloid* it can be highly accurate.

1.8. SPECIFICATION OF THE OPTICAL FIGURE

Primary mirrors and other optics are polished to meet specifications drawn up by the system designers. The optical surfaces are required to be good enough that they will not significantly degrade the system performance. Due to a better understanding of the limitations of ground-based astronomy and increased testing capability, the specifications for optical surfaces have become more stringent in recent years.

The specification of optics requires a balancing of priorities. A good specification for an optical surface must directly relate to its performance in the system and the method used to test it. The specification must contain enough information about the surface to fully predict its performance, but not so much that it needlessly increases cost and test difficulty (Parks 1983).

To achieve a specified surface accuracy for a mirror, the optical test must be known to be more accurate than the desired surface. Optical testing is usually performed to the highest possible accuracy allowed by current technology. The testing specification is then derived from an assessment of the measurement accuracy. This can cause misleading results for poorly qualified tests. The 2.08-meter primary for McDonald Observatory was measured using a knife edge test and a Hartmann test, and was determined to be perfect to 0.02 μm P-V (Plaskett 1939). The mirror was later tested and shown to have surface flaws of twenty times this amount (Texereau 1964). Modern wavefront sensing techniques have shown that other mirrors were finished with significantly worse figures than optical shop tests have indicated (Roddier and Roddier 1993).

Primary mirrors have become progressively more aspheric and difficult to test, while at the same time they have been required to give better images. Modern telescopes are designed to give 0.3 arc second images (Angel 1986) while just 25 years ago, 0.6 arc

second images were considered excellent (Meinel 1967). It is now understood that a large portion of the image degradation that was believed to limit the performance was caused by the poor thermal design of the telescope (Woolf 1982; Cowley *et al.* 1988; Racine *et al.* 1991). Modern telescopes are located at better sites and have improved thermal design allowing better images than the previous generation telescopes, so they require more accurate optics.

The degradation of the image quality depends on the magnitude and spatial scale of the surface errors. For this reason, a distinction is sometimes made between low spatial frequency figure errors, mid-frequency errors, and surface roughness (Parks 1983). These different components of the surface error may be measured using separate tests (Montagnino 1985). The surface may also be statistically specified over all spatial scales using a power spectral density or structure function.

For surface errors on a mirror defined by the function $\Phi(x, y)$, the structure function $SF(d)$ gives the mean square difference for points separated a distance d,

$$SF(d) = \left\langle \left[\Phi(\vec{r} - \vec{d}) - \Phi(\vec{r}) \right]^2 \right\rangle$$

or (1.8)

$$SF(d) = \frac{1}{2\pi A} \int_x \int_y \int_\theta \left[\Phi(x - d\cos\theta, y - d\sin\theta) - \Phi(x, y) \right]^2 d\theta dy dx$$

where the integral is taken over the mirror coordinates and direction of d. The integral is normalized by the pupil area A times 2π, the extent of the azimuthal integration. Equation (1.8) is expanded, giving

$$SF(d) = 2\left\langle \left[\Phi(\vec{r})\right]^2 \right\rangle - 2\left\langle \left[\Phi(\vec{r}-\vec{d})\Phi(\vec{r})\right]^2 \right\rangle \qquad (1.9)$$
$$= 2 \times rms^2 - 2 \times Autocorrelation\ function.$$

The power spectral density (PSD) is given by

$$PSD(f_x, f_y) = \left|\mathcal{F}\{\Phi(x,y)\}\right|^2$$

or averaging in azimuth,

$$PSD(f) = \frac{1}{2\pi}\int_{\theta=0}^{2\pi} PSD(f\cos\theta, f\sin\theta)d\theta \qquad (1.10)$$

where $\mathcal{F}$ denotes a Fourier transform

f_x, f_y = spatial frequency in x and y directions

f = directionless spatial frequency (average of all directions).

Since the integral of the PSD gives the overall mean-square variation and the inverse Fourier transform of the PSD gives the autocorrelation function, there is a one-to-one relationship between structure function and PSD.

The surface accuracy of the primary mirror is specified to have errors small enough that they will not significantly degrade the imaging performance. Since the performance of a ground-based telescope is limited by atmospheric distortion, the goal is to build telescopes that match the image quality delivered in the best seeing conditions. The allowable figure and testing errors flow down from an error budget of the entire telescope. For the LBT, as well as other telescopes, this error budget is performed using structure functions.

Structure functions are used in the error budget because they directly relate to the atmospheric distortion, imaging quality, and measurements of optical surfaces. The atmospheric blurring is characterized by a coherence length r_0 (Fried 1966) that varies from about 10 cm to 40 cm at a good site, depending on weather. The atmospheric distortion of a wavefront, treated with Kolmogorov statistics (Tatarski 1961), varies with spatial scale according to the structure function

$$SF(d) = \left\{ 0.4175\lambda \times \left(\frac{d}{r_0} \right)^{5/6} \right\}^2 \tag{1.11}$$

where $SF(d)$ = mean-square wavefront variation for points separated by distance d

λ = wavelength.

This atmospheric model also allows the computation of the long-exposure image size for telescopes with diameters much larger than the atmospheric coherence length r_0. The blur diameter at full width and half maximum is given in radians by Martin (1987) to be

$$\theta_{FWHM} = 0.976 \left(\frac{\lambda}{r_0} \right). \tag{1.12}$$

The circle that encloses 80% of the energy in the blur spot has a diameter θ_{80}, that is given in radians by Dierickx (1992) as

$$\theta_{80} = 1.848 \left(\frac{\lambda}{r_0} \right). \tag{1.13}$$

The 4.2-m Herschel Telescope was the first to use a primary mirror specification based on structure functions (Brown 1983). An analysis on the impact of using the

structure function specification on fabrication and testing is given by Anderson and Crawford (1988).

The LBT is designed to meet a structure function equivalent to an atmosphere with $r_0 = 45$ cm or images with FWHM of 0.22 arc seconds at 500 nm. In good conditions, the combined telescope, instrument, and atmosphere will deliver wavefronts with $r_0 = 30$ cm or 0.34 arc seconds FWHM (Hill 1990).

The structure function specification of the optics departs from Eq. (1.11) at large and small spatial scales. A relaxation of the specification based on Eq. (1.11) is made since wavefront errors on scales much smaller than r_0 do not blur the images. These high-frequency errors diffract light far from the central core of the image, causing a loss of light from the image and a slight increase in the background. The fractional loss from the central core is approximated by

$$loss \cong \left(\frac{2\pi\sigma}{\lambda}\right)^2 \tag{1.14}$$

where σ = rms wavefront deviation from mean.

The LBT is specified for a maximum of 5% scattered loss at 350 nm. This relaxes the specification to allow 12.5-nm rms wavefront errors from the mean, or a 17.5-nm rms deviation between any two points.

For tolerancing the optical surfaces, the wavefront structure function in Eq. (1.11) is further adjusted by removing the mean tilt since it only causes image motion or jitter. This component of the atmosphere (Martin 1987) is taken up in the error budget for pointing and tracking. The structure function with relaxation on small scales and compensated for wavefront tilt is

$$SF(d) = 2\sigma^2 + 6.88\left(\frac{\lambda}{2\pi}\right)^2\left(\frac{d}{r_0}\right)^{5/3}\left[1 - 0.975\left(\frac{d}{D}\right)^{1/3}\right], \qquad (1.15)$$

where D = telescope aperture diameter.

It is useful to create the error budget using structure functions because the system performance is easily calculated from all of the individual sources of error. Since structure functions are statistical mean square quantities, the cumulative effects of uncorrelated errors are found by adding the individual components.

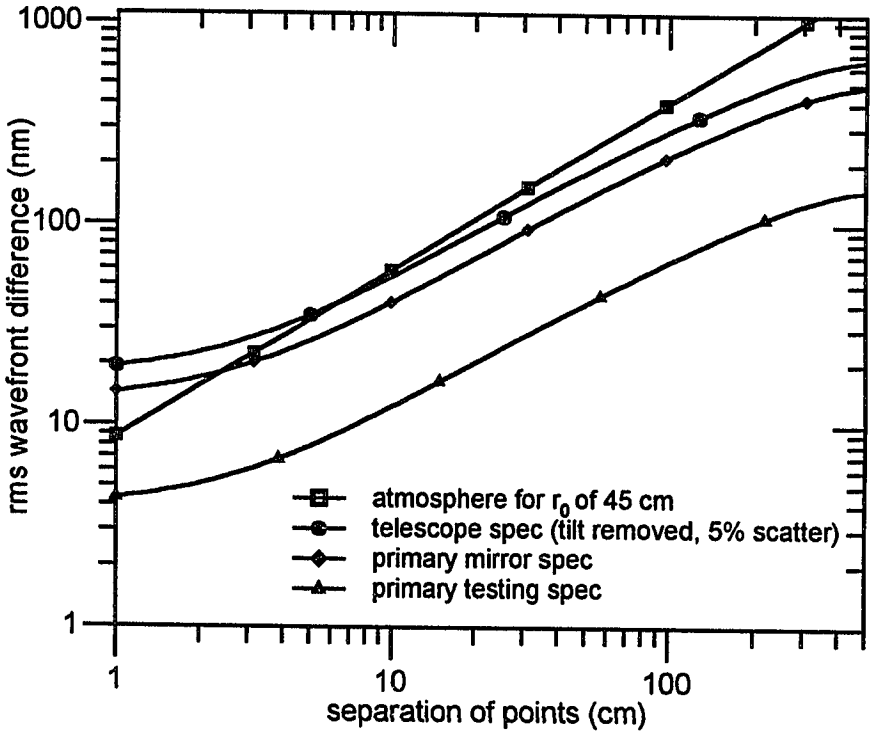

Figure 1.7. Structure function plots for the specification of an 8.4-m $f/1.14$ primary mirror. The telescope error budget gives specifications as a structure function corresponding to an atmosphere with coherence length r_0, with tilt removed and a relaxation at small scales corresponding to 5% loss due to scattering at 350 nm. The structure function gives the mean square difference, but a square root has been taken to give the root mean square (rms) value.

Distinct from the structure function specifications, requirements are placed on the radius of curvature R and conic constant K of the primary. The radius of curvature, or equivalently the focal length, is relatively easy to measure and control during fabrication. However, accurate measurement of the conic constant for large primary mirrors has historically been quite elusive. The fast primary mirrors require tighter tolerances on K than have been required by previous telescopes. The achievable tolerance of the conic constant is determined by the optical test accuracy, so a strong emphasis has been placed on developing accurate optical testing methods.

Spherical aberration, or an error in conic constant has shown up in many modern telescopes. Only after being launched into orbit was the error in conic constant discovered in the Hubble Space Telescope (Allen *et al.* 1990). This error, due to inaccuracy of the optical test (Furie *et al.* 1993), has crippled the telescope for three years and will require correction costing hundreds of millions of dollars. Roddier (1990) makes the point that, "There is evidence that current optical testing methods lack accuracy and that such an error was highly likely to happen." He used a new wavefront reconstruction technique to establish the fact that this type of error is quite common (See Table 1.1). After discussing the difficulty of absolute measurements and the tighter specification for 8-m telescopes, he concludes by making a plea for new testing methods capable of accurately measuring the conic constant.

The structure function for a wavefront with $r_0 = 45$ cm, and the telescope specification based on this atmosphere with relaxation at small scales, are given in Fig. 1.7. Also shown are specifications for the total primary mirror including support and thermal effects ($r_0 = 64$ cm) and for the optical testing of the primary mirror ($r_0 = 270$ cm).

Table 1.1. Spherical aberration measured in existing telescopes

Telescope	P-V wavefront spherical aberration (λ = 633 nm)	Error in conic constant K
Hubble Space Telescope[1]	-1.4 λ	1.2%
ESO NTT[2]	-1.2 λ	0.5%
IRTF[3]	+3.5 λ	4.9%
CFHT[3]	-1.0 λ	3.7%
University of Hawaii 88-inch[3]	-0.3 λ	0.8%

The spherical aberration in Table 1.1 is compared to the allowable variation in K of only 0.01% for the MMT primary. New optical testing techniques are presented in Chapters 4-7 that are able to achieve this accuracy.

1.9. ADVANCED OPTICAL TESTING OF PRIMARY MIRRORS

Optical testing methods have evolved to follow the increasing asphericity of primary mirrors shown in Fig. 1.8. Optical measurement techniques have also become more accurate, highly quantitative, and easier to perform. Modern optical testing has benefited from fairly recent technological advances in several areas. Stable, highly coherent laser light allows interferometry to measure the entire surface to high precision. Modern solid-state detector arrays provide accurate and automated data collection. Inexpensive, high-speed computers are used to perform the data analysis in seconds. The

[1]Allen *et al.* 1990.
[2]Wilson, Franza, and Noethe 1991.
[3]Roddier 1990.

accuracy achieved using electron beam lithography allows the manufacture of computer-generated holograms that create precise, highly aspheric wavefronts. The extensive use of computer modeling and optimization allows the design of complex optical and mechanical systems. The test systems designed for the 8-m primary mirrors would have been impossible to manufacture 20 years ago.

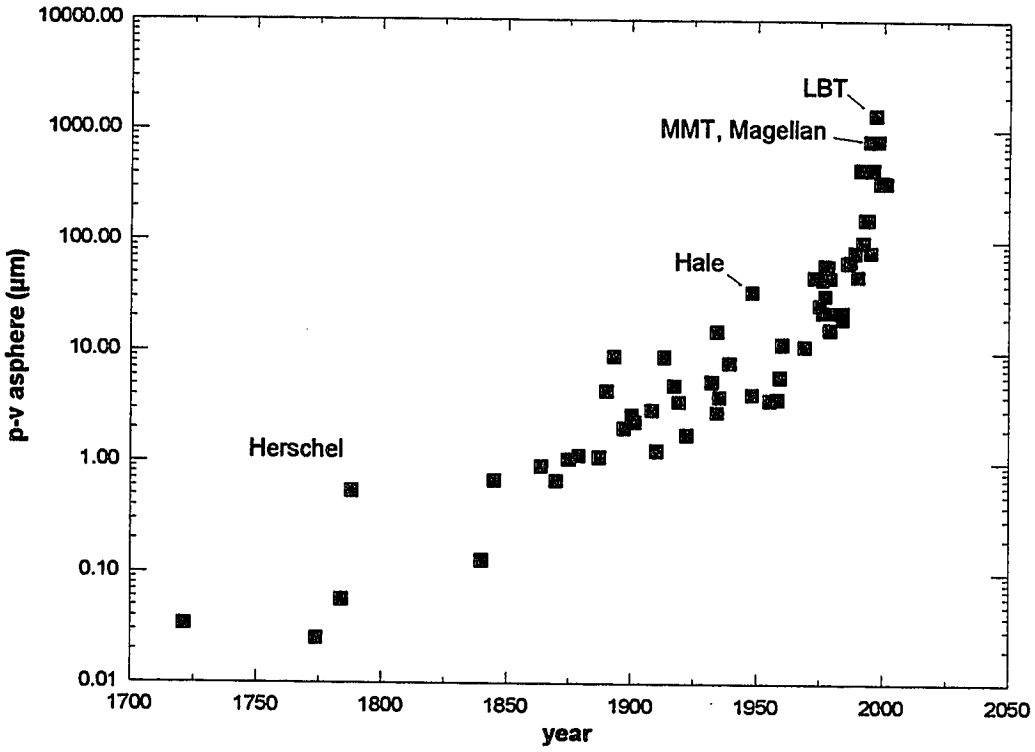

Figure 1.8. Historical increase in peak-to-valley asphericity (from best-fit sphere) of primary mirrors. The difficulty in testing the mirror is proportional to its asphericity. This data is tabulated in Appendix A. The P-V asphere shown was calculated assuming paraboloidal surfaces with the given aperture and focal ratio.

The trend towards decreasing the focal ratio of the primary mirror while increasing the diameter and tightening the specification creates a tremendous challenge for the optical measurement of these surfaces. The difficulty in the center of curvature null test

is proportional to the surface asphericity and thus inversely proportional to the cube of the focal ratio. The primary mirror for the Large Binocular Telescope is over 17 times more aspheric than any pre-1990 astronomical telescope and 40 times more aspheric than any pre-1970 telescope! This dramatic increase in surface asphericity is made clear in Fig. 1.8. Note the gentle increase (on the logarithmic scale) until the abrupt leap in the 1990's.

In response to the increasing demands on optical testing for primary mirrors, new techniques have been developed and existing methods analyzed and improved. As a direct result of this, the highly aspheric primary mirrors produced by Steward Observatory are likely to be measured more accurately than any existing telescope primaries.

The classic wire test has been pushed to new levels of accuracy (Ch. 2), enabling a rapid, inexpensive measurement of the conic constant to ±0.003. A scanning pentaprism test (Ch. 3) has been developed that can measure the conic constant to an accuracy of ±0.0002. Null correctors (Ch. 5) have been designed and analyzed to measure even the most difficult primary mirrors to the accuracy required on all spatial scales. These new null lenses are designed as part of complete instruments (Ch. 4) that are optimized not only for absolute measurement accuracy but for testing efficiency. A technique for verifying the accuracy of the null corrector using a computer-generated hologram has been developed (Ch. 6). This test provides an independent measurement of the null lens to an accuracy of ±0.00008 in the conic constant and less than a hundredth of a wave of figure errors. Precise null correctors, certified with this highly accurate holographic technique will allow the fabrication of primary mirrors meeting the demands of the next generation of optical telescopes.

SECTION I

CLASSICAL SLOPE TESTS

This first section presents two classical slope tests that were implemented and analyzed for the measurement of large, highly aspheric primary mirrors. These tests are classical in the sense that they were developed before computers and lasers were available. The tests measure the slope of the surface and must be integrated to obtain the surface profile.

The wire test, described in Chapter 2, was performed under computer control for the measurement of a 3.5-m $f/1.75$ primary mirror. A simple method of reducing the data is presented for computing the radius of curvature and conic constant of the mirror. The conic constant was measured to an accuracy of ±0.003, and improvements to the test were identified that can improve the accuracy to ±0.001. A similar test using an infrared interferometer is described that measured the shape of another 3.5-m primary mirror as the asphere was being lapped in using loose-abrasive grinding.

The scanning pentaprism test, described in Chapter 3, is a highly accurate slope test for near-paraboloidal mirrors. A computer-controlled version of this test was used at Steward Observatory to measure a 1.8-m $f/1$ primary mirror. A technique for reducing the data and aligning the test is described. This test confirmed the conic constant of the mirror to an accuracy of ±0.003, and improvements were identified that can improve the measurement accuracy to ±0.00015.

CHAPTER 2

THE WIRE TEST

2.1. INTRODUCTION

The wire test is an inexpensive, moderately accurate way to verify the conic constant of large primary mirrors. When performed with a well-calibrated steel tape, this test is also capable of measuring the radius of curvature to high accuracy. This test measures the slope of the mirror and may be integrated to give surface shape. Although this test has been used in the past to guide the polishing of primary mirrors (Fell 1968; Buchroeder *et al.* 1972), its low accuracy for steep aspheres limits its use. The accuracy of determining the conic constant K is sufficient to monitor aspherizing with loose-abrasives, but it falls short of the final telescope specification for fast primary mirrors.

This chapter describes the wire test and its implementation for testing a 3.5-m $f/1.75$ primary mirror for the ARC Telescope. An overview of the method is given in Sec 2.2. A technique for reducing the data using a polynomial fit is described in Sec. 2.3. If a beamsplitter is used in this test, it will degrade the test accuracy by asymmetrically blurring the image of reference marks. The description and analysis of this effect are given in Sec. 2.4. Test results from measuring a 3.5-m primary mirror for the ARC Telescope are given in Sec. 2.5. An alternate version of the test, using an infrared interferometer, is described in Sec. 2.6. This infrared test was used successfully to monitor aspherization of a 3.5-m $f/1.75$ mirror for the WIYN Telescope.

2.2. DESCRIPTION OF TEST

The wire test, reviewed by Ojeda-Castañeda (1992), is performed by observing the intersection of the normal rays (defined as rays perpendicular to the optical surface) with the optical axis. This axial position of intersection as a function of radial position on the mirror is known as longitudinal spherical aberration, and it defines the optical surface. These normal rays intersect the axis at the tangential center of curvature of a narrow zone. In the wire test, this intersection of the normal rays is determined by illuminating the optic with light from a pinhole and observing how the reflected light is blocked by a small wire. Light from the pinhole that is normally incident to a narrow annular zone on the aspheric mirror is reflected back on itself, re-tracing its path. A wire placed at the image of the point source blocks this reflection and shows up to the observer as a thin annular shadow at the normal zone. The measurement is accomplished by moving the wire test apparatus axially such that an annular shadow from a wire overlaps a reference pin at the mirror.

The principle used for determining the zonal center of curvature is shown in Fig. 2.1. The beamsplitter causes the point source to be effectively coincident with the wire. For a zone that has its normal ray intersecting the pinhole, the light reflects from the mirror and exactly retraces its path through the beamsplitter. The wire at the image of the pinhole then blocks the returning light from this zone, while light from other zones passes into the eyepiece and into the observer's eye. This causes an annular shadow to appear at the normal zone. Moving the wire and source axially away from the mirror causes the normal zone, thus the shadow to move outward.

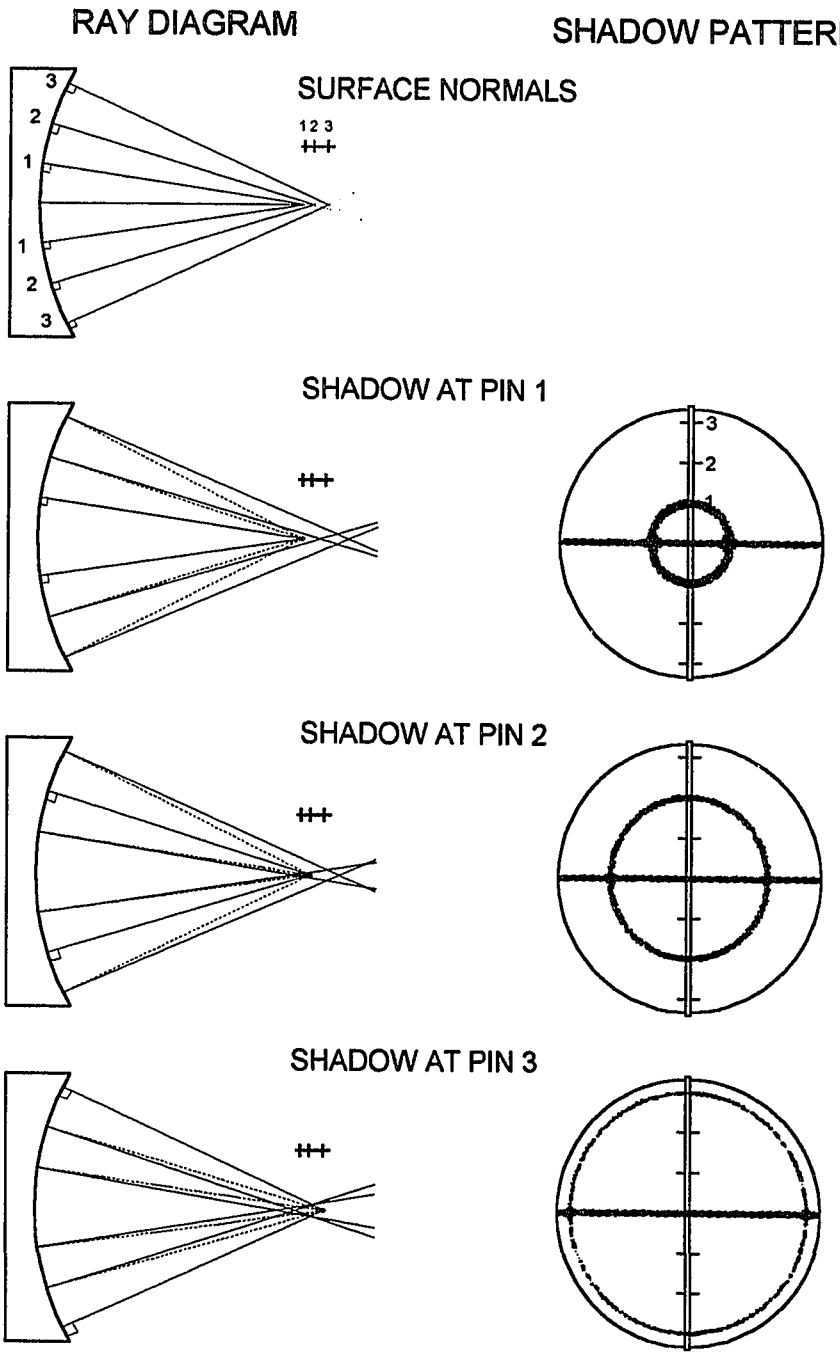

Figure 2.1. Diagram of wire test for 3 zones. As the source and wire move away from the mirror, the projected annular shadow moves outward. The data obtained from the wire test are Z -- the axial positions of the intersection of the normals defined by the wire position, and r -- the corresponding radial position on the mirror defined by the pin position.

An instrument for performing the test on a 3.5-m $f/1.75$ primary mirror for the ARC telescope is shown in Fig. 2.2. It consists of the following pieces:

- HeNe laser source with a microscope objective and pinhole
- Shack cube beamsplitter. This has a spherical surface that is concentric with the pinhole
- Wire, 75 μm diameter, positioned at the center of curvature of the sphere
- Translation stage, driven and encoded axially under computer control
- Bar with 26 reference pins, spaced at 2" intervals, supported near the surface of the mirror
- Erfle eyepiece, 32 mm focal length.

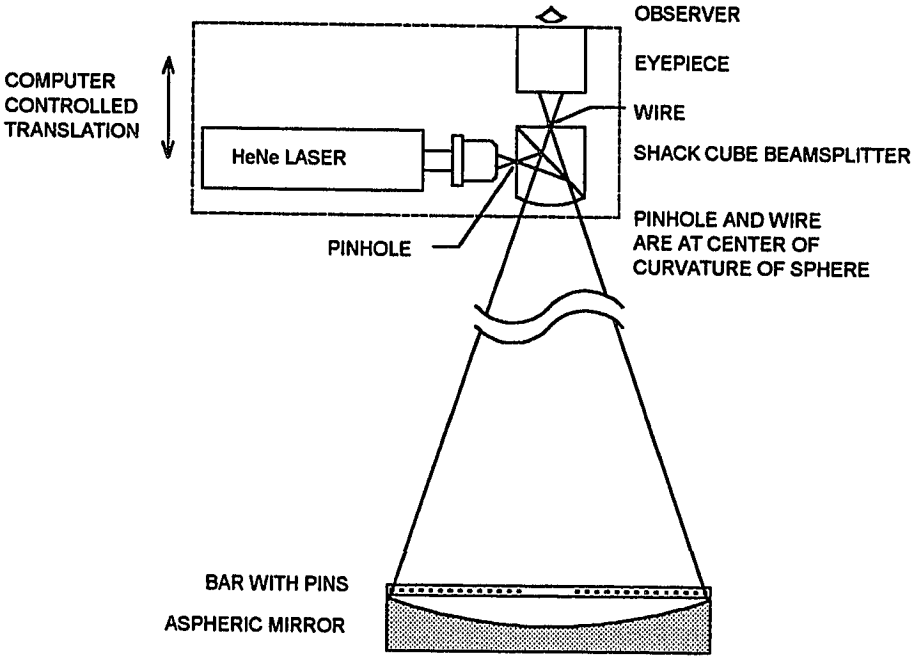

Figure 2.2. Layout of the wire test as implemented for the testing of a 3.5-m $f/1.75$ primary. The instrument was positioned near the primary center of curvature, which was 12280 mm above the mirror. The total axial motion of the instrument was 127 mm.

The test is performed by axially driving the instrument incrementally to positions where the annular shadow of the wire overlaps a reference pin on the bar across the mirror. The normal zone, which defines the shadow, is calculated by projecting the known pin position onto the mirror. Since coherent light is used, diffraction from the wire causes the shadow to show up as sharp, symmetric fringes, enabling an accurate alignment of the shadow with the pin.

The alignment of the instrument is straightforward and not critical. The lateral position of the instrument is adjusted to maintain a symmetric shadow pattern. The tip and tilt of the axial translation stage is set to minimize lateral adjustments as the stage is driven axially. The test is actually quite tolerant of small misalignments.

In retrospect, the use of the cube beamsplitter was a mistake. For the test of the ARC mirror, the largest contribution to the uncertainty in the conic constant came from an asymmetric degradation of the pin images. This effect, which was caused directly by the use of a cube beamsplitter, introduced a measurement error that caused an uncertainty of about ± 0.003 for K. Since this effect was discovered after the data had been taken, it is difficult to quantify accurately and impossible to correct. This error has been overlooked by previous researchers because they did not attempt accuracy higher than about 1% (Bender and Flint 1979). A more detailed description of this error is given below.

2.3. DATA REDUCTION

A computer program was written to perform the data analysis for this test. A least-squares fit is used to determine the radius of curvature R and conic constant K of

the mirror. The residual slopes are then calculated and integrated to show errors in the surface height.

The height of intersection of the normal rays with the axis is described, to an excellent approximation, by the equation:

$$Z = R - \frac{Kr^2}{2R}, \tag{2.1}$$

where Z = distance from mirror vertex to zonal center of curvature

R = vertex radius of curvature of mirror (12280 mm for ARC primary)

r = radial position of zone (500 to 1750 mm for ARC primary)

K = conic constant of mirror (-1.0194 for ARC primary).

The above approximation is made by truncating a series expansion. Since the terms in the series are strictly decreasing in magnitude, the error in this approximation is well represented by the next term in the series

$$\Delta Z \cong -\frac{K(K+1)r^4}{8R^3}. \tag{2.2}$$

The error in making this approximation is negligible for near-paraboloidal primary mirrors.

A single data set contains two variables, x_i the radial pin position and Z_i the height of the wire above the mirror vertex. The corresponding radial position on the mirror r_i is obtained by projecting the known pin positions from the bar to the optical surface. This projection is performed accurately using an iterative algorithm that accommodates the surface profile and the measured sag in the bar. To find R and K, a least

squares fit using singular value decomposition (Press *et al.* 1988) determines the coefficients a_0 and a_2 for the function

$$Z = a_0 + a_2 r^2$$

where (2.3)

$$R = a_0$$

$$K = -2Ra_2.$$

For determining the radius of curvature, the actual distance from the wire to the mirror may be measured using a calibrated steel tape. This measurement can be made to ±0.5 mm giving a small uncertainty in R, but large uncertainty in K.

To accurately measure K, which depends on R and the quadratic variation of Z, differential Z measurements may be used. These differential measurements give the change in wire position, not its absolute position. A computer-driven stage that provides the motion can easily measure ΔZ to ±25 μm. When fitting to differential data, the a_0 term is ignored an R must be determined independently.

After fitting a_0 and a_2 to the data, the residual slope errors are calculated and integrated to give the residual surface errors. The surface slope, defining positive slope errors as causing an increase in Z, is obtained from the relationship

$$\delta\theta = \frac{r\Delta Z}{(Z - sag)^2 + r^2} \tag{2.4}$$

where $\delta\theta(r)$ = surface slope deviation from ideal conic

ΔZ = residual longitudinal SA = $Z_{data} - Z_{fit}$

sag = surface shape given in Eq. (1.1) = $r^2/2R$ for paraboloid.

The surface errors are calculated by integrating $-\delta\theta(r)$ using Simpson's rule.

2.4. ANALYSIS OF SYSTEMATIC ERROR FROM BEAMSPLITTER

After the test had been run on the ARC primary mirror, a systematic aberration in imaging the pins was discovered. The quantity of this error depends strongly on the observer's pupil size and cannot be fully determined. The problem was caused by imaging the pins through the Shack cube. Light defining the pin position became slightly comatic due to the converging beam exiting the rear surface of the Shack cube at an angle. Since coma is an asymmetric aberration, it caused the images of the pins to blur outward. Fig. 2.3 shows the imaging geometry and Fig. 2.4 shows how the image of a point on a pin would be spread out by this aberration.

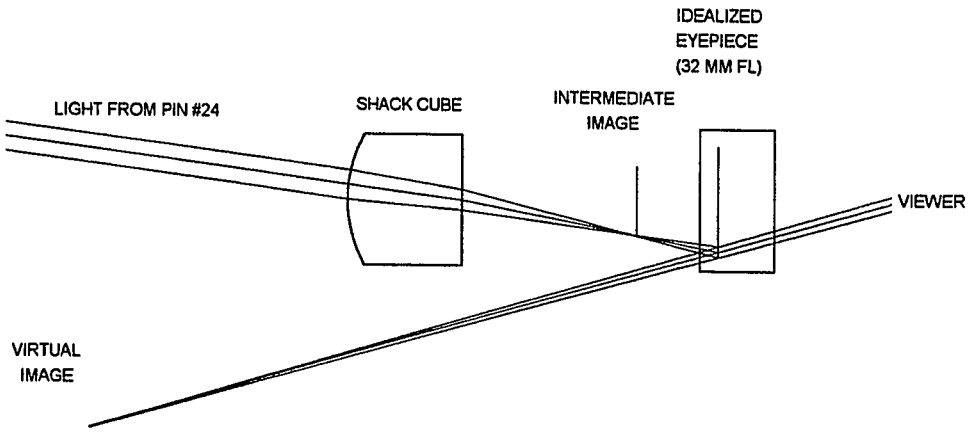

Figure 2.3. Layout of imaging geometry for the pins.

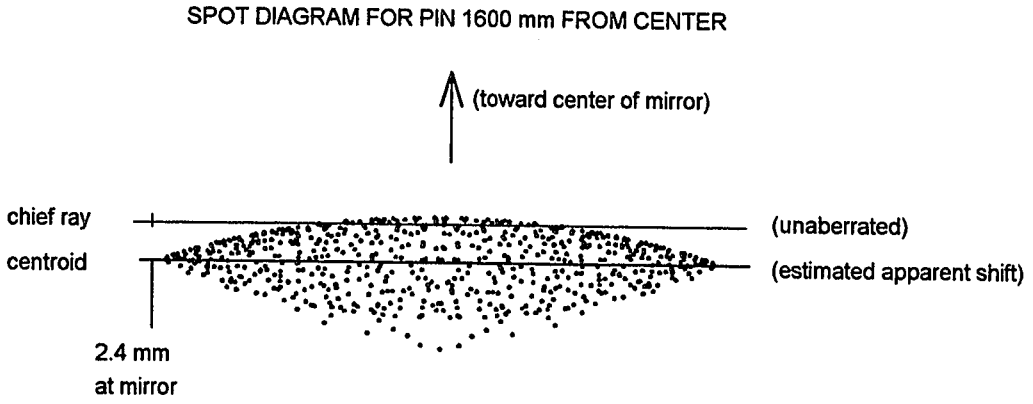

Figure 2.4. Spot diagram showing how a point on a pin near the outer edge of the mirror will be asymmetrically blurred. The image of the pin appears as a 3.175 mm wide rectangle, convolved with the above point spread function.

This blurring outward causes an apparent image shift that varies linearly with pin position. This type of error causes a direct error in the computation of the conic constant, found by differentiating of Eq. (2.1),

$$\frac{\Delta K}{K} = 2\frac{\Delta r}{r}. \tag{2.5}$$

So it takes only a 0.15% linear shift in apparent radial pin position to cause a measurement error in K of -0.003.

The amount of coma, thus the apparent shift in the pin position, is determined by the size and position of the stop in the system. For the wire test, this was defined largely by the size of the pupil of the observer's eye. It also depends on the position of the virtual image viewed by the observer, which was about 250 mm. The assumption is made that the observer's pupil is on-axis with the rest of the system.

To estimate the magnitude of this effect for the test of the ARC primary, the system was modeled and analyzed using an optical design program. The amount of im-

age shift was assumed to be equal to the difference between the position of the chief ray, which is not deviated by the beamsplitter, and the centroid of the point spread function. This shift was shown to be proportional to r, the radial position on the mirror. Figures 2.5 and 2.6 show the relationships between pupil, image shift, and induced error in the conic constant.

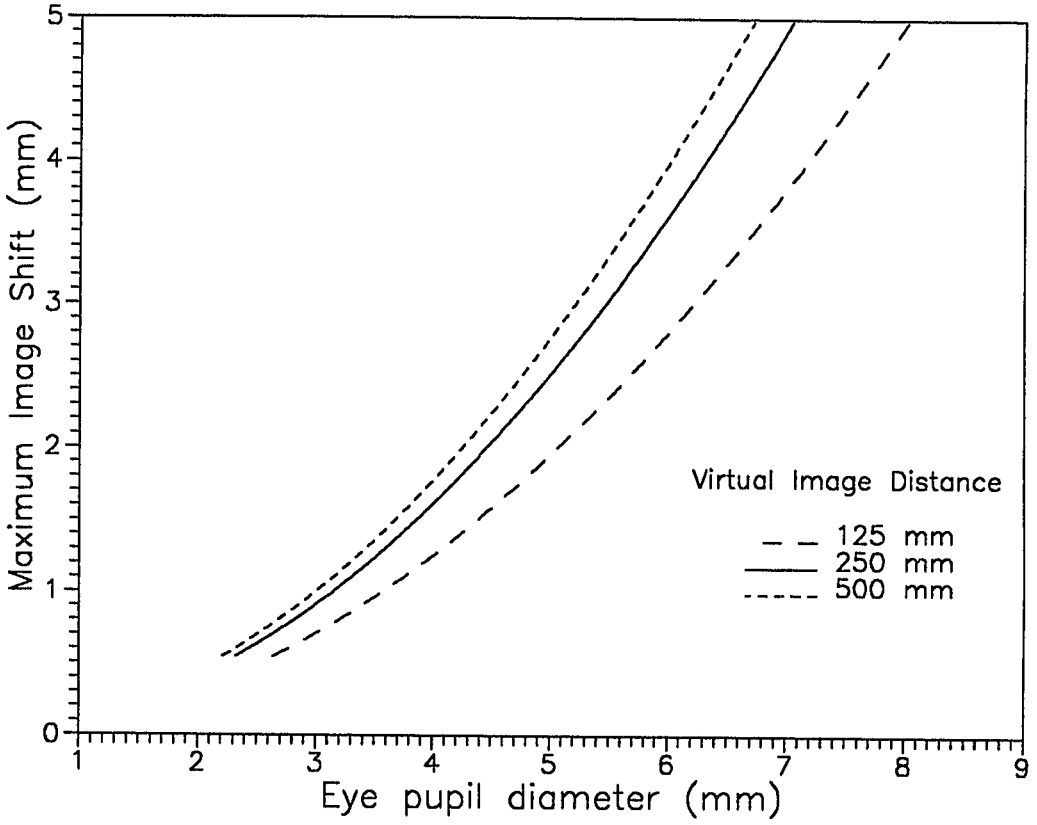

Figure 2.5. Variation in image shift of the outer pin (at 1650 mm from center) with pupil diameter. The virtual image distance depends on the placement of the eyepiece when viewing the shadow and was estimated to be 250 mm. The pupil diameter is estimated to be 5 mm ± 1.5 mm.

Assuming a likely pupil diameter of 5 mm and an image distance of 250 mm, the comatic blurring would have caused an apparent pin shift, varying linearly with radial position, of +1.5 mm per meter. In terms of angle as viewed by the observer, this shift is only 25 arc seconds per meter. This shift results in an apparent change in the conic constant K of -0.003. Allowing large uncertainties in the assumed pupil size and imaging geometry gives an uncertainty in this shift of about ±0.003. The possible pupil diameters range from about 3.5 to 6.5 mm, with either extreme unlikely (Alpern 1978). The image distance was estimated by the observers to be 250 mm plus or minus a factor of two.

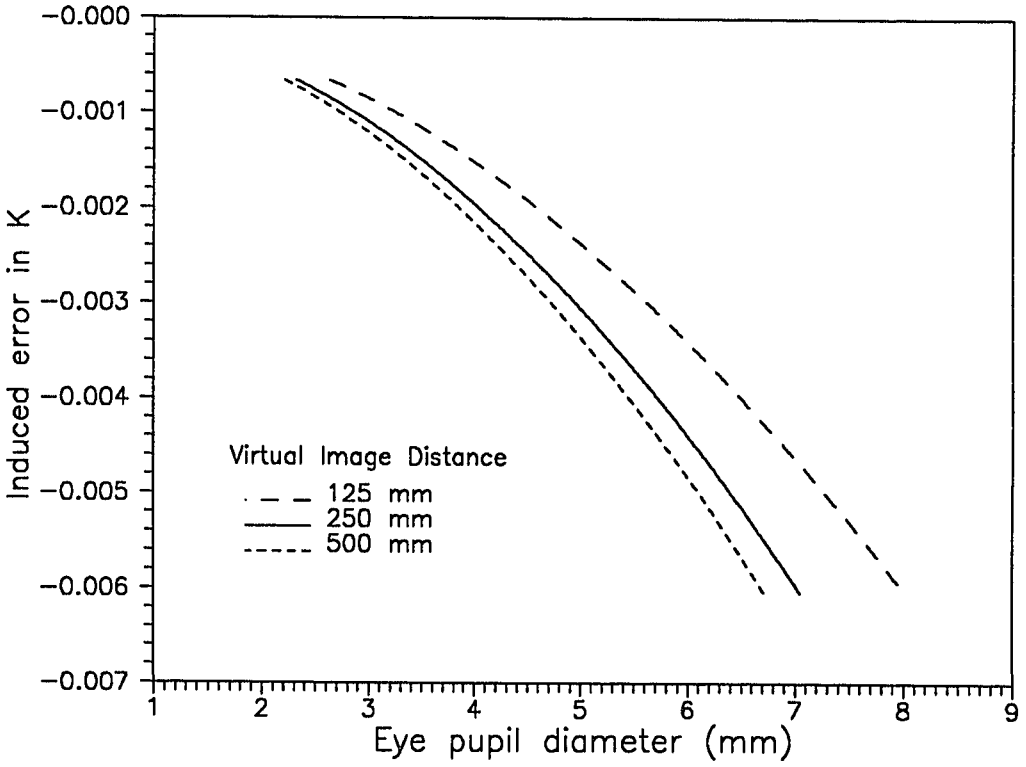

Figure 2.6. Variation of induced error in conic constant with pupil diameter. The virtual image distance was estimated to be 250 mm. The pupil diameter is estimated to be 5 mm ± 1.5 mm.

A better design of the test that eliminates this asymmetrical blurring would be required to increase the accuracy. Rather than using a beamsplitter, the source and wire can be separated laterally by several mm. However, it was impossible to repeat the test on the ARC primary because the mirror was shipped to the telescope before this effect was discovered.

2.5. RESULTS FROM TESTING A 3.5-m *f*/1.75 PRIMARY MIRROR

The wire test was performed on the finished ARC 3.5-m *f*/1.75 primary mirror to verify its radius of curvature and conic constant. A preliminary error analysis, based on a computer simulation and Monte Carlo analysis, indicated that the test would achieve an accuracy of ±0.2 mm for the radius and ±0.003 for the conic constant. The results of the test data are shown below in Table 2.1.

Table 2.1. Results from wire test on ARC 3.5-m *f*/1.75 primary.

	Nominal value	Measured value	Measurement uncertainty
Radius of curvature R	12280 mm	12279.7 mm	± 0.6 mm
Conic constant K	-1.0194	-1.019	± 0.003

For determining R, absolute Z measurements were made for seven pin positions at two azimuthal orientations. For each data point, the shadow of the wire was set on a known pin, and the distance from the mirror vertex to the wire was measured. A correction for the +0.0015 $\delta r/r$ image shift was made in the data analysis. A plot of the data is

shown below in Fig. 2.7. The fit of the radius has an uncertainty of ±0.35 mm, which is excellent. The fit of K for this data, however, has a large uncertainty of ±0.008. An analysis including the propagation of all of the measurement errors indicates that the radius of curvature is 12279.7 ± 0.6 mm

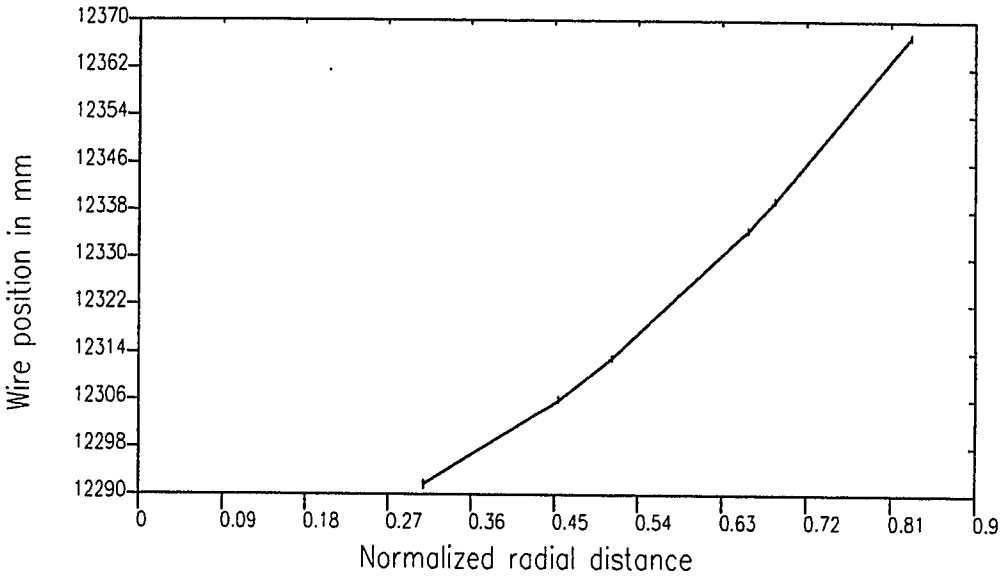

Figure 2.7. Plot of the axial wire position showing the fit of the raw data for the radius measurement of 3.5-m primary mirror. A correction was made for the 0.15% image shift of the pins due to comatic blurring. Seven data points at two azimuthal orientations were included. The fit of R is accurate, but the fit of K is not, due to the uncertainty in the tape measurements of about ±0.3 mm.

To find K, differential Z measurements were taken at 23 pin positions at four different azimuthal orientations. These measurements were made by starting at the inside pin (21 inches from the center) and moving in two-inch increments to the outside pin (at 65 inches from the center), then moving back down to the inside pin. This gave a total of 8 sets of differential data with 23 data points per set. These data had a normalizing constant term added and were averaged, keeping the variance. A least squares fit performed on the data, weighting each point appropriately by its statistical certainty,

gives a conic constant and its associated uncertainty. The +0.0015 $\delta r/r$ image shift was corrected in the data analysis.

The value of the conic constant obtained from this fit was -1.0194 with an uncertainty due to variations within the data of ± 0.0008. Including the uncertainty due to the coma in the beamsplitter, the uncertainty of the measured conic constant is ±0.003. If this error were eliminated, the test accuracy would approach ±0.001.

A plot of the calculated surface slope from all eight data sets is given in Fig. 2.8. The inner and outer points are skewed due to the relatively high slopes around the central hole and around the edge. These points only slightly affect the fit of K because they are weighted corresponding to their large uncertainties. Since the measured slope errors are generally smaller than the uncertainty in their measurement, the integrated surface profile (Fig. 2.9) contains only noise in the measurement.

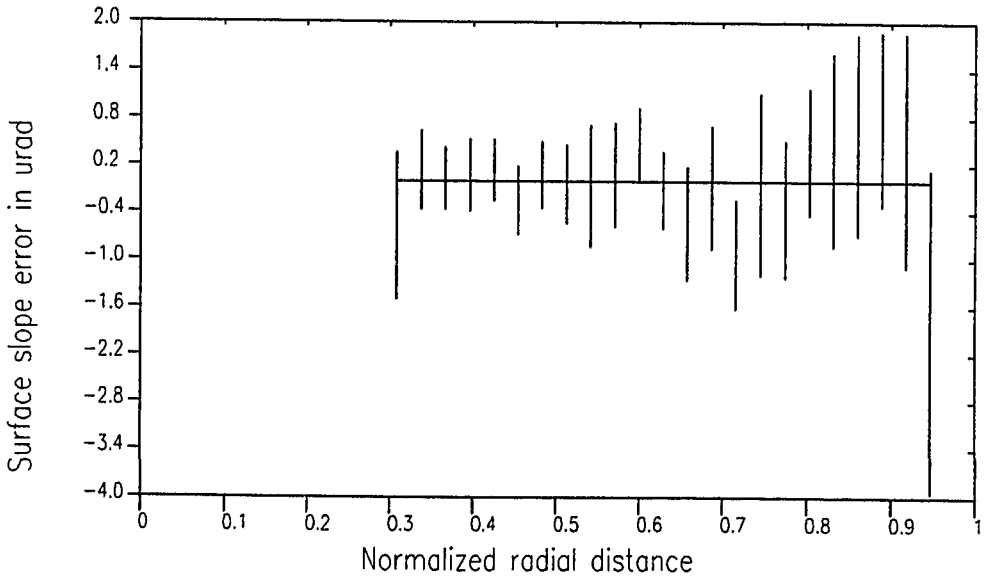

Figure 2.8. Residual surface slope errors from wire test of 3.5-m mirror. The data used were obtained by averaging 8 data sets together. The uncertainty in the fit of the conic constant to the data was ±0.0008. The error bars shown are $\pm 1\sigma$.

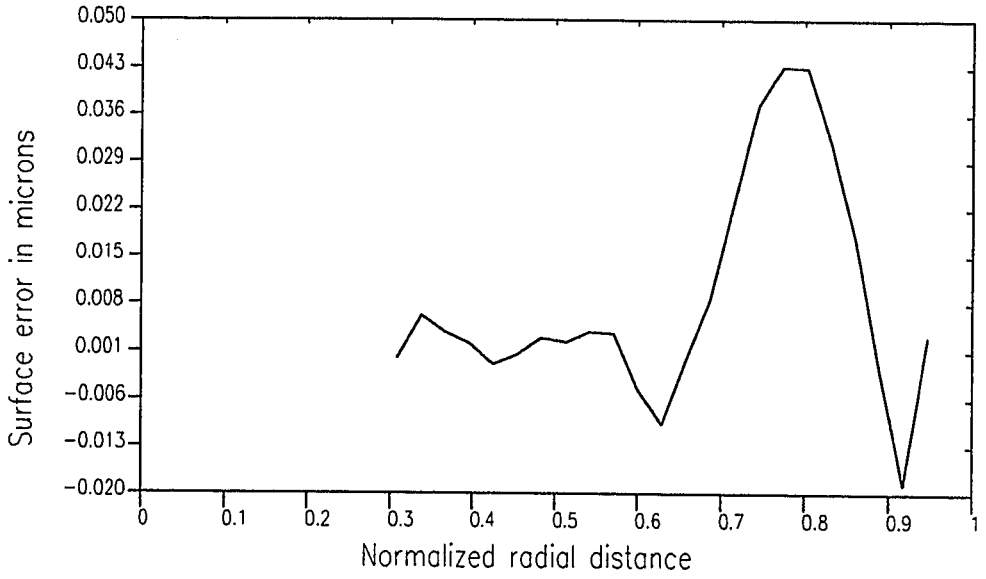

Figure 2.9. Surface profile of 3.5-m mirror computed by integration of the above slope data showing only noise in the measurement.

As described above, the estimated shift of +0.15% in pin position leads to a -0.3% change in conic constant, giving a best estimate of -1.0194 including this effect. The comatic image shift is shown in Fig. 2.10 by plotting the inferred error in determining the pin position for each data point. The error is inferred by assuming the mirror to be perfect with a conic constant of -1.0194, and the measurement to have no errors other than the pin positions. This interpretation ignores the effect of true slope errors on the mirror that would cause the measured vertical position Z to depart from its theoretical value for a particular radial position r. Instead it assigns the departure to an error in determining r. Fig. 2.10 shows the average 0.15% shift in pin position, as well as small-scale variations that would correspond to departures of the surface from the inferred hyperboloid if they were interpreted as shifts in Z due to slope errors.

The standard deviation of the data among the 4 orientations (8 measurements for each r) is shown as error bars. Normally one thinks of measuring Z as a function of r,

and recording the mean and standard deviation of Z for each r. But the data should more properly be thought of simply as point pairs (r,Z) where the major uncertainty is in the determination of r. The apparent error and standard deviation in Z were therefore converted to an apparent error and standard deviation in r by differentiating Eq. (2.1).

The width of the geometric shadow of the wire and the width of the pins are also shown in Fig. 2.10. This figure allows a visual comparison of the magnitude of the apparent image shift with the statistical uncertainty of the data, the projected shadow width, and the width of the pins.

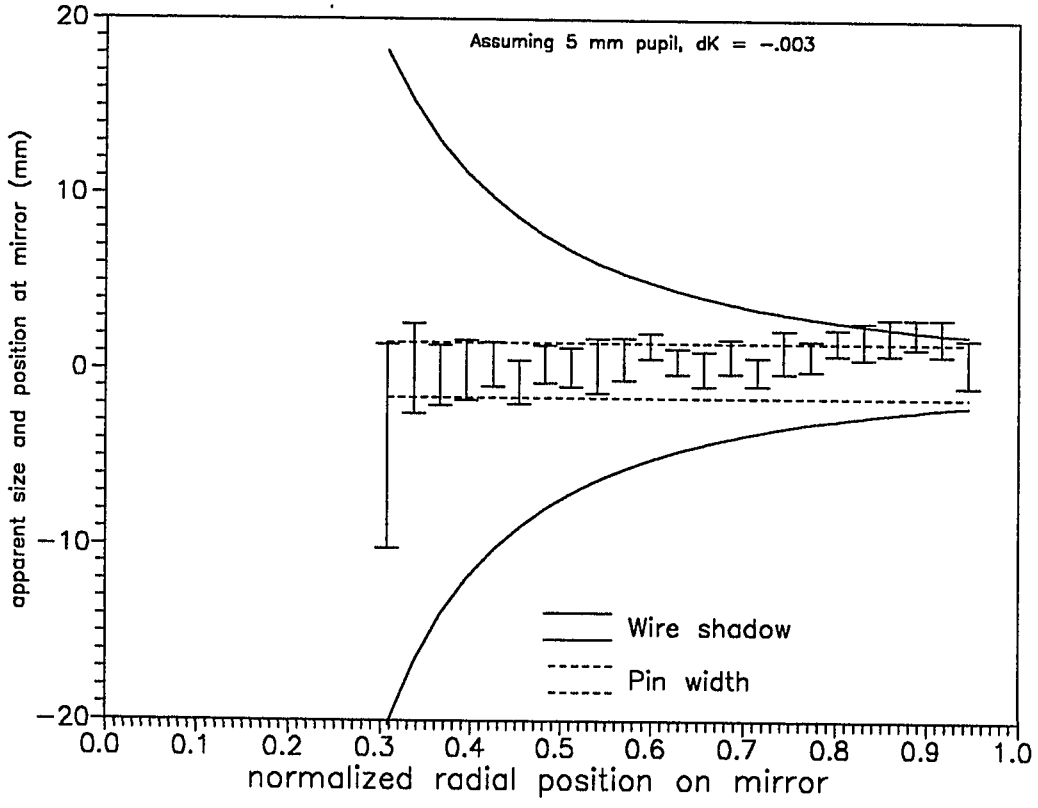

Figure 2.10. Inferred error in apparent pin position based on the measured data and assuming +0.15% image shift. The mirror is assumed to be perfect with a conic constant of -1.0194, and all fluctuations in the data are attributed to error in determining the pin position. The projected geometric widths of the wire shadow and reference pins are shown for comparison.

2.6. INTERFEROMETRIC MEASUREMENT OF LONGITUDINAL SPHERICAL ABERRATION

A variation of the wire test using an infrared interferometer was shown to be a highly effective technique for monitoring mirror shape during loose-abrasive grinding. By scanning an infrared interferometer through the normal zones and correlating radial zone position with the vertical motion, the conic constant and radius of curvature can be measured. The interference fringes may be used not only for finding the normal zone, but also for monitoring high-frequency figure errors and roll at the edge. This technique proved to be valuable for testing the WIYN 3.5-m $f/1.75$ primary while it was being ground from a sphere to a hyperboloid. This method is dramatically cheaper and simpler than methods used to guide the grinding of other mirrors. Its use combined with the loose-abrasive grinding with a sub-diameter stressed lap led to rapid convergence to the desired aspheric surface.

The wire test uses a coincident source and wire to find the radial zone on the mirror that is normal to a light ray going through that point. Another way to find the normal zone is to reflect the light from a spherical wave interferometer off the primary mirror. The spherical wavefront will reflect to form a converging wavefront with twice the spherical aberration of the primary. The amount of power in this wavefront will balance the spherical aberration such that the wavefront slope at the normal zone will be zero. The zero-slope zone may be found by observing the fringes with a small amount of tilt introduced. Because the minimum OPD occurs at the normal zone, the trough in the fringes coincides with the normal zone. This zero-slope zone is easily seen in the interferogram shown in Fig. 2.11. To perform the scanning longitudinal spherical aberration test, a bar with pins is placed on the mirror and the entire interferometer is moved axially

to line up the zero-slope zone with the image of the pins. The data analysis is identical to that for the wire test.

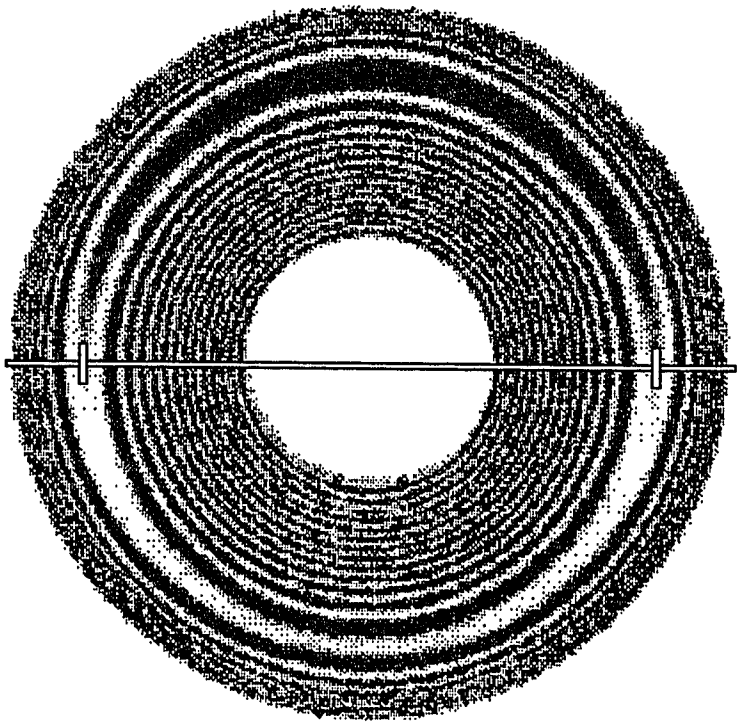

Figure. 2.11. Computer generated interferogram showing the normal zone aligned to reference marks. For outer zones on a steep asphere, this zone is much more narrow and well defined.

This test can be performed with any interferometer that creates a spherical test beam. However, infrared light must be used to during grinding because of the roughness of the ground surface. Visible wavelength light would be scattered diffusely by this surface, but infrared light is specularly reflected.

This test was used with an infrared interferometer to monitor the aspherization of the WIYN 3.5-m *f*/1.75 primary mirror. This mirror was first polished to a spherical shape for support and thermal tests, and then 171 microns of asphericity (P-V from best fit sphere) was ground in by lapping with loose abrasives. The ground surface was tested

when it was near spherical with an infrared interferometer. After the mirror had been ground to have a conic constant of -0.84, a null lens was added to guide the final grinding. There were two weeks of grinding between the time the surface was near-spherical (K greater than -0.2) to the time it had nearly the final shape (K less than -0.85). During this time, the infrared interferometric measurement of the longitudinal spherical aberration was used.

The data and the polynomial fit for an IR "wire test" of the WIYN primary are shown in Fig. 2.12. At this stage in the fabrication, the surface had over 100 microns peak to valley departure from best-fit sphere. The best-fit conic section is given by R = 12287.5 mm and K = -0.654. The integration of these data gives the surface departure from this ideal conicoid, shown in Fig. 2.13.

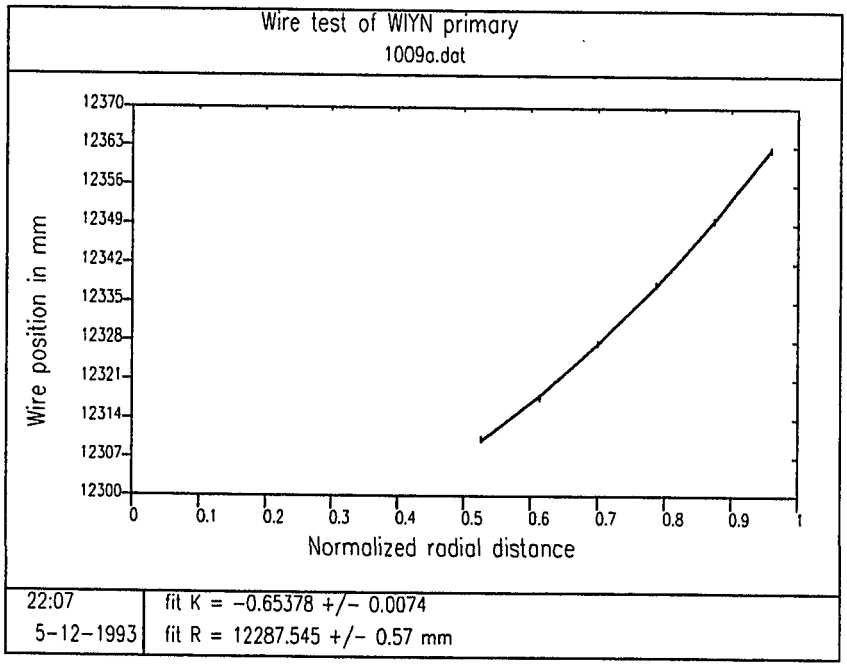

Figure 2.12. Axial center of curvature position for the infrared "wire test" of the WIYN primary mirror during asphericization. The infrared interferometer was scanned axially, using the interference fringes to determine the normal zone. The analysis is identical to that used for the wire test.

This method was shown to be adequate to guide the grinding and efficient to use. The conic constant was measured to 2% as it progressed from 0 to -1.07. Higher-order figure errors, such as those seen in Fig. 2.13, were also measured and controlled. Dave Anderson, the chief optician running the test, could perform the measurement and reduce the data in less than one hour. The simplicity of this technique is contrasted with a costly method used by Küchel and Heynacher (1988) to monitor the aspherizing of the NTT primary mirror. They used an infrared interferometer with a succession of seven different germanium and barium fluoride null lenses to monitor the grinding of a mirror with half the asphericity of the WIYN primary.

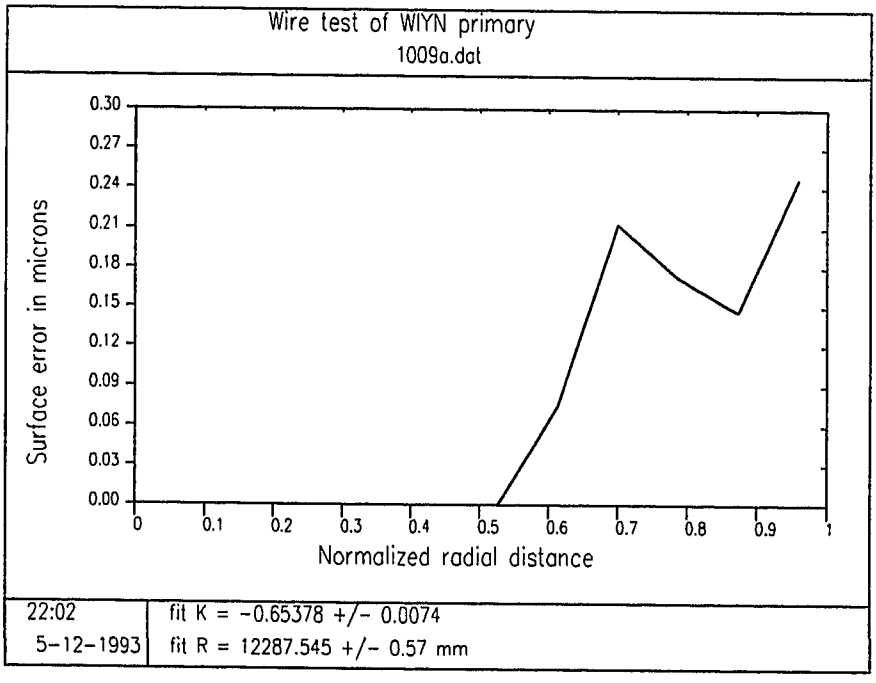

Figure 2.13. Surface profile from IR "wire test" of the WIYN primary mirror during aspherization. The surface error shown is relative to a conic section of revolution given by the K and R given. At this stage, the mirror had over 100 μm departure from the best-fit sphere.

2.7. CONCLUSION

The wire test is an inexpensive technique for measuring the conic constant of a primary mirror to moderate accuracy and the radius of curvature to high accuracy. It requires very little equipment and can be quickly performed on a polished or ground surface. It may be used as a check on the null lens to verify the shape of the primary mirror or it may be used to monitor the conic constant of a mirror while the asphere is being ground in.

The wire test performed on the ARC primary confirmed the vertex radius of curvature and conic constant of the finished mirror to an accuracy of ±0.6 mm and ±0.003, respectively. The largest contribution to the uncertainty in the conic constant came from an asymmetrical image degradation that could not be accurately quantified. This effect was estimated and incorporated into the data reduction. The uncertainty in quantifying the effect caused the stated uncertainty in conic constant. With the elimination of the cube beamsplitter, the accuracy of this test could approach ±0.1% in measuring the conic constant.

An interferometric version of the wire test was used to monitor the aspherizing of the WIYN 3.5-m *f*/1.75 primary mirror. This test used an infrared interferometer to scan axially, giving a measurement of the conic constant, radius of curvature, and zones as broad as one-fifth radius wide. It also allowed visual inspection for high frequency errors and allowed careful control to avoid rolling off the edge.

The greatest attributes of the wire test are its simplicity and low cost to set up and perform. While the accuracy is not high enough to certify modern large primary mirrors, it may be good enough for smaller mirrors and is certainly accurate enough to guide early stages of grinding. This is a test that should be considered for any primary mirror.

CHAPTER 3

THE SCANNING PENTAPRISM TEST

3.1. INTRODUCTION

The scanning pentaprism test is a highly accurate test for measuring the radial profile of a primary mirror. In this test, a collimated laser beam is scanned across the diameter of a primary mirror using a pentaprism. This beam is reflected by the primary mirror to form a sharp image at the focal point of the mirror. Motion of this image, as the beam is scanned across the mirror, is used to measure slope errors in the near-paraboloidal mirror.

The high accuracy of this test relies on two fundamental principles. First, any incident beam of light that is parallel to the axis of a paraboloidal mirror will be reflected to form a sharp image at the focal point. Second, a pentaprism deflects a beam of light by 90°, independent of small rotations of the prism. This combination gives a null test for paraboloidal mirrors that is insensitive to errors in the scanning mechanism. The image motion for testing near-paraboloidal mirrors is small enough that the sensitivity for measuring slope errors remains high.

The scanning pentaprism test is not new, and its use is not limited to testing primary mirrors. Korhonen (1987) describes the use of this test to monitor grinding of the Nordic Optical Telescope. It can also be used as an end-to-end test of an assembled telescope (Wilson 1990; Espiard and Favre 1970). The scanning pentaprism has been

used with an autocollimator to measure flat surfaces (Hochgraf 1969). The new aspects of the work presented in this chapter are the computer-controlled implementation, the error analysis, and some limitations of the test that have not been previously discussed.

This test was pursued at Steward Observatory to allow a measurement of fast primary mirrors that is completely independent of the null corrector. In the unlikely event of a flawed null corrector, this test would discover the error in the optical shop where the null lens and mirror may be corrected. The development of the holographic null lens test (Chapters 6 and 7) makes the scanning pentaprism test unnecessary as a verification of the null corrector. However, this test is useful for other applications such as monitoring the profile of a mirror during grinding.

The test is described in Sec. 3.2 and the sensitivity to alignment errors is derived in Sec. 3.3. In this section, a technique for determining the misalignment terms based on the test data is given. The scanning pentaprism test was implemented at the Steward Observatory Mirror Lab to verify the figure of a 1.8-m $f/1$ primary mirror and to serve as a prototype for testing 8-m mirrors. For the test of the 1.8-m primary, described in Sec. 3.4, the laser beam was scanned across a radius of the mirror and not a full diameter. This allowed the surface figure errors to couple with the misalignment of the test, limiting the accuracy of the conic constant measurement to 0.3%. A computer simulation was performed that predicted the accuracy to increase a factor of 20 when full diameter scans are used. This analysis is discussed in Sec. 3.5.

3.2. TEST DESCRIPTION

The scanning pentaprism test measures slope errors in paraboloidal mirrors by scanning a collimated laser beam across the surface and measuring the motion of the reflected spot. The test configuration, shown in Fig. 3.1, uses a pentaprism mounted on a

horizontal translation stage to scan the laser beam. The pentaprism keeps the beam parallel to the optical axis of the primary, even though imperfections in the rail cause the prism to rotate. A CCD array at the focal point of the primary mirror (prime focus) is used to measure the motion of the image. The test could be equivalently performed with a point source at prime focus and the detector at the focal point of the collimating lens.

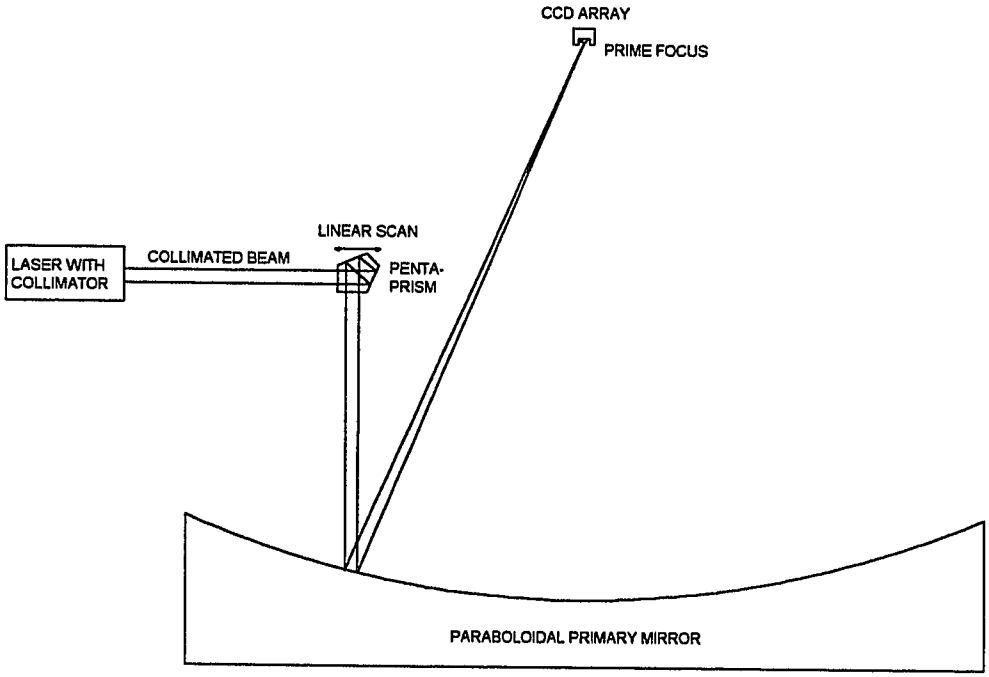

Figure 3.1. Schematic layout of the scanning pentaprism test. The pentaprism is used to scan a collimated beam across the diameter of a paraboloidal primary mirror. As the beam is scanned, image motion is measured by a CCD camera giving the slope deviation from a paraboloid.

The pentaprism is used because it deflects light 90° in the scanning direction irrespective of small rotations of the prism. So it is not the angular orientation of the prism (which moves) that determines the angle of the laser beam hitting the mirror, but the orientation of the laser collimation optics (which are fixed). This isolates the test from

mechanical errors in the translation stage. The accuracy is achieved by keeping the collimation optics, the mirror, and the camera fixed in space, while the prism is scanning.

When designing the test several basic parameters must be set. The scan should be made to go across a complete diameter of the mirror, not just a radius. This is explained more fully in Sec. 3.5. The scanning mechanism must be chosen to be sufficiently accurate in the direction perpendicular to the scan that the laser spot stays on the CCD. The alignment errors can be determined from the spot motion data, as long as the spot motion can be measured. The technique for determining alignment errors is given in the next section. The scanning mechanism must be placed far enough from the mirror that the pentaprism does not block the light reflected from the innermost tested region on the mirror. Most importantly, the assembly must allow fine linear and angular adjustments, but be both stable and stiff.

Small, systematic errors may be measured and corrected in the data analysis. These errors can originate from mechanical deflections of the support structure as the pentaprism moves. They can also be induced optically if the CCD camera has a window in front of the detector. Random errors due to vibration, atmospheric seeing, and electronic noise are reduced by averaging many measurements. This is easily accomplished by automating the data collection.

3.3. ALIGNMENT SENSITIVITY

The relationships between system misalignment and motion of the spot are derived using vector aberration methods. In this treatment, the wavefront aberrations are related to the misalignment terms. From these wavefront errors the transverse ray aberrations, or ray intercepts at the image plane are computed. When the spot motion is fit

to a polynomial, the independent misalignment degrees of freedom are shown to be separable. The polynomial coefficients are used to compute the misalignments, allowing accurate adjustments of all of the important degrees of freedom.

FIRST-ORDER ANALYSIS

A first-order analysis of the test yields a polynomial expansion for image position as a function of pentaprism position. This fit decouples misalignment terms from errors in the mirror. The first-order model is generally adequate because the computed error terms are minimized iteratively by mechanical alignment using the measurements as feedback. The second- and higher-order errors are negligible because they are proportional to the products of two or more errors that are kept small. Because the error terms are computed to an accuracy of several percent, each scan allows adjustment that can reduce the errors to several percent of the previous value. After a few iterations, the errors become small, and their effects on the measurement become negligible.

This analysis assumes that the mirror with conic constant $K = -1+\delta K$ is fixed in space. It assumes that a linear scan is made across the mirror using a collimated beam of light that is not generally parallel to the optical axis of the mirror. It also assumes that the image plane is located near the focal point of the primary mirror. This allows nine meaningful degrees of freedom consisting of the conic constant of the primary mirror, four degrees of freedom for the scan beam, and four for the image plane. These are outlined in Table 3.1, and the important errors are shown in Fig. 3.2 for the scanning beam and in Fig. 3.3 for the CCD camera.

Of the nine degrees of freedom, only four have first-order effects on spot motion. These four, the axial position of the camera, the conic constant of the mirror and the sagittal and tangential misalignments of the scanning beam, are treated in the polynomial

expansion. The rest affect the image spot motion only to second- or higher-order, and must be treated independently. All nine degrees of freedom are listed in Table 3.1. The typical values listed are based on the measurement of the 1.8-m primary mirror.

Table 3.1. Alignment degrees of freedom for scanning pentaprism test.

Expression	Description	Order	Typical value
α_x	optics pitch (radians)	1	0.0002
α_y	optics roll (radians)	1	0.03
δz	image plane axial position (units of focal length)	1	0.0001
δK	conic constant deviation ($= K+1$)	1	0.003
δx	scan position error (units of mirror half-diameter)	2	0.001
δy	scan offset (units of mirror half-diameter)	2	0.001
β	image plane rotation about optical axis (radians)	2	0.002
γ_x	image plane tilt in x direction (radians)	3	0.02
γ_y	image plane tilt in y direction (radians)	3	0.02

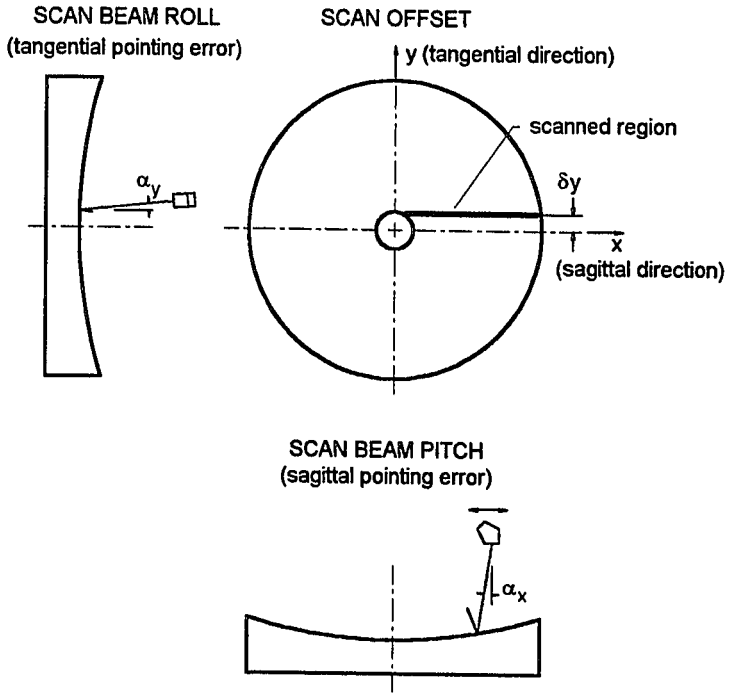

Figure 3.2. Errors in the scanning beam. Of these, only α_x and α_y affect the image motion to first order.

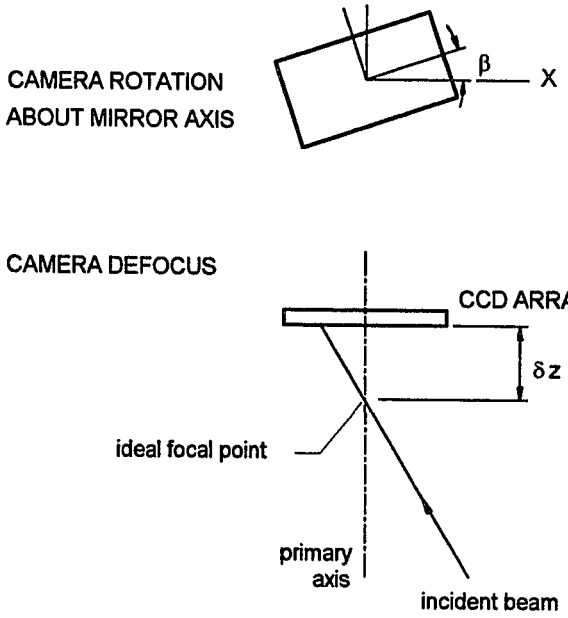

Figure 3.3. Errors in the camera position. Of these, only defocus δz affects the image motion to first order.

The scanning beam is generally affected by motion of the collimator or the pentaprism, although the motion in the sagittal plane is shown to depend only on the collimator. The degrees of freedom are defined using the roll, pitch, and yaw of the items (See Fig 3.4).

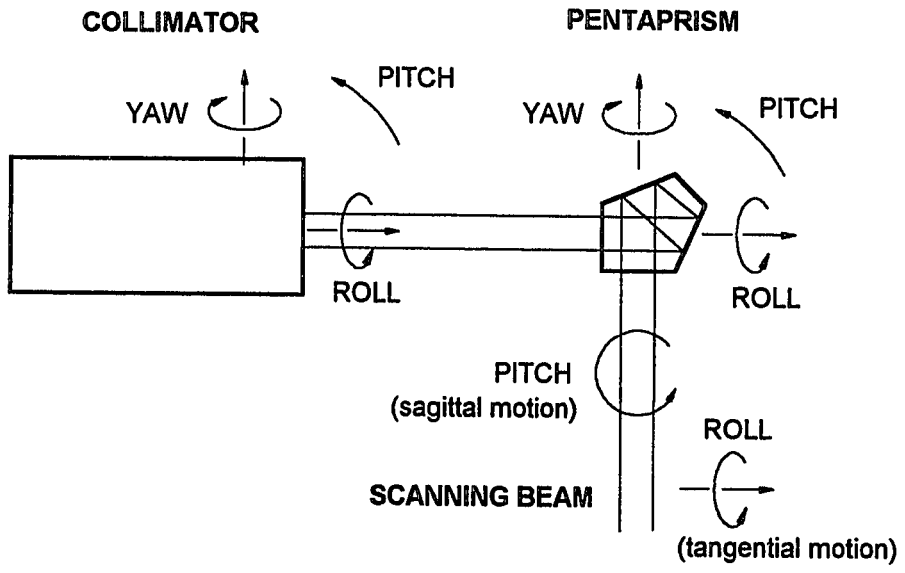

Figure 3.4. Misalignment of the collimator, pentaprism, and scanning beam.

To first order, the optical beam pitch and yaw are given by

$$\textit{beam pitch} = \textit{collimator pitch}$$

$$\textit{beam roll} = -\textit{collimator yaw} + \textit{pentaprism roll} + \textit{pentaprism yaw}.$$

Motion of the pentaprism can cause the beam to move only in the tangential (roll) direction. Motion of the collimator directly couples into the scan beam in both sagittal and tangential directions.

The first-order misalignments are analyzed by computing the wavefront aberration coefficients for the misaligned system. These coefficients give the wavefront error in pupil coordinates for focus, coma, and spherical aberration. The coefficients and the notation used for this analysis are defined by Shack (1988). The transverse ray aberrations, which give the ray intercepts with the focal plane, are then computed by taking the gradient of the wavefront error function.

The axis of the scanning beam is assumed to deviate by α_x and α_y from the optical axis of the near-paraboloidal mirror. This causes tilt in the wave aberration and a constant lateral shift in the image position, which can be ignored. It also causes coma, given by

$$W_{131} = \frac{y_p^{\,3}}{4f^2}\alpha \tag{3.1}$$

where W_{131} = wavefront coma coefficient

y_p = radius (half-diameter) of primary mirror

α = angular deviation

f = focal length of primary mirror.

This tilt also causes astigmatism that is neglected because it has a second-order dependence on α.

An error in the axial position of the image plane causes defocus given by

$$W_{020} = \frac{y_p^{\,2}}{2f^2}\delta z \tag{3.2}$$

where W_{020} = wavefront focus coefficient

δz = focal plane axial position error (in direction away from mirror).

The deviation of the conic constant K from -1 results in spherical aberration of the form

$$W_{040} = \frac{y_p^4}{32 f^3} \delta K \tag{3.3}$$

where W_{040} = wavefront spherical aberration coefficient

δK = primary conic constant departure from a paraboloid = $K + 1$.

The coma, focus, and spherical aberration are represented by the vector equation

$$\begin{aligned} W = & W_{020}(\boldsymbol{P} \cdot \boldsymbol{P}) \\ & + W_{131}(\boldsymbol{H} \cdot \boldsymbol{P})(\boldsymbol{P} \cdot \boldsymbol{P}) \\ & + W_{040}(\boldsymbol{P} \cdot \boldsymbol{P})(\boldsymbol{P} \cdot \boldsymbol{P}) \end{aligned} \tag{3.4}$$

where $\boldsymbol{P}$ = normalized vector pupil position = $\dfrac{(x, y)}{y_p}$

$\boldsymbol{H}$ = normalized vector field angle = $\dfrac{(\alpha_x, \alpha_y)}{|\alpha|}$

(x, y) = scanning beam intercept with mirror surface

(α_x, α_y) = beam angle with respect to mirror axis.

The ordered pairs are used to represent vectors in the mirror coordinates. The x-direction coincides with the sagittal direction on the surface as it is scanned. The y-direction corresponds to the tangential direction on the surface. The vector representation of the angles requires the projection of the misaligned ray onto the mirror.

The inner products in Eq. (3.4) are computed and Eqs. (3.1), (3.2), and (3.3) are substituted for W_{131}, W_{020}, and W_{040}, resulting in the general equation that describes the wave aberration,

$$W(x,y) = \frac{1}{2f^2}\delta z\left(x^2+y^2\right) + \frac{1}{4f^2}\left(\alpha_x x+\alpha_y y\right)\left(x^2+y^2\right) + \frac{1}{32f^3}\delta K\left(x^2+y^2\right)^2. \tag{3.5}$$

The transverse ray aberrations, ε_x and ε_y give the x and y ray intercepts with the image plane, where the x and y directions retain their previous definitions. The ray aberrations are given to an excellent approximation by Rayces (1964) as

$$\varepsilon_x = -f\frac{\partial W}{\partial x},\quad \varepsilon_y = -f\frac{\partial W}{\partial y}. \tag{3.6}$$

The scan is defined to be in the x-direction, and only terms with first-order dependence on the error terms are kept to arrive at the equations relating spot motion to prism position,

$$\varepsilon_x = -\frac{\delta z}{f}x - \frac{3\alpha_x}{4f}x^2 - \frac{\delta K}{8f^2}x^3 \tag{3.7}$$

$$\varepsilon_y = -\frac{\alpha_y}{4f}x^2. \tag{3.8}$$

The test is performed by measuring the spot motion (ε_x, ε_y) and the scan position x. A least-squares polynomial fit to $\varepsilon_x(x)$ gives coefficients on x^1, x^2, and x^3 that are used to calculate δz, α_x, and δK. This calculation requires the focal length f, which is usually known to several hundredths of a percent.

3.4. TEST OF A 1.8-m *f*/1 PRIMARY MIRROR

The scanning pentaprism test was run on the 1.8-m *f*/1 primary mirror for the Lennon Telescope to verify its radial profile. The telescope tolerance for conic constant was ±0.0005, but the conic constant of the mirror was verified to an uncertainty of ±0.003. The accuracy of this test was limited by an inability to decouple small alignment errors from errors in the optical surface. As a prototype for learning how to perform the test on large primary mirrors, this test was successful. It was learned that scanning only across a radius of the mirror limits the ability to measure spherical aberration in the presence of other errors.

EQUIPMENT

The hardware used to perform the test is divided into four major systems: the projection optics, the scanning mechanism, the imaging system, and the control system.

1. Laser projection optics --

   A collimated laser beam was created using a 1 mW HeNe laser, a microscope objective with spatial filter, and a collimating lens. The beam diameter and intensity were controlled using an iris and rotating polarizers.

2. Scanning mechanism --

   The pentaprism was translated along a rail using a ball screw that was driven by a stepper motor. After calibrating, the computer control of the motor provided positioning accuracy better than 1 mm.

3. Imaging optics and electronics --

   The motion of the image formed at prime focus was measured using a CCD camera with frame-grabber. The geometric centroid of the laser spot was computed for each position of the pentaprism.

4. Control computer --

   The test was automated using a single personal computer to drive the pentaprism, digitize the camera image, compute the centroid of the laser spot, and perform all of the data reduction. All operations ran under a single menu-driven program.

The entire system was mounted onto a rigid frame above the primary mirror. The deflection of the frame from the moving prism was measured using an autocollimator and was subtracted from the data, as described below. A rigid, vibration-isolated, steel structure supported both the mirror and the test frame.

ALIGNMENT PROCEDURE

The alignment of the test was performed in stages. The collimator, pentaprism, and rail were first co-aligned. This system was mechanically positioned using coarse adjustments and mechanical measurements to scan along a radius of the mirror with the scanning beam nominally parallel to the optical axis. Finally, this system and the CCD camera were aligned to the primary mirror using fine adjustments, relying on the spot motion as feedback.

The collimator, prism, and rail were co-aligned to 1 mrad. The laser beam was collimated over a 25 mm diameter using a 200 mm focal length lens. The yaw and pitch of the collimator were adjusted to make the beam point along the direction of the scanning motion. This was performed by tilting the collimator to keep the laser spot from wandering on the face of the prism as it moved down the rail. The orientation of the pentaprism was adjusted in yaw and pitch to make the collimated beam normal to the face of the cube.

The entire rail-collimator system was positioned to scan across a radius of the mirror with its scanning beam parallel to the optical axis of the mirror. A string was drawn taut across a diameter of the mirror for reference. The pentaprism was adjusted in roll to keep the beam reflected by the primary coplanar with the incident beam and the beam from the collimator. After the roll adjustment was made, a translation was required to keep the scanned beam along the radius, as defined by the string. It took several roll and translate iterations until the alignment goals of 1 mm scan offset and 1 mrad roll were reached. This task was complicated by the errors in the rail of about one mrad peak to valley.

The pentaprism was driven along the rail by a 1/8-inch-pitch ball screw turned by a stepper motor having 12800 steps per revolution. The outer edge of the primary mirror was used as the reference for relating the prism position on the rail to the laser beam position on the mirror. The measurements were taken at each point by moving the prism to the correct position, pausing 3 to 5 seconds to allow vibrations to damp out, and averaging 16 centroid measurements. A single scan of 250 points across the radius took 30 minutes, but required no operator intervention.

The rail was of poor quality, indicated by the slope errors plotted in Fig. 3.5. The test of the primary mirror was shown to be insensitive to these gross errors by shifting

the rail with respect to the mirror. A scan of the mirror was first measured with the rail at its original position. The rail was then shifted two inches and the mirror was re-measured. Even in the worst region of the rail, the sagittal data showed no significant correlation with the rail.

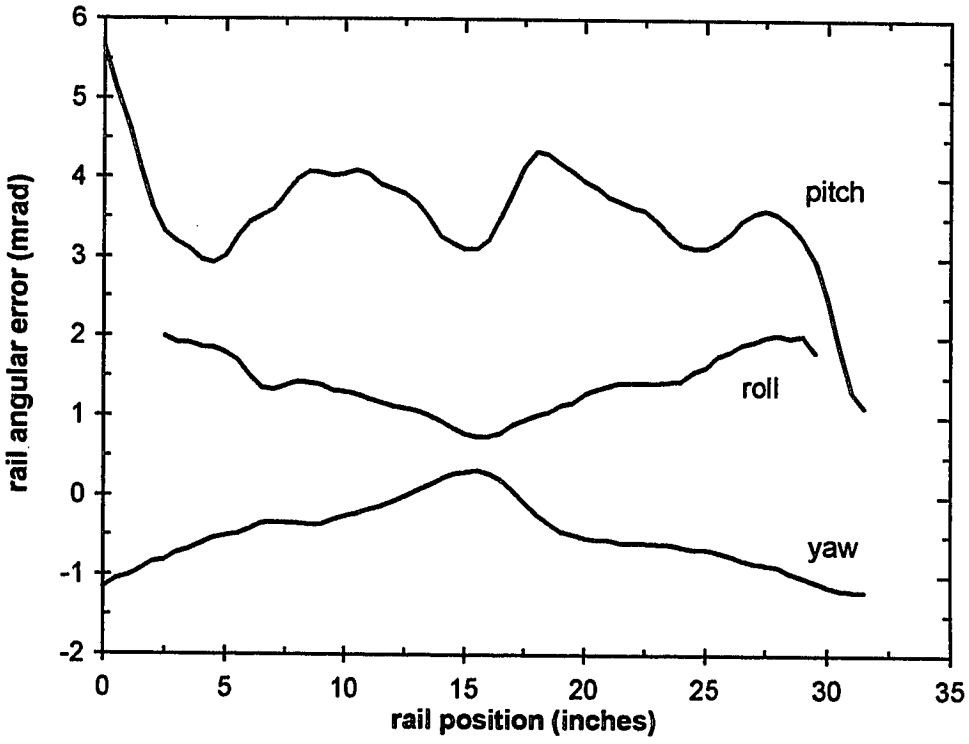

Figure 3.5. Angular errors in the rail used to test the 1.8-m primary mirror.

The orientation of the CCD camera was determined by using the tangential spot motion that was caused by the large rail errors. Since the rail errors cause image motion in the tangential plane and none in the sagittal plane, these errors were used as a reference for orienting the camera. The camera was rotated to minimize the correlation between the sagittal and tangential scans. This worked well because the rail errors were many times larger than the local slope errors in the mirror.

IMAGE PROCESSING

The accuracy of the test relies upon the ability to measure the motion of the laser spot on the CCD camera. This was performed by digitizing the image and computing the centroid of the intensity distribution. The spot size and the computer algorithm were chosen to optimize the precision of the measurement. A 12.5 mm diameter scanning beam was used, producing a clean Airy diffraction pattern.

The centroid was computed using the defining equations

$$\bar{x} = \frac{\sum_{i,j} I_{ij} x_{ij}}{\sum_{i,j} I_{ij}}$$

$$\bar{y} = \frac{\sum_{i,j} I_{ij} y_{ij}}{\sum_{i,j} I_{ij}} \qquad (3.9)$$

where $(\bar{x}, \bar{y})$ = centroid of spot in microns

(i, j) = digitized pixel indices

(x_{ij}, y_{ij}) = position of digitized pixel (i, j) in microns

I_{ij} = digitized signal of pixel (i, j) corresponding to the light intensity.

The sums in Eq. (3.9) were taken over a circular region centered on the brightest pixel in the field. The size of this region was set to the diameter of the first zero in the Airy pattern to optimize the precision of the centroid measurement. With a 12.5 mm scanning beam, the noise in the centroid position varied from 0.25 to 0.5 pixels or 1.2% to 2.5% of the Airy disk diameter.

The random errors in the centroid measurement were reduced by averaging 16 measurements for each data point. In addition, each point on the mirror was four times oversampled because a 12.5 mm scanning beam was stepped at 2.8 mm intervals.

The camera was rotated to align the sagittal plane with the "vertical" direction on the CCD. The digitized pixels in the vertical direction coincide with the video lines that are determined by the CCD detector spacing. When the frame grabber and camera are used in an interlaced mode, there is a one-to-one match between the vertical digitized pixels and rows of detectors on the chip. Since the detector spacing is known accurately, measurements can be made in units of digitized pixels and scaled by the vertical detector spacing. The horizontal pixel size is not correlated with the CCD dimensions, but with the timing of the digitization. Each video line from the CCD is read off the detector chip one pixel at a time, but the readout clock is not transmitted with the signal. The signal sent to the frame grabber consists of video lines with no information about the original horizontal pixel sizes. So the horizontal dimensions of the digitized pixels depend only on the timing in the frame grabber.

To measure the digitized pixel period, the camera was translated laterally on a micrometer-driven translation stage while a fixed spot was focused on the array. The measured image motion was used to determine the horizontal pixel spacing as 12.0 μm and confirmed the vertical pixel spacing to be 9.8 μm.

The automatic gain control of the camera was disabled, and the image on the CCD was digitized using an 8-bit frame grabber. The laser was blocked before each run to measure a dark field that contained the background illumination and fixed-pattern detector noise. This dark field was stored in memory on the computer. For the centroid measurements, the dark field was systematically subtracted from the digitized video.

MEASUREMENT PROCEDURE

After the system was well aligned, the data from the scans were used to measure the errors in the surface figure of the mirror. The mirror was sampled every 2.8 mm with a 12 mm diameter beam. Typically, the centroid was measured 16 times per scan point and 250 scan points were taken across a radius. In all, 68 scans at 12 azimuthal angles were taken for the measurement of the 1.8-m primary.

Two corrections were made to the data for known errors in the test coming from flexure of the steel support and from a window on the CCD array. As the pentaprism scanned across the mirror, flexure in the structure caused pitch rotation of the laser collimator. This motion was measured using an autocollimator and shown to have 4 arc seconds P-V motion, varying almost linearly with the scan position. The repeatability of this measurement was limited by the ±0.5 arc second precision of the autocollimator. The autocollimator data was fit to a second-order polynomial, and the coefficients were used to subtract this effect from the measurement of the mirror. A second correction was required to compensate for the beam deflection caused by the 800 μm thick window on the CCD array. The effect of this window was derived using Snell's law at the two air-glass interfaces of the plane parallel plate. The equation for the centroid shift on the CCD,

$$\Delta x = t \sin\theta \left(\frac{1}{\cos\theta} - \frac{1}{\sqrt{n^2 - \sin^2\theta}} \right), \tag{3.10}$$

where Δx = lateral shift of ray intercept at CCD

θ = ray angle with respect to normal onto window (and CCD)

t = window thickness

n = refractive index of window,

was implemented into the data analysis software and this effect was corrected. This corresponds to the axial image shift and the third-order spherical aberration that is commonly associated with plane parallel plates.

The accuracy of the prism was verified by observing the angular motion of a light beam as the prism was rotated. An autocollimator was used to verify that the angular deflection was less than 1 arc second for prism rotation of ±5°.

RESULTS FROM TESTING A 1.8-m *f*/1 PRIMARY MIRROR

The results from this test on the 1.8-m were limited by a combination of two effects. First of all, the scan was only performed across a radius of the mirror and not a full diameter. Secondly, the mirror had large slope errors including a roll-off two inches from the outer edge. The combination of these two things made it impossible to accurately separate the spherical aberration from the alignment errors. The coupling of these effects is explained more fully below.

The primary mirror had regions with large slope errors. An interferogram depicting the figure of this mirror, shown in Fig. 3.6, demonstrates some of these. This interferogram shows that many of the figure errors are not axisymmetric, so the high-frequency component in the average of 12 radial scans will not give a good representation of the average radial profile.

Figure 3.6. Computer generated interferogram showing the measured figure of the 1.8-m $f/1$ primary mirror at 633 nm, as determined using phase shifting interferometry through a null corrector. A sharp roll at the edge of the mirror was not resolved by the measurement.

The sagittal and tangential profiles of the laser spot motion are shown for a single scan of the 1.8-m primary mirror in Figs. 3.7 and 3.8. The vertical hashes give $\pm 1\sigma$ error bars showing the random distributions of the measured centroids. The polynomial fits for the data are also shown. The edge roll is apparent in the sagittal scan shown in Fig. 3.7 and the rail errors dominate the tangential scan given in Fig. 3.8.

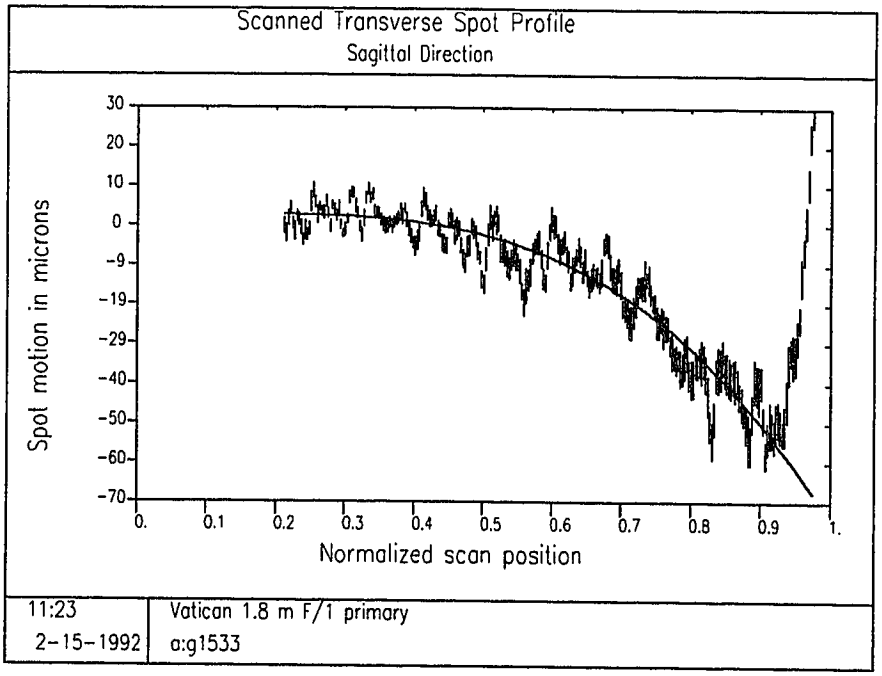

Figure 3.7. Sagittal spot motion for a single scan of the 1.8-m primary mirror. The $\pm 1\sigma$ distributions are shown as vertical hashes.

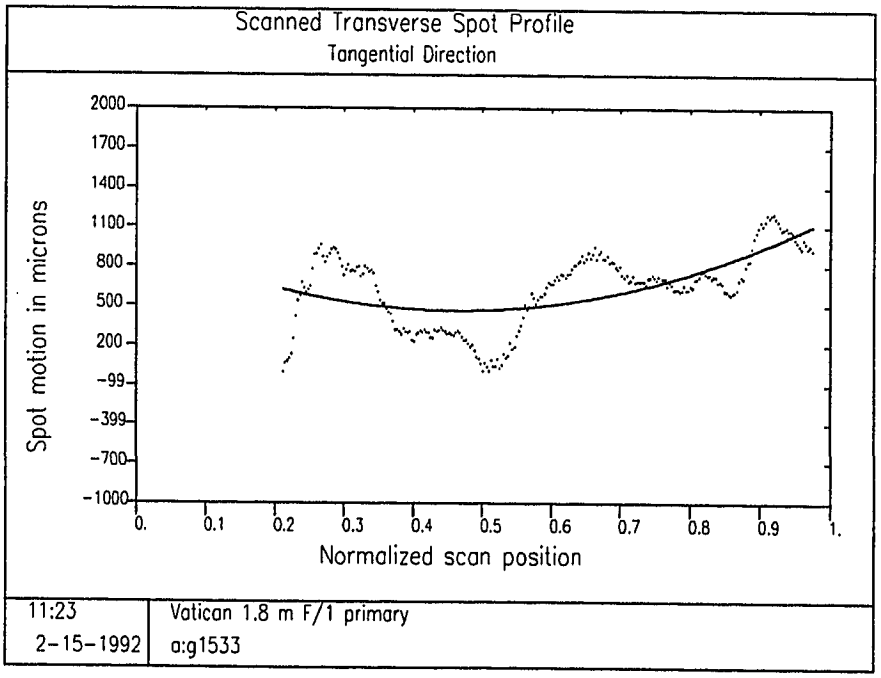

Figure 3.8. Tangential spot motion for a single scan of the 1.8-m primary mirror. The $\pm 1\sigma$ distributions are shown as vertical hashes.

All 68 measurements at 12 azimuthal angles were used to determine the conic constant of the mirror. The figure errors in the mirror and the inability to accurately determine alignment errors affected the calculation of the conic constant using the polynomial fit. When the edge data was excluded from the fit, the fit value of K varied. The conic constant from this analysis is therefore a function of the limiting outer radial position of the data used for the polynomial fit. The conic constant was calculated using data that extended to 0.85, 0.90, and 0.95 of the full 914-mm radius. The results of this are shown in Fig. 3.9. Assuming a fit to 0.92 (73 mm from the outer edge of the 1828 mm mirror), the conic constant of the mirror was estimated as -0.996 ± 0.003. The value of 0.92 was chosen to include as much good data as possible, but to leave out the edge roll. Based on the null corrector design and tolerance analysis, the mirror was expected to have a conic constant of -0.9958 ± 0.0003.

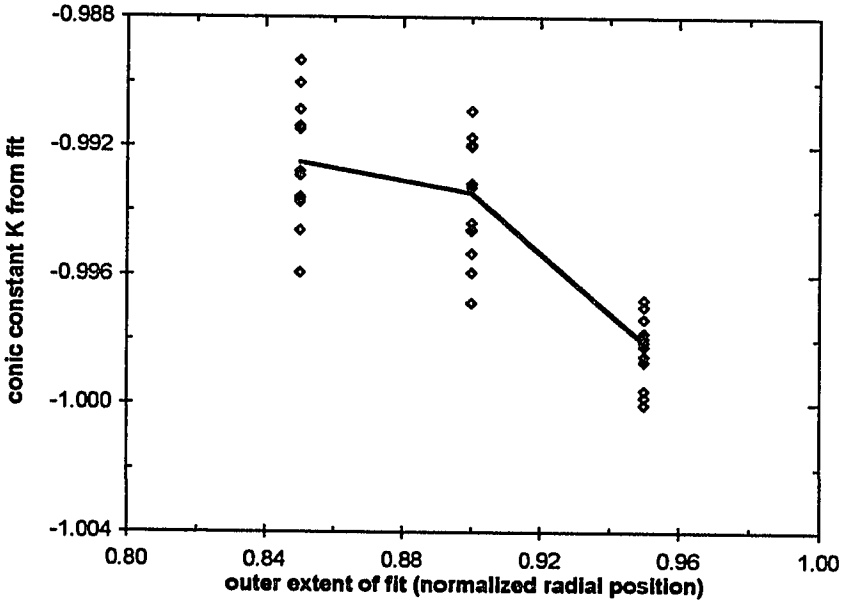

Figure 3.9. Variation in conic constant fit with the radial extent of the data used for the fit. The individual data points correspond to the different azimuthal angles. The lines shown connect the weighted averages for each fit interval.

Since the results of the polynomial fit used to determine the conic constant depended strongly on how much data was included, another approach to the data analysis was taken. Rather than attempting to measure the spherical aberration directly, the deviation from the nominal shape of the mirror was computed from the data, which included spherical aberration. The difference between the measured spot motion and the expected motion based on a mirror with the nominal conic constant was computed. A second-order polynomial fit to this data was performed to remove the alignment terms. The average radial slope and average radial profile of the surface, with respect to ideal, were calculated and plotted in Figs. 3.8 and 3.9.

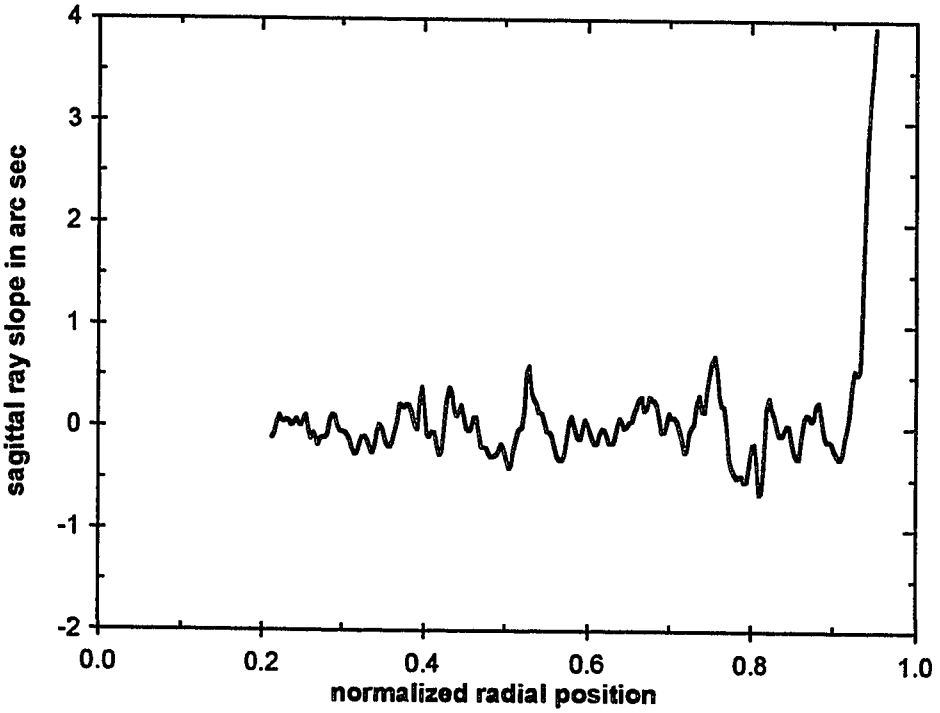

Figure 3.10. Average radial sagittal ray deviation. This was computed from the average of 68 measurements taken at 12 azimuthal orientations. The nominal conic constant of -0.99583 was assumed and no spherical aberration was fit or removed from the data.

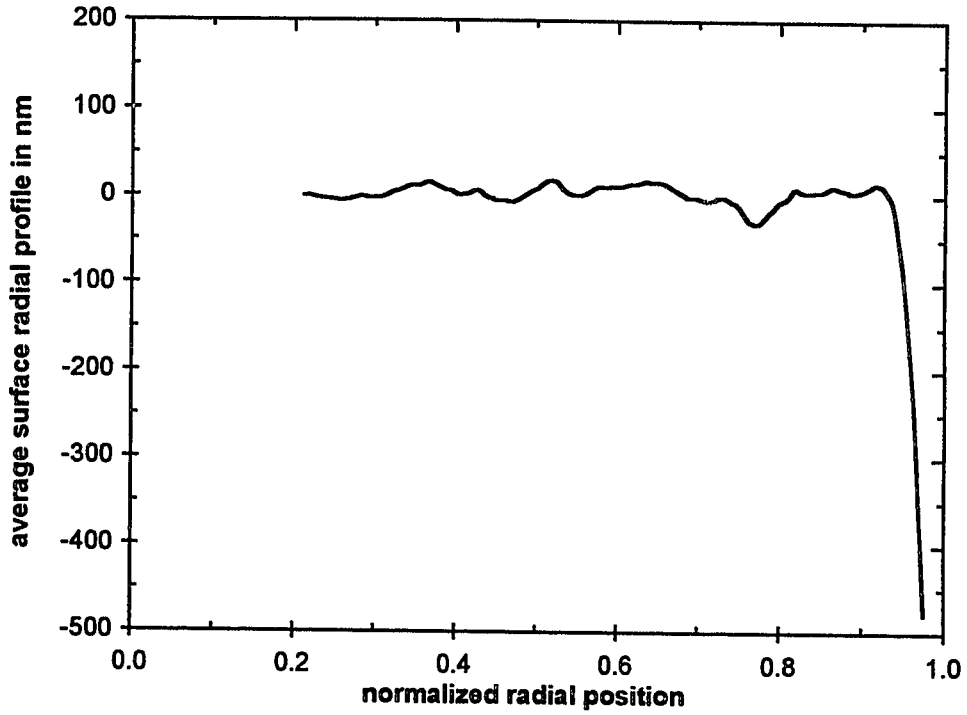

Figure 3.11. Average radial surface height. This was computed by integrating the slope from Fig 3.10.

The measured slope errors in the 1.8-m primary mirror predict a purely geometric point spread function with a full width at half maximum of 1.1 arc second. This is based on only geometric ray propagation and does not take into account the diffraction of the wavefront, so it is quite pessimistic. In fact, the surface errors were measured interferometrically to be 17 nm rms, so the mirror is essentially diffraction limited at 500 nm.

3.5. IMPROVEMENT BY SCANNING FULL DIAMETER

As mentioned above, the test of the 1.8-m primary mirror was limited by the ability to distinguish the low-order polynomial terms in the presence of mirror slope errors. Since the scans were made only across a radius, and not a diameter, it was impossible to

determine cubic spot motion accurately in the presence of these slope errors and the unknown alignment errors. Unfortunately, this limitation was not understood until the test was performed.

The spherical aberration, which is the quantity being measured, causes a cubic variation in laser spot position as a function of radial scan position x. The alignment errors, which are also unknown, cause spot motion with linear and quadratic dependence in x. The least squares fit to the data finds the combination of coefficients of these polynomial terms that give the best fit to the data.

It is useful to examine the cubic variation in the presence of alignment errors that balance some of the spot motion from the spherical aberration. The balancing low-order terms were found that give the best least squares fit to the third-order variation over the range specified. For the full-diameter scans, the only balancing comes from the linear term. For the radial scans, the third-order variation is balanced *over the radius* with quadratic, linear, and constant terms, which leaves a P-V variation twenty times smaller than the pure cubic variation. To demonstrate the balancing, the cubic variation is shown in Fig. 3.12 for three cases:

1. Pure cubic variation with no lower-order terms.
2. Cubic variation balanced across a full diameter with low-order terms (order 1).
3. Cubic variation balanced across a radius with low-order terms (orders 0, 1, and 2).

Although all three curves have the same cubic variation, there is little variation left when balanced only across the radius. Thus, noise at the level of this balanced curve will cause much larger errors in the determination of the cubic coefficient, thus the conic constant. Slope errors in the mirror with a component similar to the balanced curve will be interpreted as spherical aberration.

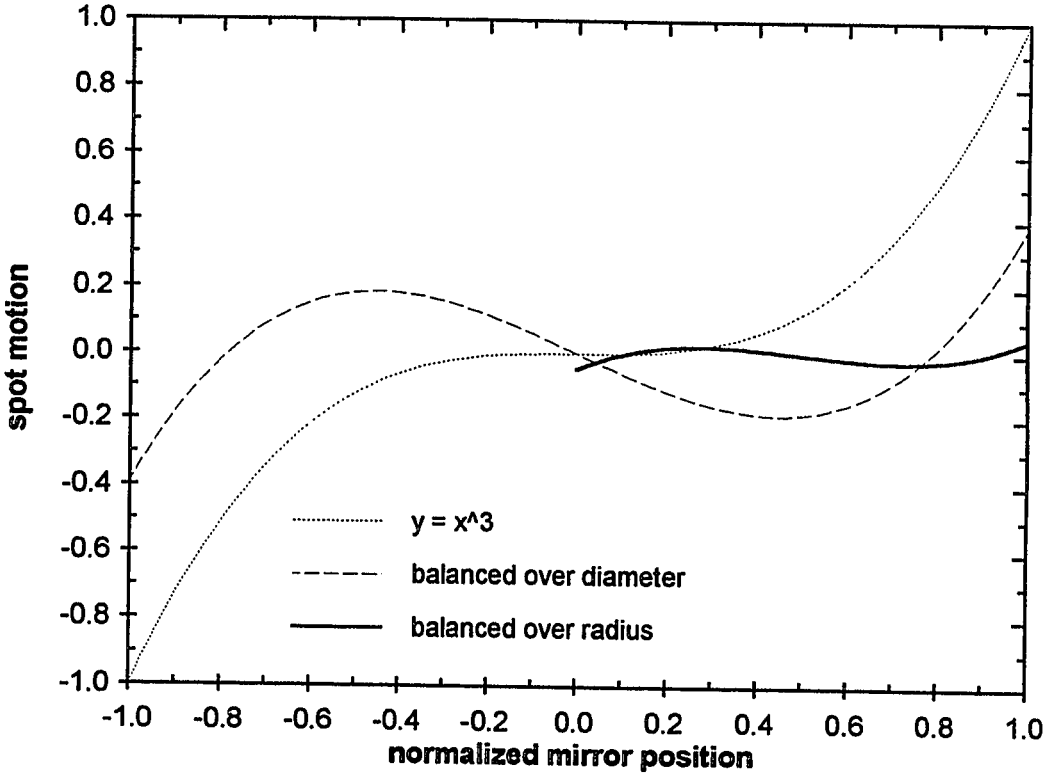

Figure 3.12. Cubic spot motion with no balancing, balanced across a full diameter, and balanced only across a radius. All three curves have identical cubic coefficients corresponding to spherical aberration in the scanning test. The balanced curves define the signature for spherical aberration.

A Monte Carlo analysis of the pentaprism test was performed to determine the improvement in accuracy when a full diameter is scanned. This analysis used a simulation of the scanning pentaprism test that included the second-order coupling of the misalignment terms. Surface errors in the 1.8-m mirror were modeled as random slope errors with correlation distances of 25 mm to 50 mm. All of the defining parameters were randomly chosen from Gaussian distributions based on the real measurements.

The conic constant determined by simulating radial scans varied with a standard deviation of 0.004, which is comparable to the measurements of the 1.8-m mirror. When

the full diameter was scanned, the standard deviation of the conic constant was reduced to only 0.0002, a factor of 20.

The simulated performance is shown in Figs. 3.13 and 3.14 for a radial and a diametrical scan. Both simulations use 250 data points, each consisting of 25 centroids. The random terms were drawn from identical distributions. The error in the conic constant for the radial fit was -0.0038, and the error for the diametrical fit was -0.00018. These values are typical.

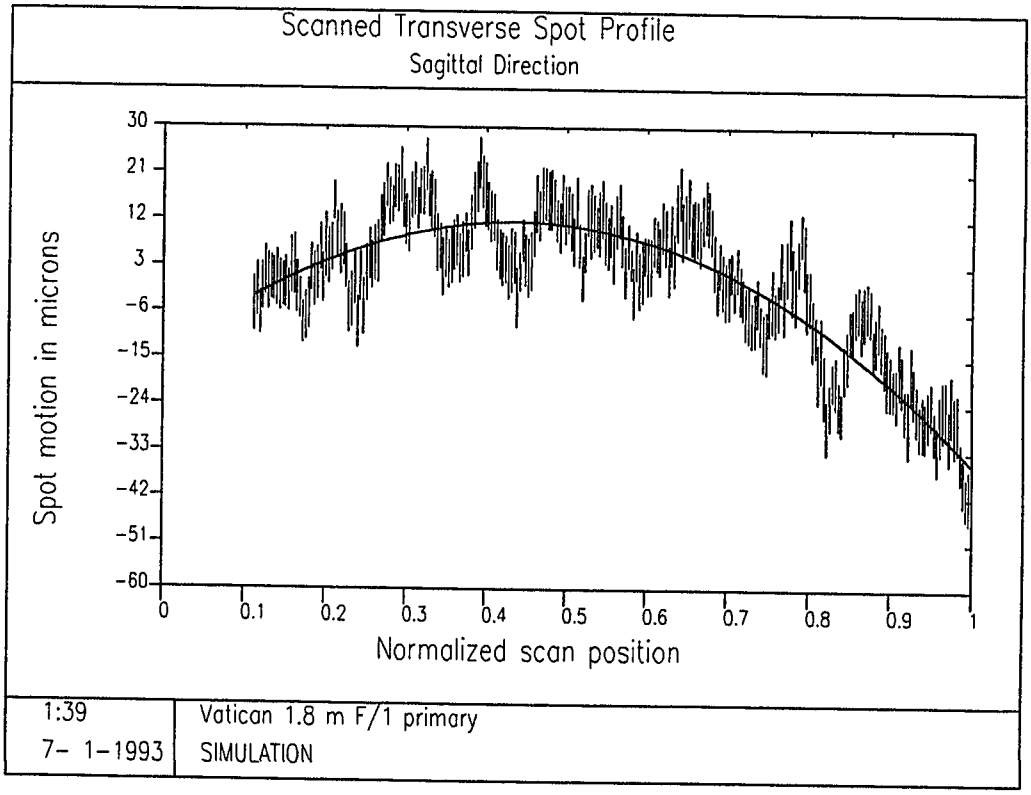

Figure 3.13. Simulation of a radial scan of the 1.8-m primary mirror. The error in the fit conic constant was +0.0038. The simulation assumes random errors and offsets similar to those obtained in the real test.

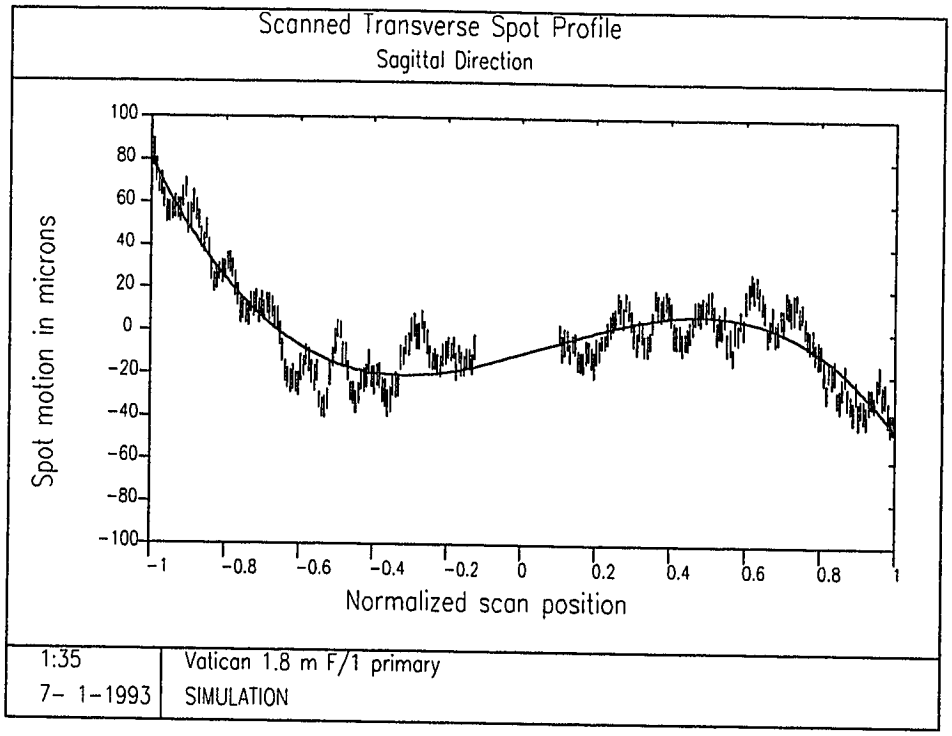

Figure 3.14. Simulation of a diametrical scan of the 1.8-m primary mirror. The error in the fit conic constant was +0.00018, a factor of 21 less than the error obtained from the radial scan with identical misalignment and random distributions. The gap in the data shows the central hole.

3.6. CONCLUSION

The scanning pentaprism test can provide useful measurements of radial profiles for near-paraboloidal primary mirrors. It may be used to guide fabrication of an optic or to verify the measurement from a null corrector. This test was analyzed and a method of determining alignment errors developed. The test was run on a 1.8-m $f/1$ primary mirror where the conic constant K was verified as correct to within an uncertainty of ± 0.003. The measurement was performed only across a radius of the mirror, which allowed the alignment errors to couple with the slope variations in the surface causing the large uncertainty in K. Further analysis showed that scanning across a full diameter would decrease the uncertainty of the conic constant measurement by a factor of 20.

SECTION II

INTERFEROMETRY WITH NULL CORRECTORS

This section contains two chapters on optical testing with null correctors. Null correctors are generally used to allow interferometric measurements of surfaces that depart from spherical by large amounts. Null correctors are designed and fabricated to compensate for the surface asphericity, so the test of optic using a null lens is identical to testing a spherical surface.

Chapter 4 presents a general description of the interferometric null test. This chapter emphasizes the design and analysis of the test system, which includes much more than the null corrector. The complete instrument for testing the mirrors comprises a null corrector, phase shifting interferometer, remote positioning system, imaging system, and laser illumination system. Several problems that are peculiar to interferometric null testing are discussed, along with the solutions developed at Steward Observatory.

The optical design and analysis of null correctors are discussed in Chapter 5. This chapter outlines a strategy for designing null correctors and presents several designs for testing large, fast mirrors required for Steward Observatory telescope projects. Some detailed discussion of error analysis for null correctors is also given.

CHAPTER 4

INTERFEROMETRIC MEASUREMENT OF PRIMARY MIRRORS WITH NULL CORRECTORS

4.1. INTRODUCTION

Primary mirrors for modern telescopes are tested interferometrically from the center of curvature using a null corrector (see Fig. 4.1). The null corrector, or null lens, compensates for the asphericity of the mirror surface. Interferometric testing with a null lens allows an accurate, high-resolution measurement of the entire surface that can be made in several minutes.

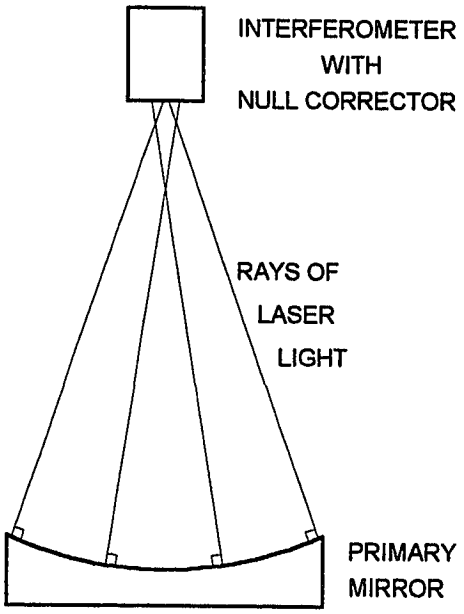

Figure 4.1. Schematic drawing of null test.

This chapter discusses the design and implementation of null tests for primary mirrors. A description of the interferometric null test is given in Sec. 4.2. Several types of null correctors are discussed in Sec. 4.3, and the alignment of null correctors is described in Sec. 4.4. The emphasis in this chapter is on the null corrector as a component in an instrument, and the details of null correctors are given in the next chapter.

A system-level optimization is discussed that involves much more than correcting a wavefront with a few lenses. The instrument, comprising the null corrector, interferometer, illumination optics, and an imaging system, is optimized for system performance. Potential problems with the instrument can be avoided by analyzing the entire system early in the design. The problems of imaging distortion, diffraction effects, and ghost reflections are discussed in Secs. 4.5-4.8.

The problems caused by vibration and turbulence, and methods for reducing these to an acceptable level, are discussed in Sec. 4.9. The invention of the holographic null lens test (Chaps. 6 and 7) has taken some of the uncertainty out of using null correctors because this new test provides an independent verification of the null lens. If a holographic test is not used, azimuthal errors in the instrument can be measured using the rotation test described in Sec. 4.10. Static fringe analysis and phase shifting methods for evaluating the interferometric data are reviewed in Sec. 4.11. Finally, some comments on system implementation for efficient testing are given in Sec. 4.12.

The motivation for this analysis of null correctors is to support the fabrication of primary mirrors at the Steward Observatory Mirror Lab (SOML). Some of the analysis in this chapter is applied to specific instruments designed or built at SOML, but the techniques are general. More detailed designs for the specific systems are given in the following chapter. Instruments using visible-wavelength laser light and infrared light

from a CO_2 laser have been designed, analyzed, and fabricated. The work at the Mirror Lab was performed to support several interferometric null tests listed in Table 4.1.

Table 4.1. Null correctors analyzed for primary mirrors at Steward Observatory.

Primary mirror	Type of null corrector
1.8-m *f*/1 for Lennon Telescope	2-element null lens with Shack cube interferometer, HeNe laser
3.5-m *f*/1.5 for Starfire Optical Range (SOR)	Ge 3-element null lens with Twyman-Green, used with CO_2 laser
	2-element null lens with Shack cube interferometer, HeNe laser
3.5-m *f*/1.75 for ARC Telescope	2-element null lens with Shack cube interferometer, HeNe laser
3.5-m *f*/1.75 for WIYN Telescope	2-element null lens with Shack cube interferometer, HeNe laser
6.5-m *f*/1.25 for MMT Conversion and Magellan Telescopes	3-element null lens with Shack cube interferometer, visible-wavelength laser
	Ge and ZnSe 3-element null lens with Twyman-Green, CO_2 laser interferometer
8.4-m *f*/1.14 for Large Binocular Telescope	Catadioptric null lens for visible light (reflective and refractive)
	Catadioptric null lens using infrared light

Primary mirrors for modern telescopes are required to have surface shapes that are correct to a small fraction of the wavelength of light. The final shape of the mirror is entirely determined by the null test since the optician will polish the surface based only on this test.

The accuracy of the surface measurement depends on the quality of the null corrector while the test repeatability depends mostly on environmental effects. A carefully designed and fabricated null corrector will introduce errors known to be much smaller than the final required surface accuracy. Small errors in the null corrector may be measured using a computer-generated hologram and corrected in the data analysis. Random errors due to vibration, atmospheric distortion, and data processing may be reduced to an insignificant level by averaging many measurements.

4.2. DESCRIPTION OF NULL TEST

The interferometric null test uses interference between light that has been reflected from the mirror, and light from a reference surface. The interferometer creates a spherical wavefront of laser light that is split into a reference and a test beam. The test beam travels through the null corrector, reflects off the mirror under test, and re-traces its path through the null corrector into the interferometer. The reference beam is reflected off a high-quality spherical or plano surface. The test beam is recombined with the reference beam causing an interference fringe pattern that corresponds to the difference between the two wavefronts. The fringe pattern is imaged onto a detector for analysis.

The null corrector is designed to modify the spherical test wavefront to produce a wavefront that matches the desired aspheric shape of the mirror. If both the null lens and

the mirror are perfect, this test wavefront will reflect exactly back on itself, ending up identical to the reference wavefront. The ensuing interference pattern will show no variation, giving a "null" result (no surface error). If the mirror does have figure errors, they will be imparted to the reflected wavefront and show up in the interference pattern. Errors in the reflected wavefront are exactly twice the size of the errors in the mirror.

It is important to note that any error in the null corrector will cause a shape change in the test wavefront that will be interpreted as a figure error in the mirror. The null test simply measures how well the mirror fits the template created by the null corrector. It requires additional testing to determine the absolute accuracy of this template.

4.3. TYPES OF NULL CORRECTORS

The progression of null corrector designs has allowed more accurate testing of mirrors with increasing asphericity (Offner and Malacara 1992). Prior to the use of null correctors, large paraboloidal primary mirrors were tested in the shop with slope tests. An interferometric phase measurement of large mirrors using an autocollimating flat mirror is prohibited by the size of the flat. Lacking a good null lens, only mirrors with a small aspheric departure could be tested from their center of curvature. This testing limitation, and the difficulty of polishing fast aspheres, restricted astronomers to slow primary mirrors since the asphericity increases with the inverse cube of the focal ratio.

The first null correctors were designed to be used in single-pass to correct the wavefront asphericity introduced by the mirror. Used in single-pass, the null correctors had to compensate a wavefront with twice the asphericity of the mirror. They were used with a knife-edge or Zernike test to measure high frequency errors. A two-element null corrector with no net power was used by Couder (1927) to test a 30-cm $f/5$ paraboloid. Burch (1936) derived designs for null correctors using spherical mirrors and tested a 91-

cm $f/3.75$ paraboloid. The most common null corrector for mirrors slower than $f/5$ or for mirrors requiring only moderate accuracy uses a single plano-convex lens (Dall 1947; Schlauch 1959). The Dall corrector has been used near the source to add the correcting compensation to the diverging light and near the image to correct the converging beam. An algebraic solution for the Dall compensator is given to fifth order by Holleran (1968). Holleran (1963) also described an interesting technique for correcting the asphericity by immersing the primary in liquid of an appropriate refractive index and depth.

An autostigmatic null test uses the null corrector in double-pass such that light from a point source goes through the null lens, reflects from the mirror, and goes back through the null lens to the point source. This technique requires some type of beam-splitter, but it eases alignment tolerances. It also allows interferometric measurements and reduces the null corrector asphericity by a factor of two. The use of a positive lens as a double-pass null corrector was described by Ross (1943). He added an aspheric plate for testing the Mt. Palomar 200-inch $f/3.33$ paraboloidal primary. A single-lens corrector with one aspheric surface is described by Puryayev (1973). Further analysis of the Ross null corrector is given by DeVoe (1989), and Stoltzman and Ceravolo (1993).

Null correctors with variable asphericity have been proposed using three aspheric plates (Hilbert and Rimmer 1970) and using a triplet of lenses with spherical surfaces (Shafer 1979). A large class of null correctors capable of testing large, fast primary mirrors was introduced by Offner (1963) and is used to test most modern telescope primaries.

The Offner refractive null lens allows the testing of fast primaries to high accuracy and with reasonable manufacturing tolerances. This null corrector consists of a large relay lens and a smaller field lens. The design principle of the null lens uses the field lens to image the primary mirror onto the relay lens. The power and shape of the

relay lens are chosen to introduce spherical aberration that compensates the asphericity of the mirror. The optimization of the two-element Offner null corrector is discussed in detail by Offner (1963), Holleran (1968), Puryaev and Shandin (1979), Moya and Landgrave (1987), Sasian (1988; 1989), DeVoe (1989), Offner and Malacara (1992), and Shafer (1992).

Optical layouts of several types of null correctors are shown below in Fig. 4.2.

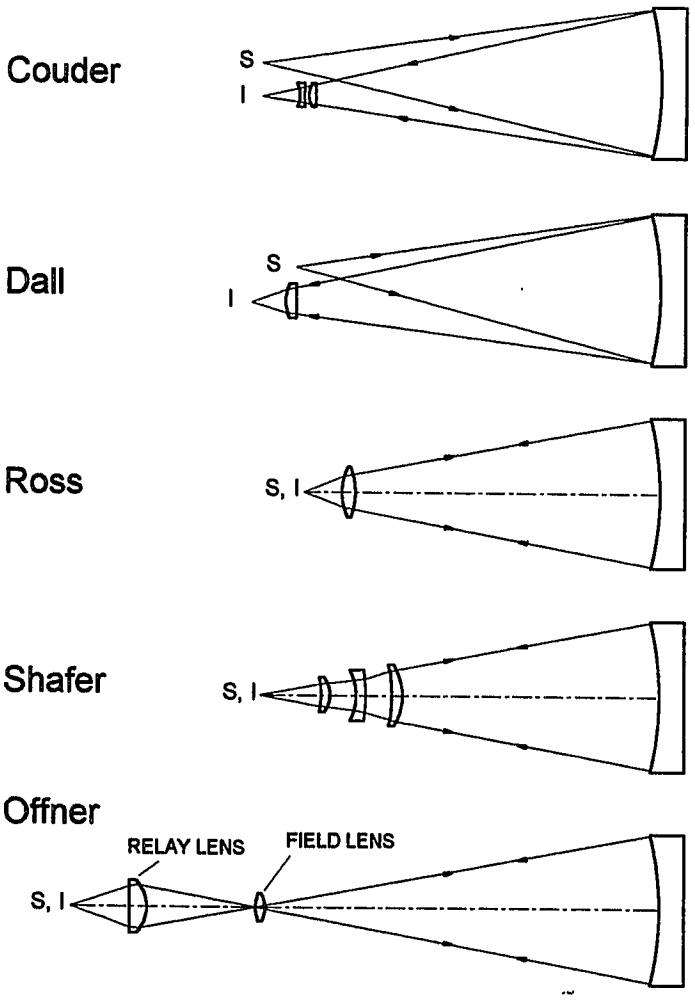

Figure 4.2. Types of refractive null correctors used for the testing of large primary mirrors. These drawings are schematic and not to scale.

The accuracy of these refractive null lenses is limited by the refractive index variation or inhomogeneity in the optical glass. This problem is avoided by the use of reflective null correctors such as the one that was used for the Hubble Space Telescope primary mirror (Montagnino and Offner 1976; Montagnino 1985). A different type of reflective null lens, introduced by Burge (1991a) and described in Sec. 5.7, has been proposed for the measurement of an 8.4-m $f/1.14$ primary. The increasing accuracy of single point diamond machining has allowed the use of small aspheric null reflectors (Gerchman 1986; McCann 1990, 1991) to test large aspheric surfaces to moderate accuracy. Null correctors using computer-generated holograms have also been used for testing aspheric surfaces. A more complete description of this method is given in Chap. 6.

The surface measurements for large primary mirrors at Steward Observatory are made using Offner null correctors with Shack cube interferometers. The use of the Shack cube interferometer (Shack and Hopkins 1979) is optimal for null correctors because of its simplicity and ease of alignment. The Shack cube and null corrector are easily integrated into a single rigid unit. The Shack cube, shown in Fig. 4.3, is fabricated with a small pinhole at the center of curvature of a spherical reference surface. The mechanical alignment of the cube to the null corrector requires only that this one spherical surface be in the correct place.

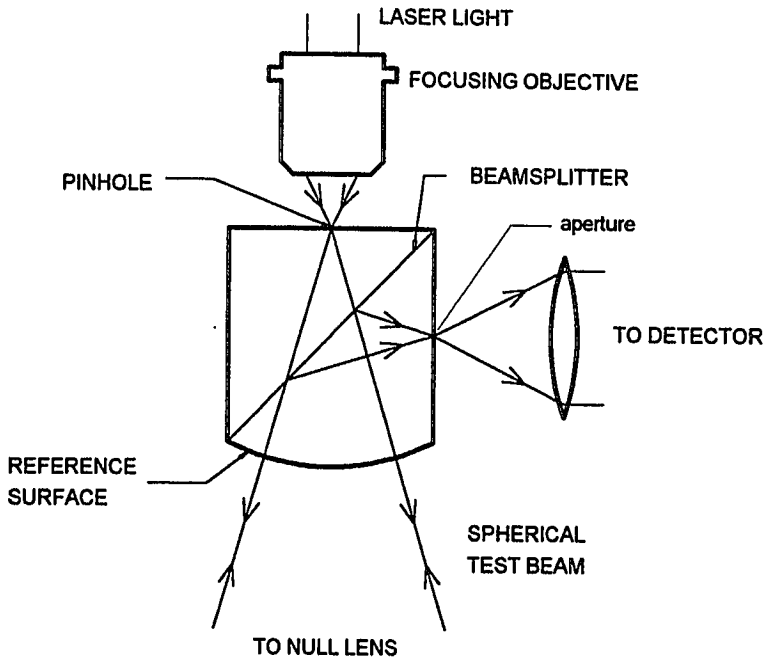

Figure 4.3. Shack cube interferometer. The laser light is fed into the cube through a small pinhole at the center of curvature of the reference surface. An additional pinhole may be put at the focus on the side of the beamsplitter to stop out stray reflections. The interferometer is phase shifted by driving the cube and objective with PZT actuators.

The design of the null lens may be performed without modeling the interferometer. A point source in air adequately defines the wavefront as spherical, centered on the point source. The Shack cube interferometer and null lens must be assembled with the center of the spherical reference surface coincident with the source point given by the optical design. This is true even if the Shack cube has a small error and the pinhole is not located exactly at the center of curvature. If this Shack cube error occurs, the wavefront that goes through the null lens and reflects off the mirror will have a small amount of aberration equal to the aberration in the test wavefront. Since the interference measures the difference between the two wavefronts, the absolute shape of the wavefront is not critical.

4.4. INTERNAL ALIGNMENT OF THE NULL LENS

Null correctors are used for testing aspheric mirrors because they can be fabricated to fully correct the asphericity and give an accurate measurement of the surface errors. The accuracy of the null test depends on accurate and stable alignment of the lenses. The null lenses used to test large, fast primary mirrors must correct hundreds or thousands of waves of asphericity, so they are quite sensitive to alignment errors. For these null lenses, the alignment procedure must assure that errors in mechanical positioning of the lens elements are held to acceptable values. A thorough error budget, described in Chap. 5, must be created to determine these tolerances.

The alignment procedure used at Steward Observatory for null correctors for highly aspheric mirrors is described by West *et al.* (1992). Using this method, the null lens is aligned onto an Invar frame that provides stability and rigidity. The entire null lens is rotated about a precisely maintained axis and the runout (or wobble) of each surface is mechanically measured and reduced to less than 5 μm. The spacings between the elements are measured using special metering rods and set to an accuracy of about 3 μm. The rigid assembly is mounted to a set of stages that provide translation in x, y, and z and rotation about the lateral axes for alignment to the primary mirror. A layout of the null corrector is shown below in Fig. 4.4.

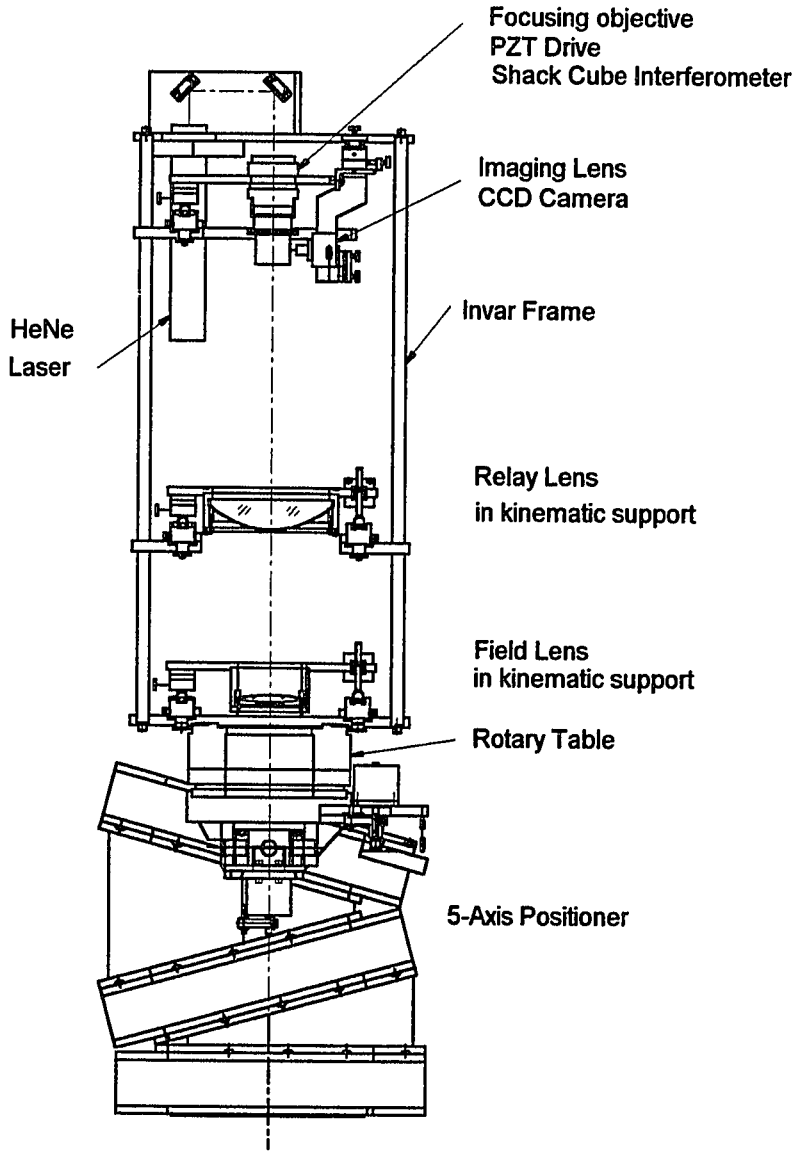

Figure 4.4. Optomechanical layout of an integral null lens with laser source, phase shifting Shack cube interferometer, imaging system, and 5-DOF positioner. Drawing by D. Murguic.

The null lens is assembled in the lab, and no subsequent internal adjustments are made. The alignment of the null corrector with respect to the primary mirror is described in detail in Chap. 5. For performing this alignment, the null lens is positioned with

respect to the primary mirror to minimize wavefront variations from several low-order components. By moving the null corrector laterally, vertically, and rotating about horizontal axes, fringes of tilt, focus, and coma may be eliminated from the interference pattern. The corresponding errors in the primary mirror -- wedge, radius of curvature, and decenter, must be measured independently.

The procedure used to determine the error budget, given in detail in Chap. 5, relies on computer modeling to determine the effects of manufacturing errors. Expected errors in the null test are simulated and the resulting errors in measuring the primary are computed. The error components from each error source are added in quadrature to estimate the likely error in the measurement of the primary mirror.

4.5. IMAGING DISTORTION

The null lens must be treated as an imaging system as well as a wavefront corrector. The Offner null lens is optimized to generate an aspheric wavefront from a spherical one, and not necessarily to provide uniform mapping from test object to image plane. This imaging distortion from the null lens can be quite severe for fast systems if efforts are not taken to minimize it. The distortion must be either backed out in software or corrected with relay optics.

The imaging distortion causes two problems in the data analysis. It causes small surface defects to appear shifted radially and it re-maps low order errors from alignment (focus, and coma) into higher order errors. A discussion of interferometric measurement errors introduced by small amounts of distortion is given by Selberg (1987).

The mapping in the presence of distortion for an axisymmetric system is approximately

$$\rho_i = m\rho_m(1+D\rho_m^2), \tag{4.1}$$

where ρ_i = radial position in normalized image coordinates

ρ_m = radial position in normalized mirror (object) coordinates

m = magnification

D = distortion.

The coordinates are normalized so $\rho_i = \rho_m = 1$ at the edge of the mirror, which requires

$$m = \frac{1}{1+D}. \tag{4.2}$$

This distortion causes an apparent shift of small-scale features. A small defect located at ρ_m on the mirror will appear to be shifted radially an amount

$$\Delta\rho = \rho_i - \rho_m = \frac{D\rho_m(\rho_m{}^2 - 1)}{1+D} \tag{4.3}$$

from its actual position.

The effect of the mapping distortion on low-frequency wavefront variation is analyzed using a polynomial representation. The wavefront may be described as a sum of functions of the form

$$W(\rho,\theta) = \sum_{n,k} a_{nk}\rho^n \cos k\theta + b_{nk}\rho^n \sin k\theta. \tag{4.4}$$

Zernike polynomials are a special case of functions of the type shown in Eq. (4.4) that are orthogonal over the unit circle.

The null lens and imaging system have circular symmetry so the mapping always preserves the azimuthal angle θ. The mapping of ρ^n is found by expanding Eq. (4.1) and keeping first-order terms in D, giving the mapping relations,

$$\alpha\rho_i^{\,n} \rightarrow \alpha\left(\rho_m^{\,n}(1-nD)+nD\rho_m^{n+2}\right)$$
$$\alpha\rho_m^{\,n} \rightarrow \alpha\left(\rho_i^{\,n}(1+nD)-nD\rho_i^{n+2}\right) \qquad (4.5)$$

Any focus or coma from alignment gets re-mapped by the distortion into higher order errors. The mapping transformation (4.5) is applied to a wavefront with focus and coma;

$$W_m(\rho_m) = A\rho_m^2 + B\rho_m^3\cos\theta \qquad (4.6a)$$

maps into

$$\begin{aligned} W_i(\rho_i) = {} & A\rho_i^2 + B\rho_i^3\cos\theta \\ & +2DA\rho_i^2 + 3DB\rho_i^3\cos\theta \\ & -2DA\rho_i^4 - 3DB\rho_i^5\cos\theta \end{aligned} \qquad (4.6b)$$

where $W_m(\rho_m)$ = actual wavefront shape due to alignment

$W_i(\rho_i)$ = apparent wavefront shape after imaging with distortion

A = wavefront focus coefficient

B = wavefront coma coefficient (in x direction).

The amount of distortion D for the ARC null lens was -6.7% so 1 wave of power would be mapped into 0.13 waves of spherical aberration and 0.85 waves of power. One wave of coma would appear as 0.80 waves of coma and 0.20 waves of fifth order coma.

The measurement error due to distortion is proportional to the surface deviation from null. The influence that the mapping error has on the surface measurement is thus minimized by measuring on a null fringe (with a single fringe covering the entire mirror). A null fringe from a perfect surface is unaffected by imaging distortion.

The nominal mapping function including distortion can be determined by using a computer simulation of the null test. Also, the real mapping from the mirror to the image plane may be measured by putting fiducial marks at known positions on the mirror. The positions of the images of these marks are measured to determine the exact object-to-image mapping function. A least squares fit to these data can provide coefficients describing the mapping.

The mapping for the SOR primary was determined by placing 54 fiducial points on the mirror and measuring the image positions in units of pixels. Coefficients were fit to the empirically determined mapping functions

$$\begin{aligned} x_i &= a_{00} + a_{10}x + a_{30}x^3 + a_{12}xy^2 \\ y_i &= b_{00} + b_{10}y + b_{30}y^3 + b_{12}x^2y \end{aligned}, \qquad (4.7)$$

where x,y = position of fiducial mark on mirror (in real mm)

x_i, y_i = position of image of fiducial mark (in pixels at the digitized image)

a, b = coefficients determined by least squares fit.

In addition to these terms, a rotational transformation was performed using the angle that minimizes the residual error from the fit. The pattern of the fiducial marks is shown in Fig. 4.5(a) and the differences between the measured and the fit locations of the fiducial marks are shown in Fig 4.5(b) in units of pixels. The pixel spacing in the image corresponds to about 15 × 18 mm on the mirror. These mapping functions were used to correct for distortion in measured influence functions of the support actuators and in diffraction analysis of the measured wavefront error.

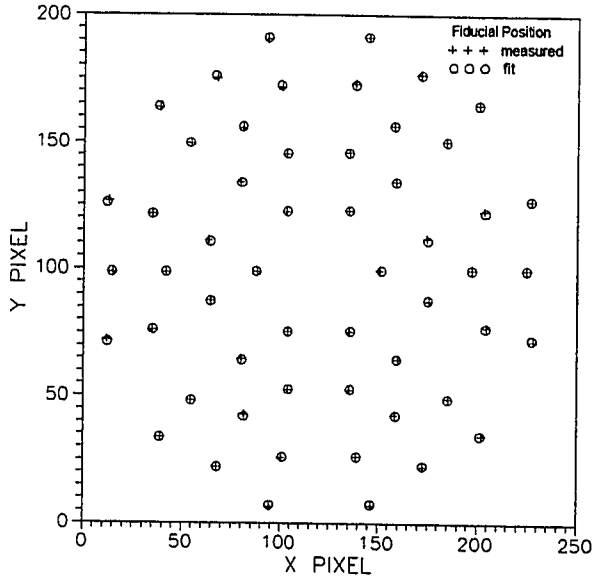

(a) Digitized fiducial mark image positions in pixels.

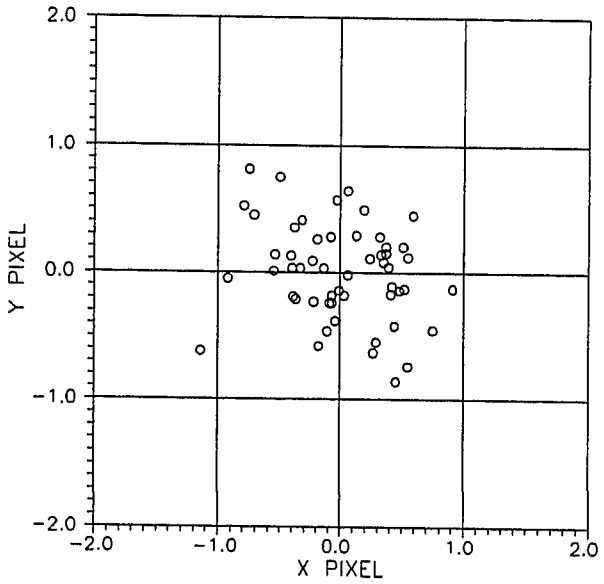

(b) Deviation of measured positions from calculated values based on the least squares fit.

Figure 4.5. Fit of mapping function to measured positions of fiducial marks for the SOR primary.

4.6. DIFFRACTION EFFECTS IN OPTICAL TESTING

Improper imaging causes diffraction "ripples" in the measured phase and causes the edge of the mirror to appear flawed. This effect, and other errors from diffraction, are minimized by using the mirror under test as the only aperture in the system and focusing it onto the detector.

The diffraction from the edge of the mirror is easily modeled as the classic Fresnel knife-edge diffraction. The real and imaginary parts of the electric field distribution are found by evaluating the Fresnel integrals using a common technique described by Born and Wolf (1980). The squared modulus gives the familiar intensity fluctuations [see Fig. 4.6(a)] and the inverse-tangent of the ratio of the imaginary to the real part gives the phase [see Fig. 4.6(b)].

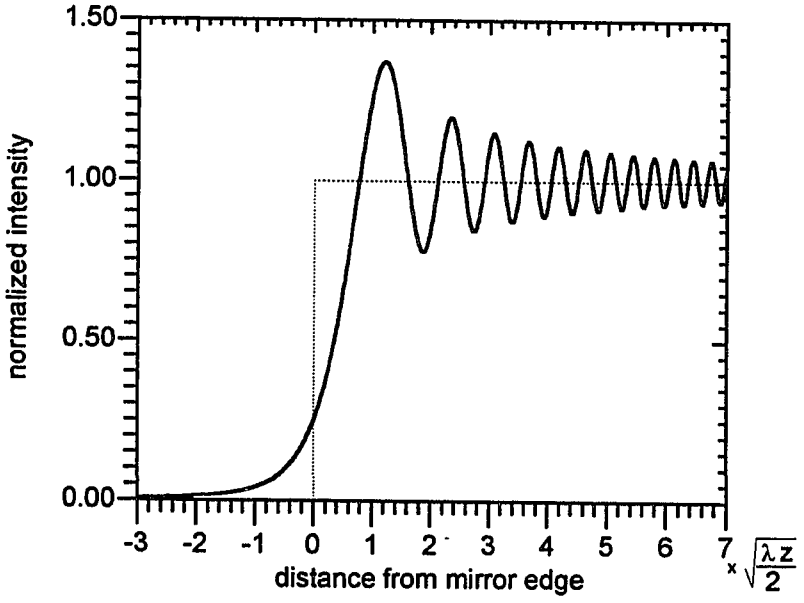

Figure 4.6 (a) The familiar intensity variation from a diffracting edge.

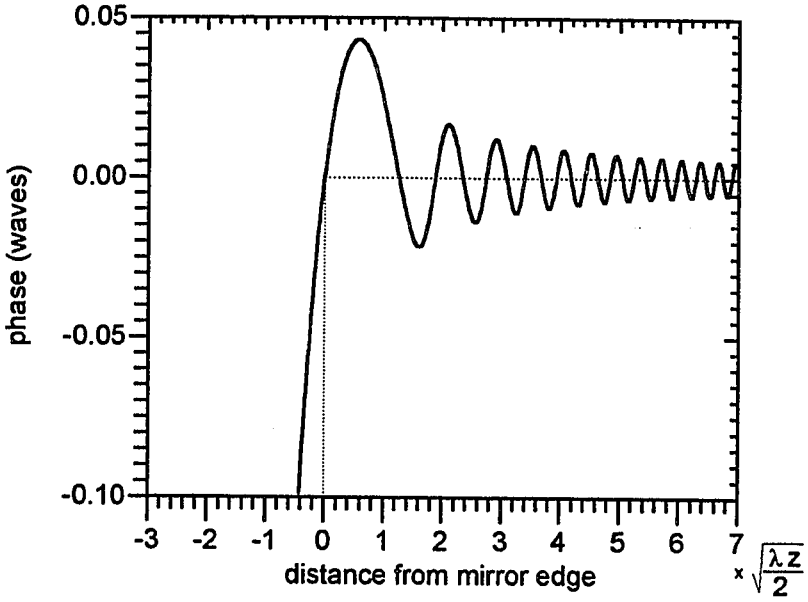

(b) The not-so-familiar phase variation from a diffracting edge.

Figure 4.6. Effect of diffraction from the edge of an optic on the (a) intensity and (b) phase distributions.

Diffraction also causes the errors in the test wavefront to change shape as the wavefront propagates (Malacara 1985). If the mirror under test is not properly imaged onto the detector, the measured errors will be different from the actual errors. The magnitude of this effect depends on the slope of the errors and the amount of defocus between the image of the optic and the detector. This wavefront distortion due to diffraction is not related to the imaging or mapping distortion described in the previous section.

In practice, the focus of the imaging system is adjusted to create a sharp image of the edge of the mirror. This can be difficult if the edge is rolled, so it is useful to put an aperture in the null lens at the image of the primary mirror. This aperture must be

slightly oversized to assure that none of the data from the primary mirror is lost. This aperture can be used to determine the focus instead of the rolled edge on the primary mirror.

4.7. GHOST REFLECTIONS AND SPURIOUS FRINGES

Reflections from the elements in the null lens can cause spurious fringes in the interferograms. Since these fringes are phase-shifted with the test beam, they cause direct errors in the measurement. These ghost fringes can be reduced in the optical design of the null corrector, by using anti-reflection coatings, and by filtering with a small pinhole.

The ghost fringes show up from reflected light that is near-normal to the optical elements. This light will reflect nearly back on itself causing interference fringes broad enough to be sampled. Surfaces that have this problem are avoided during the design of the null correctors. Since the null correctors are axisymmetric, the light is always at normal incidence at the vertices of the lenses so ghost fringes are present near the center of the mirror. However, this is not a problem when testing primary mirrors since the mirrors generally have a central hole. The null corrector design should be optimized to minimize the ghost reflections outside the central untested area.

The contrast or visibility of the spurious fringes may be reduced by using high-performance anti-reflection coatings. The visibility of the ghost fringes falls off very slowly with reflectivity as shown in Eq. (4.8) and plotted in Fig 4.7:

$$visibility \equiv \frac{I_{max} - I_{min}}{I_{max} + I_{min}}, \tag{4.8a}$$

or
$$visibility = \frac{2\sqrt{0.04R}}{0.04+R}, \tag{4.8b}$$

where I_{max} = intensity of fringe maximum

I_{min} = intensity of fringe minimum

R = reflectivity of coating.

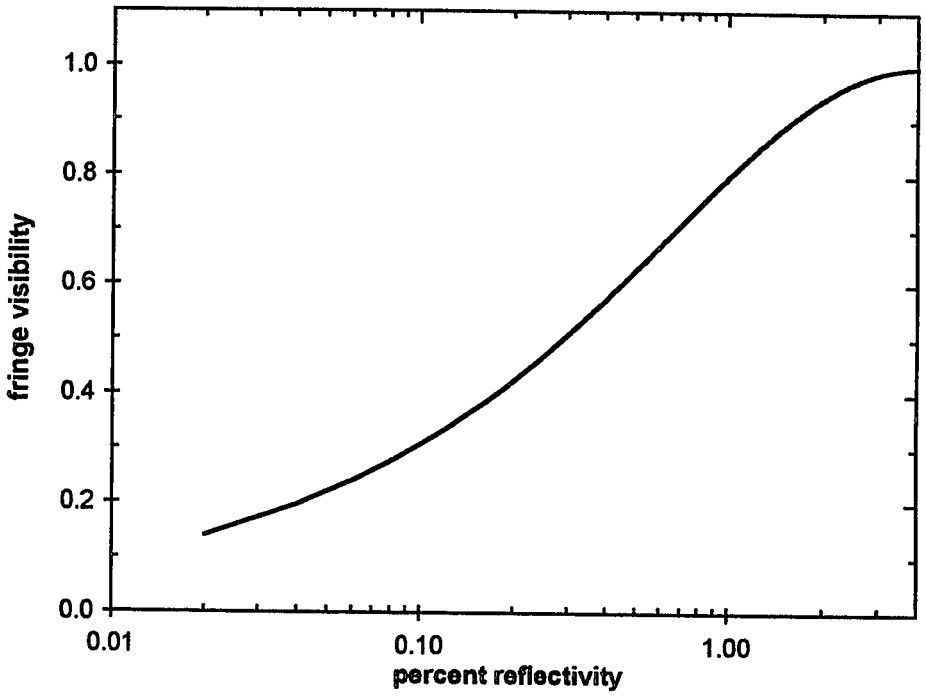

Figure 4.7. Ghost fringe visibility (or contrast) as a function of surface reflectivity. A single-layer magnesium fluoride anti-reflection coating reduces the reflectivity to about 1%, giving fringes with 80% modulation!

The use of a pinhole at the center of curvature of the Shack cube minimizes the effect of ghost fringes and reduces stray background light. The pinhole is made small enough to let only the reference and the test beams through. It must not be so small that it filters out high frequency figure information. The pinhole at the Shack cube focus be-

haves like a low-pass filter with cutoff spatial frequency derived using Fourier optics (Goodman 1968; Gaskill 1978):

$$\xi_c = \frac{NA \times \phi_f}{\lambda D} \tag{4.9}$$

where ξ_c = spatial frequency of cutoff (cycles per meter at mirror)

ϕ_f = pinhole diameter (μm)

λ = wavelength of light (μm)

D = diameter of primary (meters)

NA = final numerical aperture of converging light in which pinhole is used (equals the sine of the light cone half-angle).

Since the imaging uses coherent light, the frequency response (or MTF) due to diffraction from the pinhole is constant from $\xi = 0$ to ξ_c. There is no degradation in the resolution for spatial frequencies lower than ξ_c.

The test of the WIYN 3.5-m primary used a 200-μm pinhole at the focus of a 0.332 NA beam to give resolution of 30 cycles per meter, or 105 full cycles across the mirror diameter. This frequency matches the Nyquist sampling rate determined by the 200 pixels across the mirror. A larger pinhole would pass higher frequency information, but the digitization would cause aliasing that could lead to erroneous data. It is optimal to match the optical frequency response with the cutoff defined by the sampling.

The laser light causes noise in the image that may be eliminated by destroying the spatial coherence in the imaging system. Any small dust particles or inclusions in the glass will act as coherent point sources that cause spurious fringes or Fresnel noise in the interferogram. The effect of spurious fringes on phase shift interferometry and an algo-

rithm for reducing errors is described by Ai and Wyant (1988). Another problem due to the coherence of the laser is speckle, or granularity in the image intensity.

A rotating disk of ground glass reduces the spatial coherence of the light, eliminating speckle and Fresnel noise. The ground glass should be located at an image plane of the optic under test and should then be re-imaged onto the detector. This is a standard technique used in commercial interferometers, and will be implemented into the null test for the 6.5-m $f/1.25$ primaries.

4.8. IMAGING OPTICS

The imaging of the mirror onto the detector plane requires additional optics. These imaging optics need not be of interferometric quality since they equally affect the test and reference wavefronts. The imaging optics must focus a correctly-sized image onto the detector. An optical subsystem for imaging may be used to additionally correct distortion, eliminate noise due to coherence, and make an easy interface to the detector.

The imaging relay designed for the MMT visible null lens corrects the imaging distortion while creating a collimated image of the primary mirror. This collimated image is presented to a zoom lens that can tilt and pan to see the entire mirror at varying resolution. A rotating ground glass is placed at an intermediate image of the primary.

4.9. ENVIRONMENTAL EFFECTS

Since the measurement of the optical surface is performed using an instrument many meters away, environmental effects can cause errors in the measurement. Variations in air density can cause both random and systematic errors. Motion of the interferometer or the mirror due to vibration makes phase shifting interferometry difficult

and introduces random errors in the measurement. The random errors are reduced to an acceptable level by averaging many measurements, but systematic errors remain and degrade the test accuracy.

The random testing errors are minimized by the design of the test facility and further reduced by averaging. Vibration and air motion (seeing) are the dominant sources of random variations in the testing of large optics. These errors are kept as small as possible by using a large, well-controlled lab and vibration-isolated test tower. The remaining random measurement errors are reduced to an acceptable level by averaging large numbers of measurements. The error in the average due to the random, uncorrelated effects decreases as the square root of the number of measurements averaged together.

Measurement errors due to vibration are minimized by using an isolated test tower, short integration times, and testing on a null fringe. The testing of primary mirrors at Steward Observatory is performed on a rigid test tower that is isolated from ground vibrations by pneumatic supports (see Fig. 4.8). This test tower is 24 meters tall and weighs 400 tons. It has a rigid-body resonance of about 1.2 Hz and lowest internal mode of 9.5 Hz. The tower isolation reduces the vibration problem to a level that allows phase shifting interferometry, although with some difficulty. The use of a shuttered CCD camera that captures images using very short exposures freezes out any fringe vibration during each frame. However, the relative motion between the mirror and the interferometer between frames introduces a measurement error. The error in the phase computation due to vibration is roughly proportional to the spatial phase variation of the surface under test. For a good surface with the system aligned on null fringe, the test surface shows very little spatial variation so the effects of vibration are minimized. A

great attribute of the null test is that the testing becomes more accurate as the figure of the mirror improves.

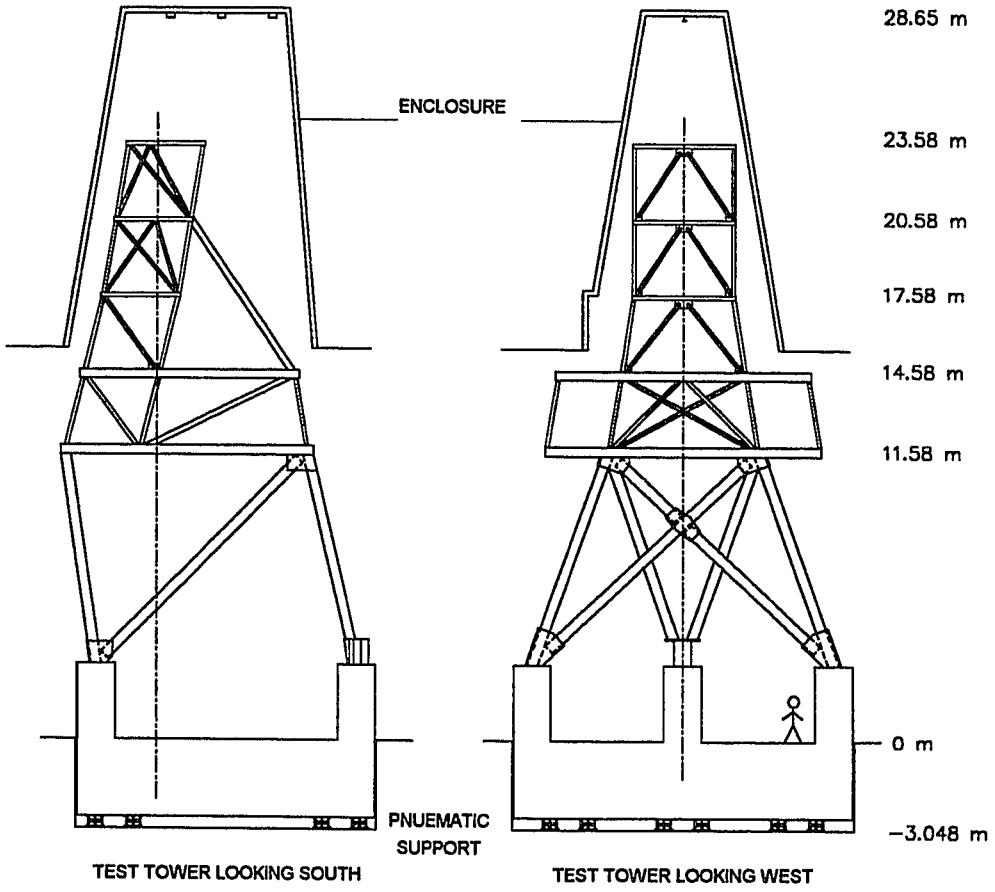

Figure 4.8. Isolated test tower at Steward Observatory Mirror Lab. The entire 400-ton concrete and steel structure is supported by 40 air-filled isolators. Drawing by E. Anderson.

Vibration problems can be minimized by keeping the null corrector and its mount as stiff as possible. It is probably a good design rule to keep the lowest resonant frequency of the null lens above the lowest tower mode. The null lens itself should be designed to be extremely stiff and stable. The positioning stages must be chosen for maxi-

mum stiffness. The stages should be mounted directly to structural members of the tower. If there is no way to stiffen the system against a troublesome vibration mode, an attempt to dampen it should be made.

The atmospheric seeing, or wavefront distortion due to air motion, causes random errors in the surface measurement. Air has refractive index variations proportional to density fluctuations, thus temperature variations. If a mass of cold, dense air floats over the mirror during a test, the test wavefront will be distorted and the measurement of the surface will indicate a low area on the mirror. The tendency to form these air masses is minimized by using a large lab with well-mixed air and minimal heat (or cold) loading. Eliminating the seeing problem by performing the test in a vacuum chamber (Wollensak and Rose 1976; Facey, Nonnenmacher, and Chadwick 1990) would be extremely expensive and difficult to implement for large mirrors.

An important point demonstrated by Martin, Burge, and West (1992) is that the random testing errors are distributed where the mirror specification has room for them. The mirror specification allows larger errors at low spatial frequency than high frequency (See section 1.8). The random testing errors tend to have mainly low frequency variation while the final mirror surface has very little large-scale variation. The combination of the surface errors at small scales and the measurement errors at large scales easily meets the telescope requirements.

The random seeing averages out, but there may also be systematic density variations that would lead to erroneous measurements. Once the air handlers in the room are turned off, any warm air rises creating a stable vertical gradient. Also, a heat source on one side of the room will cause a stable horizontal density gradient. The effect of the horizontal gradient is measured by rotating the mirror, but there is no such test for the vertical gradient.

The vertical stratification of the air causes a focal length change and a small amount of spherical aberration or change in conic constant. To quantify the effect of a vertical gradient, a computer simulation of the null test was performed, modeling the refractive index gradient using discrete steps. The null tests for a 6.5-m $f/1.25$ and a 3.5-m $f/1.75$ primary were simulated, setting the number of steps to be large enough that a further decrease in step size did not change the result. Assuming a perfect null corrector at the correct spacing, the resulting power and spherical aberration cause a change in the primary radius R and conic constant K shown to be, for both cases

$$\Delta K \cong 3.5 \cdot \Delta n$$
$$\frac{\Delta R}{R} = \frac{\Delta n}{2} \qquad (4.10)$$

where Δn = total refractive index difference (mirror to null lens).

The temperature at SOML was measured to have a variation of about 0.5° C from the tower to the shop floor. Since the refractive index of air changes by 1.0×10^{-6} per °C (Edlén 1966), this temperature gradient causes a conic constant error of less than 2 ppm (parts-per-million) and a radius error of less than 0.3 ppm. Even if this effect was several times more severe, it would remain negligible compared to the null corrector uncertainty of 80 to 150 ppm.

4.10. SUBTRACTION OF LOW-ORDER AZIMUTHAL ERRORS

Azimuthally varying errors in the null lens may be measured and systematically removed. The mirror may be measured, rotated, and re-measured to separate azimuthal null lens errors from mirror figure variations. The algorithm described by Parks (1978) computes the error in the test optics (which do not rotate) using Zernike polynomials.

Parks gives a simple equation that computes the Zernike coefficients for the test optics as a function of the measured coefficients at both angular positions and the rotation angle.

The angle of rotation between the two maps must be chosen carefully. The derivative of Parks' result gives the sensitivity in the computed Zernike coefficient to the rotation angle. A plot of the normalized sensitivity (Fig. 4.9) shows the periodic nature of this function. The rotation angle should be picked in a region where none of the curves are near zero. Rotation angles of ±55° work well to find all terms up to fifth order. It is useful to perform this test several times at different angles and average the results.

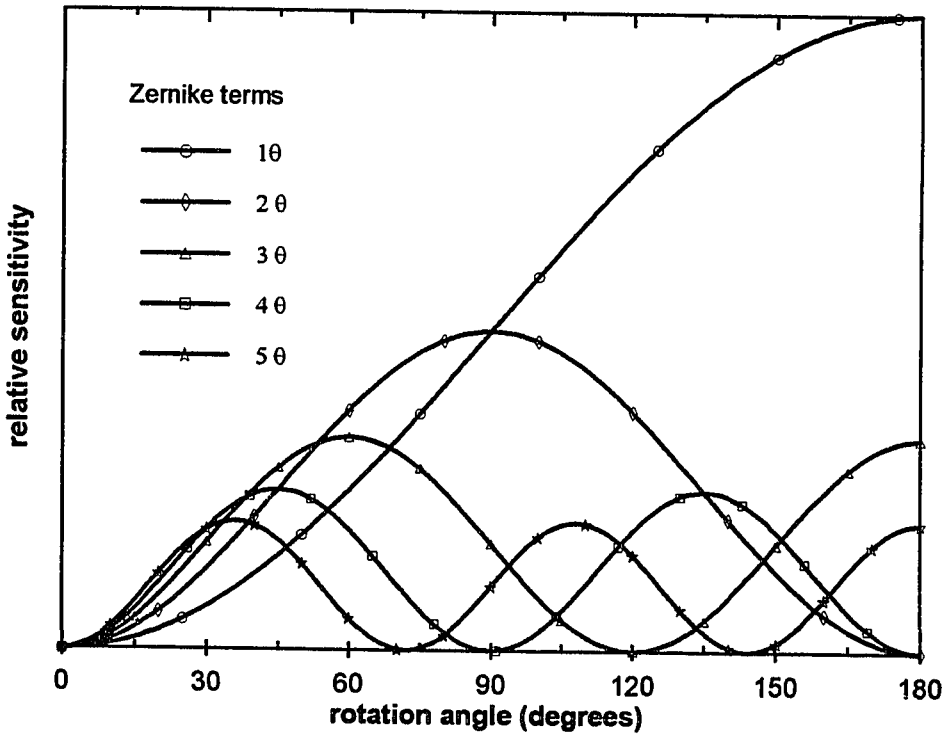

Figure 4.9. Sensitivity of Parks' algorithm for separating azimuthal test optic errors from those in the mirror. The 1 θ terms correspond to all orders of coma, the 2 θ terms astigmatism, etc.

The accuracy of the above method depends strongly on the figure of the mirror under test. It is not until the mirror is near completion that an accurate measurement of the test optics may be obtained. A preferred technique for measuring null lens errors using a computer-generated hologram is discussed in Chaps. 6 and 7. By testing the null corrector directly with a CGH, the test optic errors are determined more accurately and long before the mirror is near completion.

4.11. INTERFEROMETRIC EVALUATION TECHNIQUES

The interferometer with null corrector creates a fringe pattern from the interference between the reference and test wavefronts. It requires some analysis to compute surface shape from the interference pattern. There is a rich history of techniques for performing this analysis (Malacara and DeVore 1992; Greivenkamp and Bruning 1992; Schwider 1990). Low-order aberrations may be interpreted by inspection of the interference pattern (Kingslake 1925). Modern techniques for obtaining surface heights from the interference patterns use solid-state detectors interfaced with high-speed computers. There are a variety of algorithms that compute phase from a single digitized interferogram. There are also numerous methods for obtaining phase using a set of sequential interferograms with phase shifts introduced between them.

A single interference pattern may be captured, even in the presence of vibration, and analyzed by one of many techniques. These methods can be used to freeze out vibration, but they suffer a loss of resolution. The oldest and least accurate method simply locates fringe centers (Malacara and DeVore 1992; Shulz and Schwider 1976). Fourier transform techniques have been developed (Takeda, Ina, and Kobayashi 1982; Kreis 1986; Roddier and Roddier 1987) in which the phase is retrieved by filtering and processing the data in the spatial frequency domain. A technique proposed by Womack

(1984a, b) and used by Küchel and Wiedmann (1990) and Józwicki *et al.* (1992) performs the phase computation directly in the space domain.

Most of the modern data collection and analysis systems for the testing of optical surfaces use phase shifting interferometry (PSI). This method (Carré 1966; Bruning *et al.* 1974) uses a set of sequential interferograms recorded as the reference beam is shifted with respect to the test beam. This shift is commonly performed by moving a reference surface with piezoelectric transducers. There are several techniques for using PSI to determine wavefront phase. These are reviewed and analyzed by Creath (1986, 1988) and Greivenkamp and Bruning (1992). The surface measurements for large primary mirrors at Steward Observatory are made using phase shifting Shack cube interferometers. The Shack cube interferometer is readily phase shifted by translating the cube with PZT actuators (Koliopolis and Anderson 1986).

Since PSI assumes a controlled phase difference between the reference and test wavefronts, this technique is very sensitive to vibration. Vibrations induce small motions of the optical surfaces that cause random phase variations between the two beams. For this reason, optical testing using PSI is commonly performed on massive tables that are isolated from vibrations by pneumatic supports.

It is possible to use PSI in the presence of vibration using more sophisticated techniques. Kwon, Shough and Williams (1987) demonstrated a system that uses a grating beamsplitter and three separate detector arrays with a fixed phase shift between the arrays. By pulsing the laser and simultaneously reading out the three arrays, a complete measurement may be made. Another phase shifting technique developed at Steward Observatory (Wizinowich 1990; Colucci and Wizinowich 1992) uses only two time-critical frames that can be acquired in less than two milliseconds, fast enough to freeze out the effects of vibration. Neither of these techniques are widely implemented,

so optical testing in the presence of severe vibration is usually performed using static interferogram analysis.

Using PSI, the phase (equivalently surface height) is calculated at each pixel modulo 2π. Additional data processing resolves the 2π ambiguities to give a continuous phase map. Since the phase is measured at each sampled pixel, high resolution phase maps are made. In a controlled, well-isolated environment, PSI is the most common and most accurate technique for evaluating interferometric data.

4.12. IMPLEMENTATION OF NULL TEST

The null test is designed so that its use is as simple as possible. The null tests for primary mirrors are used daily for many months so it is cost effective to design systems that are reliable and efficient. Since the test optics are mounted several stories up on an isolated test tower, the testing is operated remotely. This avoids vibrations and air turbulence from the optician and also allows more rapid testing.

The null test for the 6.5-m $f/1.25$ primary mirrors has been designed with many useful capabilities. The optician will have remote control of the system position, zoom, focus, pan, tilt, and camera exposure time. The alignment will be facilitated by an "align mode" similar to that used in commercial interferometers. In this mode, the pinhole will pop out and a lens will pop in to image the back surface of the Shack cube onto the detector. The optician would use this align mode to perform the coarse positioning of the null lens.

The internal alignment of the null lens will be performed in the lab and all adjustments will be fixed. The laser light will be fed to the instrument by fiber optics. The only

daily adjustments required by the optician should be positioning the instrument and zooming and panning the imaging system.

4.13. CONCLUSION

The null test instrument, consisting of interferometer, null corrector, and imaging optics can be optimized for system performance. A good design should give excellent wavefront correction with moderate alignment tolerances. It should minimize measurement noise from spurious fringes but not degrade resolution. It should be mechanically stiff and stable to minimize vibration errors and maintain accuracy. Some correction or compensation should be made for imaging distortion. Since it will be used for months by the opticians, it should be reliable and easy to operate remotely. Such an instrument will quickly make accurate, high-resolution measurements of large, fast primary mirrors.

CHAPTER 5

OPTICAL DESIGN OF NULL CORRECTORS FOR HIGHLY ASPHERIC PRIMARY MIRRORS

5.1. INTRODUCTION

Null correctors are used to compensate for the surface asphericity to allow interferometric measurements of highly aspheric primary mirrors. Modern astronomical telescopes require primary mirrors with larger diameters, faster focal ratios, and better surface qualities. These make the optical design of the null correctors required more difficult. This chapter addresses techniques used in the optical design and analysis of null correctors for highly aspheric mirrors. Several specific designs for testing 6.5-m $f/1.25$ and 8.4-m $f/1.14$ primary mirrors are presented and analyzed.

A general description of the strategy for designing null correctors is given in Sec. 5.2. This section addresses important design considerations and system-level design tradeoffs. Techniques for designing null correctors using computer optimization are given in Sec. 5.3.

A null corrector is used as a reference to guide the fabrication of a primary mirror. As such, there is little room for error in the null corrector. A thorough tolerance analysis is required to insure that the null corrector is built to sufficient accuracy that the primary mirror will meet its specification. Section 5.4 describes the tolerance analysis of null correctors as implemented at Steward Observatory. The general approach to

creating an error budget for a null corrector is developed. The alignment of the null corrector with respect to the primary mirror is discussed. As an example, the tolerance analysis for the WIYN primary mirror test is discussed. Finally, a new method for performing the tolerance analysis using wavefront structure functions, which directly relate to the telescope error budget, is given.

Several optimized optical designs for null correctors for the MMT 6.5-m $f/1.25$ and LBT 8.4-m $f/1.14$ paraboloidal primary mirrors are given. A refractive null corrector is presented in Sec. 5.5 that will be used for the testing of the MMT 6.5-m mirror. This null corrector is shown to meet a stringent structure function specification. It is optimized for system performance in terms of imaging distortion, diffraction effects, and ghost reflections. A null corrector to be used with an infrared interferometer for testing the 6.5-m $f/1.25$ primary mirror during loose-abrasive grinding is presented in Sec. 5.6. This null corrector uses an aspheric surface created by single-point diamond machining. An interesting reflective null corrector for the LBT is presented in Sec. 5.8. This new null lens, which uses a large spherical mirror with a small secondary reflector, can be adapted for use with visible and infrared light. An error analysis using structure functions shows this design to meet the stringent specifications that flow down from the telescope error budget.

5.2. SYSTEM DESIGN STRATEGY FOR NULL CORRECTORS

The null correctors for highly aspheric primary mirrors are designed to achieve maximum test accuracy for the as-built system. This requires the design to have excellent ideal performance as predicted by the ray-trace simulation. It also requires that the sensitivity to manufacturing errors must correspond to the achievable mechanical tolerances. Additionally, the entire null lens must interface with an interferometer and imag-

ing system and must be mounted in a test tower for remote operation. To minimize measurement noise, the null corrector must avoid surfaces that will cause troublesome ghost reflections. Finding a good optical design that meets the above criteria generally requires the design and analysis for several null correctors, from which the best is chosen.

Null lenses based on a design by Offner (1963) are generally used for testing of fast primary mirrors. The Offner null corrector consists of a large relay optic and smaller field optics. The design principle of this null lens, described in detail in the next section, is to use field lenses to image the primary mirror onto the large relay element. The relay element, which may be a lens or mirror, is chosen to introduce spherical aberration that compensates for the asphericity of the mirror. The original implementation of this test, shown schematically in Fig. 5.1, uses two lenses.

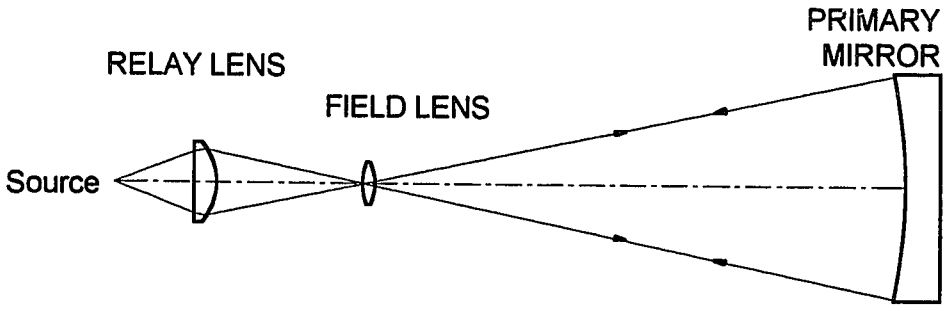

Figure 5.1. Offner-type refractive null corrector. This drawing is schematic and not to scale.

An infrared interferometer with null lens may be used to measure the surface during loose-abrasive grinding. A separate visible interferometer with a highly accurate null lens is required for final figuring. The accuracy required of the infrared null lens is relatively low; it must only measure the ground surface to an accuracy of about 200 nm rms. The visible system defines the final shape of the mirror, so it must be accurate to

better than 10 nm rms. The agreement between the IR and visible measurements offers confirmation of both systems to the accuracy of the IR measurement.

The null correctors presented here are designed to give nearly perfect correction of the wavefront in order to produce a true null test of the finished mirror. An alternate method would be to leave a known residual error in the null lens design and to correct the data. The true null test is used to minimize errors in the measurement and to simplify the data reduction. Many measurement errors are eliminated by measuring a null fringe (such as phase shift errors, detector non-linearity, and mapping distortion), so using a true null test minimizes the effects of these errors.

The null correctors presented here preserve rotational symmetry to allow accurate alignment using mechanical techniques (West *et al.* 1992). Axisymmetric null correctors may be accurately aligned using contact probes to measure surface runout and lens spacing. For this alignment procedure, the entire null lens is rotated on a precise bearing and the elements are adjusted to eliminate runout from the optical surfaces as measured by a probe mounted on a fixed reference. This insures that the axis of rotation, which is uniquely defined in space, will become the axis of symmetry for the null corrector. At the same time the runout is nulled, the correct vertex-to-vertex spacing must be held. Since only the optical surfaces are referenced, any error due to wedge in the lenses is avoided.

The number of elements is kept to a minimum to reduce the system complexity and minimize the number of error contributions. Each additional lens adds ten new possible sources of error, listed in Table 5.1, that must be controlled. Also listed in this table are typical tolerances required for an accurate null test of a highly aspheric primary mirror at Steward Observatory. If a lens is added to achieve better correction from the nominal design, the system errors from the tolerances on the additional degrees of

freedom may actually result in decreased system accuracy at a higher cost. The design should use the fewest elements that give adequate correction while keeping the size and spacing of the lenses to acceptable values.

Table 5.1 Adjustable parameters and sources of error associated with a single lens.

parameter	contributions per element	typical tolerance
spacing	1	±5 μm
thickness	1	±5 μm
index of refraction	1	±0.00001
refractive index inhomogeneity	1	$\pm 0.5 \times 10^{-6}$
radius of curvature	2	±15 ppm
surface irregularity	2	0.012 λ rms
surface runout	2	5 μm

The tolerances listed in Table 5.1 correspond to those attained on null correctors at the Steward Observatory Mirror Lab. They are quite tight, so the achievement of these values requires careful measurement and analysis. The lens curvature and thickness tolerances correspond to the uncertainties in their measurement. The actual values of these parameters may deviate slightly from the design specification, as long as the final values are measured accurately. The final lens spacings are set based on the measured lens thickness and curvatures.

The performance of the refractive null correctors presented here is limited by the refractive index inhomogeneity in the glass. For this reason, the best glass should be used, and the thickness of the lenses must be kept to a minimum. Fused Silica and BK7 are the two materials with the best homogeneity. Both can be obtained with ±0.5 ppm index variation, but BK7 is generally used because it is much less expensive. There is a design tradeoff between the total amount of glass that the light must go through and the number of elements. Because the cost for adding additional elements is so high, the designer has little choice but to use at least one thick lens. Even if select glass is used, the refractive index variation in this lens will limit the test accuracy for highly aspheric mirrors. However, most of the error caused by the index inhomogeneity can be measured using a rotation test or the holographic null lens test described in Chaps. 6 and 7.

Reflective null correctors may be used to prevent the refractive index inhomogeneity from degrading the test. Null correctors using mirrors have been designed by Burch (1936), Montagnino and Offner (1976), Offner and Malacara (1992), and Burge (1991a; 1992b). The use of mirrors solves the problem of the refractive index inhomogeneity, but at a high cost. Mirrors are four times more sensitive to figure errors than lenses, so they must be fabricated precisely. A single BK7 lens gives the designer four degrees of freedom -- thickness, two curvatures, and position. A single mirror offers only its curvature and position.

For precise testing at visible wavelengths, aspheric and diffractive elements in the null corrector are avoided. These elements are difficult to measure accurately and they generally cause high-frequency errors in the wavefront. The high-frequency errors in the null corrector must be minimized because the mirror specification often places a tight tolerance on these errors. Non-spherical optics also have additional degrees of freedom, making them difficult to align. Spherical surfaces can be made with very little figure

error and negligible high-frequency error. They may also be directly tested for figure and for radius of curvature. Spherical surfaces may be aligned by measuring only the surface runout and vertex position.

Unlike alignment of imaging systems, it is not sufficient to align a null corrector based on a measurement of its performance. It would defeat the purpose of the test to align the null corrector to give a good result when testing an unknown mirror. The CGH null lens test (Chaps. 6 and 7) is useful as a verification of the null corrector, but not as a reference for aligning it. The agreement between the null corrector and the independently manufactured CGH gives strong verification that both are correct. Use of the CGH as a reference for the null corrector could result in a flawed test if the CGH is in error.

The cost of an accurate null lens for a fast primary mirror is high, but this cost is justified by the tight tolerances on the mirror and by the large number of measurements that will be made. The null lens may be used daily for many months during the fabrication of the mirror. It may also be used for additional months on the finished mirror in its operational support cell for testing active supports or the thermal system. Several identical mirrors are often fabricated, allowing the cost of the optical test equipment to be shared. The MMT conversion and the Magellan Telescope use identical 6.5-m $f/1.25$ paraboloidal primary mirrors that will be tested by the same null correctors. The LBT (Large Binocular Telescope) will use two telescopes requiring identical primary mirrors.

5.3. COMPUTER-ASSISTED OPTICAL DESIGN OF NULL CORRECTORS

The null correctors are designed using the gradient search optimization in lens design software. The computer program requires a prescription to use as a starting point. If a previous design exists for a similar test, this will make an excellent starting point. When no previous design exists, a starting point can be found analytically that

balances the low order aberrations (Offner and Malacara 1992). For a fast mirror with large amounts of high-order aberrations, the starting point is just used to set the scale and general geometry of the null lens. The optimization causes the optical design to quickly depart from its third-order starting point.

Optical design is typically performed using commercially available software that models the optical system and adjusts parameters using a damped least squares algorithm to optimize the simulated performance. For this optimization, the user must define a merit function that quantifies how well the system performs. The merit function consists of a set of operands that the designer wishes to minimize. The software can vary parameters that the user has specified as optimization variables to find a design that minimizes the merit function. The gradient search algorithms used will always adjust the variables to decrease the merit function until a local minimum is found where any small change in the variables causes an increase in the merit function. To find the best design, as defined by the operands, the designer must choose a starting point for the optimization that is sufficiently close to the desired, but unknown design.

It is useful to think of the merit function as an n-dimensional surface where n is the number of variables. The designer wishes to find the lowest region on this surface to obtain the best optical design. The software can always move downhill on this surface to find a local minimum. But because it can only evaluate one point at a time, the computer program has no way of finding the region in design space that will have the absolute lowest or global minimum. It is up to the optical designer to use general knowledge about the system to guide the design to such a region. Unfortunately, the large number of dimensions and the complex structure of the design space preclude the designer knowing whether or not the global minimum has been found.

There is current research underway on algorithms capable of finding the global minimum for an optical design. Currently available inexpensive, high-speed computers allow the use of computationally intensive techniques for exploring large portions of the design space. One method conducts a systematic search to find promising regions of the design space (Sturlesi and O'Shea 1990). Optimization using simulated annealing has also been used (Forbes and Jones 1990; Hearn 1990). Some early research on using neural networks for optical design is described by Weller (1990). Global optimization methods are likely to become more widely used as the algorithms become more adept and widely implemented, and as the cost of high-speed computing comes down.

The Offner null lens (Offner 1963) uses a field lens near the paraxial center of curvature that images the primary mirror onto a larger relay lens. In this design, the third-order spherical aberration (SA) is balanced by the relay lens, and the fifth-order SA is controlled with the power of the field lens. An analytic expression is given by Offner and Malacara (1990) for the focal length of a plano-convex relay lens that balances the third-order SA. By optimizing the bending and position of the field lens and the bending the relay lens, Shafer (1992) has shown that two-element null correctors can also balance the seventh- and ninth-order SA. By splitting the field lens into two elements, additional correction and decreased overall size may be achieved.

The design of a null corrector is simplified by treating it in single-pass in the lens design software. This is accomplished by using a dummy aspheric mirror to create the exact wavefront that the null lens must correct (Shack 1967). This dummy reflector is defined in the lens design software by optimizing the aspheric coefficients to force the reflected wavefront to match the desired shape of the primary mirror. Designing in single-pass saves considerable time because it allows the point source position and diver-

gence angle at the source to vary. Once a good design is found, it must be modeled and analyzed in its double-pass configuration.

Design procedures for null correctors using computer optimization are outlined by Sasian (1988) and Shafer (1992). Starting from a design that meets some geometric constraints and balances power and third-order spherical aberration, the design is slowly changed to improve the wavefront. This can be a lengthy process since the design space for null correctors is highly nonlinear with many local minima. This optimization yields several good candidate designs that cannot be improved without making large perturbations in the parameters. The final design is chosen after analyzing these candidate designs and comparing residual error, alignment sensitivity, imaging performance, and cost.

When performing the preliminary design, it is important that the designer guide the optimization toward a buildable solution. Steep surfaces offer large aberrations, but also require tight tolerances. The designs should be guided towards surfaces with shallow curves and small angles of incidence. The size of the elements must not become too large or the cost and difficulty of the optical fabrication will go up. The spacing between the elements must not become so large that the mechanical design and fabrication of the support fixture are prohibitive. To avoid ghost reflections, surfaces that are normal to the rays should be avoided.

The preliminary design procedure goes through two stages of optimization. In the first stage, new variables are opened up, one at a time, to find additional zero crossings in the wavefront. The number of zero crossings in the wavefront corresponds to the order of correction. A wavefront with third-order correction has one zero; the OPD goes through zero at the edge. Fifth-order correction implies two zeros and so on. This systematic exploration of the design space can provide insight into possible tradeoffs in element size and number of elements.

Once all of the degrees of freedom are used up and no more additional zeros can be found, the system is re-optimized to give a good wavefront. This requires a new operand that ignores the order of correction, but minimizes the rms OPD over the full region used. It is also important to keep the wavefront slope at the edge from becoming too large, because this slope can drive alignment tolerances up. Tilt in the wavefront from an alignment error will cause a wavefront error proportional to the derivative of the nominal wavefront. Since the primary mirrors generally have central holes, the wavefronts are best optimized by ignoring the unused central area. Significantly better correction over the annulus of the mirror is obtained by allowing the OPD in the central unused region to deviate from the mean value (Rodgers 1986).

This preliminary design procedure will yield several distinct candidates for the final design. Sufficient analysis must be performed on each of these designs to be able to make a well-informed choice of the final design. The expected errors due to manufacturing are generally larger than the residual design error, so an analysis of the tolerances, described in the next section, must be completed for each candidate design. Also, an analysis of the imaging properties and the ghost reflections should be carried out. The criteria for picking one good design over another are not well defined. The designer must weigh the performance, the cost, and the risk associated with each design.

5.4. TOLERANCE ANALYSIS OF NULL CORRECTORS

The final quality of the mirror depends on the accuracy of the null corrector, so a detailed error budget of the null test is critical. This error budget shows the degradation in test accuracy caused by the expected errors in each parameter in the system. Alignment errors in spacing and runout, as well as optical fabrication errors in figure, curvature, and thickness are considered. Also, the glass itself will generally have some

error and spatial variation (inhomogeneity) in its refractive index. The individual error components from the tolerances on these parameters are added in quadrature to give an estimate of the accuracy of the system, as built to the given tolerances.

GENERAL APPROACH TO THE TOLERANCE ANALYSIS

The concept of "tolerances" is loosely defined for this discussion. There are really two sets of tolerances on the lens elements -- manufacturing and measurement tolerances. Small variations in the thickness, refractive index, and curvatures of an element may be compensated by changing the lens spacings as long as the errors are measured accurately. The uncertainty in the measurements defines the set of tolerances that will limit system performance. "Expected error" is perhaps a better term for describing the tolerance corresponding to measurement uncertainty.

The error budget is created through an iterative process. First, a table of sensitivities is created showing the performance degradation for small errors, as determined by computer simulation. The effects of the surface figure irregularity and refractive index inhomogeneity are calculated directly (See Table 5.2). For small errors, the system degradation is assumed to vary linearly with the errors. The sensitivities are then multiplied by expected errors (or tolerances) to compute the degradation in system accuracy. The designer can use this information to adjust the tolerances based on the fabrication and alignment process and the required system performance. Generally, the goal of tolerancing is to meet the system requirements while minimizing the cost. The subject of tolerancing optical systems is treated by Ginsburg (1981), Willey *et al.* (1983), Willey (1984), and Smith (1985).

Table 5.2. Contribution to wavefront from surface figures and index inhomogeneity.

Source	Amount	Wavefront contribution (rms)
Shack cube rms surface irregularity	ΔS_{SC}	$2\,\Delta S_{SC}$
Lens rms surface figure	ΔS_L	$2\,(n\text{-}1)\,\Delta S_L$
Lens rms index inhomogeneity	Δn	$2\,\Delta n \times thickness$

Before performing the error analysis, the optical designer must define a merit function that directly relates to both manufacturing tolerances and to the final use of the optic under test. The merit function must be simple enough to be easily calculated, but must make a meaningful prediction of system performance. The rms wavefront variation is a useful and common figure of merit for high performance imaging systems (Rimmer 1970; Parks 1980) as well as null correctors (Montagnino and Offner 1976; Robbert *et al.* 1979; Friedman and Casas 1981).

Since the optical test of the mirror is performed with the null lens positioned to get the best wavefront, the position of the mirror relative to the perturbed null lens is optimized in the computer model after the null lens has been perturbed (Burge 1991b). The telescope allows for a small variation in the conic constant K, so it is separated from the other errors. The remaining errors due to the perturbation are represented either as structure functions or simply as rms wavefront variation. The parameters are perturbed in both positive and negative directions and the worst case is taken. The error contributions from all of the parameters are added in quadrature to determine an estimate of the resulting system accuracy.

The spherical aberration of the null lens (equivalently, the conic constant error) is separated from other errors because a small error in the conic constant K can generally be accommodated by the telescope. The two-mirror telescope allows two axial adjustments -- the position of the secondary mirror and the focal position. The two motions can be used to independently eliminate small amounts of defocus and spherical aberration from the image. The allowable amount of compensation is generally limited by the range of motion of the focal plane, and by higher-order field errors that couple in. The MMT is designed to compensate for a conic constant error ΔK of 0.0001 or 82 nm P-V spherical aberration.

ALIGNMENT OF TEST OPTICS WITH MIRROR

The autostigmatic null test is fairly insensitive to the relative alignment between the null corrector and the primary mirror. For this test, the shape of the wavefront created by the null corrector defines the shape of the mirror. For a given null lens and spacing between the null lens and the primary mirror, the wavefront shape created by the null lens, thus the shape of the mirror, is fully determined.

A tolerance must be imposed on the primary radius of curvature to assure that the null lens is used at the correct distance from the primary mirror. The null corrector creates a wavefront that propagates to fit the desired shape of the mirror. Since this wavefront changes as it propagates, there is a family of different surfaces that will give a null test, only one of which has the desired shape. Each member of the family can be described to fourth-order in r by specifying a radius of curvature R and conic constant K. In practice, the null lens is positioned so that there is no power in the reflected wavefront. The distance at which this condition is satisfied depends on R. Therefore the

conic constant of the surface matching the wavefront depends on R. The change in K is related to the change in R by

$$\frac{\Delta K}{K} = -\frac{\Delta R}{R}. \tag{5.1}$$

An accuracy in K of ± 0.0001 is achieved by controlling the radius to 0.01%, which is easily done. The radius is inferred from a direct measurement of the distance between the null corrector and the primary mirror when aligned to show a null fringe. The optician monitors this distance and designs the grinding and polishing strokes to keep the radius within the $\pm 0.01\%$ tolerance.

The null test is also insensitive to optical surface decentration and tilt with respect to the axis defined by the null corrector. These pose no real problem as long as the decentration and wedge of the optical surface with respect to the blank are small enough to be accommodated in the telescope. A paraboloidal mirror that is decentered still images light from a distant star to a point. Decentration tolerances of several millimeters and wedge tolerances of several arc seconds are easily met on a large mirror. The wedge can be measured by rotating the mirror about the mechanical reference axis and measuring runout in the optical surface. The decentration can be determined from the amount of coma seen in the null test when the mirror is rotated about is mechanical axis. The centration and wedge of the optical surface are largely determined during generating. Little material is actually removed during grinding and polishing that these mechanical properties are unlikely to change.

It is easy in practice to align the null lens with respect to the mirror because the different alignment degrees of freedom cause distinct changes in the interferogram. To find the correct null lens position and orientation with respect to the mirror, the null lens is first positioned approximately to get the light to reach the detector. It is then moved

to eliminate the fringes showing tilt, focus and coma. Interferograms showing these characteristic aberrations are shown in Fig. 5.2. Lateral translation of the null lens causes straight tilt fringes in the interferogram. Vertical translation along the axis gives rise to focus in the interferogram. Rotation of the null corrector about the paraxial center of curvature corresponds to a lateral shift or decenter of the optical surface and shows up as coma in the interferogram. Since it is easy to differentiate tilt, coma, and focus in an interferogram by inspection, the alignment is done quickly and easily.

A small amount of residual alignment error always exists that must be removed in the data analysis. About a tenth of a fringe of tilt, focus, or coma will often remain after alignment. Any small mechanical instabilities will also cause small variations of these aberrations. Since any tilt, focus, or coma measured in the mirror comes from test misalignment and because these aberrations do not affect the telescope operation, they are always removed in the data analysis. These low-order terms are easily removed by first fitting Zernike polynomials to the raw data and then subtracting the appropriate terms from the data.

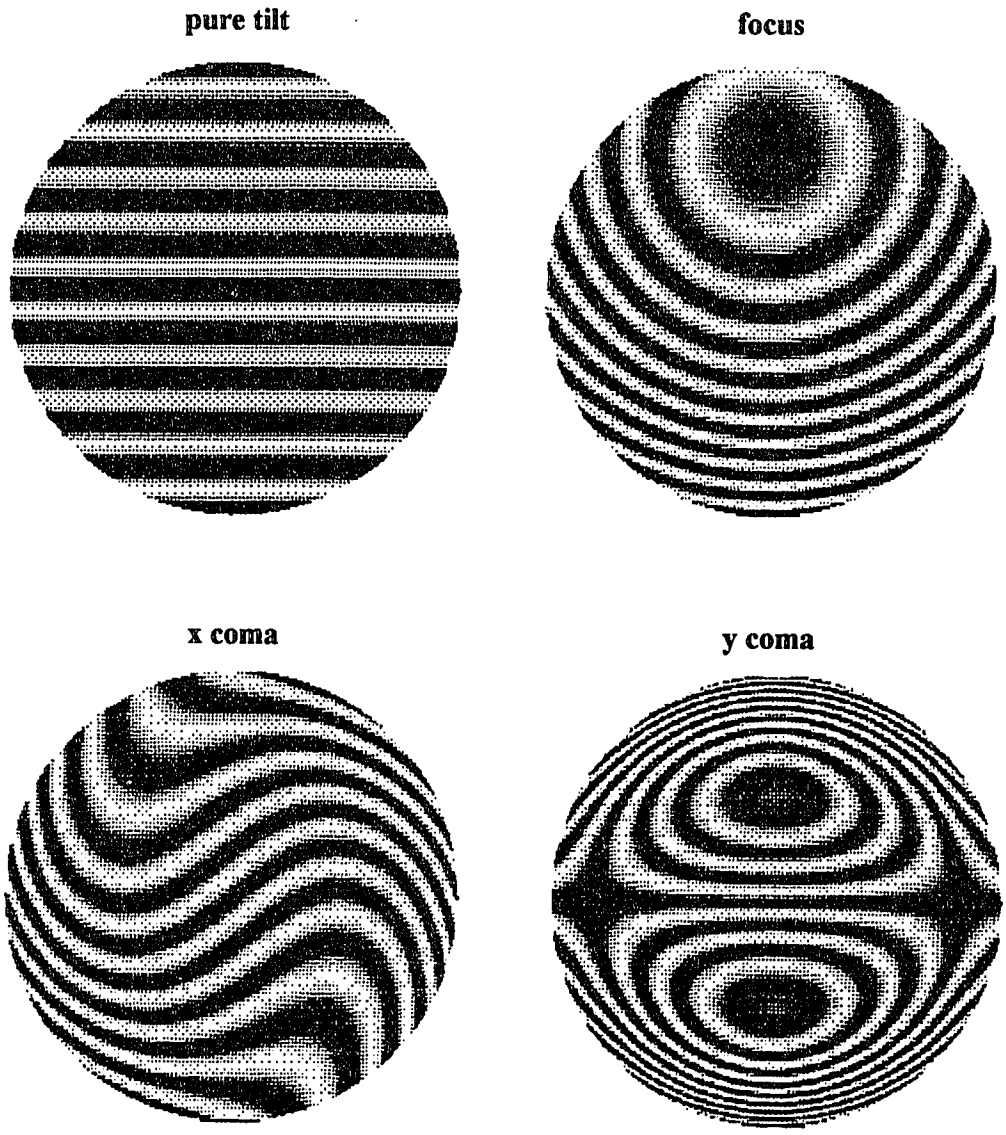

Figure 5.2. Interferograms showing alignment errors of pure tilt, focus, and coma. Some tilt has been added to the focus and coma.

TOLERANCE ANALYSIS FOR A 3.5-m *f*/1.75 PRIMARY MIRROR

A tolerance analysis performed on the null test for the 3.5-m *f*/1.75 primary for the WIYN telescope indicates an uncertainty of ±0.00012 in the conic constant and 0.023 waves rms (at 632.8 nm) in the surface figure. A detailed breakdown of this analysis is shown in Appendix B. The alignment of the null lens was performed by S. West using the procedure described above. The thicknesses of the lens elements were measured mechanically using two independent techniques. The lens surface curvatures were measured on a lens bench by D. Ketelsen using a standard interferometric procedure described and analyzed by Selberg (1992). The lens surface figures were certified using either a phase-shifting Fizeau interferometer or a test plate which in turn has been measured on a Fizeau. The value and inhomogeneity of the refractive index of the glass were supplied by the glass manufacturer and corrected for the temperature, air pressure, and wavelength at which the glass is used. The relationships between surface figure, index inhomogeneity, and rms wavefront error are given in Table 5.2.

The above analysis yields an estimate of the accuracy of the null test for the as-built system. It does not represent the actual test accuracy because it does not include the ability to measure errors and remove them. The null corrector for the WIYN primary was measured against a computer-generated hologram and shown to introduce 0.008λ rms error in the surface measurement that was subtracted from the surface data. This small measured error indicates that the estimates of the errors and uncertainties were conservative.

TOLERANCE ANALYSIS IN TERMS OF TELESCOPE ERROR BUDGET

Surface figure specifications using only rms wavefront are not sufficient for high-performance optical systems. The statistics of the spatial distribution of the wavefront error must be explicitly specified. This may be done for imaging systems using the modulation transfer function (Rimmer 1978). For optical surfaces, the specification may be in terms of a power spectral density (Church and Takacs 1992) or a structure function (Brown 1983) of the surface errors. (See Sec 1.8 on the specification of optical figures.) The structure function is calculated by taking the mean square phase difference between points on the mirror. Most ground-based telescopes use the structure function as a figure of merit because it is easily calculated and it relates directly to the image degradation caused by the atmosphere.

Since the tolerance on the primary mirror is in terms of a structure function for the University of Arizona telescopes, the error analysis for the test of these mirrors must be related to a structure function. This analysis has been performed on null correctors for testing the primary mirrors for the MMT (Burge 1992a) and the LBT (Burge 1992b). The results of these analyses are given in Sections 5.5 and 5.7.

The tolerance analysis of the interferometric test may be performed by computing structure functions for all of the independent parameters in the system and adding them. Structure functions for tolerances in all direct dimensions (spacings, curvatures, refractive index, misalignments, etc.) are computed by ray-trace simulation and analysis of the system. Structure functions from the surface figures of the optical elements are estimated by using data from finished optical surfaces. Refractive index inhomogeneity structure functions are estimated for H5 quality glass using melt data and assuming a linear dependence of rms phase difference on point separation. The structure functions from all parameters in the null test are added to give the total test optics structure func-

tion. The analysis does not take into account the ability to measure and remove errors in the null lens using the CGH null lens test.

The structure functions are computed for a given separation by evaluating the wavefront phase for large numbers of point-pairs. For the error analysis, a subroutine was implemented into an optical design program that computes the structure function directly by tracing a large number of rays through the system and calculating the mean square OPD difference between pairs of rays. This structure function was used as the figure of merit for the sensitivity analysis.

Structure functions representing the surface irregularity of the null lens elements were estimated using measured data from polished spherical surfaces. Three different concave spherical surfaces with rms surface errors of 10, 12, and 13 nm were measured by D. Anderson using phase shifting interferometry. The structure functions were calculated from these data for point separations of 1/2, 1/4, 1/8, 1/16, 1/32, 1/64, 1/128 of the outer diameter. From these structure functions, an estimate of the distribution of phase errors was made. It was assumed for this analysis that the structure function is proportional to the overall rms figure and that the spatial distribution of figure errors, normalized by the diameter, is constant. So given an rms surface figure for a spherical element in the null lens, an estimate of the structure function may be made. The measured structure function and ratio to overall rms are given in Table 5.3.

Table 5.3. Surface structure function for polished spherical surfaces.

point pair separation (fraction of diameter)	measured rms surface height difference (nm)	ratio of rms surface height difference to overall rms surface deviation
1/2	16.2 ± 2.3	1.39
1/4	15.1 ± 2.6	1.31
1/8	11.2 ± 1.3	0.97
1/16	7.6 ± 0.7	0.66
1/32	4.7 ± 0.5	0.411
1/64	2.6 ± 0.2	0.224
1/128	1.2 ± 0.05	0.101

A good structure function estimation for the refractive index inhomogeneity would require more complete specification by the optical glass manufacturers. Currently, optical glass is specified only by its *peak-to-valley* index variation. Nonetheless, knowledge of the glass structure (Reitmayer and Shuster 1972; Roberts and Langenback 1969) allows a few simplifying assumptions to obtain an estimate of the structure function. First of all, the ratio of the rms index variation n_{rms} to the peak to valley variation $n_{p\text{-}v}$ was found to be

$$\frac{n_{rms}}{n_{p\text{-}v}} = 0.16 \pm 0.02, \tag{5.2}$$

using melt data from five blocks of precision optical glass that were purchased for the MMT null lens. This ratio represents not only the glass, but the method used to measure the index variations.

As a further assumption, the magnitude of the refractive index fluctuations was assumed to be proportional to spatial scale. This is reasonable for striae-free glass over

small scales, but will not be true for large scales. At large scales, the structure function flattens off because of the insensitivity to tilt and power. At sufficiently large spatial scales, the variations appear to be uncorrelated. The rms difference in this uncorrelated region is $\sqrt{2}$ times the overall rms variation. It is impossible to accurately estimate this correlation distance without a large amount of good data. A coarse estimate of the correlation distance was made to be 3/8 of the part diameter, chosen based on the measured index inhomogeneity maps supplied with the glass. This leads to an estimated structure function contribution of

$$n_{str}(l) = \begin{cases} \sqrt{2} \times n_{rms} \times \frac{8l}{3D}: & for\ l < \frac{3}{8}D \\ \sqrt{2} \times n_{rms} \quad : & for\ l > \frac{3}{8}D \end{cases} \tag{5.3}$$

where l is the point pair separation at the lens

D is the lens diameter

n_{rms} is the overall rms index variation from Eq. (5.2)

$n_{str}(l)$ is the rms index difference for points separated by l.

Given the P-V index inhomogeneity, the structure function is estimated using Eqs. (5.2) and (5.3). The relatively low accuracy of this estimate limits the accuracy of the null lens estimate. However, the error estimate will be quite conservative since most of the error due to the refractive index inhomogeneity can be accurately measured and backed out of the mirror measurement. The inhomogeneity errors will have no tendency to have a strong axisymmetric component because the optical axis is not defined in the bulk glass. The azimuthal index variations can be accurately measured by performing a rotation test with a CGH or the primary mirror itself.

The null lens analysis using structure functions requires the computation of a structure function from each manufacturing and alignment degree of freedom including surface irregularity and index inhomogeneity. The wavefront variation is calculated from the surface irregularity and index inhomogeneity structure functions using the relationships in Table 5.2. The structure functions are uncorrelated mean square distributions, so they may be added directly to give the system structure function. This function directly relates to the telescope error budget.

5.5. REFRACTIVE NULL CORRECTOR FOR 6.5-m *f*/1.25 PRIMARY MIRRORS

A visible null corrector with a sophisticated imaging system has been designed for the testing of a 6.5-m *f*/1.25 primary mirror. The current design of the interferometer uses a stabilized argon ion laser operating at 514.5 nm, a PZT-shifted Shack cube, imaging optics, and shuttered CCD detector. The Shack cube, null lens, and imaging optics will be precisely aligned on a single rigid truss. The laser light will be fed into the system through a single mode optical fiber.

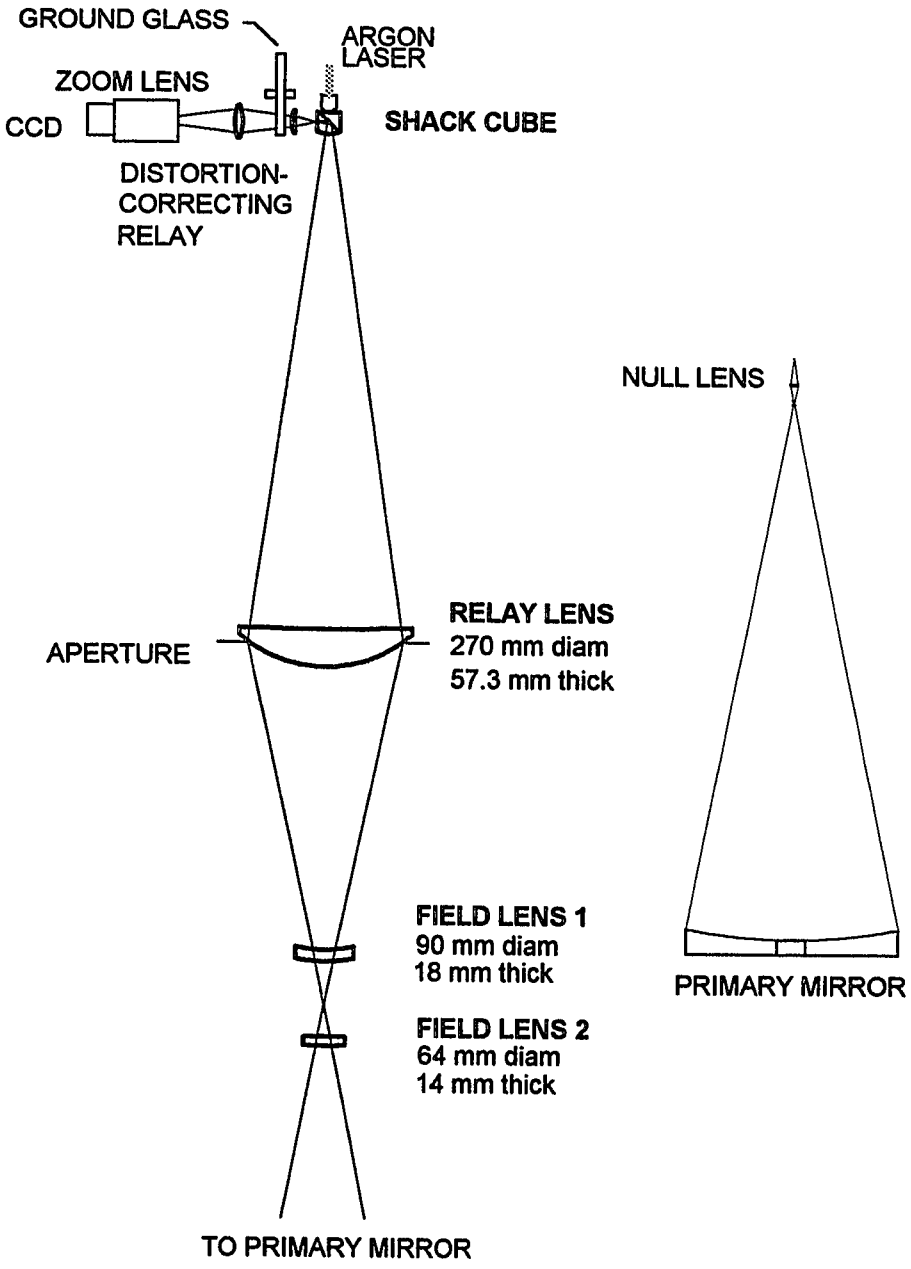

Figure 5.3. Optical layout of the visible null lens for 6.5-m $f/1.25$ primary mirrors with Shack cube interferometer and distortion-correcting relay. The inset shows the scale of the null lens with the 6.5-m mirror. The complete prescription is given in Appendix C.

The null corrector shown in Fig. 5.3 consists of the Shack-cube and three BK7 lenses: a relay lens, and two field lenses. The optical design gives a wavefront error of 4 nm rms (Fig. 5.4) and maximum mapping error of almost 5%. The null corrector will be mounted vertically to precise tolerances using the method described by West *et al.* (1992). The relative alignment between the system and the mirror will be performed by translating the entire unit in three directions and rotating about two flex-pivots. This alignment will be controlled remotely from a testing station that is not on the vibration-isolated test tower.

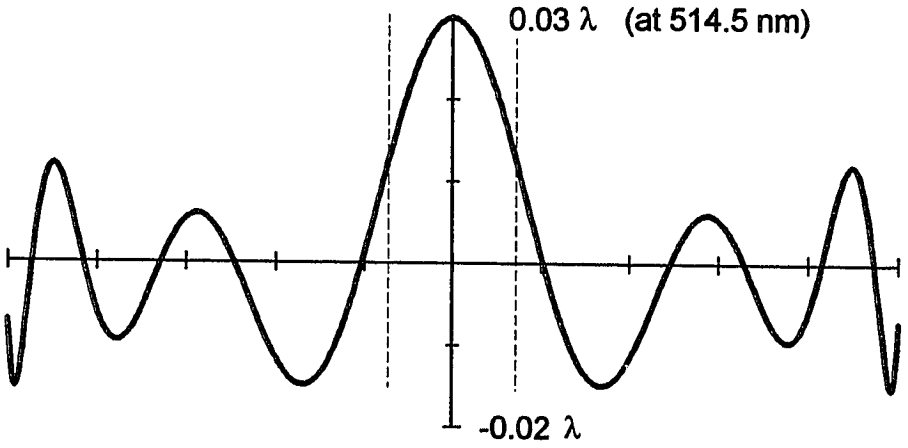

Figure 5.4. Residual wavefront errors for visible refractive null lens for testing the 6.5-m *f*/1.25 primary mirror. The wavefront has 0.008 λ rms variation at 514.5 nm. The dotted lines show the size of the central hole.

The imaging distortion introduced by the null lens will be corrected with the relay optics that are shown in Fig. 5.3. A plot of the mapping error is shown in Fig. 5.5. This two-lens relay not only corrects the mapping error, but it projects the image of the primary to infinity. This allows the use of a standard zoom lens to re-image the pupil at varying magnification. The re-imaging system consists of a 6X zoom lens fixed to the

CCD camera that is mounted on a tip-tilt stage. All of the controls will be operated remotely to allow the optician to magnify the image and to look with increased resolution anywhere on the mirror. High resolution (~6 mm pixels at the mirror) will then be attained for sub-aperture testing without increasing the array size.

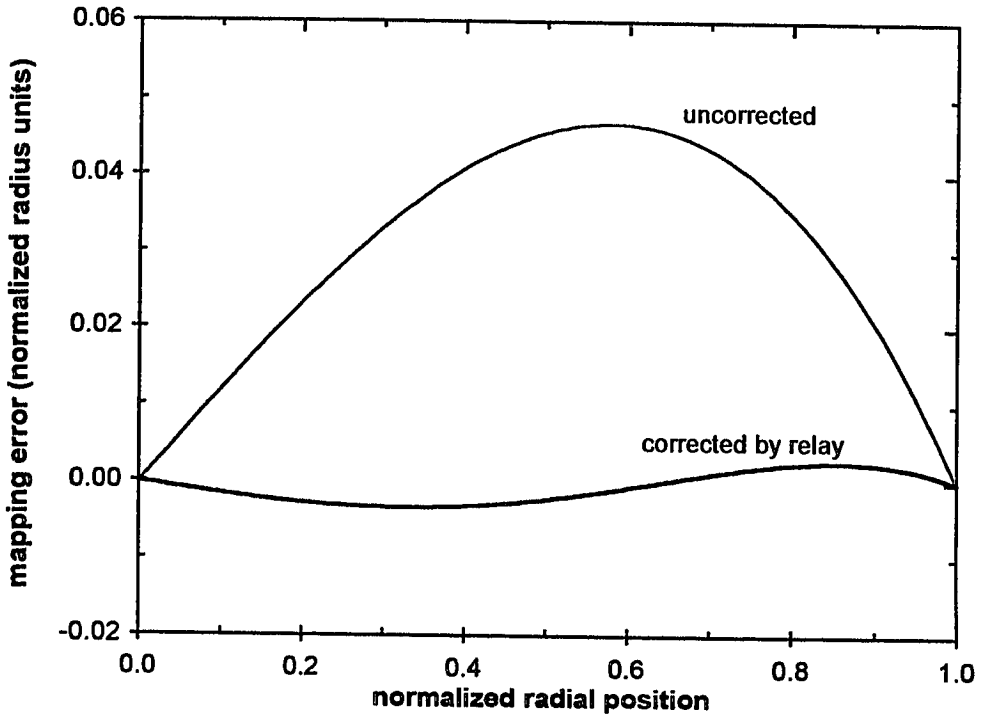

Figure 5.5. Mapping error for the null lens for testing the 6.5-m $f/1.25$ primary mirror.

The telescope error budget allots to the testing of the primary mirror a structure function corresponding to an atmosphere with coherence length r_0 of 270 cm (which gives atmospheric seeing of 0.04 arc-sec FWHM). The tolerance analysis shows that the null corrector will meet this at all spatial scales. The methods and assumptions for the structure function analysis are given above. The resulting structure function for the null lens optics is shown in Fig 5.6.

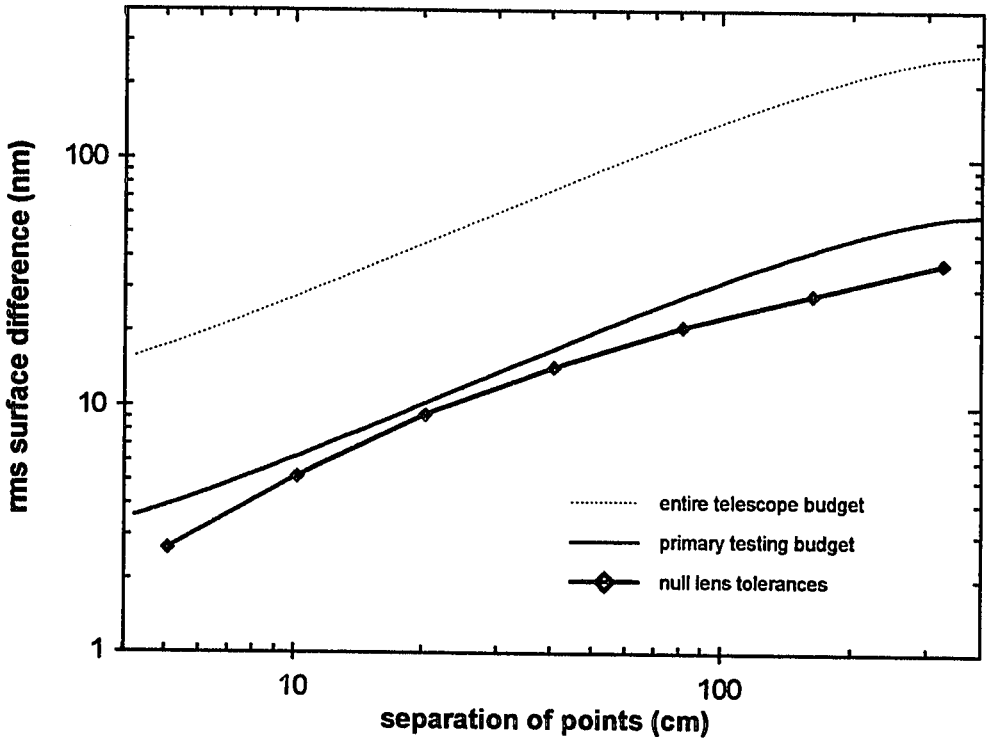

Figure 5.6. Structure function from the error analysis of the visible null corrector for the 6.5-m $f/1.25$ primary. The telescope and test optics specifications are based on a tilt-corrected Kolmogorov model of the atmosphere with a relaxation at small spatial scales.

Distinct from the structure function requirement is a tolerance on the conic constant of the primary. The null lens described introduces an uncertainty of the conic constant of ±0.00009. Also, the analysis does not take into account the ability to measure and remove errors in the null lens using a rotation test or the CGH null lens test. A complete table showing the error analysis is given in Appendix C.

The visible null corrector creates a real image of the primary mirror near the large relay lens, where a circular aperture will be placed as described in Sec. 4.6. The imaging system will correct distortion and eliminate problems from the laser coherence using

methods described in Secs. 4.7 and 4.8. The distortion-correcting relay creates an intermediate real image of the primary where a rotating ground glass disk will be placed.

In summary, the visible interferometer with null corrector for the MMT 6.5-meter $f/1.25$ primary mirror will accurately measure surface errors to guide the polishing of the optical surface. The imaging of the primary to the detector was designed to be free from mapping errors and to eliminate diffraction problems. The laser light will be fiber-optically fed to the interferometer to keep the laser heat from affecting the test. The alignment of the interferometer relative to the primary, as well as the zoom and pan of the imaging lens will be performed from a remote test station, allowing rapid collection of high-quality data.

5.6. INFRARED NULL CORRECTORS USING ASPHERIC SURFACES

An infrared interferometer with null lens is useful for measuring the rough surface during loose abrasive grinding. The use of an aspheric surface in the infrared null corrector reduces the size of the null corrector and thus can increase overall accuracy. Small, rotationally symmetric aspheric surfaces are made to sub-micron accuracy by single-point diamond turning. The machine used for this process is nothing more than a precise computer-controlled lathe that uses a small diamond as the cutting tool. The tool marks left behind do not affect the performance of the null corrector because the marks are much smaller than the 10.6-micron wavelength. The use of single-element diamond-machined null lenses is described by McCann (1991). The use of diamond turned reflectors in a null test is described by Gerchman (1986) and McCann (1990).

Single-crystal germanium and ZnSe are good materials for infrared null correctors. Single-crystal germanium has a high refractive index of 4.003 and a high dn/dT of 414 ppm per °C (Hoffman and Wolfe 1991). The refractive index inhomogeneity is

about ±0.0001 or 0.00005 rms. Zinc selenide has better optical properties. The refractive index is 2.402 with ±0.000003 rms homogeneity, and dn/dT of 58 ppm per °C (Hoffman and Wolfe 1991). However, ZnSe costs about three times as much as germanium.

An interesting compact null corrector for a 6.5-m *f*/1.25 primary mirror was designed that used two ZnSe lenses with a single aspheric surface. The null lens, shown in Fig. 5.7 uses one element to image the primary onto the aspheric surface of the other lens, which corrects the wavefront asphericity. The computer simulation of this null corrector shows the wavefront corrected to 0.002 λ rms (at 10.6 μm) and less than 2% mapping error from imaging distortion. The prescription for this design is given in Appendix D. By using a highly aspheric surface, the null corrector is kept to 113 mm total length, but the manufacturing tolerances are extremely tight. Even if the lenses could be perfectly aligned, the uncertainty in the material properties of the lenses would severely limit the accuracy. The refractive index of ZnSe is uncertain to ±0.0005, which causes an uncertainty in the conic constant of ±0.0017 and can cause 0.076 λ rms wavefront error, which are unacceptable. This design appears to be very attractive because of its compact size and excellent correction. However, due to the sensitivity to manufacturing errors, the actual performance of this null corrector is likely to be poor.

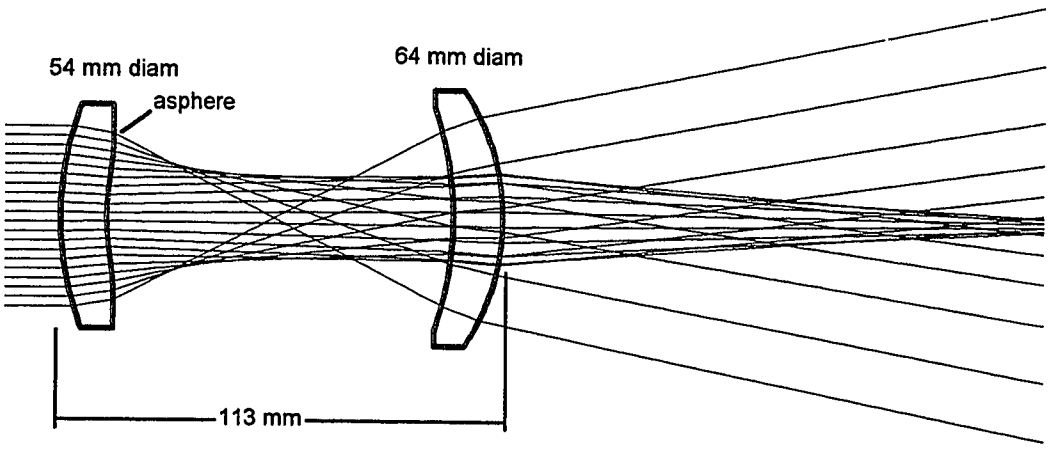

Figure 5.7. A compact infrared null corrector for the testing of a 6.5-m *f*/1.25 paraboloidal primary mirror. This design uses a single aspheric surface to correct the wavefront with negligible imaging distortion. This design is not practical because of its high sensitivity to manufacturing errors.

A much larger, but less sensitive null corrector has been designed for the 6.5-m *f*/1.25 primary mirrors, and is currently being fabricated. The null corrector, shown in Fig. 5.8, consists of three lenses: an aspheric ZnSe diverger, a plano-convex germanium relay lens, and a plano-convex ZnSe field lens. The optical design uses the aspheric surface to give a near-perfect wavefront error of 0.0014 λ rms and mapping error less than 1.3%. The aspheric surface for this null corrector was diamond turned and measured with a profilometer. The surface deviates from the best-fit sphere by 160 μm and was determined to be correct to ±0.2 μm. The prescription for this design is given in Appendix D. The null corrector will be mounted horizontally and aligned to a Twyman-Green interferometer which creates a collimated reference beam, so a diverger is re-

quired. The interferometer uses a CO_2 laser operating at 10.6 μm, a PZT-shifted reference mirror, and a pyroelectric vidicon detector (Stahl and Ketelsen 1985). The relative alignment between the system and the primary mirror will be performed by translating the interferometer-null corrector in three directions and steering the beam with a fold flat. A small aperture at the focus of the diverger will reduce stray light.

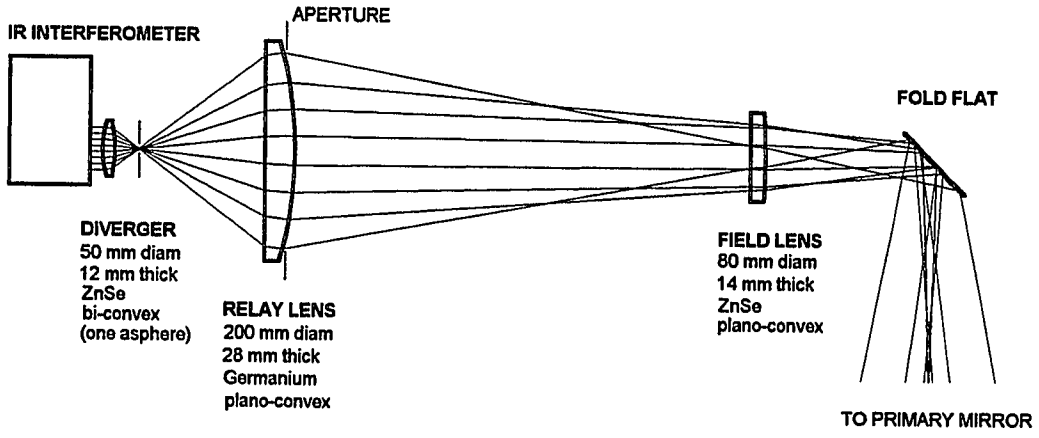

Figure 5.8. Infrared null corrector for the testing of a 6.5-m *f*/1.25 paraboloidal primary mirror. This design is optimized for wavefront correction, imaging distortion, alignment tolerances, and ghost reflections.

The elements in this null lens are the smallest that will work when aligned to machine tolerances (±50 μm over 200 mm). A thorough tolerance analysis of the system, shown in Appendix D, indicates that the null lens will contribute surface measurement errors of 1.5 μm rms. Most of this error is due to refractive index inhomogeneity of the large germanium lens. This will be measured using a rotation test and subtracted. The uncertainty of the conic constant in this null lens due to the manufacturing tolerances is ±0.00016, nearly meeting the telescope specification of ±0.0001.

This null corrector was designed to give excellent imaging performance with no troublesome ghost reflections. In order to avoid the diffraction problems associated with

infrared interferometry, the image of the primary mirror will be accurately focused onto the vidicon detector. To facilitate this, the null corrector creates a real image of the primary mirror very near the large relay lens, where a circular aperture will be accurately placed. This will provide a sharp aperture to define the focus. To minimize ghost reflections, the null lens was designed to avoid surfaces with normal ray incidence.

5.7. REFLECTIVE NULL CORRECTOR FOR 8.4-m *f*/1.14 PRIMARY MIRRORS

The Large Binocular Telescope (LBT) requires twin 8.4-meter diameter, *f*/1.14 paraboloidal primary mirrors that have 1.38 mm departure from the best fitting sphere, more than any other existing or proposed astronomical mirrors. A null lens designed for the interferometric testing of these mirrors, shown in Fig 5.9, corrects for this aberration without the inherent difficulties of more established null correctors. Offner-type (Offner 1963) refractive null correctors for large, fast aspheres require thick lenses that limit the wavefront quality due to the refractive index variations inside the glass. "Clamshell" type reflective null lenses (Montagnino and Offner 1976; Offner and Malacara 1992) use mirrors to eliminate the refractive index problem, but their geometry does not work well for fast aspheres with small central holes. The two mirrors become large and prohibitively expensive. The use of diffractive elements and aspheric surfaces is avoided because of the high frequency errors and the alignment difficulty discussed in Sec. 5.2.

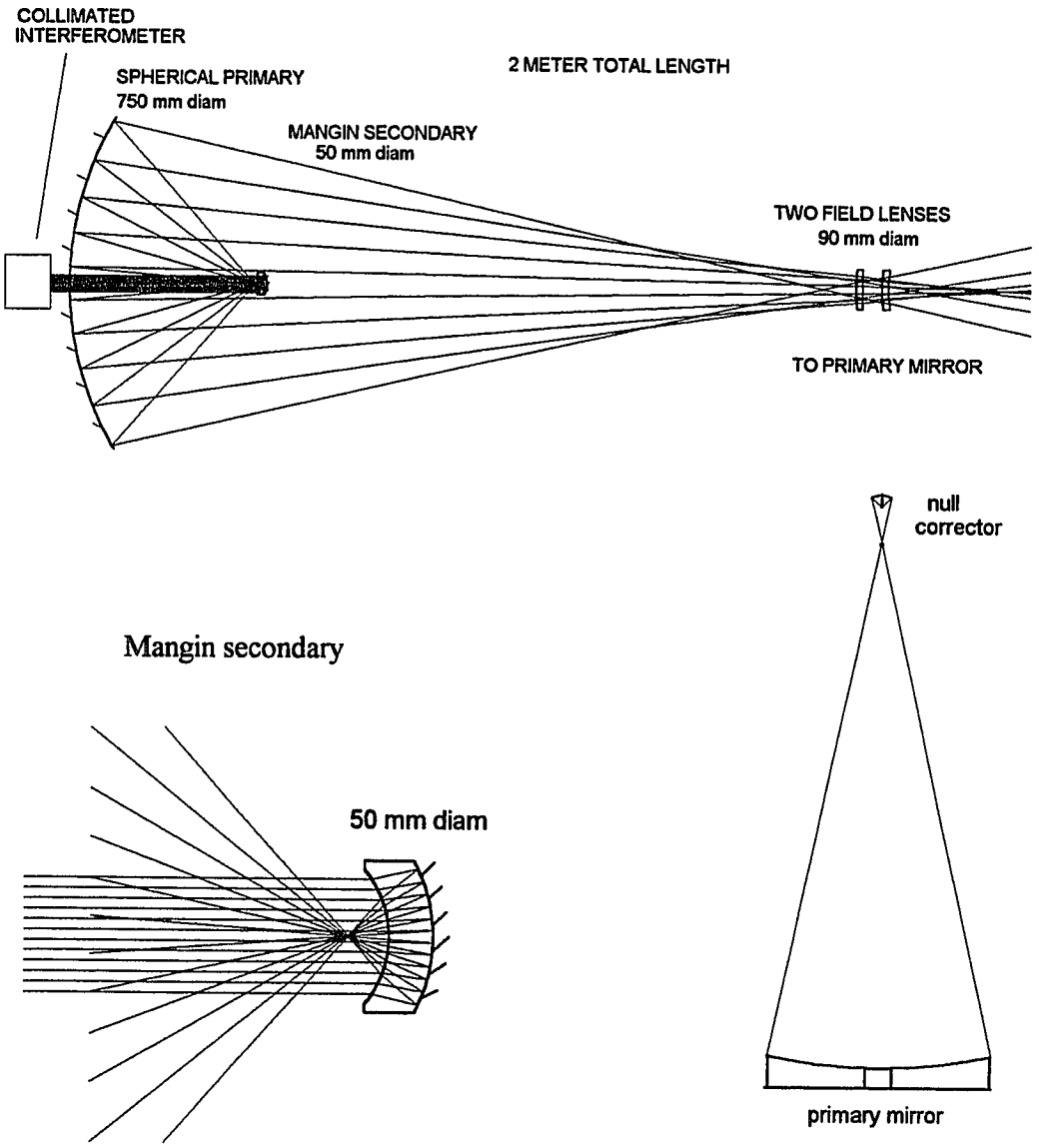

Figure 5.9. Optical layout of null lens for the LBT 8.4-meter $f/1.14$ primary mirrors. The insets show the relative size of the null corrector and the primary mirror and the ray distribution at the Mangin secondary.

The new null lens consists of a small Mangin secondary, a 75-cm diameter spherical reflector, and two small BK7 field lenses. It looks somewhat like a Gregorian telescope used at the wrong conjugates. The null corrector, shown in Fig 5.9, was de-

signed to give excellent correction with moderate alignment tolerances, and to minimize diffraction and ghost reflection problems. The optical design (with no misalignments) corrects the surface asphericity to 2.5 nm rms and the fully toleranced system meets the telescope allotted error budget for primary testing. A plot of the wavefront error introduced by this design is shown in Fig. 5.10.

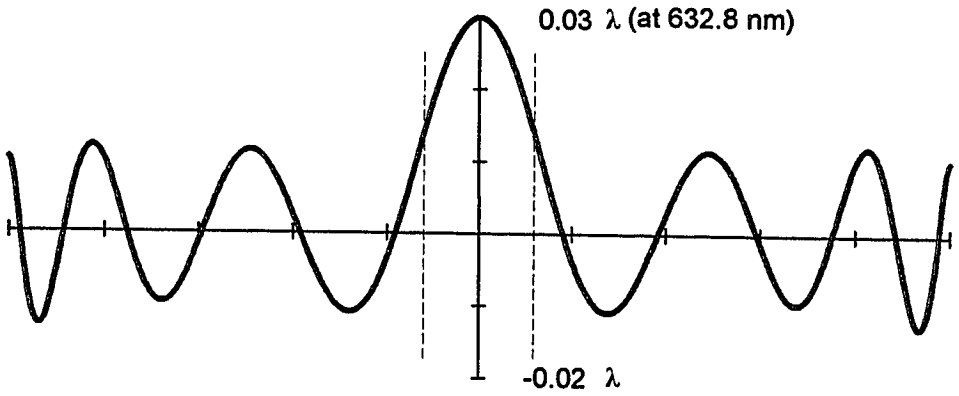

Figure 5.10. Residual wavefront errors for visible reflective null lens for testing the 8.4-m $f/1.14$ primary mirrors. The wavefront has 0.008 λ rms variation at 632.8 nm. The dotted lines show the size of the central hole.

The tolerance analysis of the null test was performed using structure functions as described above. This analysis demonstrates that the null corrector will meet its specified error budget (See Fig. 5.11). As before, this analysis does not take into account the ability to measure and remove errors in the null lens. The interferometric testing of the primary mirror was allotted a structure function corresponding to an atmosphere with coherence length r_0 of 270 cm (which gives atmospheric seeing of 0.04 arc second FWHM). A complete table showing the error analysis is given in Appendix E.

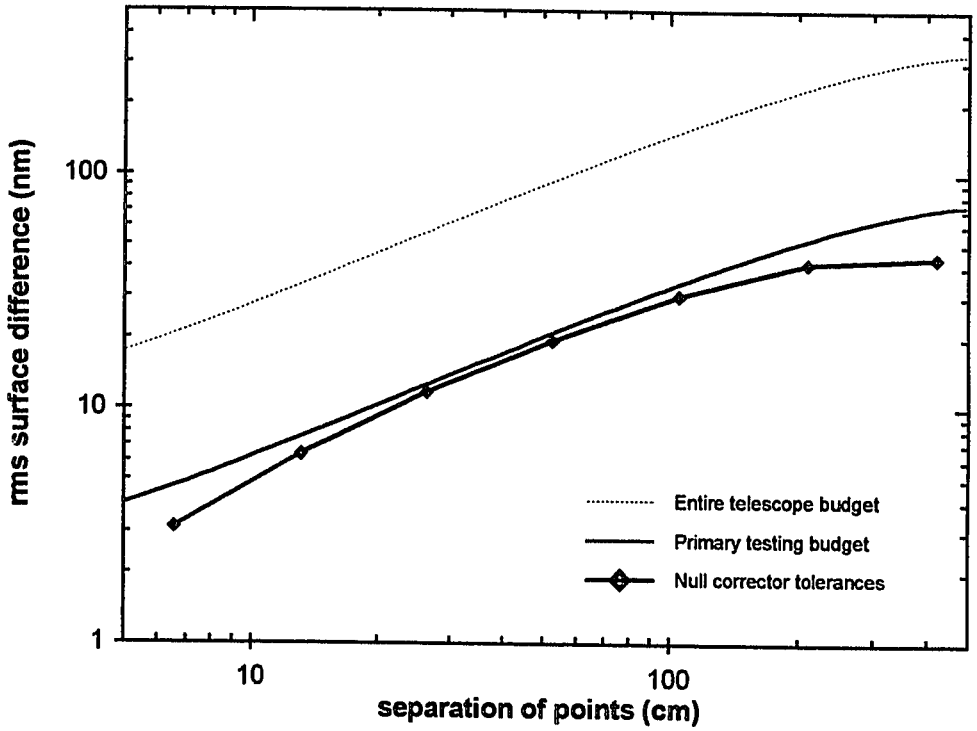

Figure 5.11. Structure function from the error analysis of the visible null corrector for the LBT 8.4-m *f*/1.14 primaries. The telescope and test optics specifications are based on a tilt-corrected Kolmogorov model of the atmosphere with a relaxation at small spatial scales.

Distinct from the structure function requirement is a tolerance on the conic constant of the primary. The null lens described introduces an uncertainty in conic constant of ±0.000145.

The optical design was optimized for imaging performance as well as wavefront correction. The system was designed to image the primary onto a CCD array with less than 1% mapping distortion. To reduce the effects of diffraction, the spider that will support the Mangin secondary lies at an intermediate focus of the primary. Thus, proper focusing of the primary onto the CCD forces the spiders to be *in* focus, minimizing the spatial extent of the diffraction ripples. A thorough analysis of ghost reflections from all

surfaces has shown that there are no ghost images that will cause troublesome spurious fringes.

The optical design was made to be versatile. Simply replacing the field lenses with ZnSe optics and replacing the Mangin secondary with a spherical concave mirror allows the null lens to be used for testing the LBT primaries with infrared light. Also, by changing only spacings and field optics, the null corrector will work for different primaries. A set of optical designs that use this null corrector for the visible and infrared testing of the LBT 8.4-m *f*/1.14 and the MMT 6.5-m *f*/1.25 primary mirrors is shown in Table 5.4 . The optical designs and tolerance tables are given in Appendix E..

Table 5.4. Null tests using the LBT Gregorian null corrector.

paraboloidal primary mirror	laser (wavelength)	residual rms wavefront variation in design	rms wavefront variation in toleranced design	conic constant uncertainty of toleranced design
LBT 8.4-m *f*/1.14	HeNe (632.8 nm)	0.008λ	0.09λ	±0.00015
LBT 8.4-m *f*/1.14	CO_2 (10.6 μm)	0.002λ	0.04λ	±0.00038
MMT 6.5-m *f*/1.25	HeNe (632.8 nm)	0.0006λ	0.08λ	±0.00015
MMT 6.5-m *f*/1.25	CO_2 (10.6 μm)	0.0063λ	0.03λ	±0.00056

This new optical design is attractive because it avoids the test uncertainty due to inhomogeneity in the refractive index. It may also be cost-effective because a single sys-

tem could work for visible and infrared testing of several mirrors. However, this null corrector will be more difficult to fabricate and align than the refractive type shown in Sec 5.5. With the invention of the CGH test for null correctors (Chaps. 6 and 7), the effects of refractive index variations will be measured and will no longer limit the test accuracy. For this reason, it is unlikely that this reflective null corrector will be used for the LBT.

5.8. CONCLUSION

The optical design of null correctors for highly aspheric primary mirrors requires a system level strategy that will result in optimal performance from the as-built system. Besides the wavefront correction, the optical designer must consider the size constraints, sensitivity to manufacturing errors, susceptibility to ghost reflections, diffraction problems, and distortion of the test optic. The designer may pursue several preliminary designs before choosing a final design to implement.

Null correctors require a thorough tolerance analysis to guide the fabrication and obtain a good estimate of the system accuracy. This analysis is ideally done so that the results may be used directly to predict degradation of the telescope performance due to the testing errors. It is useful to separate spherical aberration in the null corrector, which causes a conic constant error in the mirror, from other errors. The most likely null lens errors are spherical aberration, and the telescope can compensate for a small conic constant error. Since the error budget for modern astronomical telescopes uses structure functions, the optical testing error budget has been performed using them as well. This allows a direct conversion from testing errors to telescope performance.

A visible null corrector for the MMT 6.5-m $f/1.25$ primary mirror has been designed and is currently being fabricated. This null lens will offer distortion-free meas-

urement of the primary mirror to an accuracy of 0.04λ rms. The test was shown to meet the structure function specification from the telescope error budget. The system is designed to minimize noise from diffraction and ghost reflections, and will allow remote control of the test alignment and the imaging zoom and pan.

Several new types of null correctors have been designed that give excellent wavefront correction while minimizing diffraction, distortion, and ghost reflection problems. Refractive infrared null lenses using diamond-turned aspheric surfaces were designed for the MMT 6.5-m $f/1.25$ primary mirror. Optical designs of null correctors that use mirrors were pursued to avoid the limitation of refractive index inhomogeneity in large lenses. A reflective null corrector has been designed for the LBT 8.4-m $f/1.14$ primary mirrors that will work with visible or infrared light. This null lens was shown to meet the telescope structure function specification. By changing only a few elements, this null corrector would work for the MMT and Magellan primary mirrors as well.

New optical designs and tolerance analyses in terms of structure function promise accurate interferometric tests of large, fast aspheric mirrors. The tolerance analysis shows that the allowable measurement structure function for the high performance ground-based telescopes can be achieved. However, since there is a small possibility of a manufacturing error that falls outside of the tolerances, an independent verification of the null lens is essential. The CGH null lens test described in the following chapters has been developed to verify the accuracy of the null correctors.

SECTION III

HOLOGRAPHIC TEST OF NULL CORRECTORS

An optical test has been devised at Steward Observatory to directly test and qualify null lenses used for testing highly aspheric primary mirrors. The technique employs the unique application of a computer generated hologram (CGH) which tests the null corrector directly. The test, which is quick, inexpensive, and highly accurate, has been demonstrated on null correctors for three 3.5-m primary mirrors, and it is planned for the larger systems.

Chapter 6 gives a description and thorough analysis of the test. Background information on CGH testing and a derivation of the hologram pattern are given. The optimization of diffraction effects is discussed, and a detailed error analysis of the test is given.

Chapter 7 gives the results from performing this test on three null correctors. The results are generally excellent; two null correctors for 3.5-m primary mirrors were verified as having the correct conic constant to 78 ppm. Also, a null lens was purposely misaligned and measured to have the expected error. Unfortunately, some of the holograms had gross flaws that caused discontinuous steps in the diffracted wavefronts. The source of these errors is not understood, but a plan is described for eliminating the fabrication step that appears to cause the problem.

CHAPTER 6

HOLOGRAPHIC MEASUREMENT OF NULL CORRECTORS: THEORY AND DESIGN

6.1. INTRODUCTION

An optical test has been devised to test and qualify null correctors that are used for measuring highly aspheric primary mirrors. The technique employs a rotationally symmetric computer-generated hologram (CGH) that tests the null corrector directly by synthesizing a wavefront that would be returned by a perfect primary mirror. The test, which is quick and highly accurate, has been demonstrated on null correctors for two 3.5-m primary mirrors.

Large primary mirrors for optical telescopes are interferometrically tested from center of curvature using null correctors. In fabricating a primary mirror, the optical surface is polished to precisely match the wavefront generated by the null corrector. There is always a possibility that the null corrector could be flawed, resulting in the final shape of the mirror being incorrect. Two recent telescopes had their primary mirrors made to the wrong shape because of errors in the null correctors -- the Hubble Space Telescope or HST (Allen *et al.* 1990) and the New Technology Telescope or NTT (Wilson *et al.* 1991). If accurate testing of the null correctors had been performed, the errors would have been discovered and corrected in the shop. Instead, the errors were not discovered until the finished mirrors were in their telescopes on a mountain top or in orbit.

The holographic test of null correctors fills an important gap in the fabrication of highly aspheric optics. Because the null correctors introduce hundreds of waves of asphericity, they are complex and sensitive to manufacturing errors. A small manufacturing flaw or oversight may cause significant aberration in the null lens resulting in a mirror finished to the wrong shape. For this reason the verification of the test optics is viewed as a critical step in the fabrication of highly aspheric optics. One method of verifying the optical test is to compare results from two independent null lenses. This is expensive and can be inconclusive. (What if the two null lenses do *not* agree?) Another technique is to perform an independent test on the completed mirror such as a scanning pentaprism test. Accurate tests of this type are difficult and expensive. These tests must be performed on a completed mirror, which involves some risk to the surface. Also, if an error is detected in the finished mirror, either the mirror or the telescope must be corrected.

This chapter gives a general description and analysis of this new method of testing null correctors. The following chapter gives results and analysis from actual measurements. Readers interested only in the results of this test should read the description in Sec. 6.2 and skip to Ch. 7.

This chapter gives a complete description of the principles, design, and analysis of the CGH test for null correctors. The test geometry and principles used for the null lens test are described in Sec. 6.2. Section 6.3 gives a brief background and history of optical testing with CGH. The emphasis is placed on techniques similar to those used in the null lens test. The design and fabrication techniques used for making the CGH are described in Sec. 6.4. The CGH phase function is explicitly derived and analyzed in this section. Approximations that are used in the error analysis are also given. The complete process of specifying and fabricating the CGH is summarized. Design considerations for optimizing the test to give maximum contrast and complete rejection of stray orders are

described in Sec. 6.5. A thorough error analysis is presented in Secs. 6.5 - 6.7 that includes errors in the fabrication of the CGH, errors in performing the test, and errors in the data analysis. These sections show the derivation of the error terms and include little discussion of specific applications. The following chapter uses the equations for error analyses of specific tests with little discussion of the derivation.

6.2. DESCRIPTION OF HOLOGRAPHIC NULL LENS TEST

In the CGH null lens test, a computer-generated hologram of the mirror is tested by the null lens. The hologram is made so it will appear to the test lenses as if it were a perfect primary mirror. The test is insensitive to alignment errors and uses no optics other than the hologram. Since the null corrector and CGH are fabricated independently, agreement between the two indicates a high probability that both are correct.

The hologram is simply a circular grating or zone plate. It is made of a circular ring pattern fabricated onto a flat glass substrate. The CGH is fabricated using electron beam lithography that has been developed for the production of integrated circuits. The spacing of the grooves is determined by the mirror surface that the hologram replaces. The groove depth and width are optimized to minimize fabrication costs, while giving the correct intensity of the diffracted light.

A layout of the CGH null test, shown in Fig. 6.1, depicts the null lens and CGH. No modifications are made to the null lens to perform this test. The null corrector tests the hologram exactly as if a real mirror was being measured.

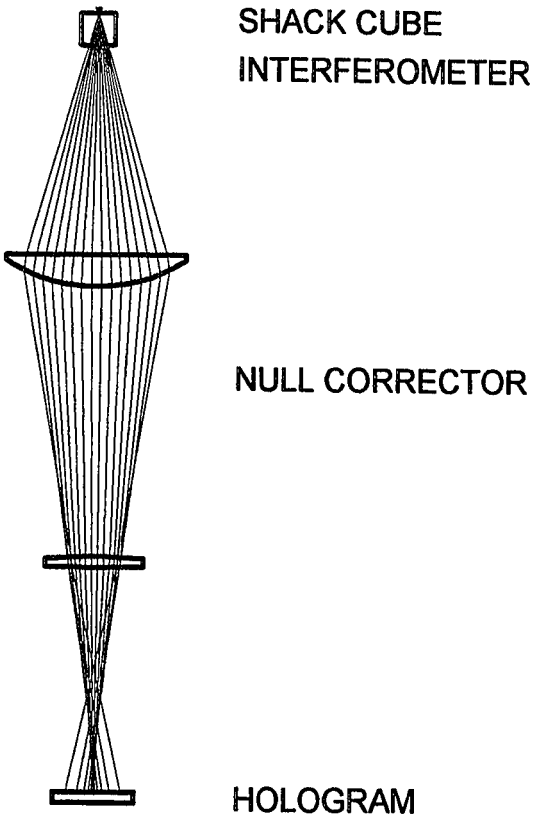

Figure 6.1. Layout of CGH test of null lens. The use of the CGH involves simply positioning the hologram at the correct location and making the measurement as if the mirror itself was being tested.

The use of the hologram to test the null corrector is surprisingly simple. The CGH is positioned in the light beam coming from the null corrector. Once the CGH is near the correct position, the fringe patterns in the interferometer are used to align the hologram. Since the CGH appears to the null corrector to be a complete primary mirror with the correct shape, the alignment of the hologram is exactly like that of the actual primary. When testing the primary mirror, the optician positions the null corrector in lateral translation, tip/tilt, and vertical translation to eliminate tilt, coma, and focus from the interferogram (See 5.4). The alignment for the hologram follows the same procedure.

The holograms are designed to give about 4% diffraction efficiency into the desired order. This gives a high contrast interference pattern that maximizes the signal-to-noise ratio of the measurement. A pinhole positioned near the Shack cube rejects the stray orders of diffraction and lets only the desired order through. The size of the pinhole is optimized so that the area corresponding to the entire tested region of the mirror is free from spurious orders.

6.3. OPTICAL TESTING WITH COMPUTER-GENERATED HOLOGRAMS

BACKGROUND ON CGH AND OPTICAL TESTING

Optical testing of aspheric surfaces using computer-generated holograms has been used for over twenty years. An excellent overview of CGH optical testing is given by Loomis (1980a). Some more recent work in the field is given in a thorough review by Creath and Wyant (1992).

A hologram is generally used to modulate the phase or amplitude of a wavefront, causing it to propagate such that it forms a desired phase front or intensity distribution. A photographically produced hologram may be used to store and play back an existing wavefront (Leith and Upatnieks 1962). Synthetic holograms may also be specified by a computer and written with an electronic plotter (Brown and Lohmann 1966).

Computer-generated holograms fall into three classes -- Fourier, Fresnel, and image holograms, depending on the propagation from the CGH (Bryngdahl and Wyrowski 1990). The far-field or Fourier hologram, widely used in signal processing, uses a modulating screen to create a desired pattern at the Fourier plane. The computation of the CGH pattern requires a Fourier transform of the desired field distribution. There are numerous applications and methods for making this type of CGH (Brown and Lowmann 1966, 1969; Lowmann and Paris 1967; Lee 1970; Lesem, Hirsch, and Jordan 1969; Chu,

Feinup, and Goodman 1973). The second type of CGH, the Fresnel hologram, is seldom used because it is computationally intensive to create and difficult to implement (Bryngdahl and Wyrowski 1990). The computation of the Fresnel CGH pattern requires a Fresnel transform of the desired light distribution.

The third type of CGH, the image hologram, is created by plotting a ruling similar to an interferogram (Wyant and Bennett 1972; Lee 1974). Because this CGH only creates a phase distribution, the computation is direct. The ruling pattern corresponds to the interferogram that would be created at the CGH plane if the incident beam were interfered with the desired beam. Diffraction from the CGH also creates several undesired wavefronts that must be filtered out. These multiple diffracted orders can be separated at the Fourier transform plane, where a correctly positioned aperture will pass only the desired wavefront. It is this type of CGH that is commonly used in optical testing, so the following discussion will be limited to this "interferogram-type" of CGH.

Pastor (1969) first suggested the testing of aspheres using a computer-generated hologram. He described testing with a binary CGH as a moiré effect. The first CGH testing was performed by MacGovern and Wyant (1971) using a Lohmann-type CGH (Lohmann and Paris 1967) to test an F/5 paraboloid. They pointed out that this type of hologram has apertures that lie along the fringe maxima of a conventional film hologram. Wyant and Bennett (1972) abandoned the established Lee (1970) and Lohmann encoding methods and used a vector plotter to trace the fringe positions. They give a detailed error analysis and results from testing wavefronts with aspheric departures of up to 65 waves. Wyant and O'Neill (1974) demonstrated the value of a CGH in combination with a null corrector for measuring more highly aspheric optics. CGH optical testing is now used routinely for measuring aspheric surfaces (Larionov *et al.* 1979; Smith 1981;

Arnold 1989). Commercial interferometers specifically designed to utilize CGH testing have been built (Emmel and Leung 1979; Arnold 1992).

The computer-generated hologram of the image- or interferogram-type may be thought of as locally acting like a simple diffraction grating. The light diffracted from this ruling splits into distinct orders given by the grating equation

$$OPD = d_o + d_m = m\lambda$$
$$\text{or} \tag{6.1}$$
$$s(\sin\theta_0 + \sin\theta_m) = m\lambda$$

where the geometry is shown in Fig. 6.2 and the terms are defined as

OPD = optical path difference for light through adjacent slits

d_0, d_m = incident and diffracted path length

θ_0, θ_m = incident and diffracted angle

m = order of diffraction

s = local ruling spacing.

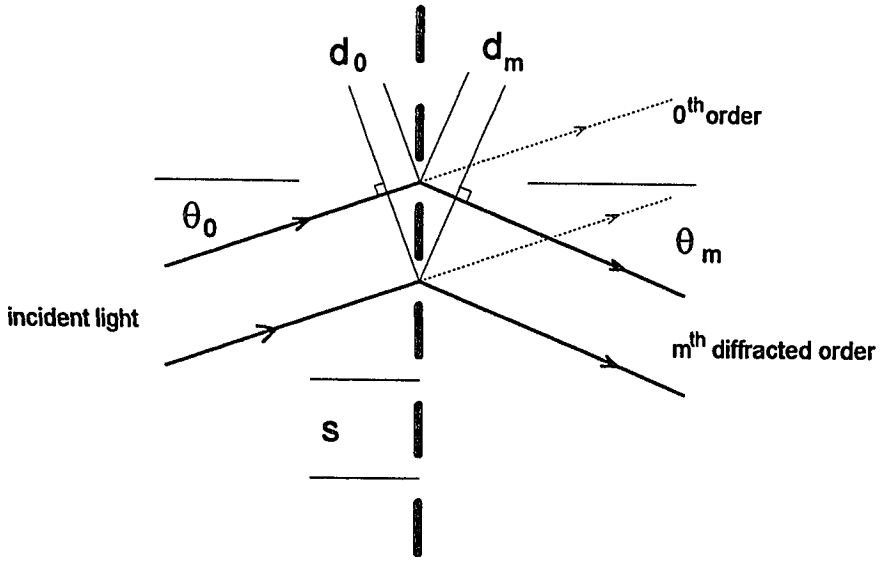

Figure 6.2. Cross-section of a transmissive diffraction ruling.

The CGH is a diffraction grating that uses a spatial variation in ruling frequency to create a desired change in wavefront. The CGH may be interpreted as causing a change in ray directions according to the grating equation (6.1), or equivalently as directly changing the wavefront phase. When used in m^{th} order, the CGH adds m waves of optical path to the wavefront for each ruling cycle.

Optical testing with a CGH is commonly performed using a configuration similar to that shown in Fig. 6.3 (Wyant and Bennett 1972; Arnold 1989). The spatial filter is required to block the unwanted orders of diffraction. The diverger lens need not be perfect, but only well known because the CGH can be designed to correct for the mirror-lens combination (Wyant and Bennett 1972).

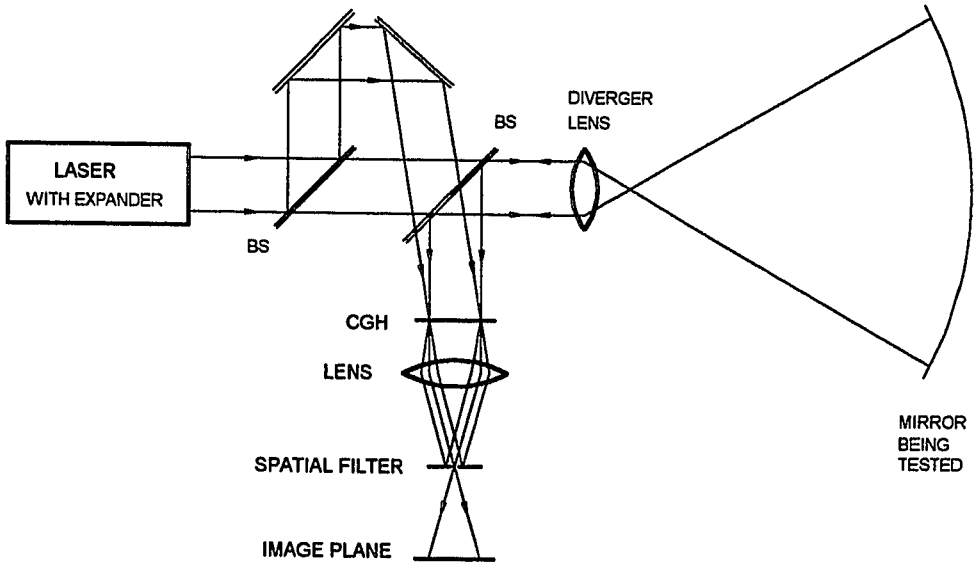

Figure 6.3. Modified Twyman-Green interferometer for testing an aspheric mirror with a CGH.

A large amount of tilt must be created by the CGH to cause the orders to fan out, enabling the isolation of a pure reference and pure test beam (Loomis 1980b). This wavefront tilt, which causes a carrier frequency in the ruling, must be three times larger

than the maximum slope of the aspheric wavefront to insure complete separation of orders (Yatagai and Saito 1978).

Since the CGH is nothing more than a pattern drawn on film, its errors take the form of spatial distortion in that pattern. The magnitude of the wavefront error due to the distortion is given by Fercher (1976) as the scalar product of the wavefront gradient and the vector distortion $E(x,y)$. This leads to

$$\Delta W(x,y) = -\nabla W_\lambda(x,y) \cdot E(x,y), \tag{6.2}$$

where ΔW = wavefront phase error due to distortion

W_λ = wavefront CGH is generating (in waves)

$E(x,y)$ = vector CGH position error (actual position - desired position)

(x,y) = position at CGH.

One fringe represents m waves OPD, so Eq. (6.2) may also be written

$$\Delta W(x,y) = -m\lambda \frac{\varepsilon_s(x,y)}{s(x,y)}, \tag{6.3}$$

where $\varepsilon_S(x,y)$ = CGH position error in direction perpendicular to fringes

$s(x,y)$ = local center-to-center fringe spacing.

Testing with a CGH may be thought of in terms of a moiré effect. The CGH is a binary representation of the expected fringe pattern formed by an aspheric test beam and a reference beam. When the live interference pattern is superimposed on the CGH, a moiré, or spatial frequency "beating" effect is observed. When properly filtered in the

frequency domain, these moiré fringes directly give the shape difference between the two wavefronts, thus the shape error in the asphere.

CGH FABRICATION

To make a CGH for optical testing, the desired wavefront $W_C(x,y)$ must be calculated. This may be done using ray-trace software (Sweatt 1977; Chen 1980), or in the case of the null lens test, it is analytically derived. Methods for encoding this into an interferogram-type CGH are described by Leung *et al.* (1980), Arnold (1988), and Logue (1988). To encode the CGH to be used at the m^{th} order, the n^{th} fringe is drawn as a half-fringe wide contour with its edges specified by the locus of points meeting the relation

$$W_C(x,y) = n \times m \times \lambda \pm \frac{\lambda}{4}. \tag{6.4}$$

This fringe contour must be approximated and digitized for the computer-controlled writer. The resolution element used for digitizing the pattern must be chosen small enough that it creates an acceptably small error in the wavefront (Chen and Osborne 1987).

The CGH may be fabricated using technology developed for making integrated circuit masks. A large-scale master may be plotted and photographically reduced (Lohmann and Paris 1967b; Lee and Casasent 1987). The accuracy of this method is limited by the distortion in photo reduction and errors in the plotter (Wyant and O'Neill 1974; Fercher 1976; Ono and Wyant 1984). The CGH may be optically written full-scale using specialized equipment (Biedermann and Holmgren 1977; Caulfield *et al.* 1981; Kajanto *et al.* 1989; Baber 1989). Currently, the most accurate method for

writing IC masks and CGH's is electron beam lithography (Leung, Lindquist, and Shepherd 1980; Leung, Arnold and Lindquist 1981; Arnold 1985; 1989).

Electron beam lithography uses a collimated electron beam to write the pattern onto a resist coated glass plate. The electron resist changes chemical properties when exposed to the electron beam enabling the resist to be dissolved in a developing chemical. The electron beam is raster scanned over small cells (~1 mm) that are stitched together by translating the workpiece using a computer-controlled stage. This method can write patterns with features as small as 0.5 μm to an accuracy of ±0.15 μm over areas as large as 150 mm square (Logue 1988). Since they are written full-scale, these masters may be used directly or they may be replicated using contact printing. The final holograms may use amplitude modulation, created by opaque fringes drawn on clear glass. Alternatively, they may use phase modulation, created by etched grooves in the glass.

CIRCULAR HOLOGRAMS

Circular holograms have been used in optical testing and are used for the CGH null lens test. Rather than using a tilt carrier to fan out the orders laterally, the rotational CGH disperses the orders axially. The use of circular holograms for optical testing was first demonstrated by Buynov *et al.* (1971). Ichioka and Lohmann (1972) discuss the use of a quadratic (focus) carrier to shift the longitudinal focus position of the unwanted orders. They used a small aperture at the focus of the desired order to restrict the interference of spurious orders to a small central area of the optic. They also show that the actual number of fringes plotted may be less for a circular hologram than for a linear hologram. Circular holograms with cone shaped carrier wavefronts were discussed by Bryngdahl and Lee (1974). In this case, the desired diffraction order was separated with

an annular mask. Further comparisons between circular and tilt carrier holograms are given by Mercier (1977), and Mercier and Lowenthal (1980).

There are several advantages of using rotational holograms for testing axisymmetric optics. By preserving the axial symmetry, the hologram design and analysis are reduced from two dimensions to one. The alignment of the centered system is straightforward using conventional techniques (Mercier and Lowenthal 1980). The symmetry also allows direct certification of the hologram by measuring ring diameters (Lukin and Mustafin 1979). For testing optics with annular apertures, the inability to test the central region is inconsequential (Aver'yanova *et al.* 1975). For testing a mirror with no central obscuration, the central region generally has very little asphericity and can be tested conventionally (Larionov *et al.* 1980).

The use of circular holograms is ideal for conditions when the desired order comes to a sharp, unaberrated focus. At this point, a small pinhole will allow the desired light cone through while blocking all other orders. Background light and spurious fringes may be further reduced by physically masking off the inner region of the light cone, corresponding to the center hole in the primary.

6.4. DESIGN AND FABRICATION OF CGH FOR NULL LENS TEST

The CGH ring pattern is computed assuming only on the shape of the primary mirror and not any specific null lens. The radial ring positions are chosen based on an exact analytical model of the rays normal to the primary mirror. Since the wavefront created by the CGH has a cusp at the center, the common method of designing the CGH by optimizing aspheric coefficients does not work well. For this design, a model is constructed using basic algebra and trigonometry that has been verified numerically. Fig. 6.4 below shows the geometry and the important dimensions. The derivation of the

CGH profile is given below for the general case, but the CGH for null lens testing is optimized for use at paraxial focus ($h = 0$).

DERIVATION OF CGH PHASE FUNCTION

The phase function of the CGH is derived and specified using an exact geometrical model. The parameters for this derivation are shown below in Fig. 6.4. This model is constructed by computing the absolute path length, along the direction of propagation, between the mirror and the hologram plane. The variation in path length across the mirror defines the wavefront that the hologram must create to appear as a perfect primary mirror.

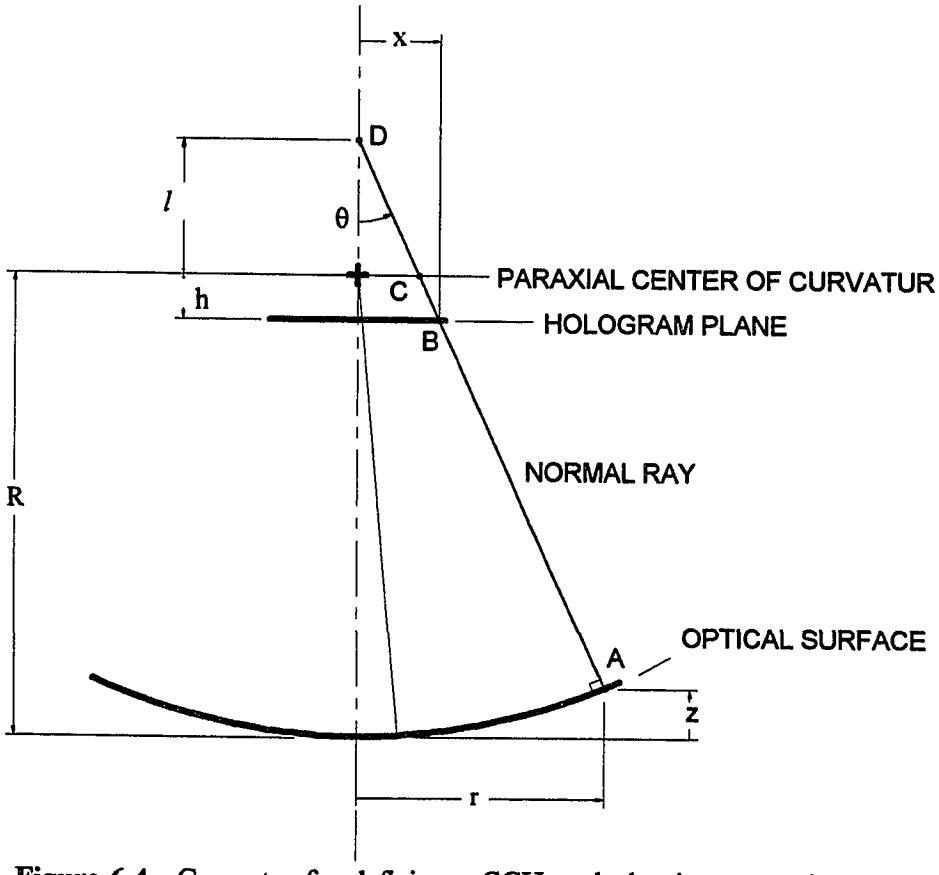

Figure 6.4. Geometry for defining a CGH such that it returns the same wavefront as a perfect primary mirror.

The variables shown in Fig. 6.4 are defined as

r = radial mirror position

R = vertex (paraxial) radius of curvature of mirror

K = conic constant of mirror

$z(r)$ = mirror surface profile

h = hologram distance from paraxial center of curvature

$x(r)$ = ray intercept position on hologram

$l(r)$ = distance from paraxial center of curvature to zonal center of curvature (longitudinal spherical aberration)

$\theta(r)$ = slope of normal ray

AD, BD = distance between points.

The shape of the optical surface is given by

$$z(r)=\frac{r^2}{R+\sqrt{R^2-(K+1)r^2}}. \tag{6.5}$$

It is easily shown (Buchroeder *et al.* 1972) for a conic of revolution,

$$l=-Kz\,. \tag{6.6}$$

Trigonometry and algebra provide the following useful relations:

$$\tan\theta=\frac{r}{R-(K+1)z} \tag{6.7}$$

$$x=(h-Kz)\tan\theta \tag{6.8}$$

$$AD=\sqrt{R^2-Kr^2} \tag{6.9}$$

$$\sin\theta = \frac{r}{AD} \tag{6.10}$$

$$DB = \frac{x}{\sin\theta} = AD\frac{x}{r}. \tag{6.11}$$

These equations lead to the optical path length (OPL) from the surface of the mirror to the hologram plane

$$OPL = AD - DB. \tag{6.12}$$

The OPL variation across the hologram is the wavefront function or optical path difference (OPD). Choosing the arbitrary reference point as the center, the OPD across the CGH is

$$OPD = OPL - (R - h) \tag{6.13}$$

The CGH is encoded by specifying a phase function for the diffraction to create. For use in the m^{th} order, this CGH will consist of one plotted fringe for every m waves in the phase function. The CGH's for testing the null correctors are used in reflection, so the phase functions must be twice the OPD given above. This gives ring positions for every $m \times \lambda/2$ of the OPD. The radial spacing s of these rings is easily calculated from the grating equation (6.1) as

$$s = \frac{m\lambda}{2\sin\theta}. \tag{6.14}$$

The shape of the OPD function (see Fig 6.5) looks conical with little slope change over most of the CGH. This fortunate shape allows the CGH to work with no

carrier at all. The radial slope in the wavefront itself is sufficient to act as a circular carrier with ring spacing nearly constant over most of the hologram (See Fig. 6.6).

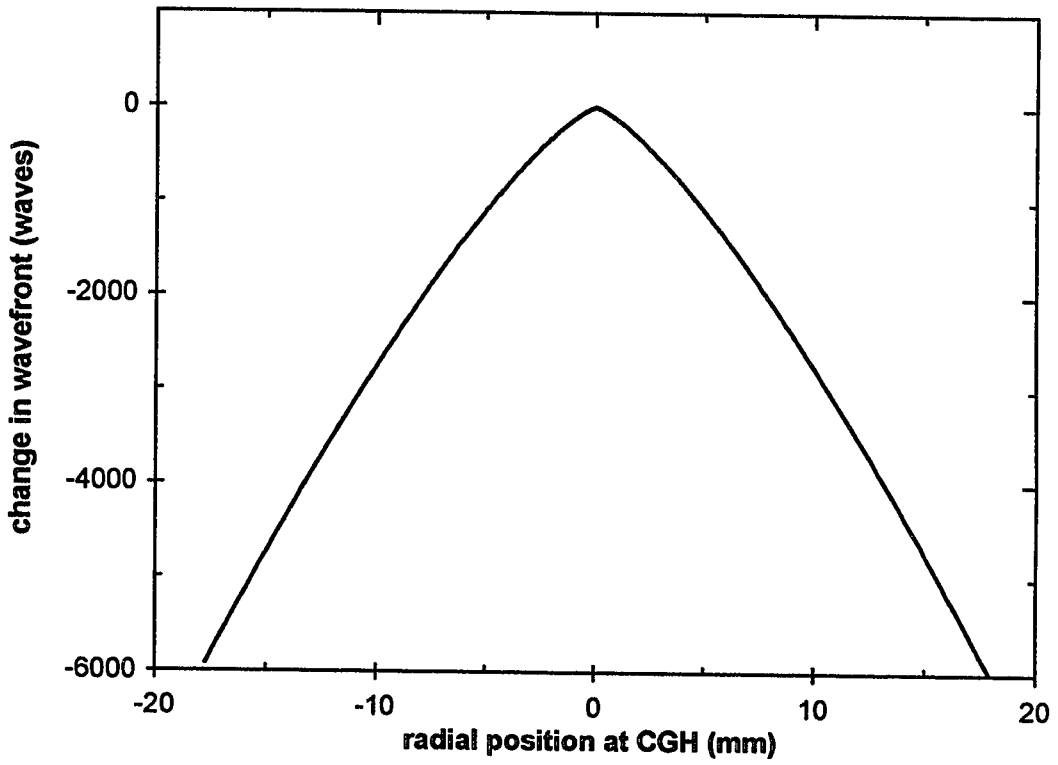

Figure 6.5. Wavefront phase function required of a paraxial-focus CGH to test a null corrector for a 3.5-m $f/1.75$ primary mirror.

The CGH function shown in Fig. 6.5 shows why the conventional method of specifying CGH functions as a power series with even terms fails to converge for designing this hologram. There is a cusp at the center that is poorly modeled using a power series with a reasonable number of terms.

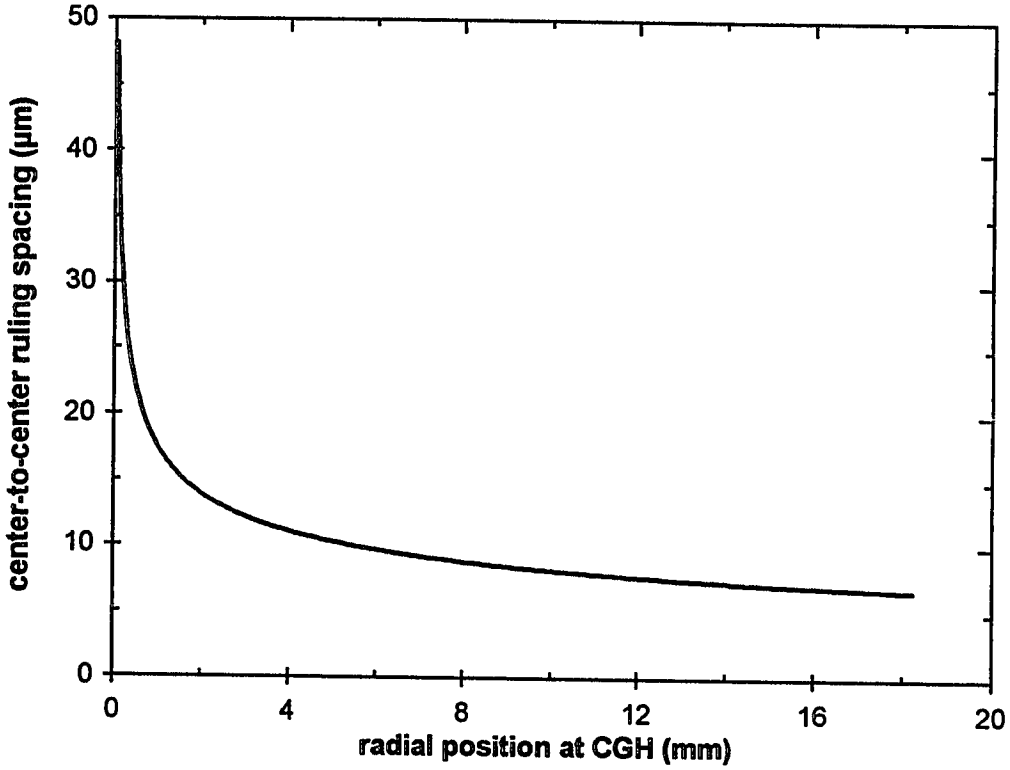

Figure 6.6. Center-to-center groove spacing for a paraxial-focus CGH used in third order to test a null corrector for a 3.5-m *f*/1.75 primary mirror.

The CGH is specified using a computer program to compute the above OPD given the appropriate values for *R*, *K*, and *h*. The software that digitizes the CGH into machine language calls a subroutine to return the phase function given *x*, the position at the CGH. The subroutine first calculates the corresponding position on the primary mirror *r* using Newton's method (Arfken 1985). Having found *r*, the computation of the OPD follows the equations above. Since the equations are exact and no integration is performed, the calculation errors in the floating point operations are negligible.

The common place to put a CGH is at the image of the optic under test to map the optic uniformly onto the hologram. The CGH test of null lenses uses the hologram at the farthest possible point from an image of the test object, at its focus. The resulting

nonlinear mapping causes no problem in the test of the null lens because the light diffracted from the CGH travels back through the null corrector and gets re-mapped to create an image identical to that of a primary mirror. However, the CGH is not focused onto the detector so it must be oversized to avoid edge diffraction.

For the CGH test of null correctors for primary mirrors, the ideal place to put the hologram is at paraxial focus, where $h = 0$. The value of h must never go negative because that would put the CGH in the caustic where the rays are crossing and the mapping from x to r is not single-valued. For positive h, the CGH must become larger with more rings, and thus it becomes more expensive.

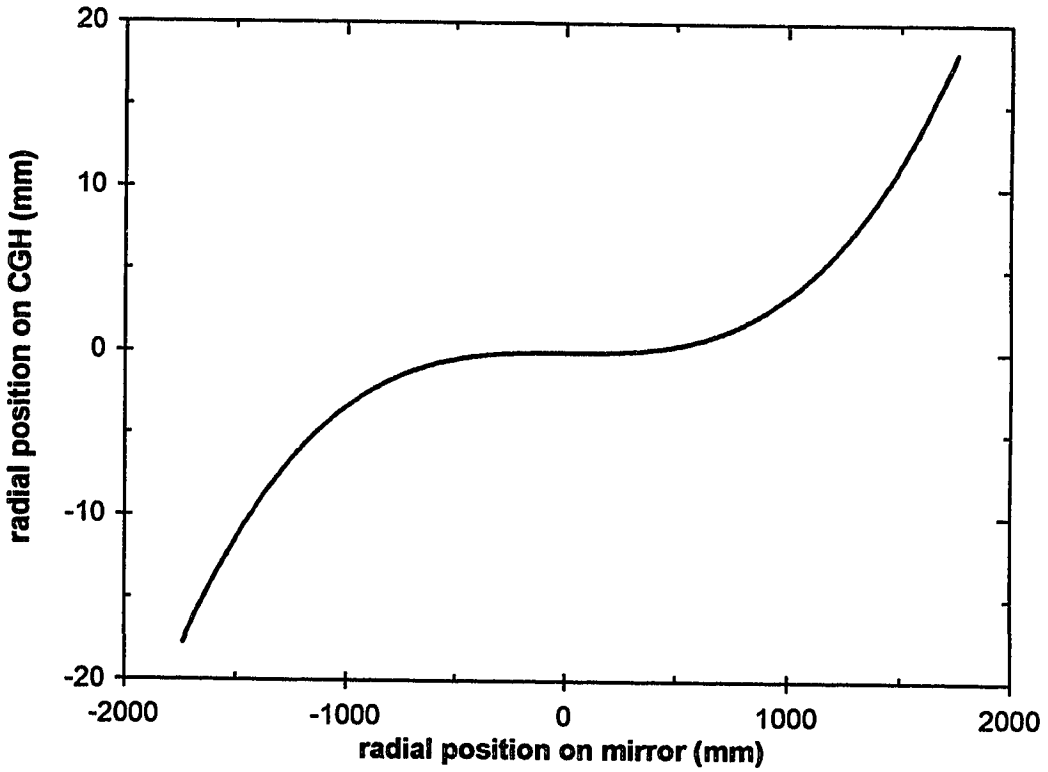

Figure 6.7. CGH mapping function showing the relationship between mirror position and position on hologram. This plot is for a CGH used in third order to test a null corrector for a 3.5-m $f/1.75$ primary mirror.

SERIES EXPANSION FOR ERROR ANALYSIS

For the error analysis, approximations were made by expanding the above equations into power series in r and truncating. The relationship between the radial position on the mirror r and the position on the CGH $x(r)$ is

$$\begin{aligned} x(r) = & \frac{h}{R} r \\ & + \frac{h + hK - KR}{2R^3} r^3 \\ & + \frac{3(1+K)(h + hK - KR)}{8R^5} r^5 + \ldots \end{aligned} \tag{6.15}$$

Likewise, the OPD is approximated by a similar series

$$\begin{aligned} OPD(r) = & \frac{-h}{2R^2} r^2 \\ & + \frac{-3h + K(-4h + 3R)}{8R^4} r^4 \\ & + \frac{-5h + K(-12h + 5R) + K^2(-8h + 7R)}{16R^6} r^6 + \ldots \end{aligned} \tag{6.16}$$

As an end-to-end check of the technique, it is useful to create a CGH of a sphere that can be accurately tested. This CGH can be specified and written in exactly the same manner as a null lens CGH, only $K = 0$ and h must take a positive value.

The truncated series representations used in the error analysis for both the CGH null lens test and the spherical CGH are given in Table 6.1. The relative error due the series truncations are only a few percent for mirrors slower than $f/1$. Since the error terms themselves are quite small, this error is negligible.

Table 6.1. Approximations to relevant functions for error analysis

CGH to test null lens	Reference CGH of sphere
$h = 0$ $K \cong -1$	$K = 0$
$x(r) \cong \frac{-Kr^3}{2R^2}$	$x(r) \cong \frac{hr}{R}\left(1+\frac{r^2}{2R^2}\right)$
$\sin\theta \cong \frac{r}{R}\left(1+\frac{Kr^2}{2R^2}\right)$	$\sin\theta = \frac{r}{R}$
$spacing \cong \frac{m\lambda R}{2r}\left(1-\frac{Kr^2}{2R^2}\right)$	$spacing = \frac{m\lambda R}{2r}$
$\tan\theta \cong \frac{r}{R}$	$\tan\theta \cong \frac{r}{R}\left(1+\frac{r^2}{2R^2}\right)$
$OPD \cong -\frac{3Kr^4}{8R^3}$	$OPD \cong -\frac{hr^2}{2R^2}\left(1+\frac{3r^2}{4R^2}\right)$

It is interesting that this OPD for the null corrector test has minus three times the aspheric deviation of the primary mirror,

$$Surface\ Asphere \cong \frac{Kr^4}{8R^3}.$$

The surface aspheric departure represents the surface deviation from a reference sphere centered at paraxial focus. The above OPD is the path difference for a real normal ray that intersects the CGH plane.

CGH FABRICATION

The fabrication of CGH's using electron beam lithography is now quite common (Arnold 1989; Urquhart *et al.* 1989). There are firms that specialize in the encoding and printing of CGH's. They have software that evaluates a phase function, usually specified in terms of polynomial coefficients, to create a data file that will drive the plotter. This involves approximating the continuous fringes as chains of trapezoids that the plotter can write (Arnold 1988). The error in making this approximation is negligible if small enough trapezoids are used.

The fabrication of the holograms for testing the null correctors at SOML uses electron beam lithography to write a master, which is then printed to the final substrate. This allows the usual practice of writing the master onto a thin, pre-coated glass slide, while the final CGH transferred to a thick, optically flat glass substrate. This method can severely limit the accuracy of the CGH if the printing is flawed. For this reason, it may be preferable to have the final CGH written directly by the e-beam writer.

The CGH is contact printed by holding the master in direct contact with the photoresist-coated blank and exposing with collimated light. The master can be certified as accurate to ± 0.15 μm, and the errors from well-controlled contact printing are less than ± 0.1 μm (Everett 1993). Since it is difficult to verify the final printing to sub-micron accuracy, an error in the printing could go undetected, leading to an inaccurate optical test.

By using the CGH in third order, the number of rings required to test a null lens is reduced and the smallest feature size is increased by a factor of three, making the part easier to fabricate. To get the desired diffraction efficiency from the third order, the CGH is made into a pure phase element by etching grooves and coating the entire surface with reflective aluminum.

The steps taken by the diffractive optics firm to produce the holograms for testing null correctors are the following:

1. Encode the phase function into machine language that will drive the e-beam writer.
2. Using electron beam lithography, write the grating pattern into electron resist on the master.
3. Process the exposed master to result in a chrome ring pattern. The exposed resist is dissolved leaving the pattern in resist. The unprotected chrome is then etched.
4. Contact print onto an optically flat substrate and process to result in a $\lambda/20$ flat with the chrome ring pattern on it. The final substrate is coated with chrome and photo resist. The master is held with its chrome pattern in close contact with the resist on the substrate. The pattern is exposed by flooding UV light through the master. The subsequent processing is identical to that in step 3.
5. Ion mill or acid etch to create $\lambda/4$ deep grooves. The chrome bands protect the glass under them.
6. Strip the chrome. This leaves only glass with concentric grooves etched into it.
7. Coat the glass with a thin layer of reflective aluminum.

Since no protective coating is applied, the aluminum will oxidize and is very susceptible to damage.

6.5. OPTIMIZATION OF DIFFRACTION EFFECTS

The holograms are designed to provide a 4% return into the Littrow order to match the intensity of the reference beam. In the Littrow configuration, the diffracted light rays exactly retrace their path. A spatial filter is positioned at the focus from the Shack cube to reject stray diffractive orders. The size of this pinhole is optimized to provide adequate stray order rejection while passing all of the desired order.

The efficiency of the diffraction ruling is modeled using Fourier optics (Gaskill 1978) based on scalar diffraction theory. Using this method, the far-field diffraction pattern is found by taking the modulus squared of the Fourier transform of the complex amplitude. The light incident onto the ruling is assumed to have uniform intensity and phase, so the complex amplitude is given by the grating function. A general square grating that modulates both phase and amplitude will produce light with a complex amplitude shown in Fig. 6.8.

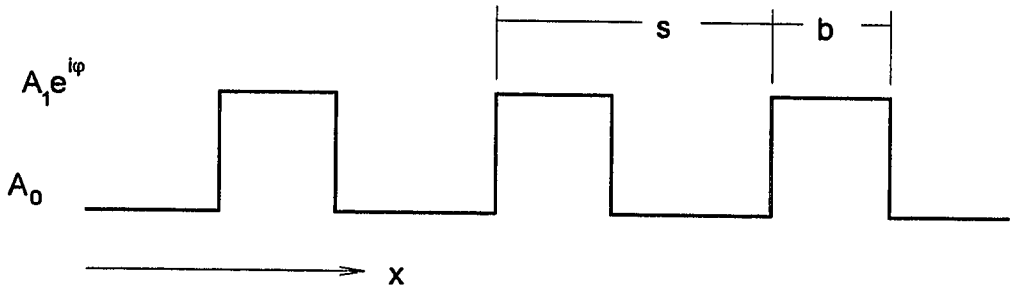

Figure 6.8. Complex amplitude of light modulated by diffraction grating.

The amplitude modulation is given by the square root of the intensity modulation. For example, reflective aluminum ($R = 0.9$) bands on bare glass ($R = 0.04$) would give A_0 of $\sqrt{0.04} = 0.2$, A_1 of $\sqrt{0.9} = 0.95$, and $\varphi = 0$.

Ignoring the finite extent of the ruling, the complex amplitude $u(x)$ is described mathematically, using Gaskill's notation, as

$$u(x) = A_0 + \left(A_1 e^{i\varphi} - A_0\right)\frac{1}{s}comb\left(\frac{x}{s}\right) * rect\left(\frac{x}{b}\right), \tag{6.17}$$

where, as illustrated in Fig. 6.8,

A_0, A_1 = amplitudes (square root of intensities) defined by the reflectance of the ruling

φ = phase shift in radians defined by groove etch depth of the diffraction ruling

b = width of a single line in the ruling

s = ruling period or center-to-center spacing.

For an etched ruling that is coated in aluminum and used in reflection, $A_0 = A_1 = \sqrt{0.9}$ and $\varphi = 2 \times 2\pi/\lambda \times depth$. The diffraction efficiency into the ±1, ±3, etc. orders is maximized for $\varphi = \pi$, or $\lambda/4$ etch depth.

The Fourier transform of the complex amplitude is

$$U(\xi) = A_0\delta(\xi) + \left(A_1 e^{i\varphi} - A_0\right)\frac{b}{s} s \times comb(s\xi) \times sinc(b\xi) \tag{6.18}$$

where ξ, the spatial frequency, is related to the angle of diffraction α by

$$\alpha = \lambda\xi. \tag{6.19}$$

The *comb* function gives non-zero values of U for discrete values of ξ, corresponding to the multiple orders of diffraction. These orders occur at integral multiples of 1/s,

$$\xi = \frac{m}{s}. \tag{6.20}$$

The relative power η in each order is computed by integrating the squared modulus of the function in Eq. (6.18) over ξ for each order defined by Eq. (6.20). Performing this integration and defining the duty cycle

$$D = \frac{b}{s}, \tag{6.21}$$

the diffraction efficiencies are found to be

$$\eta = A_0^2(1-D)^2 + A_1^2 D^2 + 2A_0 A_1 D(1-D)\cos\varphi \quad (m=0)$$
$$\eta = \left[A_0^2 + A_1^2 - 2A_0 A_1 \cos\varphi\right] D^2 sinc^2(mD) \qquad (m \neq 0) \tag{6.22}$$

Also, the ratio of the imaginary to the real part of the complex amplitude gives the dependence of the phase ψ on duty cycle and amplitude and phase modulation. These relationships, given in Eq. (6.23), are used in a later analysis of the hologram errors:

$$\tan\psi = \frac{A_1 D\sin\varphi}{A_0(1-D) + A_1 D\cos\varphi} \quad (m=0)$$
$$\tan\psi = \frac{A_1\sin\varphi}{-A_0 + A_1\cos\varphi} \qquad (m \neq 0) \tag{6.23}$$

For a reflection grating with D = 0.5, quarter-wave deep grooves, and an aluminum overcoat, the diffraction efficiency into several orders are given in Table 6.2.

Table 6.2. Diffraction efficiency for reflection CGH with Al coating, λ/4 grooves, and 50% duty cycle.

order ± *m*	diffraction efficiency η into order *m*
0	0.000
1	0.365
2	0.000
3	0.041
4	0.000
5	0.015
6	0.000
7	0.008

The expressions in Eq. (6.22) were used to analyze the sensitivity of the diffraction efficiency to fabrication errors. Figure 6.9 gives the variation in diffraction efficiency with duty cycle and Fig. 6.10 shows the effect of errors in the etch depth.

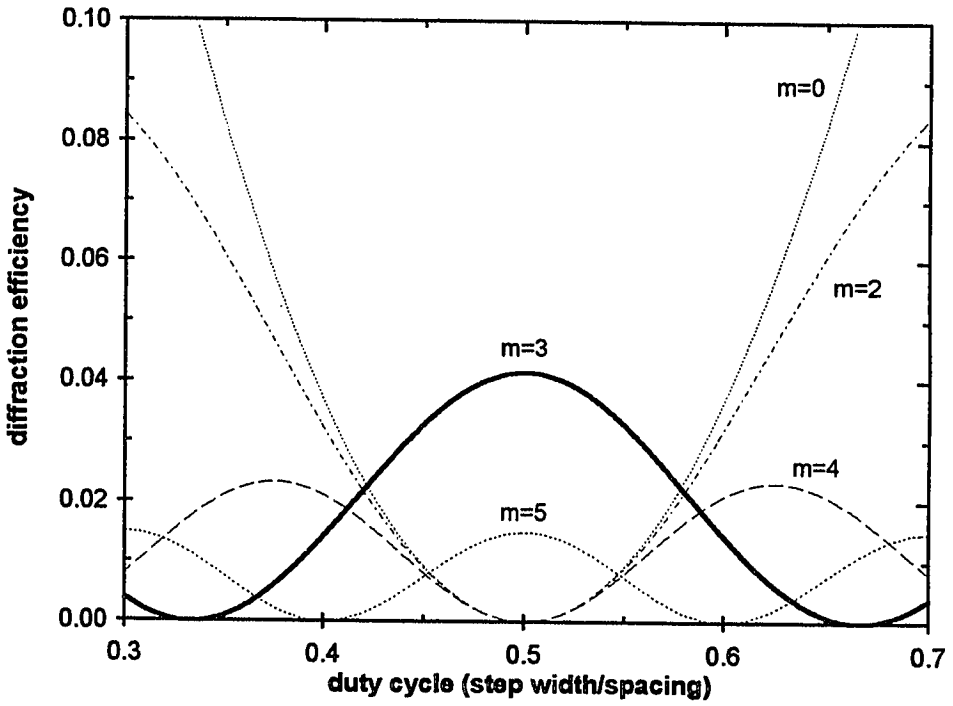

Figure 6.9. Variation in diffraction efficiency η as a function of duty cycle D for a binary phase reflective CGH with an aluminum coating and quarter wave etch depth. The first-order curve, peaking at 37%, is not shown.

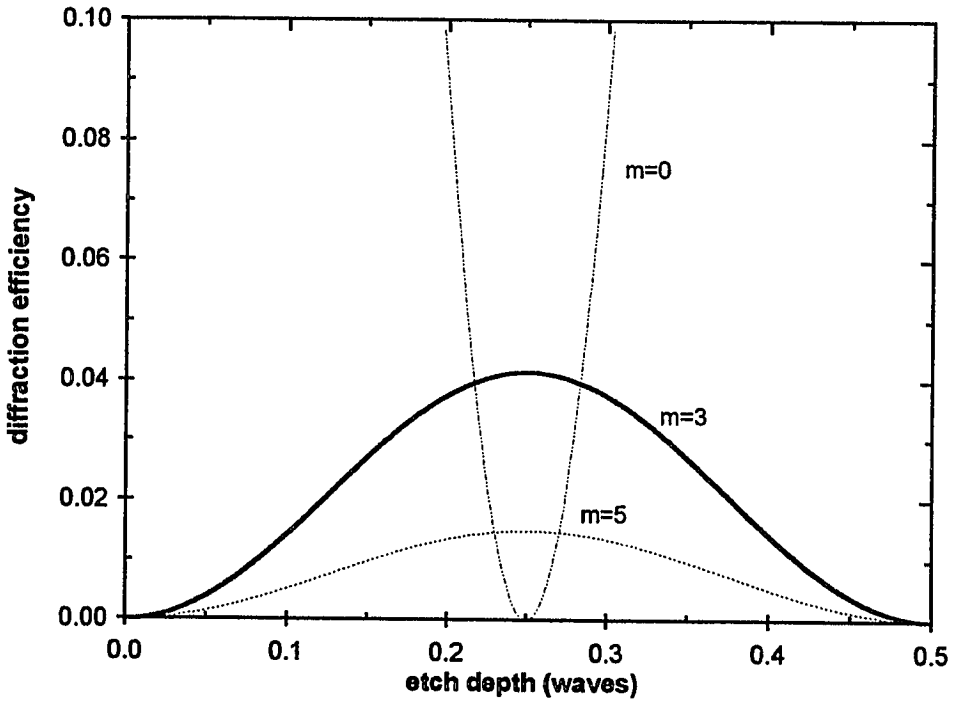

Figure 6.10. Variation in diffraction efficiency η as a function of etch depth for a binary phase reflective CGH with an aluminum coating and 50% duty cycle. All non-zero even orders have zero efficiency. The first-order curve, peaking at 37%, is not shown.

The size of the pinhole is optimized to reject the stray orders without limiting resolution. The pinhole is positioned at the center of curvature of the Shack cube where the light comes to a sharp focus. To find the relationship between pinhole size and order rejection, the null test was analyzed using lens design software. The zero-order diffraction from the CGH was simulated by placing a flat mirror at paraxial focus, where the CGH goes. The ray intercepts at the pinhole plane give the position of the zero-order ray. Since the angle of diffraction is proportional to the order number for small angles and the third-order diffraction is known to cross the axis at the pinhole, all other orders are easily calculated. This was done for several rays corresponding to different

radial positions on the mirror. The pinhole must be small enough that it blocks all but the desired order for the clear aperture tested.

Figure 6.11 shows how a stray order is blocked by the pinhole. The light from the desired order comes to a sharp focus at the pinhole. The unwanted orders are out of focus and aberrated so they do not make it through the aperture. Since an annular pupil is used, an out-of-focus stray order will cause an annular image at the aperture plane. As long as the pinhole is smaller than the inner diameter of this annulus, the light in this stray order will be completely blocked.

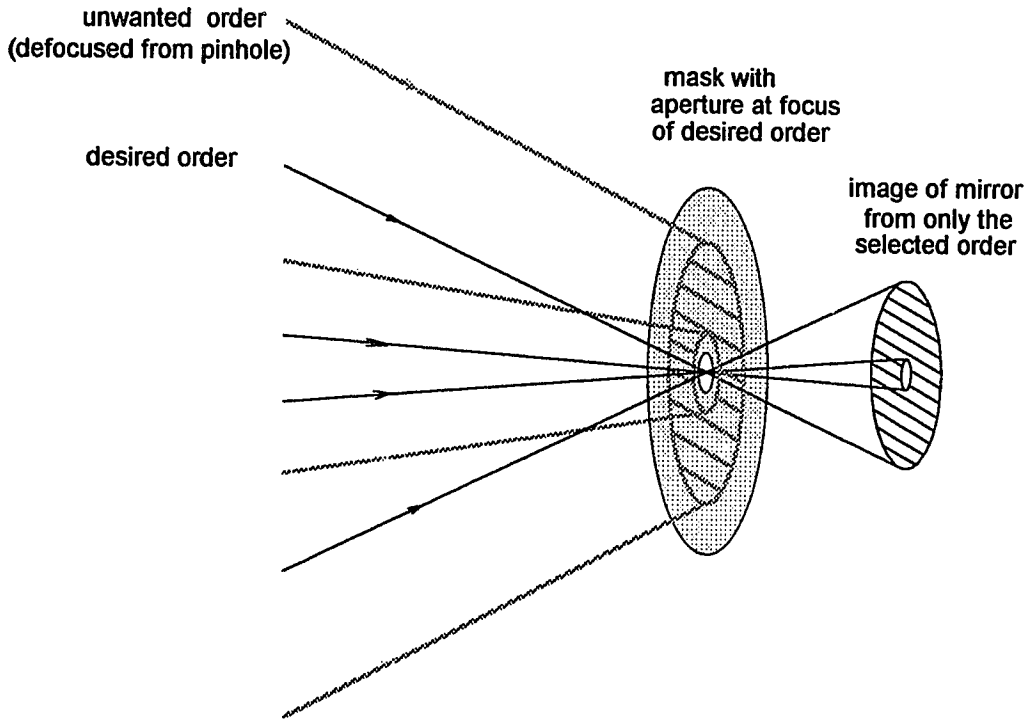

Figure 6.11. Rejection of stray diffraction orders. The order rejection relies on two principles. (1) The desired order comes to a sharp focus where all other orders are out of focus, and (2) An annular pupil is used. There is a central untested region that is blocked elsewhere.

The pinhole may not be made arbitrarily small however because it acts as a low-pass spatial filter with cutoff spatial frequency ξ_c derived using Fourier optics (Goodman 1968; Gaskill 1978) as

$$\xi_c = \frac{NA \times \phi_f}{\lambda D}, \tag{6.24}$$

where ξ_c = spatial frequency of cutoff (cycles per meter at mirror)

ϕ_f = pinhole diameter (μm)

λ = wavelength of light (μm)

D = diameter of primary (meters)

NA = final numerical aperture of converging light in which pinhole is used (equals the sine of the light cone half-angle).

For the null lens for the WIYN 3.5-m primary that uses a 0.332 *NA* beam, a 200-μm pinhole gives 30 cycle-per-meter resolution or 105 full cycles across the mirror diameter. This frequency optimally matches the Nyquist sampling rate determined by the digitization of 200 pixels across the mirror. This pinhole also completely rejects all but the desired orders of diffraction in the clear aperture.

Several high-order diffraction effects were examined and shown to be negligible. The CGH's are designed based on scalar diffraction theory, which is known to be approximate. Rigorous analysis has shown that the diffraction efficiency predicted by this approximation is accurate for rulings with spacings larger than several wavelengths (Moharam and Gaylord 1986; Kok and Gallagher 1988). The angle of the diffracted light predicted by the scalar theory is exact (Gemaux and Gallagher 1993). The phase retardation due to the angle of incidence and the complex index of refraction of aluminum was analyzed and shown to be negligible. The phase retardation between the s- and

the p- polarized light is 0.006λ for the extreme ray for a *f*/1.75 primary. The radial phase variation across the CGH due to the cosine effect in the grooves was also shown to be negligible. For quarter-wave deep grooves, this effect causes an error in W_{040} of only 0.000013λ for an *f*/1.75 primary.

6.6. ERROR ANALYSIS 1: ERRORS FROM FABRICATION OF CGH

The most obvious errors in the CGH null lens test come from the errors in the CGH itself. All of the possible error sources are evaluated and added to estimate the uncertainty in the CGH. The CGH errors can come from the substrate surface figure, e-beam writing errors, printing to the final substrate, or phase etching. They are separated as either figure or hologram errors depending on whether the phase error is caused by the surface reflection or diffraction. The figure errors affect the wavefront from all diffracted orders equally and the effects of the hologram distortion errors on the wavefronts are proportional to the order number. The hologram distortion does not affect the wavefront from the zero-order specular reflection. However, the variations in etch width and depth have a strong effect on the zero-order reflection, but a minimal effect on the other orders.

SURFACE FLATNESS

The figure error in the hologram surface adds a phase error to the diffracted wavefront that is twice the surface error of the CGH. The wavefront phase errors due to small-amplitude low-frequency figure errors are identical for all diffracted orders. In the absence of other errors, this fact would enable the direct measurement of the figure errors using a Fizeau interferometer with a flat reference. The measured figure errors could then be subtracted from the null lens measurement. However, variations in the etch

depth and duty cycle cause irregularities in the zero-order or specular wavefront that are much larger than those in the non-zero-order diffracted wavefronts. The flatness of the CGH substrate must be measured *before* the hologram is applied.

The flatness is measured using the real coordinates of the CGH, so a mapping transformation must be performed to give the resulting error in the null lens test. The nonlinear mapping between CGH and mirror coordinates is shown in Fig. 6.7 and described in Table 6.1. The equation for $x(r)$ in Table 6.1 may be used to transform the figure data from CGH to mirror coordinates. An additional transformation must be performed to correct for the imaging distortion in the null lens (See Sec. 4.6). This remapped surface figure may be subtracted from the data obtained when measuring the CGH with the null lens. An uncertainty in the hologram figure or in the mapping causes an uncertainty in the test of the null lens.

Since the null lens test is performed with the CGH rotated to many azimuthal orientations, non-axisymmetric errors in the CGH average out. The remaining rotationally symmetric surface errors may be expanded in a series and remapped using the relationship for $x(r)$ given in Table 6.1.

If the CGH figure error is written as a polynomial expansion

$$\Delta S = \sum_j a_j x^j$$

the wavefront error mapped into mirror coordinates is

$$\Delta W = 2\sum_j a_j \left(\frac{-KR}{2}\right)^j \left(\frac{r}{R}\right)^{3j}. \tag{6.25}$$

So power ($j = 2$) in the CGH surface ΔS gets mapped into sixth order spherical aberration wavefront error. In practice, the series approximation is not made because it is more accurate and no more difficult to perform the transformation directly to the data.

The error in the null lens test due to the CGH surface flatness is quite small. The substrates are specified flat to λ/20 at 546 nm and the majority of this error is likely to be astigmatism that is removed from the null lens measurement by rotating the hologram.

HOLOGRAM DISTORTION

The most severe errors in this test are the hologram errors consisting of distortion in the ruling pattern. The distortion may be caused by limitations in the e-beam writing or in the printing onto the final substrate. Distortion causes an error in a diffracted wavefront given by Eq. (6.3). For the null lens test, this error is approximated to be

$$\Delta W = \frac{2\varepsilon_x r}{R}, \tag{6.26}$$

where as before,

ΔW = wavefront error (twice surface error in measurement)

ε_x = radial CGH error (actual radial position of groove - desired position)

r = virtual radial position in mirror coordinates

R = radius of curvature of primary mirror.

The error due to distortion is independent of the order m and wavelength λ.

The effect of the CGH error for the null lens test is analyzed by making the approximations in Table 6.1. The most significant radial error in the CGH is the linear scale of the hologram which is the lowest-order distortion. A scale error C gives a shift in the pattern ε_x proportional to radial position

$$\varepsilon_x = Cx. \tag{6.27}$$

This causes the diffracted wavefront to have an error of

$$\Delta W = \frac{2r}{R} C\left(-\frac{Kr^3}{2R^2}\right) = -C\frac{Kr^4}{R^3} \tag{6.28}$$

which is simply spherical aberration W_{040}. The conic constant change in the primary mirror that would cause this W_{040} is

$$\begin{aligned} \Delta K &= \frac{4R^3}{r^4} \times W_{040}. \\ &= -4K \times C \end{aligned} \tag{6.29}$$

This result is interesting; it is only the linear component of the CGH distortion, which is a scale error, that causes an error in the measured conic constant. For a more general case, $\varepsilon_x(x)$ may be expanded into a series in x,

$$\varepsilon_x = \sum_j b_j x^j$$

and the resulting wavefront error is

$$\Delta W = 2\sum_j b_j \left(\frac{-KR}{2}\right)^j \left(\frac{r}{R}\right)^{3j+1}. \tag{6.30}$$

The first-order (magnification) term was shown above to introduce spherical aberration into the test. The zero order case is also interesting. If all of the rings are shifted radially an amount b_0, then the wavefront error would take a conical shape.

The magnitude of the hologram errors is estimated from knowledge of the encoding, writing, and printing process accuracy. The CGH encoding is performed with sufficient resolution to insure digitization errors less than the e-beam pixel size. The e-beam writers are verified to be accurate to ±0.15 μm P-V. The accuracy of the printing depends on the method used and the expertise of the technician. Contact printing has been

demonstrated to be accurate to ±0.1 μm (Everett 1993) although larger errors are expected without using careful control of the process.

The form of the hologram errors determines the type of wavefront errors induced. Most of the encoding and writing errors occur over small spatial scales causing high frequency errors that are filtered out (Kathman *et al.* 1988). Since azimuthal errors average out when rotating the CGH, the error budget must only include spherical aberration. The magnitude of the third-order spherical aberration (which has a fourth-order dependence or r) is estimated by assuming the distortion can cause pure W_{040}. This translates into a scale error given by the maximum shift ε_x divided by the radius of the CGH. The resulting wavefront error is given by Eq. (6.28).

The higher-order spherical aberration is assumed to be much smaller than the low-order error described above. The holograms are written and printed using equipment for making integrated circuits, so the higher-order writing and printing errors should have no tendency to be axisymmetric. An upper limit on the magnitude of the higher-order errors may be obtained assuming all of the grating error occurs where period is minimal. Combining Eqs.(6.3) and (6.14) with the expressions from Table 6.1 and taking the worst case, the maximum wavefront error $\Delta W_{\max}$ is given by

$$\Delta W_{\max} = \frac{2r_{\max}}{R}\left(1+\frac{Kr_{\max}^{\,2}}{2R^2}\right)\times \varepsilon_{\max}. \tag{6.31}$$

For the CGH null lens test for a 3.5-m f/1.75 primary mirror, a 0.2-μm maximum hologram error can cause a maximum wavefront error of 56 nm.

Unlike most binary optics, these holograms require poor diffraction efficiency, so they can be fabricated using a single step. Binary optics typically use several masks sequentially to increase the diffraction efficiency (Swanson and Veldkamp 1988; Cox *et al.*

1990). With the use of a single mask, the difficulty and uncertainty of the mask alignment are avoided.

ETCHING ERRORS

Variations in the depth of the etched grooves and the ruling duty cycle must also be considered as potential error sources. The dependence of the wavefront phase on these terms, given in Eq. (6.23), shows a strange result for the zero-order diffraction. For diffraction into the zero order from quarter-wave deep grooves, very small variations in duty cycle or groove depth cause large, even discontinuous phase variations. Both the real and imaginary parts of the field amplitude are very small -- zero for the ideal case -- so the ratio of these terms, thus the phase, is poorly defined. The discontinuity in phase for $\lambda/4$ depth and 50% duty cycle is meaningless because there is no energy in this order.

It is apparent from Fig. 6.12 that small fluctuations in duty cycle and etch depth can cause a large diffracted phase variation for the zero-order light. This precludes accurate measurement of the surface flatness using the zero order reflection. The substrate figure must be certified *before* the hologram is fabricated. The phase of the non-zero orders is unaffected by variations in duty cycle.

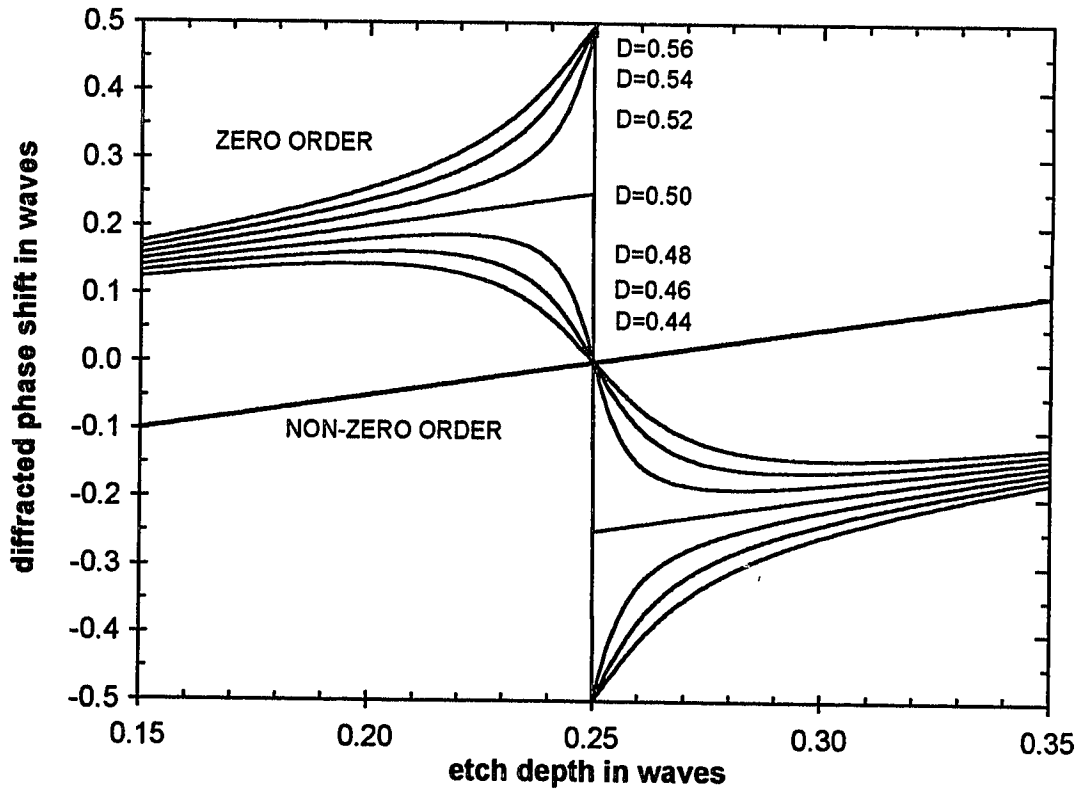

Figure 6.12. Dependence of diffracted phase variation on etch depth and duty cycle variations for a pure phase grating centered around the design values of D=0.5 and 0.25λ etch depth. The zero-order terms are shown as a set of curves with different duty cycles. The non-zero orders have no dependence on duty cycle.

For grooves nominally λ/4 deep, the wavefront variations are equal to the variations in etch depth. Groove depth variation of ±2% will give wavefront errors of ±λ/200.

6.7. ERROR ANALYSIS 2: ERRORS IN USE OF CGH

A CGH manufactured without figure or writing errors does not guarantee a perfect null lens test. The test of the null corrector will only give a null result for a flawless null lens and CGH that are designed for the same radius of curvature, conic constant, and wavelength of light. Also, a change in the temperature of the CGH will cause it to expand and induce spherical aberration. Since the CGH emulates a perfect primary mirror, the alignment does not significantly affect the test accuracy. Noise in the measurements due to vibration, seeing, random electronic noise, and digital round off errors are negligible in the average of many measurements.

The analysis of these effects is handled by treating the CGH as a plane surface that introduces a wavefront change of twice the single-pass OPD given in Table 6.1. This is a sensible thing to do because the ruling is known to introduce three waves of OPD per ring into the third order. Since the measurements are performed in terms of surface variations, this OPD is treated using an effective surface function S_{CGH} which is exactly half of the wavefront change. This surface function is equal to the single-pass OPD given in Table 6.1,

$$S_{CGH} = -\frac{3Kr^4}{8R^3} \tag{6.32}$$

where r is the virtual position at the mirror.

The null lens is designed to measure a mirror with a given radius R and conic constant K, but it will yield a null test for a family of surfaces. The actual shape of the surface depends on the distance to the primary being tested. The CGH test measures only the null corrector, so the measured errors must assume an R and K of the primary mirror. Ideally, the CGH is fabricated for exactly the R and K of the primary. If it is not, corrections to the data must be made for the known differences.

CONIC CONSTANT ERROR

There is a direct relationship between an error in the conic constant and spherical aberration in the null lens. Zernike polynomials are commonly used in interferometric measurement and analysis programs, so the spherical aberration in the surface will be represented by Z_8, the coefficient on Zernike polynomial #8. This polynomial equals $6\rho^4 - 6\rho^2 + 1$ where ρ is the normalized radial position. The equation for the surface asphere is differentiated, resulting in

$$\begin{aligned} Z_8 &= \frac{1}{6}\frac{Kr^4}{8R^3} \\ dZ_8 &= \frac{r^4}{48R^3}dK \\ dK &= \frac{48R^3}{r^4}dZ_8 \end{aligned} \tag{6.33}$$

where Z_8 = coefficient on Zernike polynomial #8 for surface asphere

dZ_8 = coefficient on Zernike polynomial #8 when measuring surface with null lens.

For a 3.5-m primary mirror with R = 12250 mm tested using a HeNe laser, $dK = 9.408dZ_8$ (with Z_8 in mm). If the mirror measurement shows dZ_8 = 32 nm, the deviation of the conic constant is +0.0003 from the desired value.

When analyzing data from a CGH null lens test, this relationship must be treated carefully to correctly determine the sign of dK. The spherical aberration measured with a CGH is the error in the null lens. If no spherical aberration is present in a measurement of a primary mirror using the null corrector, the mirror must have a figure error of *the*

opposite sign that cancels out that of the null lens. So for the measurement of a CGH with $\Delta K = K_{primary} - K_{CGH}$, the spherical aberration expected is given by Eq. (6.33)

$$\Delta Z_8 = -\frac{r^4}{48R^3} dK . \tag{6.34}$$

RADIUS OF CURVATURE ERROR

If the CGH and the null lens are designed for different values of R, the primary radius of curvature, the CGH null lens test will show spherical aberration. The relationship between the spherical aberration and R cannot be found directly from Eq. (6.32) since r is actually a function of R.. However, the ratio of r/R is equal to the sine of a ray angle coming from the null lens, so this ratio must not depend on R (since the null lens is determined independently of R). Substituting this into Eq.(6.32) and differentiating gives

$$\begin{aligned} S_{CGH} &= -\frac{3K\sin^4\theta}{8}R \\ \frac{dR}{R} &= -\frac{dK}{K} \end{aligned} . \tag{6.35}$$

So a CGH with $dR = 0.0001R$ will cause spherical aberration that has the same effect as a conic constant change of +0.0001 for a parabola. Using the above relationships between ΔK and ΔZ_8, the expected spherical aberration ΔZ_8 due to a small radius change in the null lens is

$$\Delta Z_8 = -\frac{Kr^4}{48R^4}\Delta R, \tag{6.36}$$

where ΔR is defined as $R - R_{CGH}$.

ERROR IN LASER WAVELENGTH

Since diffraction is a strongly wavelength dependent effect, a change in the laser wavelength would cause an error in the measurement. The wavelength of the laser light is dependent on the frequency of the transition for stimulated emission and the refractive index of the air. Using an unstabilized, single-mode gas laser, the frequency can take any value within the Doppler-broadened width of the gain curve. The refractive index of the air is easily calculated based on the temperature and pressure.

The function S_{CGH} is the effective surface corresponding to three waves per cycle at the design wavelength. So S_{CGH} in units of length is really a phase function times the wavelength of the light used. A change in the wavelength must cause a proportional change in S_{CGH},

$$\Delta S_{CGH} = S_{CGH}\frac{\Delta\lambda}{\lambda} = -\frac{3Kr^4}{8R^3}\frac{\Delta\lambda}{\lambda}. \tag{6.37}$$

This leads to

$$\Delta K = 3K\frac{\Delta\lambda}{\lambda} \tag{6.38}$$

and

$$\Delta Z_8 = -\frac{Kr^4}{16R^3}\frac{\Delta\lambda}{\lambda}. \tag{6.39}$$

A +2°C temperature change, causing a refractive index change of -2×10^{-6} (Edlén 1966), causes $\Delta\lambda/\lambda$ of $+2\times10^{-6}$. For testing a null lens for a 3.5-m $f/1.75$ paraboloidal primary mirror, this change in wavelength will cause spherical aberration with ΔZ_8 = +0.633 nm.

ALIGNMENT OF CGH TO NULL LENS

The procedure for aligning the CGH to the null lens is identical to the alignment for the null test of primary mirrors. The lateral translation, axial translation, and tilt of the null lens are adjusted to eliminate tilt, focus, and coma from the interferogram. This is easily done to about an eighth of a fringe and the rest is subtracted in software.

The relationships between the CGH position and the wavefront returned were derived using the functions in Table 6.1 for the null lens test. Since the alignment is performed accurately by nulling the fringes, a first-order analysis is adequate.

Tilt of the CGH about its center by an angle α causes a surface variation $\Delta S = \alpha x$. This is mapped into coma, amounting to

$$\Delta S = \frac{-Kr^3 \cos\theta}{2R^2}\alpha, \tag{6.40}$$

where θ gives the azimuthal angle from the direction of the tilt.

This tilt also causes a shift in the mapping between the CGH and the mirror, but this is a higher order effect that has only 2% of the magnitude given in Eq. (6.40) for an $f/1.75$ primary.

The effect of a lateral shift of the CGH by Δx is analyzed by taking the derivative

$$\Delta S = \frac{dS_{CGH}}{dx}\Delta x. \tag{6.41}$$

This results in wavefront tilt corresponding to

$$\Delta S = \frac{-r\cos\theta}{R}\Delta x. \tag{6.42}$$

Axial motion Δz of the CGH causes two changes: a change in the optical path length (ΔOPL) and a change in the ray mapping onto the CGH. The path length change is computed geometrically and the effect of the remapping is calculated by differentiation of the CGH phase function. These two elements are given as

$$\begin{aligned} \Delta OPL &= -\frac{r^2}{2R^2}\Delta z \\ \frac{dS}{dx}dx &= -\frac{r^2}{R^2}\Delta z. \end{aligned} \tag{6.43}$$

The combination gives

$$\begin{aligned} \Delta S &= \frac{dS}{dx}dx - \Delta OPL \\ &= -\frac{r^2}{2R^2}\Delta z. \end{aligned} \tag{6.44}$$

The amounts of tilt, focus, and coma that are caused by misalignment of the null lens are identical for testing either the CGH or the primary mirror.

RANDOM MEASUREMENT ERRORS

The individual measurements of the CGH have small errors due to environmental effects, electronic noise and digital sampling. These errors become negligible in the average of many measurements since the errors are small in amplitude and uncorrelated. The environmental effects, caused by air motion in the optical path and vibration, are much smaller for the CGH test than they are for the test of the primary mirror since the path length is so much shorter for the CGH test. For a null lens measurement consisting of 15 azimuthal rotations, 5 maps per angle, and 0.02λ rms random errors, the random component of error in the average is less than 1.5 nm rms, which is negligible.

6.8. ERROR ANALYSIS 3: ERRORS IN DATA REDUCTION

The last remaining type of error is due to possible errors in the interpretation of the data. This type of error is minimized for the null test -- a null result is absolute and requires no interpretation. The actual errors in the null lens and the CGH result in a non-zero figure measurement that must be evaluated. Also, known errors in the CGH that are subtracted from the data cause an uncertainty in the final map from uncertainties in the CGH errors and the mapping between these errors and the measured data.

The errors in the CGH are calculated in the coordinates at the real mirror. To subtract these from the data, the errors must be transformed into the data coordinates. This transformation requires knowing the imaging distortion of the null corrector and the exact relationship between the edge of the data and the edge of the mirror.

The imaging distortion of the null lens is measured to about ±0.5% and the edge is determined to within ±1 pixel. A computer program was written to re-map the CGH errors according to the imaging distortion and then fit Zernike polynomial coefficients using least squares. The fitting error was directly assessed by simulating errors in the mapping function. For a null lens with -6.7% ± 0.5% distortion, ΔZ_8, gets mapped into

$$\begin{aligned} \Delta Z_8' &= (0.989 \pm 0.002)\Delta Z_8 \\ \Delta Z_{15}' &= (0.092 \pm 0.008)\Delta Z_8 \end{aligned} \tag{6.45}$$

where ΔZ_8 = coefficient of Zernike #8 in mirror coordinates from CGH errors

$\Delta Z_8'$ = coefficient of Zernike #8 in data coordinates from CGH errors

$\Delta Z_{15}'$ = coefficient of Zernike #15 in data coordinates from CGH errors

(Z_{15} is fifth-order spherical aberration: $20\rho^6 - 30\rho^4 + 12\rho^2 - 1$).

The position of the edge of the image is uncertain by 1 pixel, causing an additional uncertainty in the ΔZ_8 term. For a data map with 200 pixels across the mirror, the

relative uncertainty *dr/r* is 1%. This causes an uncertainty in $\Delta Z_8'$ of 4% and an uncertainty in $\Delta Z_{15}'$ of 6%. The uncertainty in mapping the CGH error is independent of the uncertainty in the CGH error itself.

6.9. CONCLUSION

A null lens test using a computer-generated hologram is presented including a background on CGH testing, a detailed description of the CGH null test design and optimization, and a thorough error analysis. This new test works by using the null corrector to test a small circular hologram or zone plate placed at the paraxial focus of the null lens. The zone plate diffracts light back into the null corrector that precisely matches the light that would be reflected by a perfect primary mirror many meters away. An error measured when testing the hologram must be due to the null lens.

The CGH null lens test is used to certify a critical and precise instrument, so a thorough error analysis has been performed. The test has three types of error sources: errors in the CGH, errors in the implementation of the test, and errors in the interpretation of the results. An effort has been made to understand and minimize all three types of errors.

CHAPTER 7

HOLOGRAPHIC MEASUREMENT OF NULL CORRECTORS: MEASUREMENT RESULTS AND ANALYSIS

7.1. INTRODUCTION

Three null correctors for 3.5-m primary mirrors were measured at the Steward Observatory Mirror Lab using the holographic test. This test, described in detail in Chap. 6, uses a computer-generated hologram (CGH) to synthesize a primary mirror with the desired shape. The test of a null lens is performed by measuring the CGH through the null corrector. Apparent surface errors in this measurement can be attributed to the null lens. This chapter presents results that confirm the ease and accuracy of the test. Unfortunately, the results also show a weakness in the CGH fabrication process that can result in holograms with gross errors.

The CGH null lens test was first carried out for the verification of null correctors for two 3.5-m $f/1.75$ primary mirrors. The results of these tests, given in Sec. 7.2, were excellent. The null correctors were measured to have errors of 72 ppm and 19 ppm in the conic constant with a measurement uncertainty of ± 78 ppm. In addition, wavefront errors in the null lenses of less than $\lambda/40$ rms were measured and used to correct the measurements of the primary mirrors. The CGH tests verified the uniform, high contrast fringe modulation from the holograms and the ability to align the test using identical

methods as for testing the primary mirrors. The tests also showed high-frequency phase errors due to the encoding, digitization, and small-scale e-beam writing errors.

The two successful null lens tests demonstrated the ability to perform a near-null test on null correctors. A separate test, described in Sec. 7.3, was performed to demonstrate the ability of this test to accurately quantify the error in a null lens. One of the null correctors for the 3.5-m mirrors was purposely misaligned by a known amount and measured with a CGH. The expected error matched the measured error to within the expected uncertainty.

For further verification, holograms that synthesize spherical mirrors were fabricated and measured. These tests, described in Sec. 7.4, were intended to build confidence in the accuracy of the fabrication process. Holograms of spheres were used because they may be accurately tested using a phase shifting Fizeau interferometer. The first of seven reference holograms had a gross manufacturing error that caused a phase step in the diffracted wavefront. The six subsequent holograms did not have this error, but had small errors consistent with the error analysis. On the basis of the results from these holograms, and subsequent holograms with similar errors, it was concluded that the gross manufacturing error causes phase steps that are easily separated from errors in the null corrector. Therefore, it is unlikely that such an error affects the accuracy of the null lens tests that do not exhibit steps in the phase.

Fabrication errors similar to those of the first spherical reference hologram occurred for three holograms fabricated to test a third 3.5-m primary mirror. This test and the CGH problems are given in Sec. 7.5. Since most of the area on each hologram was not affected by these errors and three separate holograms with different errors were used, an estimate of the null lens accuracy could be made. The results of testing with all

three holograms were used to estimate that the conic constant of the null corrector was correct to ±250 ppm.

The problems with CGH fabrication and the difficulties in making larger holograms for the 6.5-m and 8.4-m telescope primary mirrors require continued research. The plans for this work, given in Sec. 7.6, include a method of eliminating a suspected step from the hologram fabrication process. Also in this section, the design and analysis of a CGH for testing the null corrector for a 6.5-m *f*/1.25 primary mirror are given. This test is expected to measure the conic constant of the null corrector to an accuracy of ±40 ppm.

7.2. CGH NULL LENS TESTS FOR TWO 3.5-m *f*/1.75 PRIMARY MIRRORS

The null correctors for the ARC and WIYN 3.5-m *f*/1.75 primary mirrors were successfully tested using computer-generated holograms. Both of these tests confirmed the null corrector conic constants to within the test uncertainty of ±0.000078. The wavefront errors for the ARC and WIYN null lenses were measured to be 0.022 λ rms and 0.016 λ rms, respectively (at 632.8 nm). The surface measurements of the primary mirrors were corrected by subtracting these measured null lens errors from the data. The results of the null corrector measurements are shown in Table 7.1.

Since the ARC and WIYN telescope designs are quite different, the primary mirrors have different conic constants. Both 3.5-m primary mirrors had nominal focal ratios of *f*/1.75, but the ARC primary required a conic constant K of -1.0194 and radius of curvature R of 12280 mm and the WIYN required K = -1.0708 and R = 12250 mm. A null corrector was fabricated for testing the ARC primary mirror. After the completion of the ARC project, the null lens was altered to test the WIYN primary. The same lenses were used in both systems, but the spacings were changed.

Table 7.1. Summary of null lens measurements for 3.5-m $f/1.75$ primary mirrors.

	ARC null lens	WIYN null lens
Conic constant of null lens measured with CGH	-1.01927 ± 0.00008	-1.07077 ± 0.00008
Expected conic constant from null lens	-1.01933 ± 0.00008	-1.07079 ± 0.00008
Wavefront measured with CGH	0.022λ rms	0.016λ rms
Expected wavefront from tolerance analysis	0.046λ rms	0.046λ rms

TEST DESCRIPTION

The null correctors were tested using computer-generated holograms as described in Sec. 6.2. The holograms were fabricated using electron beam lithography. The actual holograms were contact printed from the e-beam written masters. The holograms were ion-etched and coated with aluminum to give an ideal 4% diffraction efficiency into the third order. A complete description of the process for making the holograms is given in Sec. 6.4.

Each null corrector was tested by placing the appropriate hologram at the paraxial focus of the light from the null lens. This was easily accomplished since the paraxial focus occurs at the end of the caustic where the light forms a bright spot. The CGH was translated laterally until this spot was centered on the hologram, and it was moved vertically to minimize the size of the spot. These coarse adjustments were used to get the CGH aligned closely enough that the fringe pattern was visible. The CGH was then

translated laterally, axially, and gimbaled about horizontal axes to null the fringes of tilt, focus, and coma.

The holograms were measured using phase shifting interferometry using exactly the same procedures as the primary mirror measurements. The interference patterns had uniform, high contrast. An interferogram from the test of the ARC null lens is given in Fig. 7.1. The spurious orders of diffraction were adequately blocked by a 200-μm pinhole. A bright spot from the -1 diffracted order is visible inside of the central hole in Fig 7.1. The imaging systems were unaltered between the primary mirror testing and the CGH testing to allow direct comparison between the measurements. Because the imaging optics were designed to form an image of the primary mirror onto the detector array and the CGH was located near the center of curvature of the mirror, the hologram could not be focused onto the CCD. This fact requires the hologram to be oversized to keep edge diffraction from affecting the measurement.

The azimuthal errors in the hologram were removed from the null lens measurements by averaging many data maps taken with the CGH at different rotational positions. When an average of 15 maps is taken with the CGH at equally spaced rotational positions, the non-axisymmetric errors in the CGH with terms through $\cos(14\theta)$ order average out while the errors in the null lens remain. It was easy to make many measurements with the CGH because the short path length reduces vibration and seeing, allowing rapid collection of data with minimal noise.

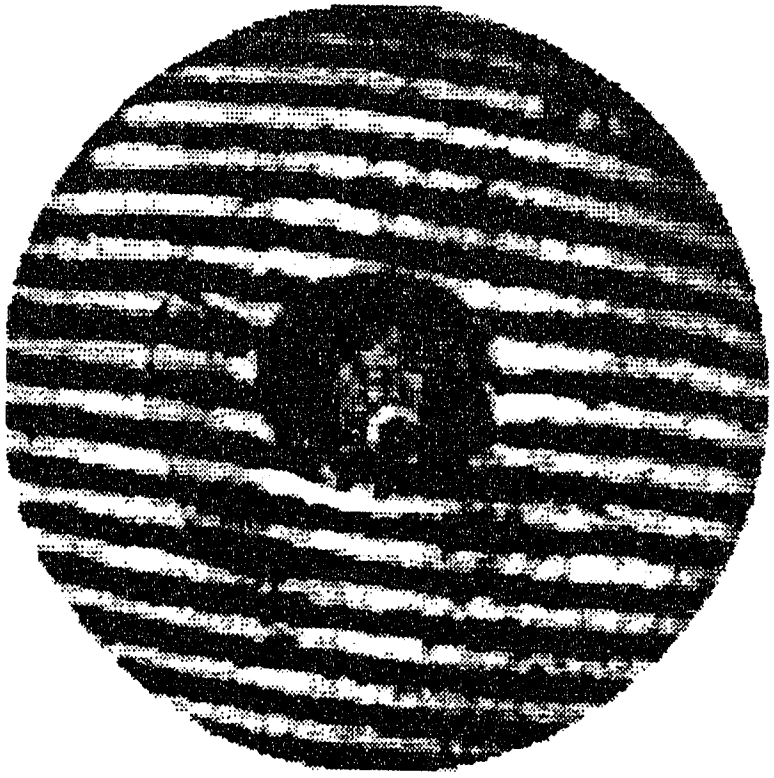

Figure 7.1. Interferogram of computer-generated hologram through the ARC null lens. This single interferogram shows speckle, non-uniform illumination, and air motion that do not affect the phase measurement when a sufficient number of maps are taken in the average. The residual coma in the interferogram is due to hologram misalignment.

HIGH-FREQUENCY HOLOGRAM ERRORS

The encoding, digitizing, and writing of the holograms cause significant high-frequency errors in the diffracted wavefront. The hologram rings were encoded as chains of polygons that approximate the desired circles. Over many rings this approximation is excellent. However, the presence of the polygon vertices and high-frequency errors in the e-beam writing cause relatively large wavefront errors over short distances.

A phase map of a single holographic measurement of the ARC null lens is shown in Fig. 7.2. High-frequency features, as well as some low-frequency variation, are apparent in this figure. The cross pattern is an artifact of the symmetry used in encoding the pattern.

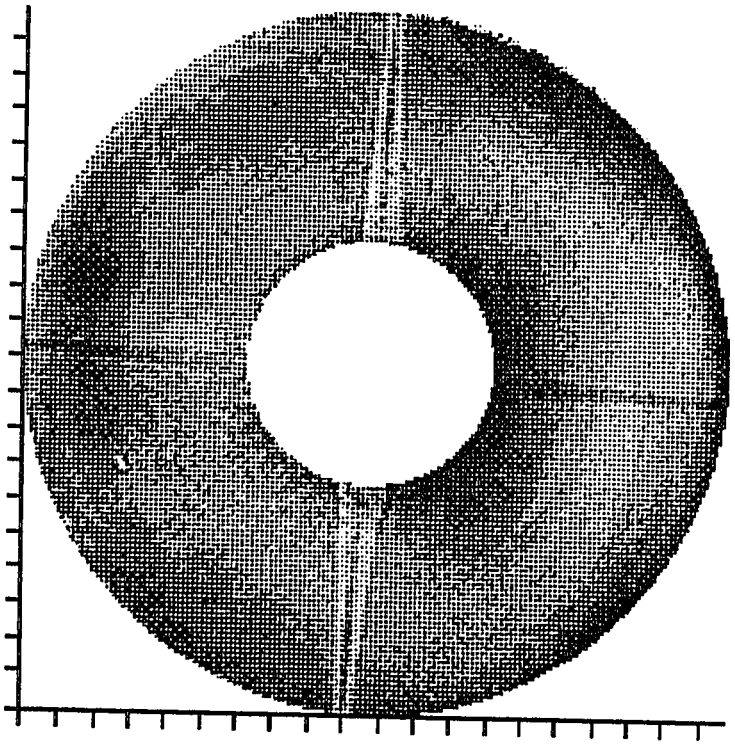

Figure 7.2. Contour map of a single CGH measurement showing high-frequency hologram errors. This map shows the surface errors (half of the wavefront errors) when testing the ARC null lens with a CGH. The contours are at 10 nm intervals showing variations from -40 to 40 nm. The total surface variation is 11.2 nm rms. The discontinuous contours show the high-frequency hologram errors

The effect of the high-frequency structure is greatly reduced by taking an average of many measurements with the hologram rotated to different orientations. To further filter out the high frequency errors from the hologram, a 36-term Zernike polynomial fit was made to the data. The null lens errors were then represented using the polynomial

fit. This fit also filters out any high-frequency errors in the null lens. However, the null lens errors, which originate from misalignment, surface figures, and glass inhomogeneity, will have a negligible high-frequency component (See Sec. 5.4).

CORRECTIONS TO THE DATA

Corrections to the data were required for the CGH test of both the ARC and the WIYN null correctors. Since the rotation test eliminated azimuthal errors, only axisymmetric errors were considered. The hologram measurements had several known errors that were quantified and subtracted from the data. These errors were due to small differences in wavelength, radius of curvature, and conic constant between those assumed for the original design and fabrication of the holograms and the final values for the measurements. A detailed description of the calculation for these error terms is given in Secs. 6.6 and 6.7.

It is important to note that the null corrector itself does not define a conic constant. For a given null lens, the conic constant of the matching mirror or hologram depends on the radius of curvature of the optic under test. A hologram is fabricated to synthesize a primary mirror with nominal conic constant K and radius of curvature R. To allow a direct comparison of the CGH measurement with the optical design, corrections are made to the CGH measurement for differences in the radius and conic constant between the values assumed in the fabrication of the hologram and those assumed for the null lens test. The final, measured value of R generally departs from its nominal value because the radius is not held to a tight tolerance during fabrication. Also, the final value of K, as defined by the null corrector and the primary radius of curvature, departs from its nominal value. The final value of K for the null lens test is determined by simulating

the null test using knowledge of the final null corrector and the primary radius of curvature.

The holograms were designed assuming a wavelength for the HeNe laser of 632.816 nm (Mielenz *et al.* 1968). After correcting the refractive index of air for the measured laboratory temperature and pressure using the relationships given by Barrell and Sears (1939), the laser wavelength in air at 21°C and 697 mm Hg was calculated to be 632.834 nm.

The corrections for the final values of K and R are made using Eqs. (6.34) and (6.36) to compute the spherical aberration that must be subtracted from the hologram measurement. The correction for the wavelength change is given in Eq. (6.37).

The spherical aberration from the radius, conic constant, and wavelength changes were added, resulting in a single correction term. Since the null lenses had considerable imaging distortion, this spherical aberration correction term required remapping before subtracting from the null lens data. The mapping distortion of the null correctors was measured by placing fiducial marks at known positions on the mirrors and analyzing the image locations. Least squares fits were used to compute coefficients of the third order mapping distortion. The measured distortion values for the two null correctors were virtually identical: -6.7% ± 0.5% for WIYN, and -6.8% ± 0.5% for ARC. To quantitatively determine the effect of this distortion on the spherical aberration, a computer simulation was performed. A wavefront with spherical aberration (at best focus) was remapped to simulate -6.7% distortion. A least squares fit was performed on this remapped function to give coefficients for the radially symmetric Zernike polynomials up to sixth order in r. To simulate the fit for a full circular pupil while using only a radial profile, a weighting function proportional to r, the radial distance was used. The resulting Zernike coefficients are

$$Z8_{image} = Z8_{mirror} \times (0.989 \pm 0.002)$$
$$Z15_{image} = Z8_{mirror} \times (0.092 \pm 0.008) \qquad (7.1)$$

where $Z8_{mirror}$ = coefficient on Zernike polynomial #8 in mirror coordinates

(Z_8 is third-order spherical aberration: $6\rho^4 - 6\rho^2 + 1$)

$Z8_{image}$ = coefficient on Zernike polynomial #8 after -6.7% ± 0.5% distortion

$Z15_{image}$ = coefficient on Zernike polynomial #15 after -6.7% ± 0.5% distortion.

(Z_{15} is fifth-order spherical aberration: $20\rho^6 - 30\rho^4 + 12\rho^2 - 1$).

The power terms $Z3$ were ignored. The Zernike polynomials $Z8_{image}$ and $Z15_{image}$ were computed using Eq. (7.1), and were subtracted from the measured data to give the null corrector error. Here, and throughout Ch. 7, all measurements and analyses are presented in terms of surface errors, which are half of the wavefront errors.

RESULTS FOR ARC NULL LENS

The ARC null lens was measured in the optics shop at 11 equally spaced rotational positions. The corrections made to the data are listed in Table 7.2. The derivation of these terms is given in Ch. 6. The conic constant and radius given in this table as final values for the CGH measurement are based on the final optical prescription of the null corrector and the measured radius of curvature of the primary. The net correction was remapped according to Eq. (7.1), giving the correction terms in image coordinates:

$$Z8_{image} = -0.0013\ \lambda$$
$$Z15_{image} = -0.0001\ \lambda.$$

These corrections were subtracted from the measurement resulting in a map of the null corrector errors showing 8.3 nm rms variation. The 36-term polynomial representation of the data shows 7.6 nm rms variation. The contour plot is shown in Fig. 7.3.

Table 7.2. Corrections for CGH measurement of ARC null lens.

	Value assumed for design of CGH	Final value for CGH measurement	Correction term $Z8_{mirror}$ (nm)
wavelength (nm)	632.816	632.834	+9
primary radius (mm)	12280	12279.7	-3
conic constant	-1.0194	-1.01933	-7
total			-1

The CGH measurement of the ARC null lens found -11.4 nm P-V spherical aberration corresponding to a conic constant error of -0.000072. Including the measured spherical aberration in the ARC primary mirror, the conic constant of the finished mirror was determined to be -1.01927 ± 0.00010.

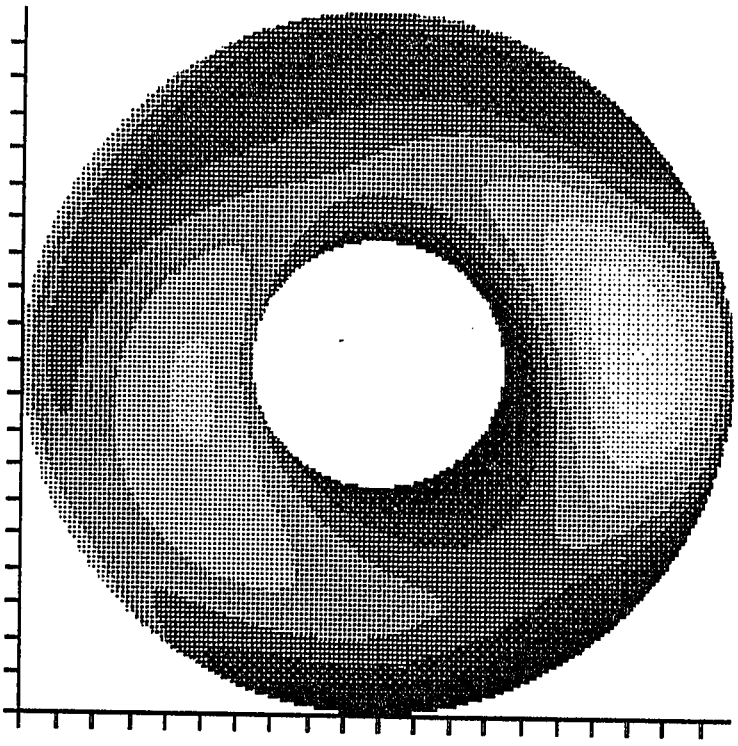

Figure 7.3. Contour map showing measured null lens error of 7.6 nm rms for ARC primary mirror as represented by a 36-term Zernike polynomial fit. Surface contours are plotted at 5 nm intervals over a range from -20 nm to 20 nm.

RESULTS FOR WIYN NULL LENS

The WIYN null lens was measured in the test tower at 15 equally spaced rotational positions. The corrections are listed in Table 7.3. The 38 nm correction was remapped giving the correction terms in image coordinates:

$$Z8_{image} = +0.0593\lambda$$

$$Z15_{image} = +0.0055\lambda.$$

These were subtracted from the measurement resulting in a map of the null corrector errors with 5.7 nm rms variation. The 36-term polynomial representation of the data, shown in Fig. 7.4, has only 5.1 nm rms variation including -3.0 nm P-V spherical aberration.

Table 7.3. Corrections for CGH measurement of WIYN null lens.

	Value assumed for design of CGH	Final value for CGH measurement	Correction term $Z8_{mirror}$ (nm)
wavelength (nm)	632.816	632.834	+10
primary radius (mm)	12250	12253.5	+32
conic constant	-1.07083	-1.07079	-4
total			+38

The spherical aberration measured in the null corrector corresponds to a conic constant error of -0.000019. The final conic constant of the WIYN primary mirror was determined to be -1.07082 ± 0.00009 which includes the measured spherical aberration in the mirror. A visual comparison between measurements of the ARC null lens (Fig. 7.3) and the WIYN null lens (Fig. 7.4) shows a strong correlation. This is expected because the largest source of error in the null lenses, the refractive index inhomogeneity, is the same for both systems. The alignment errors are expected to be different.

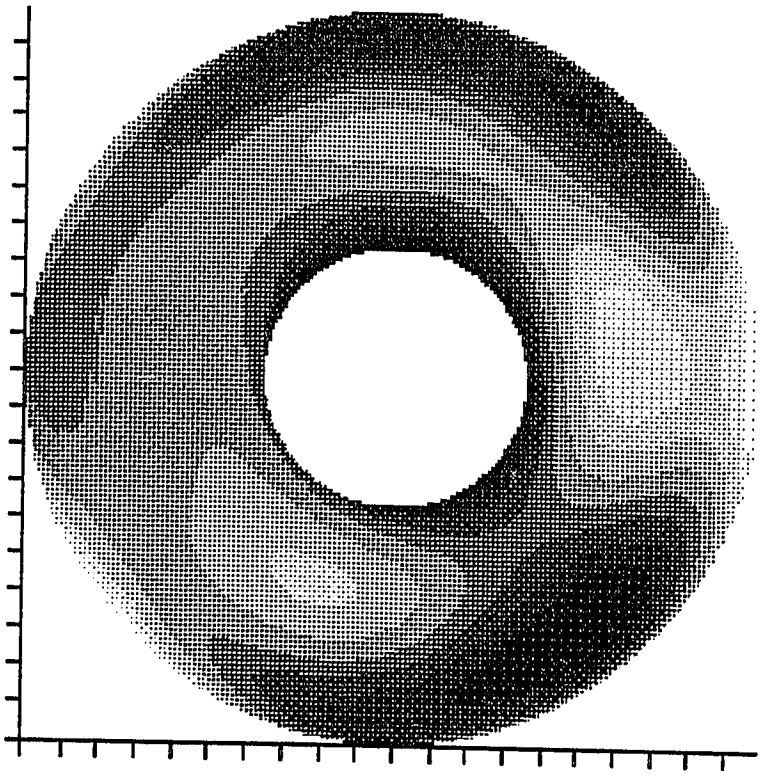

Figure 7.4. Contour map showing measured null lens error of 5.1 nm rms for WIYN primary mirror. The surface errors, computed from a 36-term Zernike fit to the data, are plotted with contours at 3 nm intervals over a range from -12 nm to 12 nm.

ERROR ANALYSIS

The error terms, as analyzed in Sec. 6.6 - 6.8, originate from three sources: the CGH itself, the implementation of the test, and the analysis of the data. A single error analysis for both ARC and WIYN tests was performed taking the worst case from both tests for each error term.

The errors in the hologram come from the surface figure, groove pattern distortion, and etch depth variations. The substrates were specified to be flat to $\lambda/20$ P-V. The component of this error that causes pure third-order spherical aberration (fourth-order dependence on r) in the null lens test has a cone-shaped appearance shown in Fig.

6.5. For the error analysis, it was assumed that this component of the figure error is less than $\lambda/20$. The e-beam writer has errors as large as 0.15 μm and printing errors can be as large as 0.2 μm. The encoding and digitization errors are not considered because they cause high-frequency errors that do not affect the conic constant. The grooves were specified to be etched to a depth of $\lambda/4$ with less than 5% depth variation over the entire aperture. The error analysis assumes the worst case of 5% depth variation causing pure spherical aberration. The gross errors discussed in Secs 7.4 and 7.5 are not included here because they cause phase discontinuities that are easily recognizable.

The uncertainty of the laser wavelength has several components. The uncertainty in the laser frequency is determined by the width of Doppler-broadened gain of the neon transition. The frequency of a single-mode, unstabilized HeNe laser will be 473612 ± 1 GHz (Mielenz *et al.* 1968). Errors in the refractive index of air caused by the uncertainty in the temperature and pressure measurement will cause an error in the wavelength. The thermal expansion of the fused silica holograms will also cause measurement errors proportional to the temperature difference between fabrication and use.

The errors in data analysis are due to the uncertainty of the Zernike polynomial fit to the data and the uncertainty of the mapping between the mirror and the image. The Zernike polynomial fit of spherical aberration is estimated to be uncertain to $\pm 0.003\ \lambda$. An error in the distortion coefficient of 0.5% would cause an error of 0.0001λ in the 0.06λ spherical aberration correction to the WIYN data. A 1% error in the definition of the edge, corresponding to 1 pixel, would cause an additional 0.0024λ error.

These errors are summarized in Table 7.4. The estimated uncertainty of the test is found by taking a root-sum-square (RSS) of the independent terms. A direct linear sum is useful for checking the highly unlikely scenario that all error terms contribute their maximum values in the same direction.

Table 7.4. Error budget for CGH null lens measurements for WIYN and ARC tests.

Error term	Value ± uncertainty	±Z8 (waves)	±dK (ppm)
Manufacturing errors			
write errors	±0.15 μm over 20 mm	0.0054	32
print errors	±0.2μm over 20 mm	0.0072	43
substrate flatness	λ/20	0.0083	50
etch depth variations	5% of λ/4	0.0010	6
Errors in use			
CGH temperature	21 ± 3° C	0.0014	8
laser frequency	473612 ± 1 GHz	0.0011	6
air pressure	697 ± 5 mm Hg	0.0010	6
air temperature	21 ± 2° C	0.0011	6
Data analysis error			
mapping distortion error	6.7 ± 0.5 %	0.0001	1
edge definition error	1 pixel	0.0024	14
fit error ΔZ8		0.0030	18
linear sum		0.0320	191
RSS		**0.0131**	**78**

The measurements of null corrector conic constants for the ARC and the WIYN primary mirrors are estimated to have a 78 ppm uncertainty. Additional uncertainty in determining the conic constant of the primary mirrors is caused by the uncertainties in the measured radii of curvature and in the measurements of the primary mirrors through the

null corrector. The conic constants of both 3.5-m $f/1.75$ primary mirrors are uncertain by 100 ppm.

7.3. MEASUREMENT OF NULL LENS WITH A KNOWN ERROR

To verify the CGH null lens measurement technique, the null lens for the ARC primary mirror was remeasured after making a deliberate spacing error of 90 μm. The spherical aberration that was measured using the CGH test closely matched the amount predicted by a computer simulation. This test confirmed the ability of the CGH null lens test to accurately quantify the null lens error.

After the ARC primary mirror had been shipped and the CGH test of the null lens was completed, a deliberate error was introduced into the null corrector. The large relay element on the null corrector was shifted 90 ± 5 μm towards the Shack cube, and the runout of the element was nulled to ± 3 μm. The CGH described in Sec. 7.2 was used to measure the respaced null lens at equally spaced azimuthal positions. The wavefront was shown to have 0.453λ P-V spherical aberration, corresponding to an effective error in the conic constant of 0.00091.

A computer simulation of the test of an ideal primary mirror with this perturbed null lens predicted a wavefront with 0.51λ P-V spherical aberration. Coefficients for third- and fifth-order spherical Zernike polynomials were fit and used to represent this wavefront. The expected wavefront was calculated by adding the Zernike terms to the measured error in the null lens from Sec. 7.1. This resulted in a wavefront with 0.477λ P-V spherical aberration -- in excellent agreement with the actual measured value. The difference between the two wavefronts has only 0.02λ rms variation. Interferograms representing the predicted and measured wavefronts are shown in Fig. 7.5.

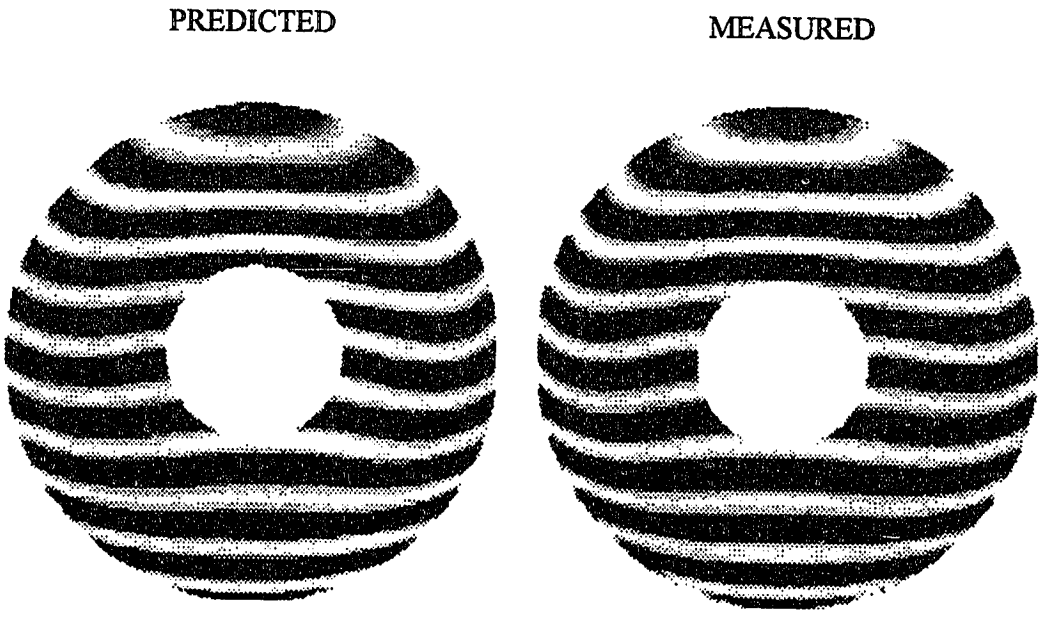

Figure 7.5. Comparison showing the excellent agreement between the predicted and actual measured effect of intentionally inducing a 90 μm spacing change in the ARC null lens. These interference patterns were calculated from the measured phase variations and those predicted by the simulation.

7.4. VERIFICATION WITH A CGH REPRESENTING A SPHERICAL MIRROR

Reference holograms were fabricated to allow direct verification of the fabrication accuracy. The reference holograms simulated spherical *f*/1.75 mirrors in order to closely match the geometry of the ARC and WIYN null lens holograms, but to allow accurate testing with a Fizeau interferometer. The two null lens holograms and the first reference sphere CGH were fabricated at the same time using identical techniques. The two null lens holograms were highly accurate, as indicated by the excellent agreement

between the holograms and the null correctors, but the reference CGH had a gross error. This error in the reference hologram caused a step in the diffracted wavefront near the edge of the part. Six more reference holograms printed from the same master did not have this error. The reprinted holograms had only small errors consistent with the error analysis in Table 7.3. Three holograms for a test of another null lens, described in the next section, also had errors of the same form.

Two important conclusions were drawn from the results of this test:

1. A fabrication error that causes a step in the phase can occur. The source of this error is not understood and this error may go undetected during fabrication.
2. If no such step error occurs, the accuracy of the holograms is described by the error analysis above.

The second point is weakly supported since it is based on such a limited number of holograms.

TEST DESCRIPTION

The reference holograms were fabricated using the method described in Chap. 6 with $K = 0$ and $h = 134.4$ mm. These holograms simulated 40 mm diameter convex or concave spherical surfaces with 134.4 mm radii of curvature. The holograms were tested both as concave and as convex spheres using a Fizeau interferometer (See Fig. 7.6). It is useful to test the CGH at both sides of focus to allow the separation of the flatness errors from the errors in the groove pattern. On either side of focus, variations in surface figure cause the same wavefront error -- a bump is a bump, although the image of the optic rotates 180°. Since the sign of the diffracted wavefront changes when the test is changed from convex to concave, the wavefront errors due to the hologram groove pattern

distortion also change sign. This allows the separation of the hologram groove errors from flatness errors. To calculate the flatness errors, the results of the two measurements are averaged (after a 180° rotation), and the diffraction errors cancel. The diffraction errors are equal to half the difference of the convex and concave measurements. Taking this difference, flatness errors in the hologram and reference surface errors with even symmetry cancel out.

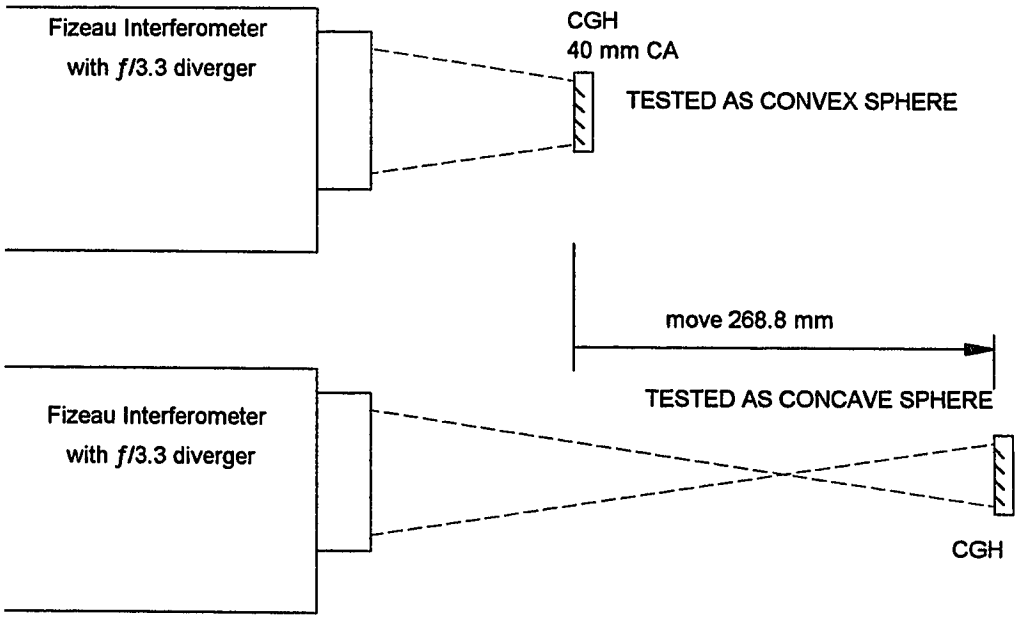

Figure 7.6. Fizeau test of CGH as both convex and concave spheres. Apart from a 180° image rotation, phase errors due to surface figure are identical for both cases and phase errors due to ruling distortion have opposite signs.

This test is insensitive to scale error in the hologram. Scale error in the CGH for the null lens test causes spherical aberration, but a scale error in the sphere hologram causes only power. Without the ability to measure the radius of curvature of the holo-

gram accurately, it is impossible to determine whether or not the CGH has the correct power from the diffracted wavefront.

RESULTS FOR A FLAWED HOLOGRAM

The first spherical hologram had a gross printing error shown in Fig. 7.7. A sharp step occurred at a narrow zone near the edge of the CGH. The error was definitely not axisymmetric -- the zonal step was off center by several mm and the phase error was larger on one side than on the other. When the ring pattern was examined with a microscope, no discontinuities were apparent. Also, the substrate was measured to be flat to $\lambda/20$. Because of its sharp nature, the error was easily verified to be in the hologram and not in the measurement optics.

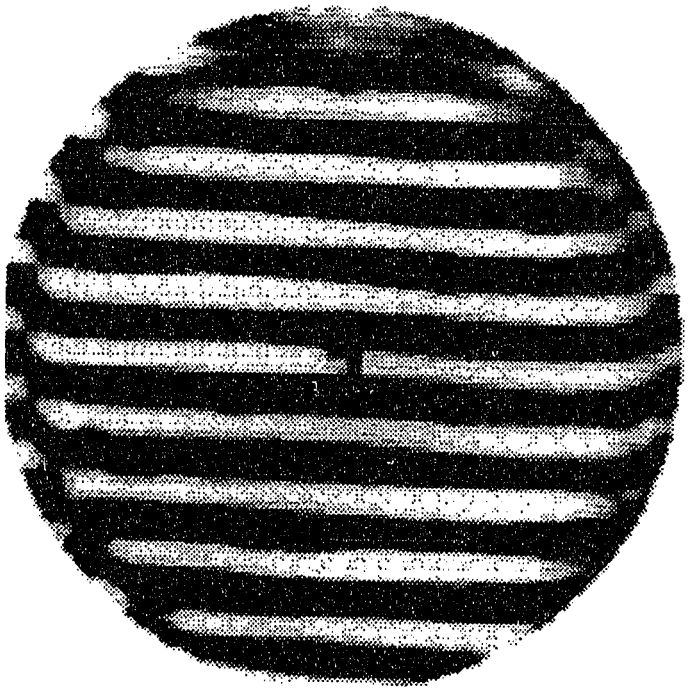

Figure 7.7. Interferogram from mis-printed CGH of a spherical reflector. A slightly offset step shows up at the outer edge.

This phase step of half a fringe corresponds to a radial shift of the ring pattern of about 1 μm. This is a factor of 5 larger than what was expected from the process. The firm that printed this hologram did not have an explanation for the origin of this error. They did reprint the hologram from the same master. Although the source of the problem was not identified, the second part did not show the error. It was then assumed that the flaw was due to an unlikely problem in the printing. Unfortunately, as the next section describes, this error has recurred during the fabrication of other holograms.

RESULTS FOR GOOD HOLOGRAMS

The reprinted reference CGH did not show the gross errors of the first, and is consistent with the assumed fabrication errors. This CGH was measured using a phase shifting Fizeau interferometer as both a convex and concave surface. By flipping and using the method described above, the optical surface was determined to deviate from flat by 3.2 nm rms and the hologram distortion caused errors of 7.6 nm rms. The diffraction error included 0.016λ P-V spherical aberration which corresponds to about 0.2 μm P-V hologram distortion. This is comparable to the expected spherical aberration for the null lens test given in Table 7.3.

Five more copies of the reference sphere were printed and tested to get an estimate of the statistics involved. None of these five had the discontinuous error described above. In fact, all five were nearly perfect. The usual high-frequency errors were present but very little spherical aberration showed up. The P-V spherical aberration varied from 0.0168λ to -0.0018λ with an average of 0.0076λ and a standard deviation of 0.0068λ. These fall inside the expected error.

Because the first CGH had a gross error that was never explained, no solid assurance can be made that the null corrector holograms do not have errors that originated from this mystery source. This is unlikely because the hologram error stood out as a discontinuity in the phase. The holograms without this type of error were as accurate as expected. On the basis of this observation, it is concluded that this error causes *only* the step-type phase errors. It follows that holograms that do not show this error are assumed accurate with the expected errors described in Table 7.3. Also, as long as the null lens agrees with the CGH, it is highly unlikely that they both are wrong by the same amount. Until more is known about the hologram fabrication error, the analysis of the test will assume that the error does not exist for holograms that do not have a phase step.

7.5. HOLOGRAM ERRORS FOR A NULL LENS TEST FOR A 3.5-m *f*/1.5 PRIMARY MIRROR

The null lens for a 3.5-m *f*/1.5 primary mirror was measured using three different computer-generated holograms. All three holograms had significant errors of the type described above causing steps in the phase. The errors were different for all three holograms and there were large regions in each hologram that did not have phase errors. The phase error precluded an accurate measurement of the null corrector, but because the three holograms had different errors and none showed significant spherical aberration, an estimate of the null lens could be made. On the basis of results from all three holograms, it was determined that a null lens error corresponding to ΔK greater than ±250 ppm was unlikely.

The non-axisymmetric errors in the null corrector were measured independently using the rotation test with the primary mirror, described in Sec. 4.10. On the basis of seven independent measurements, the azimuthal errors were determined to be 5.4 nm

rms. Because the null lens was known to have such small azimuthal errors and since the holograms were so badly flawed, the CGH test attempted to verify only the spherical aberration or conic constant of the null lens.

The first hologram was fabricated using the method described above. The CGH was measured by the null lens and shown to cause wavefront errors of about $\lambda/5$ rms. There was a large region on the CGH that could not be measured due to low fringe contrast and an apparent discontinuity. The CGH was rotated 180° and remeasured to separate azimuthal errors in the CGH from those in the null lens. Since the errors rotated with the CGH, the problem was confirmed to be in the CGH and not in the null lens. The resulting map derived from these two measurements is shown in Fig. 7.8.

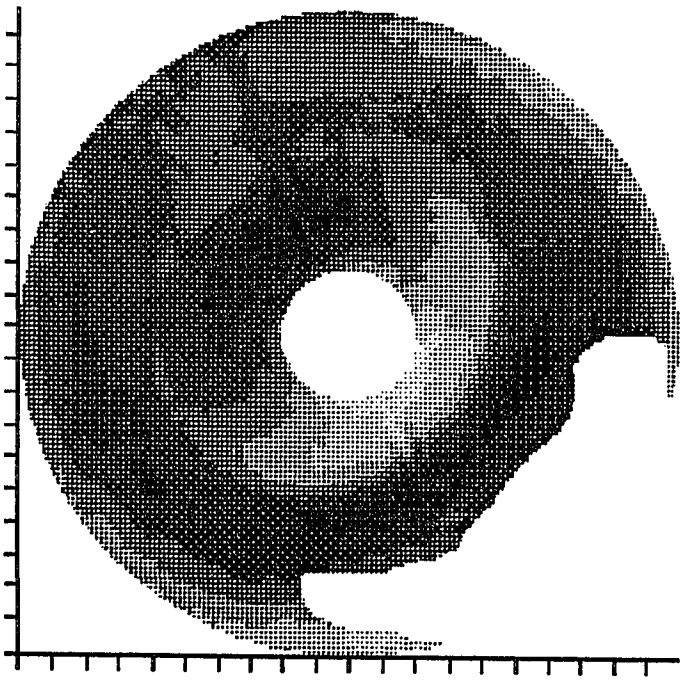

Figure 7.8. Contour map of the errors in the hologram for testing a null lens for a 3.5-m $f/1.5$ primary mirror. The large region at the lower right could not be measured due to low diffraction efficiency.

The error in this CGH caused the center region to appear as a plateau. Because the phase shift error was continuous in this region, it could be phase measured. This plateau dominates the Zernike polynomial fit to this data, resulting in a fit of 0.176λ P-V spherical aberration (SA). Because this plateau is clearly a hologram error that affects the spherical aberration, this measurement indicates only that the spherical aberration in the null lens is probably less than 0.176λ.

A different company was found to print two more copies of the CGH, using the same e-beam written master. Both of these prints also had gross errors of the same form, but with the errors occurring in different parts of the hologram. In addition, these two holograms do not show spherical aberration as the first CGH did. On the basis of the interference patterns from these holograms, shown in Fig 7.8, it was estimated that less than one-fifth of a fringe, or a λ/10 P-V surface spherical aberration was present.

Figure 7.9. Interferograms showing the measurements of the second and third holograms with the null corrector for a 3.5-m *f*/1.5 primary mirror. The spherical aberration in these is estimated to be less than a fifth of a fringe.

The estimate of $\lambda/10$ in the surface as a limit for the amount of spherical aberration (or ΔK of ± 250 ppm) is imprecise. Until a better result is obtained, this result is useful because it confirms that the primary mirror is unlikely to miss its ± 500 ppm conic constant specification due to a null lens error.

The hologram fabrication errors caused the null lens measurement to fall short of its expectations for the null corrector for a 3.5-m $f/1.5$ primary mirror. We are currently pursuing another fabrication process, defined in the next section, to manufacture holograms directly onto the final substrate. We are also researching methods of directly measuring the distortion of the final CGH, and may be able to certify the next holograms.

7.6. FUTURE RESEARCH FOR HOLOGRAPHIC TESTING OF NULL CORRECTORS

The holographic null lens test has proven to be a powerful technique for confirming the accuracy of null correctors. Further work is required to solve the fabrication problems before making the holograms for testing the null correctors for the 6.5-m and 8-m mirrors. These holograms will be larger, thus more difficult and expensive, than those for the 3.5-m mirrors, so the cost of a flawed printing will be high.

Since variations are found among holograms printed from the same master, an error in contact printing is likely to be the source of this problem. The holograms are fabricated by writing a chrome master pattern onto a thin photo mask with the e-beam writer. This pattern is transferred to the final thick substrate using contact printing. In contact printing, the master pattern is held in vacuum contact with the final substrate that has been coated with chrome and photoresist. Collimated ultraviolet light is projected through the master to expose areas defined by the gaps in the chrome pattern. After developing and etching, a chrome pattern remains that is the negative of the master.

DIRECT WRITING TO ELIMINATE PRINTING ERRORS

The CGH test of null correctors is limited by the unpredictable fabrication errors. Unfortunately, the companies that fabricate the diffractive optics are not interested in performing the research necessary to determine the origin of this problem. This leaves the user of the diffractive optics several unappealing options:

1. Give up entirely on CGH as an accurate means of testing.
2. Redesign the optical test to ease the requirements on the diffractive optics.
3. Initiate a research project to develop accurate printing capabilities.
4. Circumvent the problem by using a different fabrication process.

It seems that choice #4 offers the clearest route to a solution for testing null correctors. The printing errors can be avoided by eliminating the printing step from the fabrication process. This may be done by writing the hologram onto its final substrate with the e-beam writer, so that no transfer of the pattern is required. Since the flatness of the hologram surface is critical, special substrates must be prepared that are flat to $\lambda/20$. The substrates must be coated, e-beam written, and etched.

Unfortunately, the e-beam writers will only accept standard size substrates that are very thin and are difficult to polish to such precision. The standard 4-inch square substrate is only 0.090 inches thick so it will deflect according to its support forces.

To get around this problem, the thin substrates will be mounted onto a master flat that is thick enough to hold its figure when simply supported. The back surface of the hologram substrate will be in close enough contact with the reference surface of the flat that the molecular forces will hold it there. This is a common technique that opticians use for holding optics. The front surface of the substrate will then be polished to $\lambda/20$ as it is supported in this manner. When removed and placed back on to the master flat, in

the same position with the same orientation, the figure of the top surface of the substrate should be repeatable. This can easily be verified to high accuracy.

The substrate will be mounted onto the master flat and polished flat to λ/20. It will be removed from the flat, coated with chrome and resist, and written by the e-beam writer. When it is removed from the master flat, the figure will no longer be flat. This does not affect the fabrication of the CGH: the commercially available "ultra flat" substrates are only flat to 2 μm. It will be processed, etched, and coated to form the final hologram. It will then be mounted back onto the master flat, recreating the flatness of the substrate.

HOLOGRAM FOR A 6.5-m *f*/1.25 PRIMARY MIRROR

The CGH null lens test is planned for all of the telescope projects at Steward Observatory. The computer-generated hologram for testing the 6.5-m *f*/1.25 has been designed. This hologram will be 136 mm in diameter and consist of 10757 grooves. This is within the realm of existing lithographic technology, but it will be difficult and expensive to fabricate.

This hologram will be directly written on the final substrate that is 7 inches square and 0.25 inches thick. This substrate will be polished flat to λ/10 as it is supported on a master flat as described above. An estimate of the error budget for this test is listed below in Table 7.5. This analysis assumes much larger errors for the 136 mm CGH than for the 40 mm holograms. The absolute accuracy of the wavefronts from the large holograms will not be as high as for the previous holograms. However, the ratio of the errors to the total surface asphericity, which determines the uncertainty in the conic constant, will be smaller.

Table 7.5. Error budget for CGH null lens measurements for a 6.5-m $f/1.25$ primary mirror.

Error term	Value ± uncertainty	±Z8 (waves HeNe)	$\pm\Delta K$ (ppm)
Manufacturing errors			
write errors	0.5 μm over 68 mm	0.0253	25
processing errors	0.2 μm over 68 mm	0.0101	10
substrate flatness	λ/10	0.0167	19
etch depth variations	5% of λ/4	0.0010	1
Errors in use			
CGH thermal expansion, ΔT	3° C	0.0067	8
laser frequency	2 ppm	0.0052	6
air pressure	697 ± 5 mm Hg	0.0047	5
air temperature	21 ± 2° C	0.0052	6
Data analysis error			
edge definition error	1 pixel	0.0024	3
fit error dZ8		0.0030	3
linear sum		0.0803	93
RSS		**0.0340**	**40**

A prototype of this hologram will be fabricated before the full CGH is made. This prototype, consisting of only a narrow diametrical slice across the circular hologram, will allow a test of the fabrication technique that requires only a small fraction of

the cost of the full hologram. This diametrical slice will be useful for measuring spherical aberration.

The CGH for testing the null corrector for the LBT 8.4-m $f/1.14$ primary mirrors will be 208 mm in diameter and require 17919 rings. This is larger than the capacity of current e-beam writers. Luckily, this CGH will not be required for several years, after which time the explosive growth of the electronic industry is likely to have spurred the development of larger and more accurate e-beam writers.

7.7. CONCLUSION

The holographic test is a powerful new way of confirming the accuracy of null correctors. It was verified on two null correctors for highly aspheric mirrors, where the conic constants were measured to an accuracy of ±78 ppm. In addition, the measurement of a null lens with a known error showed excellent agreement with the predictions.

The holograms were fabricated from masters that were written using electron beam lithography. Large errors have occurred in the printing of the final holograms from the masters. These errors show up in the optical test as steps in the phase, but they are not evident during fabrication. The test of the conic constant of a third null corrector was limited to an accuracy of ±250 ppm by these errors. The source of these errors is unknown, so future holograms will be written directly onto the final substrate, requiring no printing.

Continued research is underway with the goal of providing an accurate test of the null corrector for the 6.5-m $f/1.25$ primary mirrors. This test is expected to measure the

conic constant of the null corrector to an accuracy of 40 ppm. This can be achieved using available e-beam writers and specially prepared substrates.

The excellent results achieved in the first two null lens measurements have demonstrated the power and potential accuracy of this test. This test is planned for the verification of all future null correctors at Steward Observatory.

CONCLUSION

A complete description of optical shop testing for primary mirrors has been given. A background on optical measurement was developed to put the work of this dissertation into perspective. Two slope tests, the wire test and the scanning pentaprism test, were improved and carefully analyzed, only to discover new limitations. Interferometric testing using null correctors was carefully analyzed from a system point of view. Many important aspects of the null test design that are unique to these systems were discussed in considerable detail. Optical design methods and several novel null correctors were presented. A new test of null correctors using computer-generated holograms was developed and analyzed. Measured results and an analysis of the errors were given for several null lens tests, establishing that three null correctors for 3.5-m mirrors comfortably met their specifications.

As successful as this new null lens test has been, the development of this test is not complete. Several holograms showed gross errors that appear to be due to errors in the printing of the parts. The fabrication of holograms of large, fast aspheres will require additional research and development.

This dissertation describes techniques for measuring large, steeply aspheric *concave* optical surfaces. Another great challenge in testing large optics is the measurement of secondary mirrors that have steeply curved convex surfaces. These mirrors must be fabricated and tested to an accuracy similar to that required for the

primary mirrors. Classic optical tests of secondary mirrors are prohibitively expensive for large (> 1 m) mirrors. It will require significant research to develop cost-effective optical testing methods that will lead to secondary mirrors that will not degrade the pristine images provided by the primary mirrors.

The work in this dissertation represents a significant step forward in optical testing technology for large primary mirrors. This research, like most, was born out of necessity. Astronomers require larger telescopes to develop a more complete understanding of the cosmos. It was decided that the potential scientific gains were worth the cost of overcoming the technical problems of building 8-meter telescopes.

Optical testing is one of the many technical challenges posed by the fabrication of these telescopes. Many talented scientists and engineers are solving problems of casting, polishing, supporting, handling, transporting, and coating giant optics. At the same time, they are tackling the challenges of structural design, pointing and tracking, thermal design, optical alignment, and computer control of these new sophisticated telescopes. The design and fabrication of the sensitive instruments required by these new telescopes also pose a challenge to the optics community. All these components must come together to form the most powerful systems ever built to allow people to translate faint specks of light into understanding of physical processes in distant stars and galaxies.

APPENDIX A

PRIMARY MIRRORS FOR ASTRONOMICAL TELESCOPES

A sample of the world's largest primary mirrors for astronomical optical telescopes is listed in chronological order in Table A.1. Primary mirrors for Schmidt telescopes and military systems are not included in the table. An effort has been made to include mirrors with large aperture or small focal ratio for their time.

Table A.1. Primary mirrors for astronomical telescopes.

telescope	observatory	location	diameter (cm)	focal ratio	year	source
	Newton	England	3.4	5	1668	(a)
	Hadley	England	15.2	10.3	1721	(a)
	Herschel	England	22.9	13	1774	(a)
	Herschel	England	47.8	12.7	1784	(a)
	Herschel	Slough, Eng	121.9	8.2	1788	(b)
	Rosse	Parsontown, Ire.	91.4	12	1840	(a)
	Rosse	Parsontown, Ire.	182.9	8.7	1845	(b)
	National Obs.	Marseilles, France	80.0	6	1864	(c)
	Grubb	Melbourne, Aust	121.9	7.6	1870	(b)
	Paris Obs.	St. Michel	119.4	6.5	1875	(b)
	Lick Obs	Mt. Hamilton, CA	91.4	5.8	1879	(b)
	Obs. de Toulouse	Toulouse, France	83.8	5.7	1887	(b)
	Calver	Cambridge, Eng	91.4	3.7	1890	(b)
	Obs. de Paris	Meudon, France	100.0	3	1893	(c)
	Royal Greenwich Obs.	England	76.2	4.5	1897	(c)
	Harvard	Cambridge, MA	154.9	5.2	1900	(b)
	Yerkes Obs.	Williams Bay, WI	61.0	4	1901	(c)
	Mt. Wilson Obs.	Pasadena, CA	152.0	5	1908	(b)
	Lowell Obs.	Flagstaff, AZ	106.7	5.9	1910	(c)
	Bergedorf (Zeiss)	Hamburg, Ger	99.1	3	1913	(b)

Table A.1. *continued.*

telescope	observatory	location	diameter (cm)	focal ratio	year	source
Hooker Telescope	Mt. Wilson Obs.	Pasadena, CA	254.0	5	1917	(b)
	Dominion Ast. Obs.	Victoria, Canada	182.9	5	1919	(b)
	Steward Obs.	Tucson, AZ	91.0	5	1922	(c)
	Perkins Obs.	Delaware, OH	175.0	4.3	1932	(b)
	University Obs.	Turku, Finland	50.0	2	1934	(c)
	Harvard Coll. Obs.	Cambridge, MA	154.9	5.1	1934	(c)
	Dunlap Obs.	Richmond Hill, CA	188.0	4.9	1935	(b)
	McDonald Obs.	Ft. Davis, TX	208.3	4	1939	(b)
	Radcliffe Obs.	Pretoria, S. Africa	188.0	4.8	1948	(c)
Hale Telescope	Palomar Obs.	Mt. Palomar, CA	508.0	3.3	1948	(d)
	Mt. Stromlo Obs.	Canberra, Aust.	188.0	5	1955	(c)
	Obs. de Haute Prov.	St. Michel, Fr.	193.0	5	1958	(c)
Shane Telescope	Lick Obs.	Mt. Hamilton, CA	305.0	5	1959	(d)
Shajn Telescope	Crimean Astrop. Obs.	Simeis, Ukrainia	264.0	3.8	1960	(d)
107-inch Telescope	MacDonald Obs.	Mt. Locke, TX	272.0	3.9	1969	(d)
Mayall	Kitt Peak Natl Obs.	Tucson, AZ	381.0	2.7	1973	(d)
Anglo-Australian	Anglo-Austr. Obs.	Siding Spr., Aus	389.0	3.3	1975	(d)
duPont		Las Campanas	254.0	3	1976	(d)
4-m Telescope	CTIO	Cerro Tololo	400.0	2.8	1976	(d)
LAT	Special Astrophys. Obs.	Caucuses, Rus.	600.0	4	1976	(d)
Wyoming	Wyoming IR Obs.	Jelm Mt., WY	229.0	2.1	1977	(d)
3.6-meter Telescope	ESO	La Silla, Chili	357.0	3	1977	(d)
UKIRT		Mauna Kea, HI	380.0	2.5	1978	(d)
CFHT		Mauna Kea, HI	358.0	3.8	1979	(d)
IRTF	NASA	Mauna Kea, HI	300.0	2.5	1979	(d)
MMT	Smithsonian/ U. Arizona	Mt. Hopkins, AZ	182.9	2.7	1979	(d)
INT		La Palma, Spain	250.0	3	1984	(d)
3.5-m Telescope		Calar Alto, Spain	350.0	3.5	1984	(d)
Hiltner Telescope		Kitt Peak, AZ	234.0	2.07	1986	(d)
William Herschel	Roque de los Muchachos	La Palma, Spain	420.0	2.5	1987	(d)
Nordic Opt. Tel.	Roque de los Muchachos	La Palma, Spain	256.0	2	1989	(d)
NTT	ESO	Chili	350.0	2.2	1989	(d)
Hubble ST	NASA	space	240.0	2.3	1990	(d)
Keck 1	Cal, Keck Obs.	Mauna Kea, HI	982.0	1.75	1991	(d)
LMT	Univ. BC and Laval Univ.	Vancouver, Can.	270.0	1.887	1992	(d)
Lennon	Vatican Obs.	Mt. Graham, AZ	182.9	1.0	1993	(e)
ARC 3.5-meter	Astrophys. R. Cons.	Apache Pt., NM	348.0	1.75	1993	(d)
WIYN	KPNO	Kitt Peak, AZ	350.5	1.75	1994	(d)
Galileo	TNG	La Palma, Spain	350.5	2.2	1995	(d)
MMT	Smithsonian/ U. Arizona	Mt. Hopkins, AZ	650.2	1.25	1995	(d)
Keck 2	Cal, Keck Obs.	Mauna Kea, HI	982.0	1.75	1996	(d)

Table A.1. *continued.*

telescope	observatory	location	diameter (cm)	focal ratio	year	source
LBT	Columbus Project	Mt. Graham, AZ	840.7	1.14	1997	(d)
Magellan	Carnegie	L. Campan., Chili	650.2	1.25	1998	(d)
Gemini (North)	NOAO	Mauna Kea, HI	810.0	1.8	1999	(d)
Suburu Telescope	JNLT	Mauna Kea, HI	830.0	1.8	1999	(d)
VLT	ESO	C. Paranal, Chili	820.0	1.8	2000	(d)
Gemini (South)	NOAO	C. Pachon, Chili	810.0	1.8	2001	(d)

References for Table A.1.:

(a) King (1955).
(b) Dimitroff and Baker (1945).
(c) Kuiper and Middlehurst (1960).
(d) Sinnott and Nyren (1993).
(e) Anderson *et al.* (1991).

APPENDIX B

NULL CORRECTOR TOLERANCES FOR THE WIYN 3.5-m *f*/1.75 PRIMARY MIRROR

A tolerance analysis (described in Chap. 5) was carried out for the null corrector used to test the WIYN 3.5-m *f*/1.75 primary mirror. Table B.1 shows the complete prescription and error budget. Figures B.1 and B.2 graphically show the contributions to the rms wavefront and the conic constant error of the test. The conic constant of the null corrector was subsequently confirmed to ±0.00008 and the rms wavefront 0.016 λ using a computer-generated hologram (See Chap. 7).

Table B.1. Table of tolerances and error budget for null corrector for WIYN 3.5-m *f*/1.75 primary.

Parameter	Units	Measured value	Expected error	Conic error	Wavefront rms (@ 632.8 nm)
Shack Cube:					
Thickness	mm	39.216	0.006	0.000035	0.0006
Radius of curvature 2	mm	-39.081	0.005	0.000029	0.0005
Surface irregularity (rms)	waves	0.005	0.005		0.0141
Surface runout 2	µm		5	0.000000	0.0003
Airspace	mm	219.131	0.003	0.000017	0.0003
Relay Lens:					
Curvature 1	/mm	2.36E-07	1.00E-08	0.000002	0.0000
Thickness	mm	36.482	0.005	0.000020	0.0004
Radius of curvature 2	mm	-114.891	0.012	0.000043	0.0010

Table B.1. *continued*

Parameter	Units	Measured value	Expected error	Conic error	Wavefront rms (@ 632.8 nm)
Surface irregularity 1 (rms)	waves	0.014	0.002		0.0146
Surface irregularity 2 (rms)	waves	0.014	0.011		0.0184
Index of refraction		1.51585	1.00E-05	0.000030	0.0002
Refractive index inhomogeneity	rms		2.50E-7		0.0288
Surface runout 1	μm		4		0.0009
Surface runout 2	μm		4		0.0006
Airspace	mm	333.837	0.003	0.000014	0.0005
Field Lens:					
Radius of curvature 1	mm	501.922	0.012	0.000020	0.0011
Thickness	mm	11.798	0.005	0.000001	0.0002
Radius of curvature 2	mm	742.612	0.014	0.000010	0.0007
Surface irregularity 1 (rms)	waves	0.016	0.002		0.0166
Surface irregularity 2 (rms)	waves	0.013	0.002		0.0136
Index of refraction		1.51587	1.00E-05	0.000027	0.0013
Refractive index inhomogeneity	rms		2.50E-07		0.0093
Surface runout 1	μm		3	0.000000	0.0012
Surface runout 2	μm		3	0.000000	0.0014
Residual Wavefront Error:	rms			0.000000	0.0030
Primary Radius	mm	12253.5	0.5	0.000043	0.0001
RSS				**0.000094**	**0.0463**

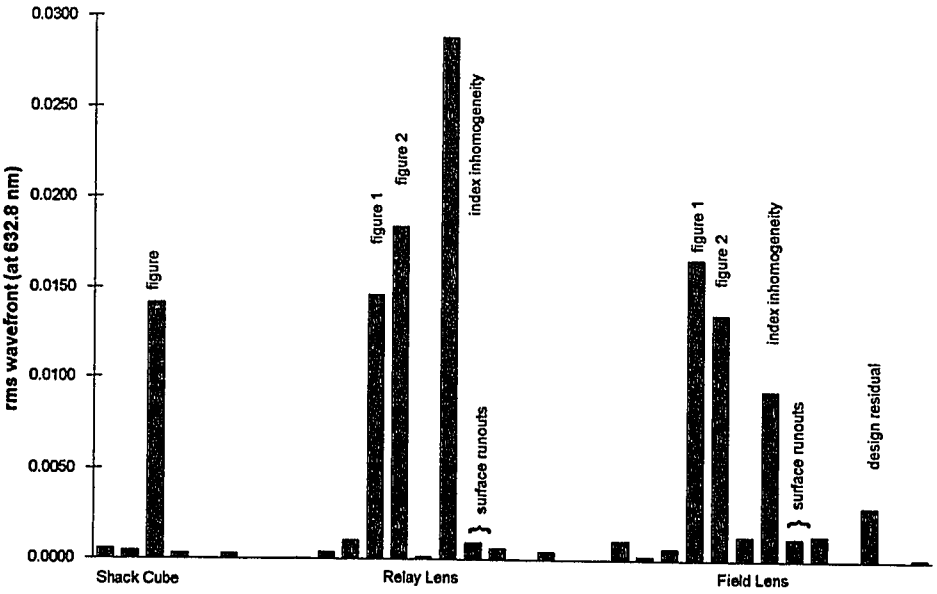

Figure B.1. Contributions of each error in the WIYN null lens to the system uncertainty in rms wavefront. The large contributions to the uncertainty are labeled.

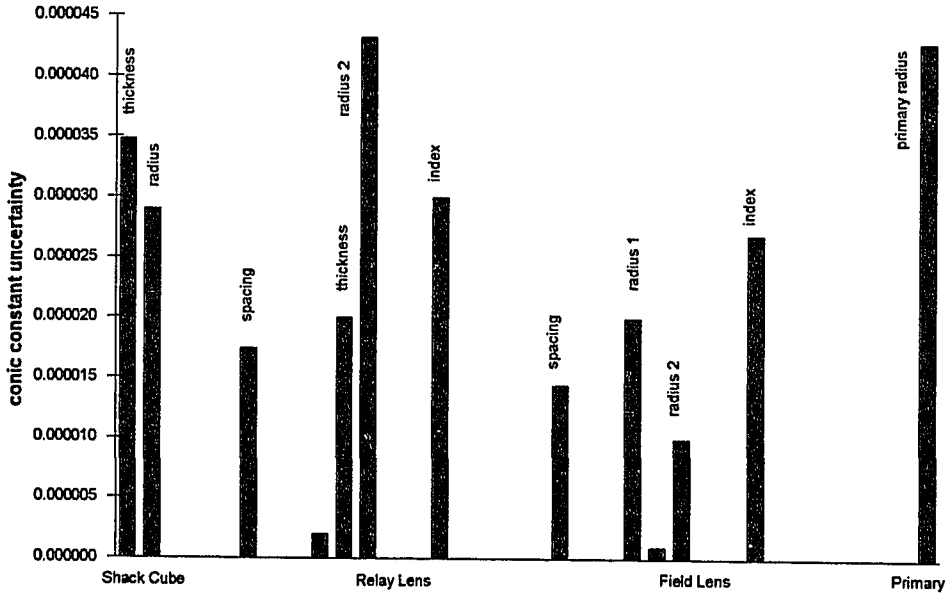

Figure B.2. Contributions of each error in the WIYN null lens to the system uncertainty in conic constant. The large contributions to the uncertainty are labeled.

APPENDIX C

VISIBLE NULL CORRECTOR FOR A 6.5-m *f*/1.25 PRIMARY MIRROR: OPTICAL PRESCRIPTION AND TOLERANCE ANALYSIS

This appendix contains the optical prescription and error analysis for the null corrector designed for testing a 6.5-m *f*/1.25 primary mirror using visible laser light. The null corrector, shown in Fig. C.1 will be used to guide final polishing of the primary mirror. The error budget for the null corrector is analyzed using a structure function of the mirror surface. The structure function contributions from the null lens tolerances, after the removal of conic constant errors, are shown in Table C.1. The error analysis using rms wavefront is given in Table C.2.

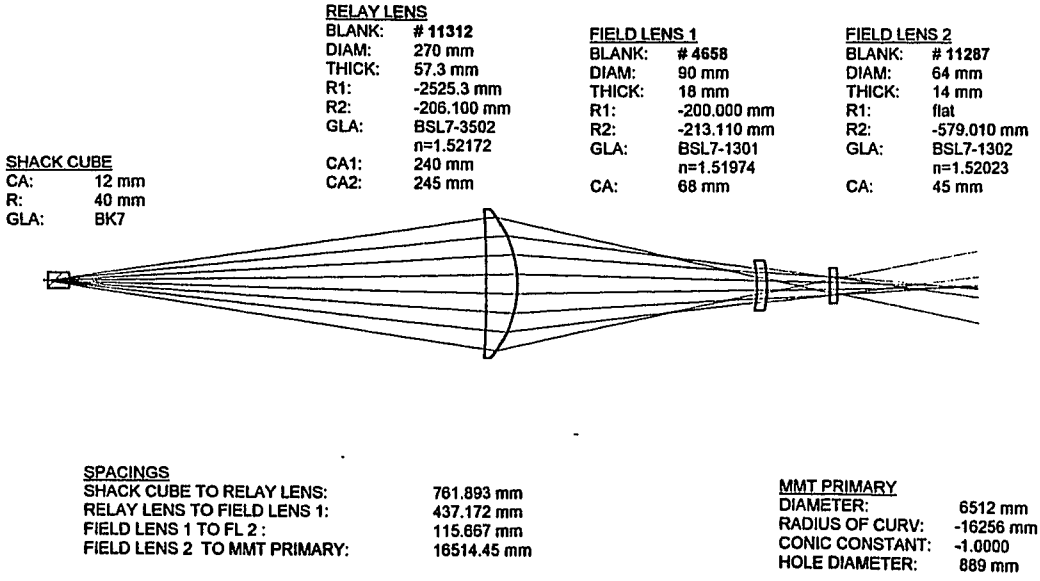

Figure C.1. Layout of the visible null corrector for the 6.5-m *f*/1.25 primary mirrors.

Table C.1. Table of tolerances showing the structure function for the null corrector

				STRUCTURE FUNCTIONS						
	units	Design value	tolerance	spatial scales in mm 3256	1628	814	407	204	102	51
				rms wavefront difference in nm						
Shack Cube	mm	12								
Radius	mm	-40	0.005	0.30	0.26	0.12	0.23	0.20	0.12	0.06
Surface (rms)	nm		6.328	17.59	16.58	12.28	8.35	5.19	2.78	1.28
Runout	µm		5.000	1.98	1.64	2.11	1.14	0.89	0.62	0.34
Airspace	mm	761.893	0.020	1.21	1.04	0.47	0.90	0.80	0.48	0.26
Relay Lens :	mm	270								
Radius 1	mm	-2525.3	0.500	1.20	0.94	0.46	0.93	0.85	0.51	0.27
Thickness	mm	57.3	0.010	0.78	0.70	0.53	0.63	0.49	0.29	0.16
Radius 2	mm	-206.1	0.010	2.50	2.35	1.05	1.61	1.53	0.93	0.50
Surface 1 (rms)	nm		7.594	10.87	10.25	7.59	5.16	3.21	1.72	0.79
Surface 2 (rms)	nm		7.594	10.87	10.25	7.59	5.16	3.21	1.72	0.79
Index of refraction		1.52172	1.00E-5	1.13	0.99	0.12	0.74	0.76	0.46	0.25
Index Inhomogen	rms		1.72E-7	27.79	13.90	6.95	3.47	1.74	0.87	0.43
Runout surface 1	µm		10.000	1.68	1.54	2.24	1.21	0.96	0.67	0.36
Runout surface 2	µm		10.000	2.67	2.21	2.71	1.56	0.87	0.64	0.35
Airspace	mm	437.172	0.020	1.86	0.47	1.46	1.73	1.77	1.07	0.56
Field Lens 1:	mm	90								
Radius 1	mm	-200	0.005	7.68	7.92	5.52	4.81	3.93	2.36	1.29
Thickness	mm	18	0.005	1.48	3.28	3.63	1.36	2.12	1.31	0.68
Radius 2	mm	-213.11	0.005	3.30	4.96	4.85	0.66	2.27	1.41	0.71
Surface 1 (rms)	nm		7.594	10.87	10.25	7.59	5.16	3.21	1.72	0.79
Surface 2 (rms)	nm		7.594	10.87	10.25	7.59	5.16	3.21	1.72	0.79
Index of refraction		1.51974	1.00E-5	0.28	0.18	0.49	0.26	0.24	0.16	0.08
Index Inhomogen	rms		1.20E-7	6.09	3.05	1.52	0.76	0.38	0.19	0.10
Runout surface 1	µm		5.000	38.75	27.06	20.12	13.98	8.28	4.57	2.41
Runout surface 2	µm		5.000	33.66	24.31	18.29	12.77	7.66	4.24	2.23
Airspace	mm	115.667	0.010	1.77	1.28	0.95	1.31	1.34	0.81	0.43
Field Lens 2:	mm	64								
Curvature 1	/mm	0	1.25E-7	6.46	8.31	7.45	2.83	2.02	1.32	0.60
Thickness	mm	14	0.010	1.51	1.23	0.41	1.08	1.05	0.64	0.34
Radius 2	mm	-579.01	0.010	1.86	0.64	1.69	1.56	1.69	1.03	0.54
Surface 1 (rms)	nm		7.594	10.87	10.25	7.59	5.16	3.21	1.72	0.79
Surface 2 (rms)	nm		7.594	10.87	10.25	7.59	5.16	3.21	1.72	0.79
Index of refraction		1.52023	1.00E-5	4.00	3.94	2.31	2.53	2.24	1.36	0.73
Index Inhomogen	rms		1.20E-7	4.74	2.37	1.18	0.59	0.30	0.15	0.07
Runout surface 1	µm		5.000	20.73	14.64	10.82	8.05	5.25	3.03	1.65
Runout surface 2	µm		5.000	24.75	16.62	11.53	8.02	4.99	2.81	1.49
Airspace	mm	16514.4	1.000	1.07	0.94	0.37	0.63	0.70	0.43	0.23
MMT Primary	mm	6512								
Radius	mm	16256	1.000							
Design Residual	λ	0	0.008	6.77	6.64	7.84	6.26	4.22	2.35	1.20
Worst Case				290.85	231.47	174.99	120.94	83.95	47.92	24.35
RSS WVFRONT				75.77	56.37	41.86	28.78	18.44	10.34	5.30
RSS SURFACE				**37.89**	**28.18**	**20.93**	**14.39**	**9.22**	**5.17**	**2.65**

Table C.2. Table of tolerances showing the dependence of the rms wavefront and conic constant on the fabrication tolerances.

	units	Design value	tolerance	Conic Constant error	Wavefront rms at 514.5 nm
Shack Cube	mm	12			
Radius	mm	-40	0.005	0.000005	0.0006
Surface Irregularity (rms)	wv HeNe		0.010		0.0246
Runout	µm		5.000	0.000000	0.0013
Airspace	mm	761.893	0.020	0.000018	0.0017
Relay Lens :	mm	270			
Radius 1	mm	-2525.3	0.500	0.000019	0.0016
Thickness	mm	57.3	0.010	0.000008	0.0011
Radius 2	mm	-206.1	0.010	0.000011	0.0030
Surface 1 Irregularity (rms)	wv HeNe		0.012		0.0154
Surface 2 Irregularity (rms)	wv HeNe		0.012		0.0154
Index of refraction		1.52172	1.00E-5	0.000025	0.0013
Index Inhomogeneity	rms dn		1.72E-7		0.0383
Runout surface 1	µm		10.000	0.000000	0.0026
Runout surface 2	µm		10.000	0.000000	0.0019
Airspace	mm	437.172	0.020	0.000071	0.0045
Field Lens 1:	mm	90			
Radius 1	mm	-200	0.005	0.000034	0.0105
Thickness	mm	18	0.005	0.000025	0.0079
Radius 2	mm	-213.11	0.005	0.000029	0.0101
Surface 1 Irregularity (rms)	wv HeNe		0.012		0.0153
Surface 2 Irregularity (rms)	wv HeNe		0.012		0.0153
Index of refraction		1.51974	1.00E-5	0.000001	0.0002
Index Inhomogeneity	rms dn		1.20E-7		0.0084
Runout surface 1	µm		5.000	0.000000	0.0300
Runout surface 2	µm		5.000	0.000000	0.0308
Airspace	mm	115.667	0.010	0.000036	0.0032
Field Lens 2:	mm	64			
Curvature 1	/mm	0	1.25E-7	0.000009	0.0147
Thickness	mm	14	0.010	0.000023	0.0023
Radius 2	mm	-579.01	0.010	0.000002	0.0046
Surface 1 Irregularity (rms)	wv HeNe		0.012		0.0154
Surface 2 Irregularity (rms)	wv HeNe		0.012		0.0154
Index of refraction		1.52023	1.00E-5	0.000002	0.0051
Index Inhomogeneity	rms dn		1.20E-7		0.0065
Runout surface 1	µm		5.000	0.000000	0.0140
Runout surface 2	µm		5.000	0.000000	0.0184
Airspace	mm	16514.45	1.000	0.000060	0.0011
MMT Primary mirror	mm	6512			
Radius	mm	16256	1.000		
Null Corrector residual	waves	0	0.008	0.000000	0.0079
Worst Case				**0.000377**	**0.3503**
RSS				**0.000121**	**0.0815**

APPENDIX D

INFRARED NULL CORRECTORS USING ASPHERIC SURFACES: OPTICAL PRESCRIPTION AND TOLERANCE ANALYSIS

This appendix contains the optical prescriptions for two IR null lenses that each use a single aspheric surface. The first optical design, shown in Fig. D.1, is of limited practical value because of its extreme sensitivity to manufacturing errors. The second null corrector, shown in Fig D.2, will be used to test the MMT primary mirror. A complete tolerance table for this null corrector is given in Table D.1.

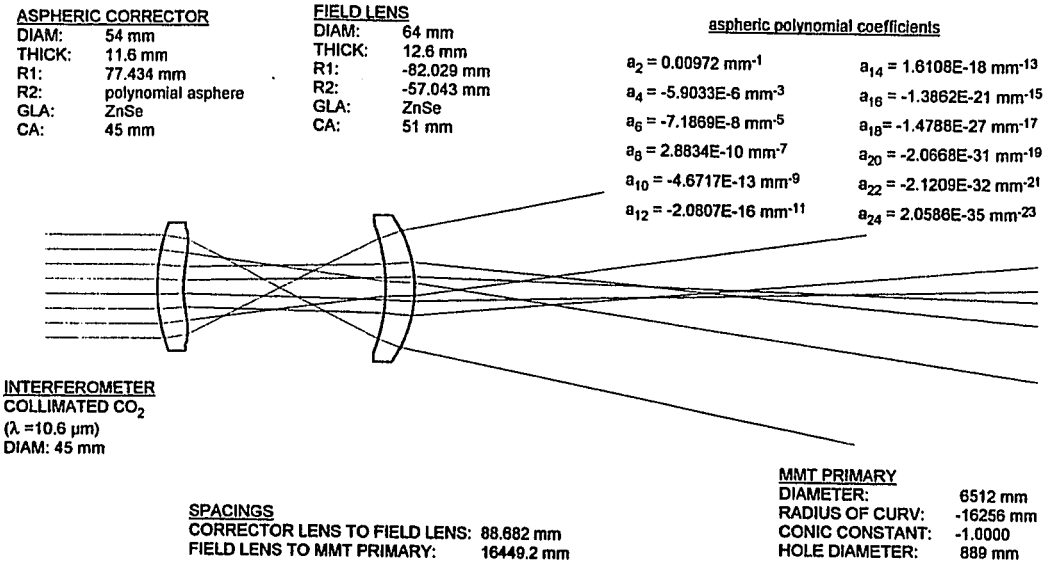

Figure D.1. Layout with prescription of an interesting infrared null corrector for a 6.5-m $f/1.25$ primary mirror.

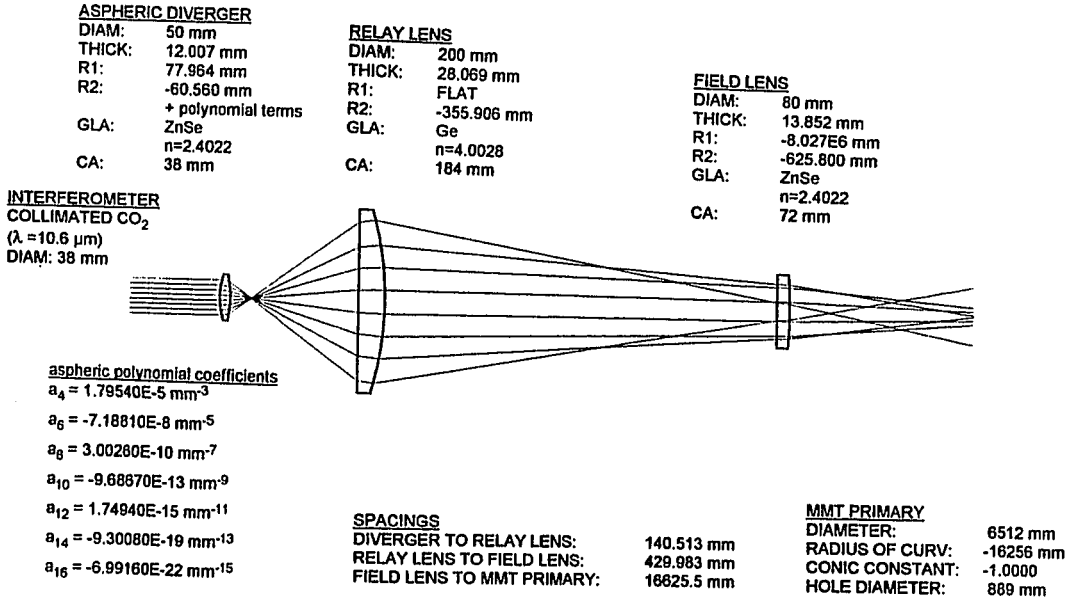

Figure D.2. Layout with prescription of the infrared null corrector that will be used for testing the 6.5-m $f/1.25$ primary mirrors.

Table D.1. Table of tolerances for the MMT IR null corrector.

	units	Design value	tolerance	Conic Constant error	Wavefront rms (at 10.6 μm)
Interferometer	mm	38			
Power	μm	0	0.000	0.000000	0.0000
Reference surface (rms)	wv HeNe		0.01	0.000000	0.0012
Alignment w/null	deg		0.100	0.000000	0.0018
Aspheric Diverger	mm	50			
Radius 1	mm	77.964	0.05	0.000020	0.0032
Thickness	mm	12.007	0.04	0.000000	0.0016
Radius 2	mm	-60.56	0.025	0.000012	0.0028
Surface 1 Irregularity (rms)	wv HeNe		0.5	0.000000	0.0837
Surface 2 Irregularity (rms)	wv HeNe		0.1	0.000000	0.0167
Index of refraction (ZnSe)		2.4022	0.0005	0.000006	0.0031
Index Inhomogeneity	rms dn		3.00E-06	0.000000	0.0068
Runout surface 1	μm		50	0.000000	0.0014
Runout surface 2	μm		50	0.000000	0.0056
Decenter surface 2	μm		50	0.000000	0.0153
Airspace	mm	140.513	0.050	0.000068	0.0089
Relay Lens :	mm	200			
Curvature 1	/mm	0	5.00E-07	0.000030	0.0034
Thickness	mm	28.069	0.050	0.000023	0.0026
Radius 2	mm	-355.906	0.100	0.000036	0.0069
Surface 1 Irregularity (rms)	wv HeNe		0.1	0.000000	0.0359
Surface 2 Irregularity (rms)	wv HeNe		0.1	0.000000	0.0359
Index of refraction (Germanium)		4.0028	1.00E-3	0.000038	0.0066
Index Inhomogeneity	rms dn		5.00E-5		0.2648
Runout surface 1	μm		50	0.000000	0.0220
Runout surface 2	μm		50	0.000000	0.0337
Airspace	mm	429.983	0.100	0.000062	0.0056
Field Lens :	mm	80			
Curvature 1	/mm	1.25E-07	1.00E-6	0.000077	0.0139
Thickness	mm	13.852	0.020	0.000005	0.0005
Radius 2	mm	-625.8	0.100	0.000020	0.0037
Surface 1 Irregularity (rms)	wv HeNe		0.1	0.000000	0.0167
Surface 2 Irregularity (rms)	wv HeNe		0.1	0.000000	0.0167
Index of refraction (ZnSe)		2.4022	0.0005	0.000044	0.0081
Index Inhomogeneity	rms dn		3.00E-06	0.000000	0.0078
Runout surface 1	μm	50	50	0.000000	0.0096
Runout surface 2	μm	50	50	0.000000	0.0147
Airspace	mm	16625.5	1.000	0.000060	0.0000
MMT Primary mirror	mm	6512			
Radius	mm	16256	1.000		
Null Corrector residual	waves	0	0.008	0.000000	0.0076
Worst Case				**0.000500**	**0.6686**
RSS				**0.000158**	**0.2888**

APPENDIX E

GREGORIAN NULL CORRECTORS: OPTICAL PRESCRIPTION AND TOLERANCE ANALYSIS

This appendix contains the optical prescriptions and tolerance tables for four Gregorian null correctors. These systems were designed to use common optical and mechanical components for visible and infrared testing of the MMT and Magellan 6.5-m $f/1.25$ and the 8.4-m $f/1.14$ primary mirrors. This appendix follows the original scenerio of using all four systems, although an alternative design has since been chosen for the MMT and Magellan.

The first large mirror to be tested is the MMT 6.5-m $f/1.25$ primary mirror. The first Gregorian null corrector would be used for infrared testing of the MMT primary mirror during loose-abrasive grinding. The design for this test is shown in Fig. E.1. The tolerance analysis is given in Table E.1. For adapting the system for visible testing, the concave secondary reflector would be replaced by a Mangin mirror and glass field optics would replace the ZnSe field lens. The layout of the visible test is shown in Fig. E.2, and the tolerances are tabulated in Table E.2.

The next large mirrors planned at the University of Arizona after the identical MMT and Magellan primaries are the two LBT 8.4-m $f/1.14$ primary mirrors. The infrared Gregorian null test for these mirrors would require the null corrector to be refit with ZnSe field optics and a concave secondary mirror. The layout for this test is shown

in Fig. E.3 and the tolerances are given in Table E.3. For the visible test of the LBT primaries, the concave secondary reflector would be replaced by the Mangin mirror from the MMT test. Glass field optics would replace the ZnSe field lenses. The layout of this visible test is shown in Fig. E.4, and the usual table of tolerances is given in Table E.4. In addition to the usual tolerances on rms wavefront and conic constant, an error analysis using structure functions has been performed. The structure functions are tabulated in Table E.5 and the results are plotted in Chapter 5.

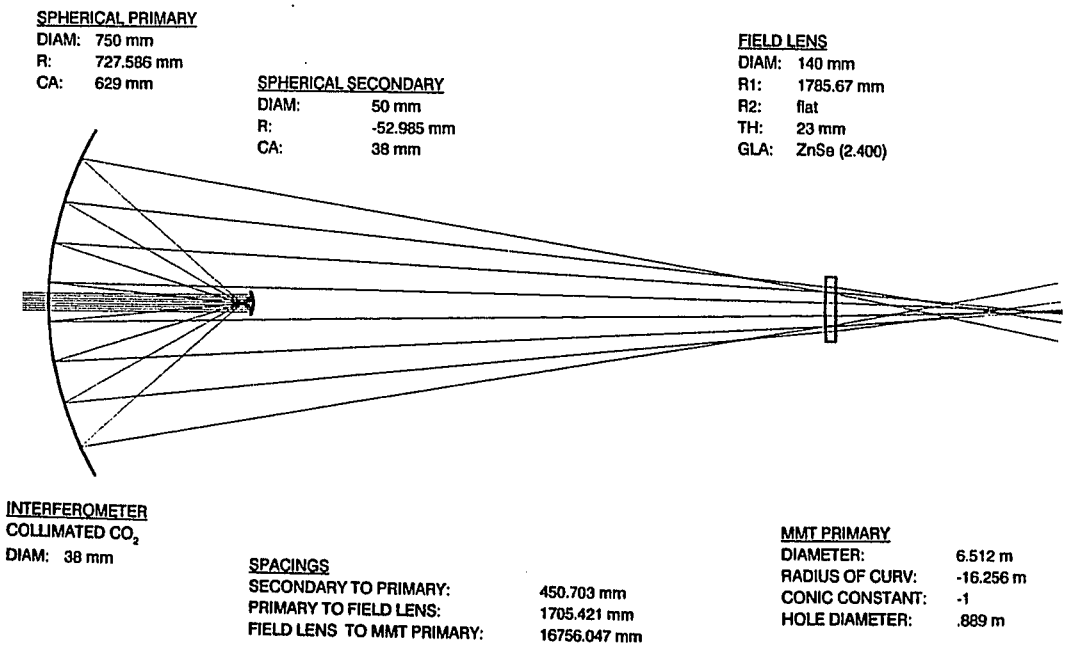

Figure E.1. Layout with prescription of the Gregorian null corrector for infrared testing of the MMT and Magellan 6.5-m $f/1.25$ primary mirrors.

Table E.1. Tolerances for the infrared Gregorian null test of the 6.5-m $f/1.25$ primary mirrors.

	units	Design value	tolerance	Conic Constant error	Wavefront rms @ 10.6 μm
Interferometer	mm	42			
reference surface (rms)	λ (.633μ)	0	0.010	0.000000	0.0012
alignment with optic axis	deg	0	0.100	0.000003	0.0002
residual power	waves	0	0.500	0.000037	0.0016
Secondary mirror:	mm	44			
Radius	mm	-52.985	0.005	0.000076	0.0037
Surface Irregularity (rms)	λ (.633μ)		0.050		0.0119
Runout	μm		50.000	0.000016	0.0055

Table E.1. *continued.*

	units	Design value	tolerance	Conic Constant error	Wavefront rms @10.6 μm
Airspace	mm	450.703	0.050	0.000142	0.0018
Primary corrector mirror:	mm	750			
Radius	mm	727.586	0.020	0.000125	0.0020
Surface Irregularity (rms)	λ (.633μ)		0.010		0.0024
Runout	μm		50.000	0.000016	0.0027
Airspace	mm	1705.421	0.100	0.000284	0.0036
ZnSe Field Lens :	mm	140			
Radius 1	mm	1784.67	0.500	0.000252	0.0047
Thickness	mm	23	0.100	0.000015	0.0002
Curvature 2	/mm	0	1.00E-7	0.000155	0.0044
Surface 1 Irregularity (rms)	λ (.633μ)		0.075		0.0125
Surface 2 Irregularity (rms)	λ (.633μ)		0.075		0.0125
Index of refraction		2.4	5.00E-4	0.000322	0.0054
Index Inhomogeneity	rms dn		3.00E-6		0.0130
Runout surface 1	μm		25.000	0.000006	0.0036
Runout surface 2	μm		25.000	0.000006	0.0046
Airspace	mm	16756.05	1.000	0.000061	0.0003
MMT Primary mirror	mm	6512			
Radius	mm	16256	1.000		
Null Corrector residual	waves	0		0.000000	0.0063
Worst Case				**0.001516**	**0.1042**
RSS				**0.000565**	**0.0292**

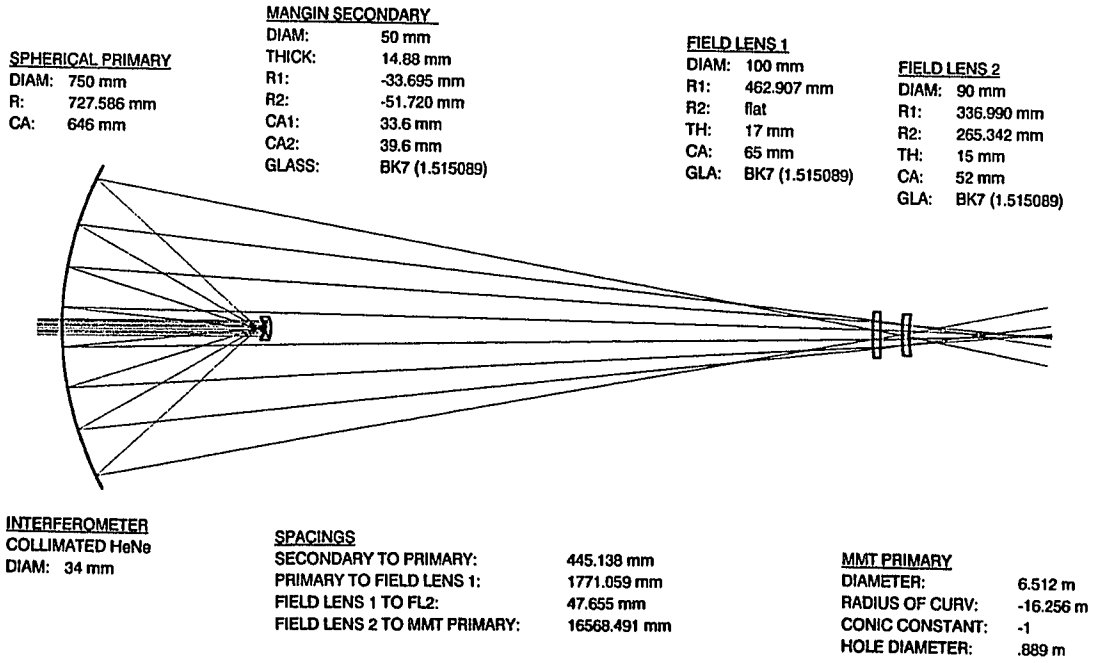

Figure E.2. Layout with prescription of the Gregorian null corrector for visible testing of the MMT and Magellan 6.5-m $f/1.25$ primary mirrors.

Table E.2. Tolerances for the visible Gregorian null test of the MMT and Magellan primary mirrors.

	units	Design value	tolerance	Conic Constant error	Wavefront rms at 633 nm
Interferometer	mm	33.4			
reference surface (rms)	waves	0	0.007	0.000000	0.0140
alignment of beam	deg	0	0.100	0.000000	0.0030
residual power	waves	0	1.000	0.000004	0.0004
Mangin secondary mirror:	mm	44			
Radius 1	mm	-33.695	0.005	0.000019	0.0009
Thickness	mm	14.88	0.005	0.000003	0.0008
Radius 2	mm	-51.72	0.005	0.000008	0.0008
Surface 1 Irregularity (rms)	waves		0.010		0.0206
Surface 2 Irregularity (rms)	waves		0.007		0.0424
Index of refraction		1.515089	1.00E-5	0.000000	0.0000
Index Inhomogeneity	rms dn		1.60E-7		0.0150
Runout surface 1	μm		10.000	0.000000	0.0019
Runout surface 2	μm		10.000	0.000000	0.0049

Table E.2. *continued.*

	units	Design value	tolerance	Conic Constant error	Wavefront rms at 633 nm
Airspace	mm	445.138	0.025	0.000026	0.0008
Primary corrector mirror:	mm	750			
Radius	mm	727.586	0.020	0.000104	0.0036
Surface Irregularity (rms)	waves		0.010		0.0400
Runout	µm		20.000	0.000000	0.0038
Airspace	mm	1771.059	0.025	0.000070	0.0065
Field Lens 1:	mm	100			
Radius 1	mm	462.907	0.006	0.000004	0.0063
Thickness	mm	17	0.010	0.000010	0.0000
Curvature 2	/mm	0	3.00E-8	0.000003	0.0068
Surface 1 Irregularity (rms)	waves		0.012		0.0124
Surface 2 Irregularity (rms)	waves		0.012		0.0124
Index of refraction		1.515089	1.00E-5	0.000006	0.0096
Index Inhomogeneity	rms dn		1.60E-7		0.0086
Runout surface 1	µm		5.000	0.000000	0.0073
Runout surface 2	µm		5.000	0.000003	0.0099
Airspace	mm	47.655	0.015	0.000024	0.0004
Field Lens 2:	mm	90			
Radius 1	mm	336.99	0.005	0.000000	0.0095
Thickness	mm	15	0.005	0.000026	0.0044
Radius 2	mm	265.342	0.005	0.000002	0.0148
Surface 1 Irregularity (rms)	waves		0.012		0.0124
Surface 2 Irregularity (rms)	waves		0.012		0.0124
Index of refraction		1.515089	1.00E-5	0.000001	0.0031
Index Inhomogeneity	rms dn		1.60E-7		0.0076
Runout surface 1	µm		5.000	0.000004	0.0109
Runout surface 2	µm		5.000	0.000001	0.0111
Airspace	mm	16568.49	1.000	0.000059	0.0008
MMT Primary mirror	mm	6512			
Radius	mm	16256	1.000		
Null Corrector residual	waves	0		0.000000	0.0006
Worst Case				**0.000377**	**0.3206**
RSS				**0.000148**	**0.0775**

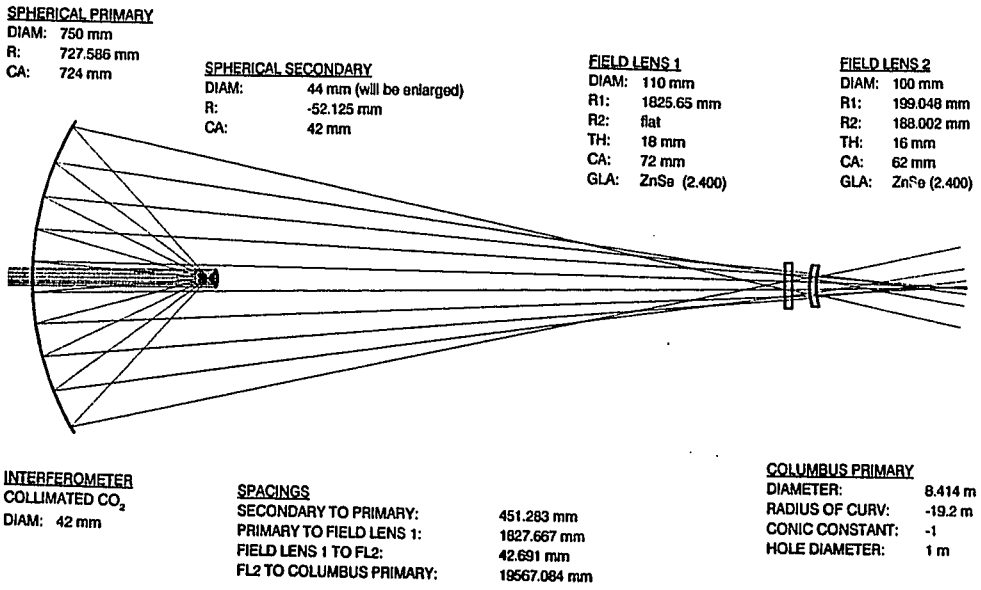

Figure E.3. Layout with prescription of the infrared Gregorian null test for the LBT primary mirrors.

Table E.3. Tolerances for the infrared Gregorian null test of the LBT primary mirror.

	units	Design value	tolerance	Conic Constant error	Wavefront rms at 10.6 μm
Interferometer	mm	42			
reference surface (rms)	λ (.633μ)	0	0.010	0.000000	0.0012
alignment with optic axis	deg	0	0.100	0.000000	0.0006
residual power	waves	0	0.500	0.000034	0.0021
Secondary mirror:	mm	44			
Radius	mm	-52.125	0.010	0.000019	0.0076
Surface Irregularity (rms)	λ (.633μ)		0.050		0.0119
Runout	μm		50.000	0.000018	0.0008
Airspace	mm	451.283	0.100	0.000013	0.0015

Table E.3. *continued.*

	units	Design value	tolerance	Conic Constant error	Wavefront rms at 10.6 μm
Primary corrector mirror:	mm	750			
Radius	mm	727.586	0.020	0.000116	0.0017
Surface Irregularity (rms)	λ (.633μ)		0.010		0.0024
Runout	μm		50.000	0.000007	0.0007
Airspace	mm	1827.667	0.100	0.000296	0.0036
Field Lens 1:	mm	110			
Radius 1	mm	1825.65	0.500	0.000058	0.0062
Thickness	mm	18	0.100	0.000015	0.0004
Curvature 2	/mm	0	1.00E-7	0.000034	0.0042
Surface 1 Irregularity (rms)	λ (.633μ)		0.075		0.0125
Surface 2 Irregularity (rms)	λ (.633μ)		0.075		0.0125
Index of refraction		2.4	5.00E-4	0.000075	0.0081
Index Inhomogeneity	rms dn		3.00E-6		0.0102
Runout surface 1	μm		25.000	0.000006	0.0086
Runout surface 2	μm		25.000	0.000006	0.0099
Airspace	mm	42.691	0.100	0.000034	0.0007
Field Lens 2:	mm	100			
Radius 1	mm	199.048	0.010	0.000011	0.0052
Thickness	mm	16	0.005	0.000140	0.0058
Radius 2	mm	188.002	0.005	0.000001	0.0055
Surface 1 Irregularity (rms)	λ (.633μ)		0.075		0.0125
Surface 2 Irregularity (rms)	λ (.633μ)		0.075		0.0125
Index of refraction		2.4	5.00E-4	0.000032	0.0010
Index Inhomogeneity	rms dn		3.00E-6		0.0091
Runout surface 1	μm		25.000	0.000005	0.0094
Runout surface 2	μm		25.000	0.000008	0.0093
Airspace	mm	19567.084	1.000	0.000050	0.0001
Columbus Primary mirror	mm	8414			
Radius	mm	19200	1.000	0.000050	0.0001
Null Corrector residual	waves	0		0.000000	0.0017
Worst Case				**0.001028**	**0.1796**
RSS				**0.000375**	**0.0401**

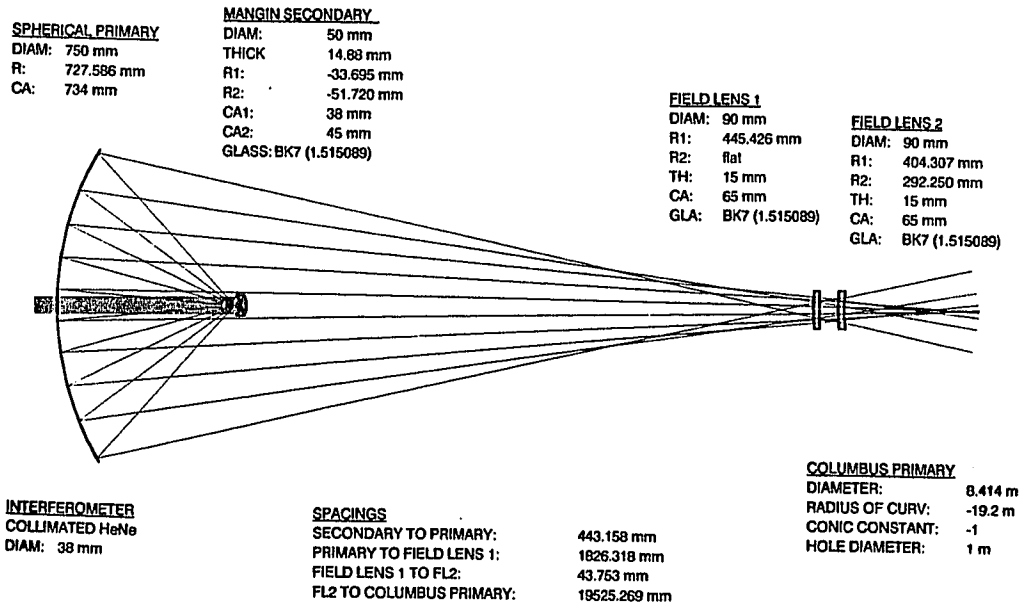

Figure E.4. Layout with prescription of the visible Gregorian null test for the LBT primary mirrors.

Table E.4. Tolerances for the visible Gregorian null test of the LBT primary mirror.

	units	Design value	tolerance	Conic Constant error	Wavefront rms at 633 nm
Interferometer	mm	38			
reference surface (rms)	waves	0	0.007	0.000000	0.0140
alignment of beam	deg	0	0.100	0.000000	0.0048
residual power	waves	0	1.000	0.000003	0.0005
Mangin secondary mirror:	mm	44			
Radius 1	mm	-33.695	0.005	0.000019	0.0026
Thickness	mm	14.88	0.005	0.000003	0.0018
Radius 2	mm	-51.72	0.005	0.000007	0.0020
Surface 1 Irregularity (rms)	waves		0.010		0.0206
Surface 2 Irregularity (rms)	waves		0.007		0.0424
Index of refraction		1.515089	1.00E-5	0.000000	0.0001
Index Inhomogeneity	rms dn		1.60E-7		0.0150
Runout surface 1	μm		10.000	0.000000	0.0048
Runout surface 2	μm		10.000	0.000000	0.0088

Table E.4. *continued.*

	units	Design value	tolerance	Conic Constant error	Wavefront rms at 633 nm
Airspace	mm	443.158	0.025	0.000033	0.0027
Primary corrector mirror:	mm	750			
Radius	mm	727.586	0.020	0.000102	0.0090
Surface Irregularity (rms)	waves		0.010		0.0400
Runout	µm		20.000	0.000000	0.0074
Airspace	mm	1826.318	0.025	0.000074	0.0145
Field Lens 1:	mm	90			
Radius 1	mm	445.426	0.006	0.000005	0.0173
Thickness	mm	15	0.010	0.000014	0.0027
Curvature 2	/mm	0	3.00E-8	0.000006	0.0188
Surface 1 Irregularity (rms)	waves		0.012		0.0124
Surface 2 Irregularity (rms)	waves		0.012		0.0124
Index of refraction		1.515089	1.00E-5	0.000001	0.0022
Index Inhomogeneity	rms dn		1.60E-7		0.0076
Runout surface 1	µm		5.000	0.000000	0.0143
Runout surface 2	µm		5.000	0.000000	0.0163
Airspace	mm	43.753	0.015	0.000030	0.0045
Field Lens 2:	mm	90			
Radius 1	mm	404.307	0.005	0.000008	0.0169
Thickness	mm	15	0.005	0.000007	0.0089
Radius 2	mm	292.25	0.005	0.000008	0.0176
Surface 1 Irregularity (rms)	waves		0.012		0.0124
Surface 2 Irregularity (rms)	waves		0.012		0.0124
Index of refraction		1.515089	1.00E-5	0.000001	0.0021
Index Inhomogeneity	rms dn		1.60E-7		0.0076
Runout surface 1	µm	5	5.000	0.000000	0.0140
Runout surface 2	µm	5	5.000	0.000000	0.0165
Airspace	mm	19525.269	1.000	0.000050	0.0020
LBT mirror	mm	8414			
Radius	mm	19200	1.000		
Null Corrector residual	waves	0		0.000000	0.0080
Worst Case				**0.000371**	**0.4176**
RSS				**0.000145**	**0.0885**

Table E.5. LBT Gregorian null test -- tolerance table showing structure functions.

	units	Design value	tolerance	spatial scale in cm 420.7	210.4	105.2	52.6	26.3	13.1	6.6
				wavefront difference in nm						
Interferometer	mm	38								
ref surface (rms)	waves	0	0.007	12.31	11.61	8.59	5.85	3.63	1.95	0.89
alignment	deg	0	0.100	5.19	4.84	2.10	0.69	1.22	1.19	0.62
residual power	waves	0	1.000	0.94	1.06	1.31	1.59	1.07	1.18	0.63
Mangin secondary:	mm	44								
Radius 1	mm	-33.695	0.005	2.24	3.01	0.10	1.31	0.68	0.33	0.16
Thickness	mm	14.88	0.005	1.60	2.18	0.75	0.87	0.63	0.36	0.20
Radius 2	mm	-51.72	0.005	1.83	2.45	0.70	0.94	0.69	0.40	0.22
Surface 1 (rms)	waves		0.010	18.12	17.08	12.64	8.60	5.34	2.87	1.32
Surface 2 (rms)	waves		0.007	37.31	35.16	26.04	17.72	11.01	5.91	2.71
Index of refraction		1.515089	1.00E-5	0.15	0.22	0.10	0.09	0.04	0.02	0.01
Index Inhomo	rms dn		1.60E-7	13.43	8.95	4.48	2.24	1.12	0.56	0.28
Runout surface 1	µm		10.000	4.64	4.03	2.26	1.71	0.74	0.29	0.08
Runout surface 2	µm		10.000	14.27	10.03	7.43	5.25	3.19	1.77	0.93
Airspace	mm	443.158	0.025	1.78	2.30	0.71	1.00	0.23	0.29	0.18
Prim corr mirror:	mm	750								
Radius	mm	727.586	0.020	4.69	4.24	5.60	1.53	0.88	0.54	0.29
Surface Irr (rms)	waves		0.010	35.18	33.16	24.55	16.71	10.38	5.57	2.56
Runout	µm		20.000	10.28	7.45	5.36	3.90	2.13	1.11	0.55
Airspace	mm	1826.318	0.025	12.14	14.61	8.89	6.18	3.02	1.41	0.68
Field Lens 1:	mm	90								
Radius 1	mm	445.426	0.006	12.29	13.18	12.04	5.27	2.84	1.54	0.79
Thickness	mm	15	0.010	0.20	1.68	1.39	1.29	0.46	0.12	0.10
Curvature 2	/mm	0	3.00E-8	12.04	12.89	11.82	5.16	2.77	1.50	0.77
Surface 1 (rms)	waves		0.012	9.06	8.54	6.32	4.30	2.67	1.43	0.66
Surface 2 (rms)	waves		0.012	9.06	8.54	6.32	4.30	2.67	1.43	0.66
Index of refraction		1.515089	1.00E-5	18.99	20.90	17.76	8.50	4.46	2.34	1.19
Index Inhomo	rms dn		1.60E-7	6.77	4.51	2.26	1.13	0.56	0.28	0.14
Runout surface 1	µm		5.000	17.64	14.47	8.87	6.33	4.31	2.53	1.39
Runout surface 2	µm		5.000	23.50	16.81	9.85	5.69	3.42	1.92	1.01
Airspace	mm	43.753	0.015	1.77	1.74	2.86	1.63	0.39	0.34	0.22

Table E.5. *continued.*

	units	Design value	tolerance	spatial scale in cm 420.7	210.4	105.2	52.6	26.3	13.1	6.6
				wavefront difference in nm						
Field Lens 2:	mm	90								
Radius 1	mm	404.307	0.005	12.14	13.00	11.93	5.20	2.81	1.52	0.78
Thickness	mm	15	0.005	7.72	9.47	5.08	3.98	1.91	0.87	0.41
Radius 2	mm	292.25	0.005	26.15	30.76	21.05	13.16	6.53	3.14	1.54
Surface 1 (rms)	waves		0.012	9.06	8.54	6.32	4.30	2.67	1.43	0.66
Surface 2 (rms)	waves		0.012	9.06	8.54	6.32	4.30	2.67	1.43	0.66
Index of refraction		1.515089	1.00E-5	8.53	10.47	5.89	4.55	2.19	0.99	0.47
Index Inhomo	rms dn		1.60E-7	6.77	4.51	2.26	1.13	0.56	0.28	0.14
Runout surface 1	µm	5	5.000	22.50	17.75	10.91	7.45	5.02	2.93	1.60
Runout surface 2	µm	5	5.000	22.60	18.55	12.43	9.24	6.61	3.94	2.18
Airspace	mm	19525.27	1.000	1.12	1.84	1.24	0.84	0.35	0.09	0.02
LBT Primary	mm	8414								
Radius	mm	19200	1.000							
Design Residual	waves			7.04	7.26	7.24	7.43	5.01	2.86	1.54
Worst Case				420.08	396.32	281.80	181.37	106.90	58.68	29.22
RSS WAVEFRONT				88.35	83.26	60.59	38.90	23.44	12.77	6.29
RSS SURFACE				**44.18**	**41.63**	**30.30**	**19.45**	**11.72**	**6.39**	**3.15**

REFERENCES

Ai, C. and J. C. Wyant, "Effect of spurious reflection on phase shift interferometry," Appl. Opt. **27**, 3039-3045 (1988).

Allen, L., J. R. P. Angel, J. D. Mongus, G. A. Rodney, R. R. Shannon, C. P. Spoelhof, "The Hubble Space Telescope optical systems failure report," NASA Report (NASA, Washington, D. C., November 1990).

Alpern, M., "The eyes and vision," in *Handbook of Optics*, W. G. Driscoll and W. Vaughan, Editor, (McGraw-Hill, New York, 1978) pp. 12-1 to 12-35.

Anderson, D. S. and R. C. Crawford, "The MMT7 mirror: analysis of the rms difference specifications and their impact on the fabrication and testing," in *Advances in Fabrication and Metrology for Large Optics,* J. B. Arnold, R. E. Parks, Editors, Proc. SPIE **966**, 332-340 (1988).

Anderson, D. S., J. R. P. Angel, J. H. Burge, W. B. Davison, S. T. DeRigne, B. B. Hille, D. A. Ketelsen, W. C. Kittrell, H. M. Martin, R. H. Nagel, T. J. Trebisky, S. C. West, and R. S. Young, "Stressed-lap polishing of 3.5-m *f*/1.5 and 1.8-m *f*/1.0 mirrors," in *Advanced Optical Manufacturing and Testing II*, V. J. Doherty, Editor, Proc. SPIE **1531**, 260-269 (1991).

Anderson, J. A. and R. W. Porter, "Ronchi's method of optical testing," *Astrophysical Journal* **70**, 175-181 (1929).

Angel, J. R. P., "8- m borosilicate honeycomb mirrors," in *ESO Conference on Very Large Telescopes and Their Instrumentation,* M.-H. Ulrich, Editor, Proc. ESO **30**, (European Southern Observatory, Garching, Germany, 1988) pp. 281-300.

Angel, J. R. P., "The revolution in ground-based telescopes," *Quart. J. Roy. Astron. Soc.*, **31**(2), 141-152 (1990).

Angel, J. R. P., "Designing 8-m mirrors for the best sites," in *Identification, Optimization, and Protection of Optical Telescope Sites,* R. L. Millis Editor, (Lowell Obs. Press , Flagstaff, 1986) pp. 167-175.

Arfken, G., *Mathematical Methods for Physicists*, (Academic Press, Orlando, 1985).

Arnold, S. M., "Electron beam fabrication of computer-generated holograms, "Opt. Eng. **24**, 803-807 (1985).

Arnold, S. M., "Desktop computer encoding of electron-beam written holograms," in *Computer-Generated Holography II,* S. H. Lee, Editor, Proc. SPIE **884**, 23-26 (1988).

Arnold, S. M., "How to test an asphere with a computer-generated hologram," in *Holographic Optics: Optically and Computer Generated,* I. N. Cindrich and S. H. Lee, Editors, Proc. SPIE **1052**, 191-197 (1989).

Arnold, S. M., "An interferometer for aspheric testing: calibration and error compensation," *Precision Interferometric Metrology*, Proc. ASPE **5**, 83-86 (1992).

Aver'yanova, G. I., N. P. Larionov, A. V. Lukin, K. S. Mustafin, and R. A. Rafikov, "The testing of large aspherical surfaces by means of synthetic circular holograms," Sov. J. Opt. Tech. **42**, 347-349 (1975).

Baber, S. C., "Application of high resolution laser writers to computer generated holograms and binary diffractive optics," in *Holographic Optics: Optically and Computer Generated*, I. N. Cindrich and S. H. Lee, Editors, Proc. SPIE **1052**, 66-76 (1989).

Bahcall, J., Editor, *The Decade of Discovery in Astronomy and Astrophysics* (National Academy Press, Washington D. C., 1991).

Baker, L. R., "Specification and measurement of optical component flaws," in *Optical Component Specifications for Laser-Based Systems and Other Modern Optical Systems*, R. E. Fischer and W. J Smith, Editors, Proc. SPIE **607**, 2-13 (1986).

Barr, L. D., "The U. S. national large telescope project: The NNTT and others," in *ESO Conference on Very Large Telescopes and Their Instrumentation,* M.-H. Ulrich, Editor, Proc. ESO **30**, (European Southern Observatory, Garching, Germany, 1988) pp. 73-92.

Barr, L. D., J. M. Beckers, E. T. Pearson, T. W. Hobbs, and J. Sprangenberg-Jolley, "Reducing mirror seeing problems in meniscus mirrors," in *ESO Conference on Very Large Telescopes and Their Instrumentation,* M.-H. Ulrich, Editor, Proc. ESO **30**, (European Southern Observatory, Garching, Germany, 1988) pp. 595-613.

Barrell, H. and J. E. Sears, "The refraction and dispersion of air for the visible spectrum," Phil. Trans. Roy. Soc. London Ser. **A 238**,1-64 (1939).

Beckers, J. M. and M. Tarenghi, "ESO - VLT program status report," in *ESO Conference on Progress in Telescope and Instrumentation Technologies,* M.-H. Ulrich,

Editor, Proc. ESO **42**, (European Southern Observatory, Garching, Germany, 1992) pp. 13-24.

Biedermann, K. and O. Holmgren, "Large-size distortion-free computer-generated holograms in photoresist," Appl. Opt. **16**, 2104-2016 (1977).

Born, M. and E. Wolf, *Principles of Optics,* (Pergamon, Oxford, 1980).

Bowen, I. S., "Final adjustments and tests of the Hale Telescope," *Pub. Astron. Soc. Pac.* **62**, 91-97 (1950).

Brown, B. R. and A. W. Lohmann, "Complex spatial filtering with binary masks," Appl. Opt. **5**, 967-969 (1966).

Brown, B. R. and A. W. Lohmann, "Computer-generated binary holograms," *IBM Journal of Research and Development* **13**, 160-168 (1969).

Brown, D. S., "Optical specification of ground based telescopes," in *Optical System Design, Analysis, and Production,* P. J. Rogers and R. E. Fischer, Editors, Proc. SPIE **399**, 12-14 (1983).

Bruning, J. H., D. R. Herriott, J. E. Gallagher, D. P. Rosenfeld, A. D. White, and D. J. Brangaccio, "Digital wavefront measuring interferometer for testing optical surfaces and lenses," Appl. Opt. **13**, 2693-2703 (1974).

Bryngdahl, O. and F. Wyrowski, "Digital holography -- computer-generated holograms," in *Progress in Optics* **28**, E. Wolf, Editor (Elsevier, New York, 1990) pp. 1-86.

Bryngdahl, O. and W. Lee, "Shearing interferometer in polar coordinates," JOSA **64**, 1606-1615 (1974).

Buchroeder, R. A., L. H. Elmore, R.V. Shack, and P. N. Slater, *Optical Sciences Technical Report No. 79*, (University of Arizona, Tucson, 1972) pp. 18-21.

Burch, C. R., "On reflection compensators for testing paraboloids," Mon. Not. R. Astron. Soc. **96**, 438-461 (1936).

Burge, J. H., "Null test optics for large aspheric mirrors," *OSA Annual Meeting Technical Digest, 1991* (Optical Society of America, Washington D. C.) **17**, pp. 124-125 (1991a).

Burge, J. H., "Null test optics at Steward Observatory," *Columbus Project Technical Memo* **UA-03-91**, Steward Observatory, University of Arizona, Tucson AZ (1991b).

Burge, J. H., "Interferometric metrology for a 6.5-meter *f*/1.25 paraboloidal mirror," in *Optical Fabrication and Testing Workshop Technical Digest, 1992* (Optical Society of America, Washington, D. C.) **24**, 172-175 (1992a).

Burge, J. H., "Design and analysis of null test optics for large aspheric mirrors," in *Progress in Telescope and Instrumentation Technologies*, M.-H. Ulrich, Editor, Proc. ESO **42**, (European Southern Observatory, Garching, Germany, 1992b) pp. 273-276.

Buynov, G. N., N. P. Larionov, A. V. Lukin, K. S. Mustafin, and R. A. Rafikov, "Holographic interferometric inspection of aspherical surfaces," *Optical Technology* **38**, 194-197 (1971).

Carré, P., "Installation et utilisation du comparateur photoélectriqu et interférentiel du Bureau International des Poids et Mesures," *Metrologia* **2**, 13-23 (1966).

Caulfield, H. J., P. Mueller, D. Dvore, A. Epstein, and J. S. Loomis, "Computer holograms for optical testing," in *Contemporary Methods of Optical Fabrication*, C. L. Stonecypher, Editor, Proc. SPIE **306**, 154-157 (1981).

Chaffee, F. H. and R. H. Cromwell, "Seeing measurements at the Multiple Mirror Telescope obtained with a very high quality primary mirror," in *Advanced Technology Optical Telescopes IV*, L. D. Barr, Editor, Proc. SPIE **1236**, 13-17 (1990).

Chaffee, F. H., D. R. Blanco, C. B. Foltz, C.C. Janes, H. N. Lester, A. D. Poyner, J. T. Williams, S. C. Criswell, D. G. Fabricant, and G. D. Schmidt, "The MMT Conversion: a status report," in *Advanced Technology Optical Telescopes IV*, L. D. Barr, Editor, Proc. SPIE **1236**, 507-519 (1990).

Chen, C. T., "Using a conventional optical design program to design holographic optical elements," Opt. Eng. **19**, 649-653 (1980).

Chen, C. L. and T. R. Osborne, "Quantization effects on the fields of electron-beam generated cylindrical zone plates," Appl. Opt. **26**, 2342-2347 (1987).

Cheng, Y. Y., and J. C. Wyant, "Two-wavelength phase shifting interferometry," Appl. Opt. **23**, 4539-4543 (1984).

Chu, D. C., J. R. Fienup, and J. W. Goodman, "Multiemulsion on-axis computer generated hologram," Appl. Opt. **12**, 1386-1388 (1973).

Church, E. L. and P. Z. Takacs, "Specification of the surface figure and finish of optical elements in terms of system performance," in *Specification and Measurement of Optical Systems*, L. R. Baker, Editor, Proc. SPIE **1781**, (1992).

Collier, R. J., C. B. Burckhart, and L. H. Lin, *Optical Holography*, (Academic Press, San Diego, 1971).

Colucci, D. and P. Wizinowich, "Millisecond phase acquisition at video rates," Appl. Opt. **31**, 5919-5925 (1992).

Cornejo, A. and D. Malacara, "Caustic coordinates in Platzeck-Gaviola test of conic mirrors," Appl. Opt. **17**, 18-19 (1978).

Cornejo-Rodriguez, A., "Ronchi Test," in *Optical Shop Testing*, D. Malacara, Editor, (Wiley, New York, 1992) pp. 321-365.

Couder, A., "Procédé d'examen d'un miroir concave non-sphérique," Rev. Opt. Theor. Instrum., **6**,49-55 (1927).

Cowley, D. J., J. A. Sovka, D. Salmon, and R. A. McLaren, "Control of dome seeing," in *ESO Conference on Very Large Telescopes and Their Instrumentation*, M.-H. Ulrich, Editor, Proc. ESO **30**, (European Southern Observatory, Garching, Germany, 1988) pp. 897-906.

Cox, J. A., T. Werner, J. Lee, S. Nelson, B. Fritz, and J. Bergstrom, "Diffraction efficiency of binary optical elements," in *Computer and Optically Formed Holographic Optics*, I. Cindrich and S. H. Lee, Editors, Proc. SPIE **1211**, 116-124 (1990).

Creath, K. and J. C. Wyant, "Holographic and speckle tests," in *Optical Shop Testing*, D. Malacara, Editor (Wiley, New York, 1992) pp. 599-651.

Creath, K., "Comparison of phase-measurement algorithms," in *Surface Characterization and Testing*, K. Creath, Editor, Proc. SPIE **680**,19-28 (1986).

Creath, K., "Phase-measurement interferometry techniques," in *Progress in Optics* **26**, E. Wolf, Editor (Elsevier, New York, 1988) pp. 349-393.

Creath, K. and J. C. Wyant, "Direct phase measurement of aspheric surface contours," in *Optical Manufacturing, Testing, and Aspheric Optics*, G. M. Sanger, Editor, Proc. SPIE **645**, 101-106 (1986).

Dall, H. E., "A null test for paraboloids," J. Br. Astron. Assoc. **57**, 201-205 (1947).

DeVoe, C. E., "Limitations on aspheric surface testing with simple null correctors," Master Thesis, Optical Sciences Center, University of Arizona, Tucson (1989).

Dierickx, P., D. Enard, F. Merkle, L. Noethe, R. N. Wilson, "ESO VLT II: Optical specifications and performance of large optics," in *Advanced Technology Optical Telescopes IV*, L. D. Barr, Editor, Proc. SPIE **1236**, 138-151 (1990).

Dierickx, P., "Optical performance of large ground-based telescopes," J. Mod. Opt. **39**, 569-588 (1992).

Dimitroff, G. Z. and J. G. Baker, *Telescopes and Accessories*, (Blakiston Co., Philadelphia, 1945).

Dörband, B. and H. J. Tiziani, "Testing aspheric surfaces with computer-generated holograms: analysis of adjustment and shape errors," Appl. Opt. **24**, 2604-2611 (1985).

Dressler, A., "Progress report on the Magellan 8-m telescope project," in *Advanced Technology Optical Telescopes IV*, L. D. Barr, Editor, Proc. SPIE **1236**, 42-46 (1990).

Edlén, B., "The refractive index of air," Metrologia **2**, 71-80 (1966).

Emmel, P. M. and K. M. Leung, "A new instrument for routine optical testing of general aspherics," in *Optical Components: Manufacture and Evaluation*, D. Nicholson, Editor, Proc. SPIE **171**, 93-99 (1979).

Espiard, J. and B. Favre, "Contrôle en laboratoire de la qualité du système optique d'un télescope de 1,524 m de diamètre," *Nouvelle Rev. d'Optique Appliquée*, **1** (6), 395-400 (1970).

Evans, D. S. and J. D. Mulholland, *Big and Bright A History of the McDonald Observatory*, (University of Texas Press, Austin, 1986).

Everett, P. N., "Metrology of lithographic features: balanced illumination eliminating diffractive bias," Appl. Opt. **32**, 1216-1224 (1993).

Facey, T. A., A. L. Nonnenmacher, D. P. Chadwick, "Fabrication of large aperture mirrors for astronomical telescopes," in *Advanced Technology Optical Telescopes IV*, L. D. Barr, Editor, Proc. SPIE **1236**, 597-604 (1990).

Fell, B., ""Optical surfaces": computer program facilitates work in optical shop," *Opt. Sci. Newsletter* **2** (5) 127-133 (Optical Sciences Center, University of Arizona, Tucson, 1968).

Fercher, A. F., "Computer-generated holograms for testing optical elements: error analysis and error compensation," Opt. Acta **23**, 347-365 (1976).

Forbes, F., "The effects of wind loads on large telescopes," in *ESO Conference on Very Large Telescopes and Their Instrumentation*, M.-H. Ulrich, Editor, Proc. ESO **30**, (European Southern Observatory, Garching, Germany, 1988) pp. 831-843.

Forbes, G. and A. Jones, "Toward global optimization with adaptive simulated annealing," in *International Lens Design Conference*, G. N. Lawrence, Editor, Proc. SPIE **1354**, 144-153 (1990).

Foucault, L. M., "Memoire sur la Construction des Telescopes en Verre Argente," Annales de l'Observatoire de Paris, **5**, 197-237 (1859).

Fried, D. L., "Optical resolution through a randomly inhomogeneous medium for very long and very short exposures," J. Opt. Soc. Am. **56**, 1372-1379 (1966).

Frieden, B. R., *Probability, Statistical Optics, and Data Testing*, (Springer-Verlag, Berlin, 1983).

Friedman, I. and R. E. Casas, "Design and tolerance analysis of two null corrector designs for the Space Telescope fine guidance aspheric collimating mirror," in *Contemporary Methods of Optical Fabrication*, C. L. Stonecypher, Editor, Proc. SPIE **306**, 176-182 (1981).

Furey, L., T. Dubos, D. Hansen, and J. Samuels-Schwartz, "Hubble Space Telescope primary-mirror characterization by measurement of the reflective null corrector," Appl. Opt. **32**, 1703-1714 (1993).

Gascoigne, S. C. B., K. M. Proust, and M. O. Robins, *The Creation of the Anglo-Australian Observatory*, (Cambridge University Press, Cambridge, 1990).

Gaskill, J. D., *Linear Systems, Fourier Transforms, and Optics*, (Wiley, New York, 1978).

Gaviola, E., "On the quantitative use of the Foucault knife-edge test," J. Opt. Soc. Am. **26**, 163-169 (1936).

Gerchman, M. C., "Testing generalized rotationally-symmetric aspheric optical surfaces using null reflective compensating components," in *Ultraprecision Machining and Automated Fabrication of Optics*, D. L. Decker and R. A. Jones, Editors, Proc. SPIE **676**, 60-65 (1986).

Ghozeil, I, "Hartmann and other screen tests," in *Optical Shop Testing*, D. Malacara, Editor, (Wiley, New York, 1992) pp. 367-396.

Ghozeil, I. and J. E. Simmons, "Screen test for large mirrors,"Appl. Opt. **13**, 1773-1777 (1974).

Ginsburg, R. H., "Outline of tolerance from performance specification to toleranced drawings," Opt. Eng. **20**, 175-180 (1981).

Goodman, J. W., *Introduction to Fourier Optics*, (McGraw-Hill, San Francisco, 1968).

Gray, D. S., "Tolerance sensitivity and optimization," Appl. Opt. **9**, 523-526 (1970).

Greivenkamp, J. E., "Sub-Nyquist interferometry," Appl. Opt. **26**, 5245-5258 (1987).

Greivenkamp, J. E. and J. H. Bruning, "Phase shifting interferometry," in *Optical Shop Testing*, D. Malacara, Editor, (Wiley, New York, 1992) pp. 501-598.

Gremaux, D. A. and N. C. Gallagher, "Limits of scalar diffraction theory for conducting gratings," Appl. Opt. **32**, 1948-1953 (1993).

Hariharan, P., *Optical Holography,* (Cambridge University Press, Cambridge, 1984).

Hartmann, J., "An improvement of the Foucault knife-edge test in the investigation of telescope objectives," Astrophys. J. **27**, 254-259 (1908).

Hearn, G., "Practical use of generalized simulated annealing optimization on microcomputers," in *International Lens Design Conference*, G. N. Lawrence, Editor, Proc. SPIE **1354**, 186-191 (1990).

Hilbert, R. S. and M. P. Rimmer, "A variable refractive null lens," Appl. Opt. **9**, 849-852 (1970).

Hildebrand, B. P., K. A. Haines, and R. Larkin, "Holography as a tool in the testing of large aperture optics," Appl. Opt. **6**, 1267-1269 (1967).

Hill, J. M., "Optical design, error budget, and specifications for the Columbus Project Telescope," in *Advanced Technology Telescopes IV,* L. D. Barr, Editor, Proc. SPIE **1236**, 86-107 (1990).

Hochgraf, N. A., "Autocollimator, scanning pentaprism used to measure angular collimation," Optical Sciences Center Newsletter, Jan-Mar pp. 41-42 (1969).

Hoffman, J. M., and W. L. Wolfe, "Cryogenic refractive indices of ZnSe, Ge, and Si at 10.6 μm," Appl. Opt. **30**, 4014-4016 (1991).

Holleran, R.T., "Immersion null test for aspherics," Appl. Opt. **2**, 1336-1337 (1963).

Holleran, R.T., "An algebraic solution for the small lens null compensator," Appl. Opt. 7, 137-144 (1968).

Houston, J. B. Jr., C. J. Buccini, and P. K. O'Neill, "A laser unequal path interferometer for the optical shop," Appl. Opt. **6**, 1237-1242 (1967).

Ichioka, Y. and A. W. Lohmann, "Interferometric testing of large optical components with circular holograms," Appl. Opt. **11**, 2597-2602 (1972).

Józwicki, R., M. Kujawinska, and L. Salbut, "New contra old wavefront measurement concepts for interferometric optical testing," Opt. Eng. **31**, 422-433 (1992).

Kajanto, M., E. Byckling, J. Fagerholm, J. Heikonen, J. Turunen, A. Vasara, and A. Salin, "Photolithographic fabrication method of computer-generated holographic interferograms," Appl. Opt. **28**, 778-784 (1989).

Kathman, A. D., R. L. Clark, H. J. Rogers, M. G. Temmen, P. E. Fileger, and C. F. Hester, "Wave optics modeling of CGH designs," in *Computer-Generated Holography II*, S. H. Lee, Editor, Proc. SPIE **884**, 13-22 (1988).

King, H. C., *The History of the Telescope*, (Dover, New York, 1955).

Kingslake, R., "The interferometer patterns due to the primary aberrations," *Trans. of the Optical Society* **27**, 94-105 (1925).

Kodaira, K., "Japan National Large Telescope (Suburu) Project," in *ESO Conference on Progress in Telescope and Instrumentation Technologies*, M.-H. Ulrich, Editor, Proc. ESO **42**, (European Southern Observatory, Garching, Germany, 1992) pp. 43-46.

Kok, Y. and N. C. Gallagher, "Relative phases of electromagnetic waves diffracted by a perfectly conducting rectangular-grooved grating," J. Opt. Soc. Am. A **5**, 65-73 (1988).

Koliopolis, C. L. and D. S. Anderson, "High resolution phase measurements of optical surfaces," in *Ultraprecision Machining and Automated Fabrication of Optics*, D. L. Decker and R. A. Jones, Editors, Proc. SPIE **676**, 90-93 (1986).

Korhonen, T. K., "Interferometric method for optical testing and wavefront error sensing," *Advanced Technology Optical Telescopes II*, L. D. Barr and B. Mack, Editors, Proc. SPIE **444**, 249-252 (1984).

Korhonen, T. K., "Optics for the Nordic Optical Telescope," *Observational Astrophysics*, R. F. Nielson, Editor, Proc. of "Nordisk Forskerkursus," (Copenhagen University Observatory, 1987) pp. 198-209.

Kreis, T., "Digital holographic interference-phase measurement using the Fourier-transform method," J. Opt. Soc. Am. A **3**, 847-855 (1986).

Küchel, M. and W. Wiedmann, "In-process metrology for large astronomical mirrors," in *Advanced Optical Manufacturing and Testing,* L. R. Baker, P. R. Reid, and G. M. Sanger, Editors Proc. SPIE **1333**, 280-294 (1990)

Küchel, M. and E. Heynacher, "Testing as an integral tool for fabrication of large mirrors," *ESO Conference on Very Large Telescopes and Their Instrumentation,* M.-H. Ulrich, editor, Proc. ESO **30**, (European Southern Observatory, Garching, Germany, 1988) pp. 495-504.

Kuiper, G. P. and B. M. Middlehurst Editor, *Telescopes,* (Univ. of Chicago Press, Chicago, 1960).

Kwon, O. Y., D. M. Shough, and R. A. Williams, "Stroboscopic phase-shifting interferometry," Opt. Lett. **12**, 855-857 (1987).

Landgrave, J. E. A. and J. R. Moya, "Dummy lens for the computer optimization of autostigmatic null correctors," Appl. Opt. **26**, 2673-2675 (1987).

Larionov, N. P., A. V. Lukin, and R. A. Rafikov, "Holographic inspection of aspherical surfaces," Sov. J. Opt. Tech. **46**, 229-231 (1979).

Larionov, N. P., A. V. Lukin, and R. A. Rafikov, "Testing of aspherical surfaces by means of axial synthesized holograms," Sov. J. Opt. Tech. **47**, 667-670 (1980).

Lee, A. J. and D. P. Casasent, "Computer generated hologram recording using a laser printer," Appl. Opt. **26**, 136-138 (1987).

Lee, W. H., "Sampled Fourier transform hologram generated by computer," Appl. Opt. **9**, 639-643 (1970).

Lee, W. H., "Binary synthetic holograms," Appl. Opt. **13**, 1677-1682 (1974).

Lee, W. H., "Computer-generated holograms: techniques and applications," in *Progress in Optics* **16**, E. Wolf, Editor (Elsevier, New York, 1978) pp. 119-232.

Lee, W. H., "Recent developments in computer-generated holograms," in *Recent Advances in Holography,* T. C. Lee and P. N. Tamura, Editors, Proc SPIE **215**,52-58 (1980).

Lesem, L. B., P. M. Hirsch, J. A. Jordan, Jr. "The kinoform: A new wavefront reconstruction device," *IBM J. Res. Develop.* **13**, 150-155 (1969).

Leung, K. M., J. C. Lindquist, and L. T. Shepherd, "E-beam computer-generated holograms for aspheric testing," in *Recent Advances in Holography,* T. C. Lee and P. N. Tamura, Editors, Proc. SPIE **215**, 70-74 (1980).

Leung, K. M., S. M. Arnold, and J. C Lindquist, "Using e-beam written computer-generated holograms to test deep aspheric wavefronts," in *Contemporary Methods of Optical Fabrication,* C. L. Stonecypher, Editor, Proc. SPIE **306**, 161-167 (1981).

Lieth, E. N. and J. Upatnieks, "Reconstructed wavefronts and communication theory," J. Opt. Soc. Amer. **52**, 1123-1130 (1962).

Linfoot, E. H., "On interpretation of the Foucault test," Proc. R. Soc. London, Ser. A **193**, 248-259 (1948).

Logue, J., "Fabrication of binary optics using electron beam lithography," in *Computer-Generated Holography II,* S. H. Lee, Editor, Proc. SPIE **884**, 95-99 (1988).

Lohmann, A. W. and D. P. Paris, "Binary Fraunhofer holograms, generated by computer," Appl. Opt. **6**, 1739-1748 (1967).

Loomis, J. S., "Computer-generated holography and optical testing," in *Recent Advances in Holography,* T. C. Lee and P. N. Tamura, Editors, Proc. SPIE **215**, 59-69 (1980a).

Loomis, J. S., "Computer-generated holography and optical testing," Opt. Eng. **19**, 679-685 (1980b).

Lukin, A. V. and K. S. Mustafin, "Holographic methods of testing aspherical surfaces," Sov. J. Opt. Tech. **46**, 237-244 (1979).

MacGovern, A. J. and J. C. Wyant, "Computer-generated holograms for testing optical elements," Appl. Opt. **10**, 619-624 (1971).

Malacara, D., "Imaging the wavefront under test in interferometry," in *Southwest Conference on Optics,* R. S. McDowell and S. C Stotlar, Editors, Proc. SPIE **540**, 34-40 (1985).

Malacara, D., A. Cornejo, and M. V. R. K. Murty, "Bibliography of various optical testing methods," Appl. Opt. **14**, 1065-1080 (1975).

Malacara, D. and S. L. DeVore, "Interferogram Evaluation and Wavefront Fitting," in *Optical Shop Testing,* D. Malacara, Editor, (Wiley, New York, 1992) pp. 455-499.

Malacara, D. and A. Cornejo, "Null Ronchi test for aspherical surfaces," Appl. Opt. **13**, 1778-1780 (1974).

Martin, H. M., "Image motion as a measure of seeing quality," Publ. Astron. Soc. Pacific **99**, 1360-1370 (1987).

Martin, H. M., J. M. Hill, and R Angel, "The new ground-based optical telescopes," Physics Today **44**(3), 22-30 (1991).

Martin, H. M., D. S. Anderson, J. R. P. Angel, J. H. Burge, W. B. Davison, S. T. DeRigne, B. B. Hille, D. A. Ketelsen, W. C. Kittrell, R. McMillan, R. H. Nagel, T. J. Trebisky, S. C. West, and R. S. Young, "Stressed-lap polishing of 1.8-m *f*/1 and 3.5-m *f*/1.5 primary mirrors," *ESO Conference on Progress in Telescope and Instrumentation Technologies,* M.-H. Ulrich, Editor, Proc. ESO **42**, (European Southern Observatory, Garching, Germany, 1992) pp. 169-172.

Martin, H. M., J. H. Burge, and S. C. West, "Environmental effects in the testing of large astronomical mirrors," in *Precision Interferometric Metrology* (The American Society for Precision Engineering, Raleigh NC, 1992) Proc. ASPE **5**, pp. 72-75.

McCann, J. T., "Applications of diamond turned null reflectors for generalized aspheric metrology," in *Optical Metrology and Testing III: Recent Advances in Industrial Optical Inspection*, C. P. Grover, Editor, Proc. SPIE **1332**, 843-849 (1990).

McCann, J. T., "The design, fabrication, and application of diamond machined null lenses for testing generalized aspheric surfaces," in *Advanced Optical Manufacturing and Testing II*, V. J. Doherty, Editor, Proc. SPIE **1531**, 134-146 (1991).

McHugh, T. J. and H. A. Levenstein, "An overview of binary optics at the Perkin-Elmer Corporation," in *Computer-Generated Holography II,* S. H. Lee, Editor, Proc. SPIE **884**, 100-104 (1988).

Meinel, A. B., "Design of Reflecting Telescopes" in *Telescopes*, G. P. Kuiper and B. M. Middlehurst, Editors, (Univ. of Chicago Press, Chicago, 1960) pp. 25-42.

Meinel, A. B., "Astronomical Telescopes" in *Applied Optics and Optical Engineering* **5**, R. Kingslake, Editor, (Academic Press, New York, 1969) pp. 133-182.

Mercier, R., "Holographic testing of aspheric surfaces," in *First European Conference on Optics Applied to Metrology*, M. Grosmann and P. Meyrueis, Editors, Proc SPIE **136**, 208-214 (1977).

Mercier, R. and S. Lowenthal, "Comparison of in-line carrier frequency holograms in aspheric testing," Opt. Comm. **33**, 251-256 (1980).

Michelson, A. A., "On the correction of optical surfaces," Astrophys. J. **47**, 283-288 (1918).

Mielenz, K. D., K. N. Nefflen, W. R. C. Rowley, D. C. Wilson, and E. Engelhard, "Reproducibility of helium-neon laser wavelengths at 633 nm," Appl. Opt. **7**, 289-292 (1968).

Miroshnikov, M. M., S. V. Lyubarskii, and Y. P. Khimich, "Optical telescope mirrors," Sov. J. Opt. Technol. **57**, 523-535 (1990).

Moharam, M. G. and T. K. Gaylord, "Rigorous coupled-wave analysis of metallic surface-relief gratings," JOSA A **3**, 1780-1787 (1986).

Montagnino, L. A. and A. Offner, "Design and testing with a reflective null system," *The Space Telescope*, NASA SP-392, 135-138 (1976).

Montagnino, L. A., "Test and evaluation of the Hubble Space Telescope 2.4-meter primary mirror," in *Large Optics Technology*, G. M. Sanger, Editor, Proc. SPIE **571**, 182-190 (1985).

Morales, A. and D. Malacara, "Geometric parameters in the Hartmann test of aspherical mirrors," Appl. Opt. **22**, 3957-3959 (1983).

Moya, J. R. and J. E. A. Landgrave, "Third-order design of refractive Offner compensators," Appl. Opt. **26**, 2667-2672 (1987).

Müller, R. and H. Höness, "Manufacturing of mirror substrates for large telescopes made from Zerodur glass ceramic," in *ESO Conference on Very Large Telescopes and Their Instrumentation*, M.-H. Ulrich, Editor, Proc. ESO **30**, (European Southern Observatory, Garching, Germany, 1988) pp. 313-318.

Nelson, J. E., "Segmented mirror design for a 10-meter telescope," in *Instrumentation in Astronomy III*, D. L. Crawford, Editor, Proc. SPIE **172**, 31-38 (1979).

Nelson, J. E. and T. Mast, "Current performance of the Keck Telescope," *ESO Conference on Progress in Telescope and Instrumentation Technologies*, M.-H. Ulrich, Editor, Proc. ESO **42**, (European Southern Observatory, Garching, Germany, 1992) pp. 3-11.

Offner, A., "A null corrector for paraboloidal mirrors," Appl. Opt **2**, 153-155 (1963).

Offner, A., and D. Malacara, "Null tests using compensators," in *Optical Shop Testing*, D. Malacara, Editor, (Wiley, New York, 1992) pp. 427-454.

Ojeda-Castañeda, J., "Foucault, Wire, and Phase Modulation Tests" in *Optical Shop Testing*, D. Malacara, Editor, (Wiley, New York, 1992) pp. 265-320.

Ono, A. and J. C. Wyant, "Plotting errors measurement of CGH using an improved interferometric method," Appl. Opt. **23**, 3905-3910 (1984).

Osmer, P. "The Gemini Project: overview," *ESO Conference on Progress in Telescope and Instrumentation Technologies*, M.-H. Ulrich, Editor, Proc. ESO **42**, (European Southern Observatory, Garching, Germany, 1992) pp. 35-37.

Parks, R. E., "Removal of test optics errors," in *Advances in Optical Metrology I*, N. Balasubramanian and J. C. Wyant, Editors, Proc. SPIE **153**, 56-63 (1978).

Parks, R. E., "Optical component specifications," in *International Lens Design Conference*, R. E. Fischer, Editor, Proc. SPIE **237**, 462-463 (1980).

Parks, R. E., "Optical specifications and tolerances for large optics," in *Optical Specifications: Components and Systems*, W. J. Smith and R. E. Fischer, Editor, Proc. SPIE **406**, 98-105 (1983).

Pastor, J., "Hologram interferometry and optical testing," Appl. Opt. **8**, 525-531 (1969).

Patterson, J. S. and R. R. Crout, "Optical quality requirements for large mirror systems," in *Optical Systems Engineering III*, W. H. Taylor, Editor, Proc. SPIE **389**, 18-21 (1983).

Pietraszkiewicz, K., "Tolerance of the refractive index gradient in optical materials," Appl. Opt. **17**, 1697-1700 (1978).

Plaskett, J. S., "The 82-inch mirror of the McDonald Observatory," Astrophys. J. **89**, 84-98 (1939).

Platzeck, R. and E. Gaviola, "On the errors of testing and a new method for surveying optical surfaces and systems," J. Opt Soc. Am. **29**, 484-500 (1939).

Press, W. H., B. P. Flannery, S. A. Teukolsky, and W. T. Vetterling, *Numerical Recipes in C*, (Cambridge University Press, Cambridge, 1988).

Puryaev, D. T. and N. S. Shandin, "Design of lens compensators for testing the concave astronomical mirrors of large telescopes," Sov. J. Opt. Technol. **46**, 207-209 (1979).

Puryayev, D. T., "Compensators for inspecting the quality of large-diameter parabolic mirrors," Sov. J. Opt. Technol. **40**, 238-241 (1973).

Racine, R., D. Salmon, D. Cowley, and J. Sovka, "Mirror, dome, and natural seeing at CFHT," Publ. Aston. Soc. Pac. **103**, 1020-1032 (1991).

Rank, D. H., P. Yoder, Jr., and J. Vrabel, "Sensitivity of a rapid test for high speed parabolic mirrors," J. Opt. Soc. Am. **39**, 36-38 (1949).

Rayces, J. L., "Exact relation between wave aberration and ray aberration," Opt. Acta **11**, 85-88 (1964).

Reitmayer, F. and E. Schuster, "Homogeneity of optical glass," Appl. Opt. **11**, 1107-1111 (1972).

Rimmer, M., "Analysis of perturbed lens systems," Appl. Opt. **9**, 533-537 (1970).

Rimmer, M., "A tolerancing procedure based on modulation transfer function (MTF)," in *Computer Aided Optical Design*, R. E. Fischer, Editor, Proc. SPIE **147**, 66-70 (1978).

Ritchey, G. W., "On methods of testing optical mirrors during construction," Astrophys. J. **19**, 53-69 (1904).

Robbert, C. F., P. R. Yoder, and L. A. Montagnino, "Typical error budget for testing a high-performance aspheric telescope mirror," in *Contemporary Optical Systems and Components Specification*, R. E. Fischer, Editor, Proc. SPIE **181**, 56-63 (1979).

Roberts, F. E. and P. Langenbeck, " Homogeneity evaluation of very large disks," Appl. Opt. **8**, 2311-2314 (1969).

Roddier, C. and F. Roddier, "Wavefront reconstruction from defocused images and the testing of ground-based optical telescopes," J. Opt. Soc. Am. A in press (1993).

Roddier, C. and F. Roddier, "Interferogram analysis using Fourier transform techniques," Appl. Opt. **26**, 1668-1673 (1987).

Roddier, F., "Mirror aberration communication," *Physics Today* **41** (11), p.117 (1990).

Rodgers, J. M., "A null-lens design approach for centrally obscured components," in *Current Developments in Optical Engineering and Diffraction Phenomena*, Proc. SPIE **679**, 17-20 (1986).

Ronchi, V., "Le Frange di Combinazioni Nello Studio delle Superficie e dei Sistemi Ottici," *Riv. Ottica Mecc. Precis.*, **4**, 9 (1923).

Ronchi, V., "Forty years of the grating interferometer," Appl. Opt. **3**, 437-451 (1964).

Ross, F. E., "Parabolizing mirrors without a flat," Astrophys. J. **98**, 341-346 (1943).

Rubin, P. L., "Refractive null correctors for aspheric surfaces," Appl. Opt. **15**, 3080-3083 (1976).

Sasian, J. M., "Design of null lens correctors for the testing of astronomical optics," Opt. Eng. **27**, 1051-1056 (1988).

Sasian, J. M., "Optimum configuration of the Offner null corrector: testing an *f*/1 paraboloid," in *Surface Characterization and Testing II*, J. E. Greivenkamp and M. Young, Editors, Proc. SPIE **1164**, 8-17 (1989).

Saunders, J. B., "An improved optical test for spherical aberration," J. Opt. Soc. Am. **44**, 664 (1954).

Saunders, J. B. and R. J. Bruening, "A new interferometric test and its application to the 84-inch reflecting telescope at Kitt Peak National Observatory," Astron. J. **73**, 415-430 (1968).

Schlauch, J., "Construction of a Dall null tester," *Sky and Telescope* **18**, 222-226 (1959).

Schwarzschild, B., "Hubble's primary mirror has the wrong shape," Phys. Today **43** (8), 17-19 (1990).

Schwider, J., "Advanced evaluation techniques in interferometry," in *Progress in Optics* **28**, E. Wolf, Editor (Elsevier, New York, 1990) pp. 271-359.

Selberg, L. A., "Interferometer accuracy and precision," in *Metrology: Figure and Finish*, B. Truax, Editor, Proc. SPIE **749**, 8-18 (1987).

Selberg, L. A., "Radius measurement by interferometry," Opt. Eng. **31**, 1961-1966 (1992).

Shack, R. V. and G. W. Hopkins, "The Shack interferometer," Opt. Eng. **18**, 226-228 (1979).

Shack, R. V., Course notes from "Principles of Optical System Design," Optical Sciences 506 , University of Arizona (1988).

Shack, R. V., "A short-cut procedure for designing autostigmatic null correctors", Optical Sciences Center Newsletter **1**, 13 (University of Arizona, Tucson, 1967).

Shafer, D., "Zoom null lens," Appl. Opt. **18**, 3863-3865 (1979).

Shafer, D., "Null lens design techniques," Appl. Opt. **31**, 2184-2188 (1992).

Shulz, F. and J. Schwider, "Interferometric testing of smooth surfaces," in *Progress in Optics* **13**, E. Wolf, Editor (Elsevier, New York, 1976) pp. 93-167.

Sinnott, R. W. and K. Nyren, "S & T's guide to the world's largest telescopes," *Sky and Telescope*, **86** (1), 27-32 (1993).

Smith, D.C., "Testing diamond turned aspheric optics using computer-generated holographic (CGH) interferometry," in *Contemporary Methods of Optical Fabrication*, C. L. Stonecypher, Editor, Proc. SPIE **306**, 112-121 (1981).

Smith, W. J., "Fundamentals of establishing an optical tolerance budget," in *Geometrical Optics*, R. E. Fischer, W. H. Price, and W. J. Smith, Editors, Proc. SPIE **531**, 196-204, (1985).

Stahl, H. P. and D. Ketelsen, "Aspheric figure generation using feedback from an infrared phase-shifting interferometer," in *Large Optics Technology*, G. M. Sanger, Editor, Proc. SPIE **571**, 22-29 (1985).

Stoltzmann, D. E., and P. Ceravolo, "Ross null test for conic mirrors,"Appl. Opt. **32**, 1189-1199 (1993).

Strittmatter, P., "Columbus Project Telescope," in *Advanced Technology Optical Telescopes IV*, L. D. Barr, Editor, Proc. SPIE **1236**, 71-84 (1990).

Sturlesi, D. and D. C. O'Shea, "Future of global optimization in optical design," in *International Lens Design Conference*, G. N. Lawrence, Editor, Proc. SPIE **1354**, 54-68, (1990).

Swanson, G. J. and W. B. Veldkamp, "Infrared applications of diffractive optical elements," in *Holographic Optics: Design and Applications*, I. N. Cindrich, Editor, Proc. SPIE **883**, 155-162 (1988).

Sweatt, W. C., "Describing holographic optical elements as lenses," J. Opt. Soc. Am. **67**, 803-808 (1977).

Takahashi, T., K. Konno, M. Kawai, and M., Isshiki, "Computer-generated holograms for testing aspheric lenses," Appl. Opt. **15**, 546-549 (1976).

Takeda, M., H. Ida, and S. Kobayashi, "Fourier-transform method of fringe-pattern analysis for computer-based topography and interferometry," J. Opt. Soc. Am. **72**, 156-160. (1982)

Tarenghi, M., "European Southern Observatory (ESO) 3.5 m New Technology Telescope," in *Advanced Technology Optical Telescopes III*, L. D. Barr, Editor, Proc. SPIE **628**, 213-220 (1986)

Tatarski, V. I., *Wave Propagation in a Turbulent Medium*, (McGraw-Hill, New York, 1961).

Texereau, J., "Refiguring the 82-inch McDonald Reflector's Optics," Sky and Telescope **28** (12.) 345-348 (1964).

Twyman, F., "Interferometers for the experimental study of optical systems from the point of view of the wave theory," *Philosophical Magazine* **35**, 49-58 (1918).

Urquhart, K. S., S. H. Lee, C. C. Guest, M. R. Feldman, and H. Farhoosh, "Computer aided design of computer generated holograms for electron beam fabrication," Appl. Opt. **28**, 3387-3396 (1989).

Van Dyke, N., "Eight meter fused silica mirror blank fabrication," in *ESO Conference on Very Large Telescopes and Their Instrumentation*, M.-H. Ulrich, Editor, Proc. ESO **30**, (European Southern Observatory, Garching, Germany, 1988) pp. 319-327.

Welford, W. T., "On the limiting sensitivity of the star test for optical instruments," J. Opt. Soc. Am. **50**, 21-23 (1960).

Weller, S. W., "Neural network optimization, components, and design selection," in *International Lens Design Conference*, G. N. Lawrence, Editor, Proc. SPIE **1354**, 371-378 (1990).

West, S. C., J. H. Burge, R. S. Young, D. S. Anderson, C. Murguic, D. A. Ketelsen, and H. M. Martin, "Optical metrology of two large highly aspheric telescope mirrors," Appl. Opt. **31**, 7191-7197 (1992).

Willey, R. R., R. George, J. Odell, W. Nelson, "Minimized cost through optimized tolerance distribution in optical assemblies," in *Optical Systems Engineering III*, W. H. Taylor, Editor, Proc. SPIE **389**, 12-17 (1983).

Willey, R. R., "The impact of tight tolerances and other factors on the cost of optical components," in *Optical Systems Engineering IV*, P. R. Yoder, Jr., Editor, Proc. SPIE **518**, 106-111 (1984).

Wilson, R. N., F. Franza, and L. Noethe, "Active optics I. A system for optimizing the optical quality and reducing the costs of large telescopes," J. Mod. Optics **34**, 485-509 (1987).

Wilson, R. N. and L. Noethe, "Mirrors and supports," in *ESO Conference on Very Large Telescopes and Their Instrumentation*, M.-H. Ulrich, Editor, Proc. ESO **30**, (European Southern Observatory, Garching, Germany, 1988) pp. 373-388.

Wilson, R. N., F. Franza, L. Noethe, and G. Andreoni, "Active optics IV. Set up and performance of the optics of the ESO New Technology Telescope (NTT) in the observatory," J. Mod. Optics **38**, 219-243 (1991).

Wilson, R. N., "'Matching error' (spherical aberration) in the Hubble Space Telescope (HST): some technical comments," ESO Messenger **61**, 22-24 (1990).

Wizinowich, P. L., "Phase shifting interferometry in the presence of vibration: a new algorithm and system," Appl. Opt. **29**, 3271-3279 (1990).

Wollensak, R. J. and C. A. Rose, "Fabrication and test of 1.8-meter (71-inch) diameter, high-quality U.L.E.™ mirror," *The Space Telescope*, NASA SP-392, 123-134 (1976).

Womack, K. H., "Instantaneous phase measurement using spatial synchronous detection," Opt. Eng. **23**, 391-395 (1984a).

Womack, K. H., "Frequency domain description of interferogram analysis," Opt. Eng. **23**, 396-400 (1984b).

Woolf, N. J., "High resolution imaging from the ground," Ann. Rev. Astron. Astrophys. **20**, 367-398 (1982).

Wyant, J. C., "Testing aspherics using two-wavelength holography," Appl. Opt. **10**, 2113-2118 (1971).

Wyant, J. C., "Interferometric testing of aspheric surfaces," in *Interferometric Metrology*, N. A. Massie, Editor, Proc. SPIE **816**, 19-39 (1987).

Wyant, J. C. and V. P. Bennett, "Using computer-generated holograms to test aspheric wavefronts," Appl. Opt. **11**, 2833-2839 (1972).

Wyant, J. C. and P. K. O'Neill, "Computer-generated hologram; null lens test of aspheric wavefronts," Appl. Opt. **13**, 2762-2765 (1974).

Yatagai, T. and H. Saito, "Dual computer-generated holograms for testing aspherical surfaces," Opt. Acta **26**, 985-993 (1979).

Yoder, P. R., "Further analysis of the 'Lower' test for high-speed parabolic mirrors," J. Opt. Soc. Am. **49**, 439-440 (1959).